ABSTRACT

Title of dissertation: EVOLUTIONARY SPACECRAFT
DESIGN USING A GENERALIZED
COMPONENT-RESOURCE MODEL

Matthew Leo Marcus
Doctor of Philosophy, 2019

Dissertation directed by: Professor Raymond Sedwick
Department of Aerospace Engineering

A new framework is proposed for modeling complex multidisciplinary systems as a collection of components and resource flows between them. The framework is developed for modeling and optimizing conceptual spacecraft designs. Its goal is to remain sufficiently general to address any space mission without modification of the developed model or code. Spacecraft are modeled as a collection of components and the resources that flow between them. New missions can be considered and capabilities added by simply adding components and resources. Constraints can be imposed on a component basis or system-wide, and are based on the flow of the resources within the system. Additionally, the proposed component-resource model and framework can address many complex systems engineering problems beyond spacecraft design by a similar implementation.

Design optimization is performed by a genetic algorithm utilizing a variable length genome. This allows the algorithm to represent the variable number of components that could be present in a system design, enabling a more open-ended design

capability than previous frameworks of this nature. Systems are evaluated through a user-defined simulation, and results can be presented in any trade space of interest based on the designs' performance in the simulation. We apply the framework to the design of a simple Earth orbiting, data gathering mission, as well as to the design of low Earth orbit active debris removal spacecraft constellations.

EVOLUTIONARY SPACECRAFT DESIGN USING
A GENERALIZED COMPONENT-RESOURCE MODEL

by

Matthew Leo Marcus

Dissertation submitted to the Faculty of the Graduate School of the
University of Maryland, College Park in partial fulfillment
of the requirements for the degree of
Doctor of Philosophy
2019

Advisory Committee:
Professor Raymond Sedwick, Chair/Advisor
Professor David Akin
Professor Shapour Azarm
Professor Christine Hartzell
Professor Marshall Kaplan
Professor Linda Schmidt

Acknowledgments

The proceeding chapters of this dissertation document work that I have done. That information is more or less already documented in one location or another, so the task is merely one of compilation. In this section, however, I must attempt to capture all the work that others have done on my behalf, making it possible for me to complete this work. Inevitably I will leave something and someone (or many somethings and someones) out, so if that is you, I apologize, and assure you it was merely an oversight resulting from my overworked, overtired state.

First and foremost I'd like to thank my advisor, Professor Raymond Sedwick for the opportunity to work on this project over the past four to six years, depending on how you count it, as well as supporting me in my many parallel endeavors over the same time period.

I must also thank the other members of my committee, Professors David Akin, Sharpour Azarm, Christine Hartzell, and Marshall Kaplan for agreeing to serve on my committee and for sparing their invaluable time reviewing the manuscript. A particular thanks to Professors Akin and Azarm for their invaluable advice and guidance throughout my studies, with their particular expertise on the subject matter.

Thanks to my colleagues in the Space Power and Propulsion Laboratory and the Center for Orbital Debris Education and Research for their friendship and support throughout my graduate tenure.

Table of Contents

List of Tables

List of Figures

List of Abbreviations

ADR   Active Debris Removal

COTS Commercial Off-The-Shelf
CR   Component-Resource

DO   Debris Object
DP   Deorbit Package
DPS   Dedicated Propulsion System
DSS   Distributed Satellite System

EDL   Entry, Descent, and Landing
EELV Evolved Expendable Launch Vehicle
EIRP   Effective Isentropic Radiated Power
ESPA EELV Secondary Payload Adapter

GA   Genetic Algorithm
GESDA Generalized Evolutionary Spacecraft Design Architecture
GINA Generalized Information Network Analysis

HGA   High Gain Antenna

ISS   International Space Station

L1   Level 1 (genome)
L2   Level 2 (genome)
L3   Level 3 (genome)
LAT   Laser Ablation Tug
LEO   Low Earth Orbit
LGA   Low Gain Antenna

MBSE Model Based Systems Engineering
MMH Monomethyl Hydrazine
MP   MegaPixels

NEAR Near Earth Asteroid Rendezvous
NSGA-II Non-Dominated Sorting Genetic Algorithm II
NTO   Nitrogen Tetroxide

ODAR Orbital Debris Assessment Report

OEDMS	Orbital Express Demonstration Manipulator System
PS2	PlanetScope 2
PVA	Photovoltaic Array
RTG	Radioisotope Thermoelectric Generator
SA	Simulated Annealing
SCC	Similar Component Crossover
SMA	S-band Multiple Access
TASC	Triangular Advanced Solar Cells
TDRS	Tracking and Data Relay Satellite
TDRSS	Tracking and Data Relay Satellite System
TLE	Two-Line Element
TRL	Technology Readiness Level
TWTA	Traveling Wave Tube Amplifier
VEGA	Vehicle Encoding Genetic Algorithm
WTRL	Weighted Technology Readiness Level
EDDE	Electro-Dynamic Debris Eliminator
GMAT	General Mission Analysis Tool
GOLD	Gossamer Orbit Lowering Device
KSII	KnightSat II
NASA	National Aeronautics and Space Administration
STK	Systems Toolkit
SMAP	Soil Moisture Active Passive Spacecraft
SPOON	Satellite Parts On Orbit Now database
TRIS	Towed Rigidizable Inflatable Structure

Chapter 1: Introduction

1.1 Motivation

Space mission design and selection occurs in a competitive, resource con-
strained environment. Current practice is struggling to keep up with increasing
demands. There are limited resources available not only for developing and flying
missions, but also for producing the proposals for these missions. Demands are
growing on the concurrent design teams that develop these proposals. They are
being asked to work on more design proposals than ever before, each of which is in-
creasingly complex. Mission managers and principal investigators bring forth many
questions about the designs produced. They wonder how the overall trade space is
affected by seemingly specific decisions in one part of the design.

Additionally, there is an ongoing proliferation of small satellites and cubesats
[1–6], and launch costs for such spacecraft have fallen rapidly in the previous decade
[7]. These factors have fostered a growing interest in the design, fabrication, and
flight of spacecraft and payloads at a university and small business level, without
access to concurrent design teams. In fact, the work of this dissertation includes such
a design problem, detailed in Chap. 2, investigating the removal of debris objects
from Low Earth Orbit (LEO). This design problem is particularly timely. The same

factors mentioned above have combined, dramatically accelerating the rate at which new objects are placed in orbit. This rate is expected to further accelerate in the coming decade, with the advent of "megaconstellations" and further reductions in launch cost.

The work detailed in Chap. 2 motivates the remainder of this dissertation. The proceeding chapters present a new model-based framework for complex system design, with a focus on spacecraft design, to meet these needs. The tools and models presented in this dissertation share a philosophy with model-based systems engineering (MBSE), an emerging systems engineering technique [8]. MBSE seeks to manage complex multidisciplinary systems with a unified digital model, tracking decision variables and other properties of the system. This model then provides this information as necessary to discipline-specific submodels and tracks them for systems engineering purposes.

The Component-Resource (CR) model and framework proposed in this dissertation has arrived at a similar design philosophy in parallel. The CR model analyzes a complex system by reducing it to a collection of components and resources that flow between them. This may also include resources flowing between the system and the external environment. The ultimate goal is to implement this model in an automated design framework, pairing it with a multiobjective optimization scheme. This combined framework would perform multidisciplinary, multiobjective optimization in a rapid, automated manner, augmenting existing design teams, working to solve the emerging issues outlined above. Such a model would additionally allow a

systems engineer to make changes to a specific area of a complex system design and observe how those changes affect the system as a whole.

1.2   The Orbital Debris Problem

Over the last decade or so, there has been a growing interest in the reduction of inactive mass in orbit, composed of defunct satellites, spent upper stages of launch vehicles, and smaller fragments of hardware placed in orbit. Additionally, as stated above, the proliferation of smallsats and cubesats, combined with a drop in launch costs, has led to acceleration of the increase of the on-orbit population. Further acceleration is anticipated in the near future with megaconstellations expected to increase the number of active objects on orbit by an order of magnitude.

The majority of these new objects are and will be placed in LEO, where relative velocities during a conjunction can be several km/s. As a result, any collision in this region between two intact debris objects, or a debris object and a large fragment will likely be catastrophic, fragmenting the intact objects and creating thousands of additional pieces of debris [9]. This, along with a handful of explosions and intentional fragmentation actions by major spacefaring nations has lead to a growing concern in the population of debris objects in LEO [10]. Kessler and Cour-Palais theorized as early as 1978 that such growth in the orbital population, if left unchecked, could lead to a cascade of fragmentation collisions [11]. They predicted that such an "ablation cascade" could lead to the formation of debris belts around the Earth, following processes similar to the formation of the asteroid belt.

As shown by Liou [9], the debris population is already unstable, and will continue to grow even with no new launches. Liou went on to simulate the debris evolution over the next two hundred years and found that, assuming a repeating launch cadence matching that between 2002 and 2010, the removal of 5-10 large, intact objects per year was required to stabilize the debris population. In reality, the worldwide launch cadence has accelerated by 35% in the eight years since Liou's study was published, and it is now common for multiple spacecraft to be deployed from each launch. As a result, 5-10 objects per year should be considered a bare minimum. As will be discussed further in Chap. 2, this was used as a baseline, developing a program to actively remove 100 objects from LEO over ten years. These objects were drawn from Liou's list of objects with the highest mass collision probability products.

1.3   Metaheuristic Multiobjective Optimization

On its own, the CR model is capable of modeling complex systems such as a spacecraft. It provides a similar capability to MBSE, ensuring that at a high level a design closes. However, this capability alone is not the true purpose of the model. The model is not necessarily the best option for that task alone. The CR model enables design space exploration in open-ended component selection problems like spacecraft design. In this class of problems, exhaustive design space searches are not possible due to an ambiguous number of components [12].

Austin and others [13,14] have proposed graph-based methods for MBSE-based down-selection processes for similar types of component selection problems. Their scheme involves loading complete component libraries and predetermining feasible combinations of components given inter-component dependencies, thus limiting the size of the design space before beginning any optimization.

As these authors indicate, their scheme works for a relatively small number of components and design solutions, and when the topology between component classes is well defined. However, as the complexity of the design space and the possible interactions between components grows, one must be careful to not inadvertently eliminate feasible yet nonintuitive combinations of components. As the size of a complex design space grows, it becomes labor intensive to define the topology and interoperability between components in the general case. The down selection procedure must also be repeated for each design problem, even if they use the same component libraries. The authors note this, particularly in [13], concluding the work with a call for a smaller number of more general inference rules.

Complex interactions between different disciplines involved in the problem, as well as the discrete design space, make it difficult to address the problem using analytic design space exploration tools. Therefore, metaheuristic optimization options were considered, with a particular focus on genetic algorithms (GAs), which have seen extensive use in other Aerospace design problems [15].

Metaheuristics are stochastic search methods that employ a general strategy, often nature inspired, to find sufficiently good solutions to complex optimization problems [16]. For GAs, the strategy is to mimic the processes of biological evolution,
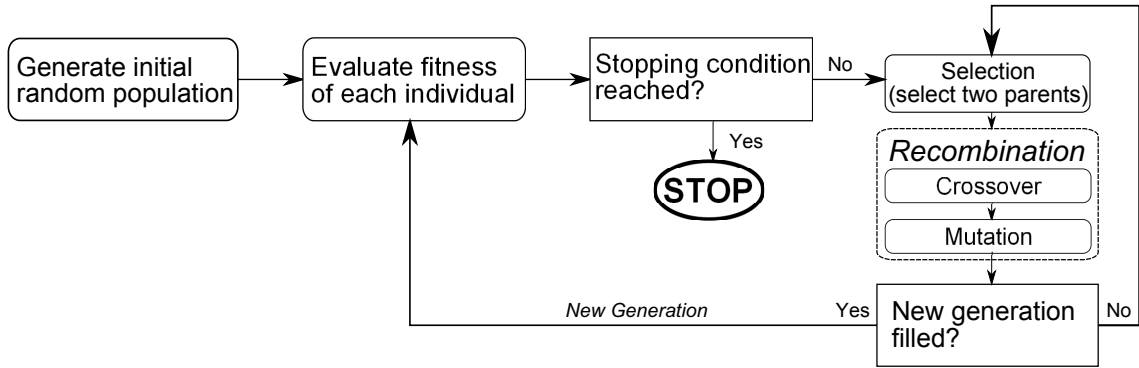
Figure 1.1: Genetic algorithm process. The algorithm is initialized with a population of random individuals. For each generation, the fitness is evaluated, and parents are selected from the population. Recombination produces child genomes from the parent genomes, populating the next generation. This process iterates over successive generations until some stopping condition is reached.

as outlined in Fig. 1.1. The design variables for the problem are considered "genes", and are concatenated into a "genome" array. An initial population of designs is created with random genomes. All members of the population are assigned a fitness score, which is a function of the user's objectives. Pairs of parents are selected from the population based on their fitness scores. The parent genomes are then mixed and matched to create child designs through a processes known as recombination. Crossover swaps genes between the two parent genomes (design vectors), producing two child designs. Mutation then changes a small number of randomly chosen genes to some random value. The mutation operator prevents the GA from becoming trapped in a local minimum by introducing genes not present in the population.

Recombination is repeated with different pairs of parents until a new generation of designs is filled. In some implementations, an additional step known as

elitism is added, where the most fit portion of the current generation is "cloned" directly into the new generation. Successive generations are iterated until some stopping condition is reached, often either convergence or sufficient performance with respect to all objective functions.

The design vector for an individual may be expressed through the genome in a number of ways. Each gene may be expressed as a binary value (a binary-coded genome), a real number (real-coded), or an integer (integer-coded). Two common types of crossover operators exist; n-point crossover, and uniform crossover. In n-point crossover, illustrated in Fig. 1.2, a number n of crossover points are placed at random locations in each of the parent genomes. Each child inherits genes from a given parent until it reaches a crossover point, at which it flips, inheriting genes from the other parent. In uniform crossover, illustrated in Fig. 1.3, a child inherits each individual gene randomly from one parent or the other. Each gene in a child genome then has some random probability of mutation p_m. Operating variables such as n, p_m, the population size, and the elitism fraction, are specified by the user, tuning the algorithm. This tuning is critical for ensuring good performance of the GA.

1.4   Integrated Space Mission Design

1.4.1   The Current State of Integrated Mission Design

The primary intent of this work is addressing the increasing demands on the the concurrent space mission design process. It therefore seems warranted to briefly discuss current practice in that field. Proposal-level design efforts are performed by
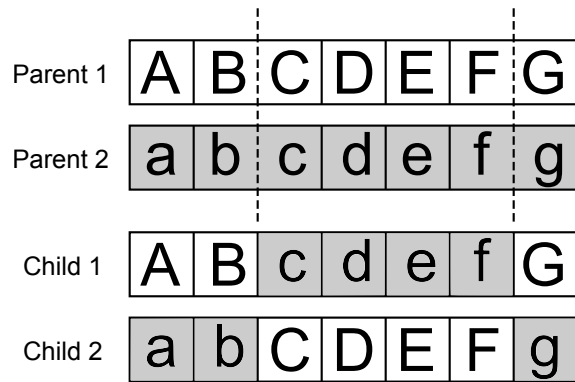
Figure 1.2: n-point crossover, with n = 2. Crossover points are randomly chosen for each pairing of parents, when performing recombination.
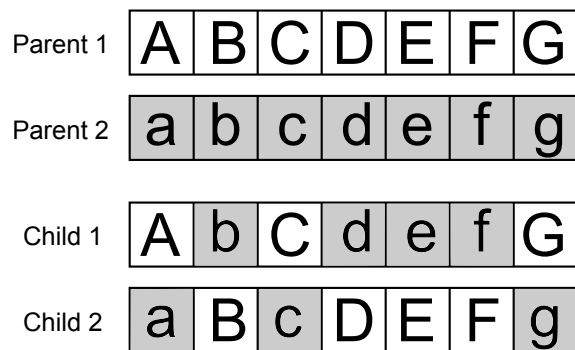
Figure 1.3: Uniform crossover. Each gene is randomly inherited from one parent or the other.

an integrated team of engineers from all subdisciplines of spacecraft design. Over the course of their week(s) long design study, they develop a feasible design. Ideally, this design maximizes the productivity of the mission while minimizing its mass, risk, and/or cost [17]. This optimization continues to grow in importance as mission selections grow more competitive.

Simultaneously, the proposed missions grow more complex, and the resources available to conduct design studies remains constant at best. These studies are expensive, and the personnel that staff the design teams are limited. As a result, the concurrent design workload is growing faster than the teams' ability to address it. Many concepts under consideration are for competed missions. This leads to a rush to perform many mission studies simultaneously to respond to a given announcement of opportunity.

These practical limitations lead to very few design alternatives being evaluated. Often only a single major vehicle design is considered, confirming feasibility but not optimality. The proposed design is either a modification of a previous design, or is otherwise based on the previous experience of the design team [18]. Increasing levels of automation have been adopted to some extent at the subsystem level. This work presents a method for performing an automated high-level design of the entire vehicle. The framework simultaneously performs high-level multidisciplinary design optimization, presenting mission design teams with an optimized trade space of design alternatives. A point design can then be chosen, replacing the simply feasible point from which the team currently starts with a quasi-optimal one. Concurrent

design teams would then conduct their full design study using the chosen design as a starting point.

1.4.2   Prior Attempts to Automate Vehicle Design

The concept of employing automation to solve complex systems design problems is not novel. Several schemes have been developed which utilize GAs to perform design optimization, dating back to at least the 1990s. Mosher created a basic GA package for spacecraft design which could explore a large portion of a satellite design space, considering a large number of dissimilar spacecraft designs [19] (far more than the less than ten designs usually considered by conventional mission design teams). This allowed for a more complete exploration of the design space, unbiased by previous experience of the design engineer.

Mosher used his framework to compare a complete enumeration approach and a GA-based approach for a case study replicating the mission requirements for the Near Earth Asteroid Rendezvous (NEAR) Shoemaker mission. Even with the enumeration approach, only one design was found that met all constraints. Interestingly, the actual NEAR Shoemaker mission also failed to meet all specified constraints, requiring a rocket modification. Several designs were found that were close to compliance with the constraints. This indicates that there is an important value to simply imposing a penalty function on designs that violate some constraints, rather than immediately eliminating them.

The GA found an optimal solution 95% of the time, and when it did so it found the solution in less than half of the time required for complete enumeration. The work was performed with only six design variables. For a larger number of design variables, the speedup from using a GA was expected to grow. It should be noted that Mosher performed this work during NASA's "faster, better, cheaper" era [20]. Since NASA's satellite mission design philosophies have since changed, the goal of this type of work may have also changed. Nonetheless, much of the general motivation behind the work, such as avoiding bias due to past experience, and allowing a more complete exploration of the design space, still applies.

Sorgenfrei and Chester investigated use of a GA for designing a Mars Entry, Descent, and Landing (EDL) system, consisting of an aeroshell and parachute [21]. Three sets of optimizations were performed using separate fitness functions. In their implementation, each fitness function reduces what is a multiobjective design optimization problem to a single objective problem. This is done by converting all but one objective to constraints. A "death penalty" (extremely low fitness score) is imposed for any constraint violation. While, as the authors acknowledge, these fitness functions may not be the best metrics of performance for such an EDL vehicle, the general framework serves as a good proof of concept of application of GAs to this sort of design problem. Overall, this work provides a good description of and example of the implementation of GAs in space systems design.

1.4.3 Generalized Spacecraft Design

The above case studies in automated spacecraft design share a major draw-back; they all utilize specialized schemes unique to their specific design problem. Modification of any to address additional design problems would, optimistically, require substantial modification of their existing problem framework. There have been some prior investigations into possibilities for generalized spacecraft design. It is largely this idea that is driving the adoption of MBSE.

One academic example of such an attempt is the work by Shaw to develop a Generalized Information Network Analysis (GINA) methodology and model for analyzing designs of any spacecraft or constellation of spacecraft [22]. The GINA methodology treats any satellite system as an information transfer network. The idea is that any space-based system (that is, a system involving a spacecraft or collection of spacecraft) can be modeled as collecting information from some source, processing that information, and transmitting it to some customer.

Shaw considered satellite navigation systems such as GPS, global communications networks such as Iridium, information transfer systems such as the many proposed and operational satellite internet services, and global reconnaissance services. While Shaw did not consider scientific space missions, it is clear that most Earth science, planetary science, and astrophysics missions have analogues to the mission types considered, with the caveat that substantial additional considerations may be required for non-Earth-orbiting missions.

It is not immediately clear how this model would apply to human spaceflight systems or other complex space systems such as active debris removal (ADR), planetary defense, and robotic satellite servicing missions. These systems break the assumption that a spacecraft merely collects information from a source and transmits it to an end user. They do involve information transfer, but in most cases the performance metric involves interaction of the spacecraft with the local environment. The information transfer in most of these cases is simply for monitoring purposes, and is not itself a performance metric.

Jilla and Miller presented a framework for performing multi-objective, multidisciplinary design optimization of distributed satellite systems (DSS) following the GINA model. Their work is aimed at finding an optimal starting point for a notional DSS architecture [18]. It shows a move towards more generalized design, presenting a framework that can theoretically be used for any DSS architecture.

As a case study and proof of concept, they used their framework to perform a simplified design space exploration for a terrestrial planet finder mission. They performed this case study in a simplified design space, varying four discrete parameters; orbit radius, collector geometry, number of collector apertures, and aperture diameter. This simplification was performed to allow complete enumeration of the design space in order to evaluate the performance of each optimization technique used. Of the optimization techniques considered, simulated annealing (SA) was found to best approximate the true Pareto front, and was therefore used as the optimization method for the authors' proposed framework. Interestingly, a GA was not considered for the optimization algorithm. A GA seems like a natural choice

for Pareto front identification. It naturally determines a Pareto front from an entire "population" of designs, with well known multi-objective GAs such as NSGA-II well documented in literature [23].

GINA is a powerful framework for evaluating design options, but does not in-and-of itself perform design optimization. The goal of GINA is trade analysis of systems that have already been designed. It provides a model through which any architecture option can be interpreted, allowing a fair comparison to be made between different architectures. GINA does not perform design of the spacecraft itself. It models each satellite, subsystem, and ground station as a node of the overall system. As will be detailed in this dissertation, the CR model and the Generalized Evolutionary Spacecraft Design Architecture (GESDA), focus on the space segment, and modeling the flow of multiple resources through the spacecraft in a similar manner to which GINA models information flow.

1.5 Variable Length Genome GAs

Variable length genome GAs are useful for optimizing systems with a variable number of design parameters. This naturally lends itself to CR problems, where the optimal number of components may not be known *a priori*.

Previous investigations have considered the use of variable length genome GAs. Lee and Antonsson proposed exG, a framework for managing a genome of varying length [24]. In exG, a traditional single string genome is augmented with an index string, each gene of which acts as an index for a corresponding data gene. Design

traits are assigned to ranges of the index string rather than to specific values of the original encoding string. This allows genomes with a variable number of genes describing each trait to be decoded assuming constant range bounds for the index string.

Variable length crossover is achieved by picking a sub-range of the value bounds for the index string, and exchanging genes within this range between the two parent designs. The authors argue that this variable length genome (VLG) crossover operator eliminates the need for a VLG mutation operator that can change the genome length. A dedicated mutation operator is not needed to change the length of a genome. However, including a traditional mutation operator still seems necessary to preserve the GA's ability to add options not present in the population to the encoding string, in order to avoid local minima.

Ting et al. [25] proposed use of a multiobjective variable-length genetic algorithm to solve a heterogeneous transmitter placement problem. NSGA II is used for genetic selection to handle the multiobjective nature of this design problem. The algorithm used a variable length chromosome representation, due to the variable number of components in potential design solutions. The authors proposed a novel hybrid crossover, which uses varying combinations of uniform crossover between individual components and single point crossover of the entire parent chromosomes by components. The latter allows the variable length chromosome GA to find the optimal number of components, without the need for any length mutation operator.

More recently, Ryerkerk et al. investigated the performance of several variable-size genetic algorithm implementations [15]. Their implementation involves a vari-

able length genome, and special recombination and mutation operators to handle them. The variable-length cut-and-splice (based on the work of [25]), spatial recombination, and synapsing variable length crossover (SVLC) were evaluated. Additionally, a new crossover operator, similar component crossover, was proposed. This method attempts to perform respectful recombination by pairing similar components, ensuring that a component of each pair will be inherited by each child design.

All variable length operators with the exception of cut and splice performed somewhat better than the fixed length representation, while cut and splice performed far worse than the fixed length representation. When the optimal number of components is not known *a priori*, use of a variable length crossover, proved desirable. This is because it will optimize the number of components as well as the configuration thereof.

The authors do note that in later generations, these schemes seem to become stuck in sub-optimal solutions, which would require multiple concurrent mutations to reach a better optimum. It may therefore be of interest to consider an algorithm where the mutation rate increases in later generations, as improvement from generation to generation slows.

1.6   The Present Work

Jilla and Miller's work provides an interesting parallel to the work of this dissertation. The motivation of their work is essentially identical. It served as a proof

of concept for the application of automated, metaheuristic design optimization in the conceptional design phase. However, much like the body of work in the field, their work was tailored to a specific problem. Nonetheless, the general DSS architecture which they address is a broad design problem. Their work is therefore a substantial step in the direction of generalized spacecraft design.

GINA is described by Shaw as being reduced to how to "move some entity from one point to another in an underlying network...as effectively as possible, both to provide good service to the users...and to use the underlying transmission facilities effectively". The goal of the CR model detailed in this dissertation can be similarly described as analyzing the flow of multiple entities (resources) from sources to sinks. These sources and sinks can be components within the system (spacecraft, in our case), or exist outside of it (the Sun, for one example, being a radiation source in our case).

1.6.1   The Problem Statement

The overarching purpose of this work is to develop a generalized framework that can, with little to no modification, address any spacecraft design problem. The framework must understand the objectives, constraints, and operating properties of any spacecraft. For any payload and any relevant objectives, it must be able to perform trade space exploration and multiobjective design optimization, producing feasible, Pareto-optimal vehicle designs for the given mission.

1.6.2   Contributions of the Present Work

The first contribution of this work is somewhat standalone compared to the others, though it does originally motivate them, and, ultimately, serve to validate them. That contribution is an attempt at an objective comparison of proposed LEO ADR payloads. The work of Chap. 2 in this dissertation presents the first attempt at this. This work, along with parallel research being carried out by the author at the time, motivated the generalized CR model that comprises the remainder of this dissertation.

As has been alluded to, this work is not the first attempt to automate vehicle design optimization, or even specifically spacecraft design optimization. Nor is it the first attempt to create a generalized scheme for spacecraft trade space analysis. The most significant contribution of this work is the CR model, which can be applied to any spacecraft design. In fact, the CR model is generalizable to a much wider range of systems engineering problems. Any system that can be modeled as a collection of components and resources that flow between them can likely be addressed by this model.

The goal of the CR model is to describe a complex system such as a spacecraft in a way that the system and its operational constraints can be easily understood by an algorithm, including metaheuristic optimization algorithms. The model provides a uniform method of handling constraints of the whole system as well as of individual components that comprise it.

This work presents a design optimization and trade space exploration framework based around the CR model. This model allows generalized simulation and optimization of a large class of complex systems including spacecraft design. It allows such systems to be easily understood and processed by computer algorithms. This facilitates automated optimization of complex multidisciplinary, multiobjective problems. The CR model allows a computer to interpret complex systems, facilitating simulation, automated optimization, and trade space exploration. The latter two are accomplished through a specialized variable length genome GA. The novel genome encoding scheme and crossover operator developed for this GA comprise the second contribution of the present work.

In the context of this work, the optimization problem is essentially a component selection problem. Since the intended application of the work is spacecraft design optimization, this component selection problem requires a library of spacecraft components. Aggregating proposed and historical spacecraft components is a non-trivial task. Additionally, while the core CR model is applicable to a wide range of problems, it must be combined with problem specific simulations and considerations to create an optimization framework which allows the CR model to be used for satellite design optimization. The third major contribution of this work is therefore the spacecraft environment and component-level simulations required to apply the CR model to spacecraft design optimization.

1.6.2.1 A Technology Comparison for Low Earth Orbit Active Debris Removal

The first contribution of this work entails a GA-based vehicle designer which takes the different ADR payloads as input, produces spacecraft around each of them, and evaluates their performance conducting an active debris removal program. The first attempt at this, for which the model was very problem-specific is presented in Chap. 2. This problem is revisited with the generalized framework presented later in this dissertation. This second analysis of the LEO ADR problem offers the ADR vehicles in additional detail, with the problem setup and final results presented in Chap. 9.

1.6.2.2 The Component-Resource Model

The most significant contribution of this work is the component-resource (CR) model it proposes. Many complex systems, including all spacecraft, can be modeled as a collection of components and resources that flow between them. Each component can be a source, sink, or store (referred to in general as nodes) for each resource within the system. Sources produce a resource, sinks consume a resource, and stores contain an internal reservoir for a resource, operating as a source or sink depending on the state of the rest of the system, as indicated by Fig. 1.4. A given component may be a source, sink, and/or store simultaneously for different resources or different states of the system. Flowrates of resources produced and consumed across the
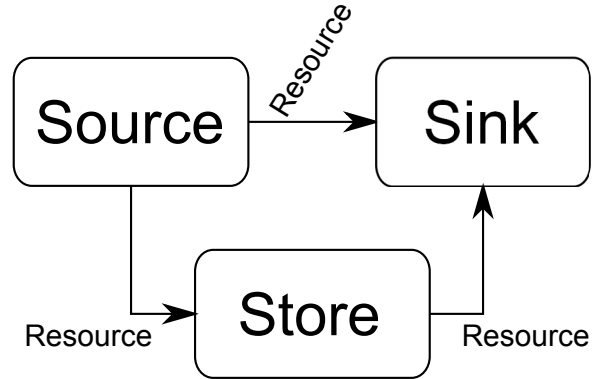
Figure 1.4: Simplified diagram of resource flows between sources, sinks, and stores. This diagram assumes only a single resource. A component may be a source for a given resource and a sink for another, and therefore may appear as a store in this sort of diagram. A component is only a store if it can operate as a source or sink for the **same** resource, and contains an internal reservoir for that resource.

entire system are tabulated. The net flowrate of each resource across the system is then constrained to be greater or less than some value. This process naturally handles most constraints of complex systems optimization problems, such as whole spacecraft design. The CR model can therefore evaluate the feasibility of a very large class of systems optimization problems. Such a model is easily understandable by a automated framework. It can therefore be used to perform multidisciplinary multiobjective optimization for a large class of complex systems. As will be shown in this dissertation, when modeling a system in this way, nearly all constraints can be handled by constraining the total amount of a resource produced within the system to be either greater than or less than the total amount of that resource consumed.

The framework is intended for high-level trade analysis performed at the beginning of the design process. It is a simplistic representation to disregard many

holistic system aspects and decisions, such as, in the case of satellite design, the mechanical configuration of the spacecraft. However, even with these simplifications, quality trade analysis is possible as long as these simplifications are made uniformly among all design options considered.

As has been stated, the underlying principles of the framework are easily transferable to a large class of systems engineering problems. Any system that can be defined as a collection of components and resources that flow between them can be analyzed using the CR model. Therefore, an attempt will be made when describing the framework to speak generally about systems, rather than specifically about spacecraft.

1.6.2.3   The Vehicle Encoding Genetic Algorithm

The third major contribution is the specialized genetic algorithm developed for optimization. The CR model frames problems of interest as component selection problems. The Vehicle Encoding Genetic Algorithm (VEGA) provides an encoding mechanism for defining system designs as an organized collection of components, as well as a GA for optimizing designs using this encoding scheme. Each gene in an individual genome corresponds to a single component in the system. A variable length GA is therefore utilized to optimize the number of components as well as the specific combination of components. This includes a variable length crossover operator and a division of the genome into individual "chromosomes" for each component class.

1.6.2.4 A Generalized Evolutionary Spacecraft Design Architecture

The final contribution is the specific spacecraft design architecture, built around the CR model. This entails the definition and initial population of a spacecraft component library and the associated simulations, both at a system or environment level, and at an individual spacecraft component level. In practice, the component libraries are largely drawn from NASA's Satellite Parts On-Orbit Now (SPOON) database [26]. It is therefore acknowledged that the component libraries presented here do not themselves constitute a contribution.

The remainder of this contribution is the associated spacecraft and component-level simulations. Great effort was made throughout the development of this spacecraft design analysis framework to preserve generality across different space missions, allowing the framework to be applied to a wide range of missions with little to no modification.

1.7 Content of the Document

The remainder of this dissertation is outlined as follows. Chap. 2 presents a conventional spacecraft design optimization problem; the design of active debris removal spacecraft to operate in LEO. This problem motivates the development of the CR model in the remaining chapters of this dissertation.

Chap. 3 presents the simplest form of the CR model; the general static CR model. In the static model, all resource flows are steady state. Tabulating resource relations once for a given system snapshot is sufficient to fully understand the be-

havior and feasibility of the system. The basic functioning of components as sources, sinks, and stores is discussed in detail. Resource flow in this case is also described, and an example is detailed to make clear how this most basic form of the model functions.

Chap. 4 describes the optimization model and GA developed for this dissertation. It details the different levels of the genome, describing the collection of components present, properties of an individual component, and system-level properties. It also describes the form of the GA itself. A particular focus is given to the selection and crossover operators developed, and genome structure. The chapter demonstrates how the framework handles single objective and multiobjective problems. It discusses the internal constraint handling process, particularly how resource relations implicitly handle most component and system level constraints.

Chap. 5 provides a simple example of a Static CR design problem, working through setting up the design problem in the context of the CR model. It compares optimization results obtained with the theoretical optimum for that design problem.

Chap. 6 extends the CR model to dynamic problems, where the system behavior changes over time. This is important for the spacecraft design problem, since spacecraft behavior changes over the course of an orbit or interplanetary trajectory, as well as between the multiple operating modes a spacecraft may have. Dynamic resource availability over time within a given mode will be discussed, in particular focusing on edge resources, which flow between the system and the environment.

Chap. 7 uses the framework developed in Chaps. 3-6, presenting the satellite framework based on the CR model and VEGA. It covers the specific resources

included for this set of design problems, the spacecraft component classes developed, and simulation and fitness score evaluation for space missions.

Chap. 8 presents a mission concept for a Earth imaging satellite used to develop and verify the framework. The LEO ADR design problem of Chap. 2 is revisited with the framework in Chap. 9, serving as an ultimate benchmark of the framework.

Finally, Chap. 10 presents some conclusions and areas identified for further future investigation.

Chapter 2: LEO Active Debris Removal Technology Assessment

2.1 Overview

On-orbit satellite debris is a growing problem, particularly in LEO [9]. The continuous growth in the number of objects on orbit increases the likelihood of an ablation cascade, a catastrophic series of collisions initiated by the destruction of a small number of large objects on orbit [11]. Such an event would result in debris clouds that could render many common orbits unusable. Several technologies have been proposed to address the growing debris problem using airborne, ground-based, and space-based systems. The work detailed in this chapter evaluates and compares proposed orbital technologies for removing debris objects (DOs) from LEO. The focus was placed on large intact debris objects, since a collision with one of these could produce many small fragments, each of which could lead to additional collisions.

To perform this comparison, spacecraft were designed around several proposed active debris removal payloads. A genetic algorithm was employed to find the most efficient designs for orbital debris removal, with special attention given to minimizing the financial cost of such systems, and the risk they pose to infrastructure and human life in orbit and on the ground. Listings of the Pareto-optimal designs are presented at the end of the chapter.

The work detailed in this chapter is intended to provide an objective comparison of proposed orbital solutions that remove large, intact objects from low Earth orbit. To accomplish this, a satellite design software package was developed to produce spacecraft that utilize the proposed active debris removal (ADR) technologies. Designs were selected for further investigation based on financial cost per object removed and risk to infrastructure and human life, both in orbit and on the ground.

2.2   Theory and Approach

Seven proposed ADR systems were considered for analysis. These were sorted into two groups; orbital tender vehicles and orbital tugs. Similar trajectories and mission operations were present among the designs within a given group. Orbital tender vehicles contain one to several "deorbit packages," (DPs), equal to the number of DOs they are designed to deorbit. They travel between DOs, attaching these packages to them. The packages then act to deorbit the DO independently of the orbital tender vehicle. A DO is considered successfully deorbited by an orbital tender vehicle once a deorbit package is attached. An example mission profile for an orbital tender vehicle is given in Fig. 2.1.

Orbital tugs travel between DOs, grappling them and lowering their perigee to 200 km, low enough for their orbit to rapidly decay due to atmospheric drag. At this point the lowered DO is considered successfully deorbited, and the tug may re-boost to capture another DO. An example mission profile for a tug is given in Fig. 2.2. For systems that did not specify a grapple mechanism, a robotic arm modeled after

27
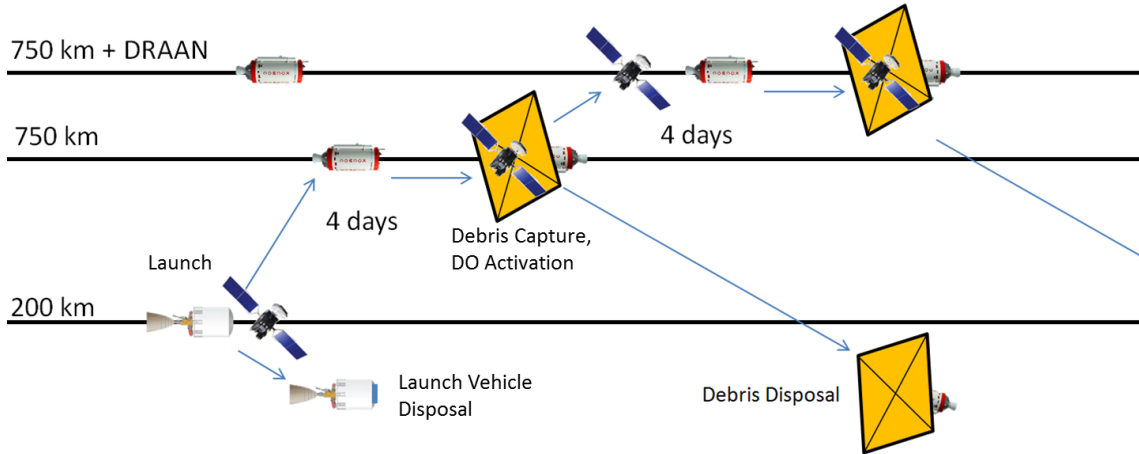
Figure 2.1: Orbital tender vehicle mission profile, shown here with a gossamer sail deorbit package as an example.

the Orbital Express Demonstration Manipulator System (OEDMS) [27] was used. This arm was assumed to have a mass of 71 kg, require 131 W while operating, and to be currently developed to Technology Readiness Level (TRL) 7, for the purpose of this debris removal mission. The next two sections provide details of the proposed ADR systems, suggested by previous work, that were considered in this analysis.

2.2.1 Deorbit Packages Included in Analysis

All DPs considered here were assumed to require no power draw from the tender vehicle except in some cases during initial deployment, once the DP has been attached to the DO. With the exception of Terminator Tether, all DPs listed here worked by increasing the surface area, and therefore decreasing the ballistic coefficient of the DO, increasing drag to shorten its lifetime on orbit. For the purposes of this analysis, it was assumed that once a DP is attached to a DO and
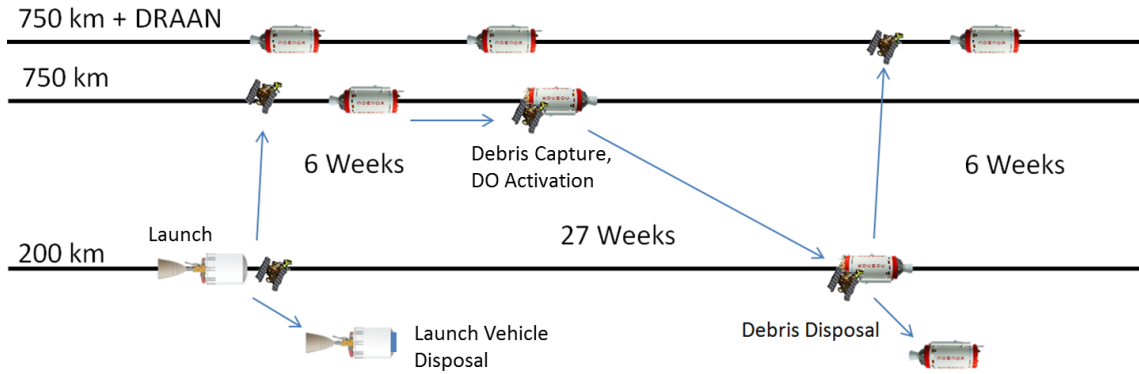
Figure 2.2: Tug mission profile, shown here with a laser ablation tug (LAT) as an example.

released by the tender vehicle, the mass of that DP can be completely subtracted from the total mass of the tender vehicle. Furthermore, it was assumed that the attachment of DPs to the DOs requires no additional hardware beyond that stated below, with the exception of a robotic arm for initial attachment. It is assumed that the manipulator described above can perform this task itself without additional hardware.

Table 2.1: Deorbit Package Parameters.

ADR system	Mass (kg)	Power (W)
KSII	74	10
TRIS	106	1
GOLD	70	0
Terminator Tether	28	0

2.2.1.1 KnightSat II (KSII)

KSII was a self-contained Gossamer Sail (aerodynamic decelerator) proposed by the University of Central Florida [28]. It utilizes magnetic torque rods for attitude control. The mass and power consumption assumed for KSII are given in Table 2.1.

2.2.1.2 L'Garde Towed Rigidizable Inflatable Structure (TRIS)

The TRIS is a self-contained aerodynamic decelerator based on a device tested on STS-77 [29]. TRIS includes a dish-like decelerator deployed and supported by inflatable, rigidizable booms. The mass and power consumption assumed for the TRIS are given in Table 2.1.

2.2.1.3 Gossamer Orbit Lowering Device (GOLD)

GOLD is a self-contained DP developed by Global Aerospace Corporation and ILC Dover [30]. It comprises an inflatable Gossamer sphere that can be attached to a DO and then remotely or autonomously inflated at a later point. The device has the ability to modulate the extent to which it is inflated at lower altitudes to facilitate targeted reentry. The GOLD package contains its own solar power system, so it does not impose a power requirement on the DO or tender vehicle. The mass assumed for GOLD is given in Table 2.1.

2.2.1.4 Terminator Tether

Terminator Tether was a self-contained DP developed by Tethers Unlimited [31]. Terminator Tether comprises a several kilometer long electrodynamic drag tether that deorbits the DO and provides electrical power to the system. Terminator tether is stated as having a mass of 1-2% of the DO, so a worst case 28 kg was assumed for the DO population described above.

2.2.2 Orbital Tug ADR Systems Included in Analysis

The following ADR technologies, suggested by previous work, were considered for this analysis. The mass and power requirements for each tug ADR system are provided in Table 2.2.

Table 2.2: Orbital Tug Payload Parameters.

ADR system	Mass (kg)	Power (W)
EDDE	80	0
LAT	42	250
Conventional Tug	0	0

2.2.2.1 Electro-Dynamic Debris Eliminator (EDDE)

EDDE [32] is a several kilometer long conducting tether, with solar panels spaced periodically along its length, and with avionics and capture nets at either end. It uses electric current through and around the tether to produce a force perpendicular to the Earth's magnetic field, enabling it to maneuver throughout

low Earth orbit. Upon arriving at a DO, EDDE rotates perpendicular to the tether axis with a net deployed at one end to capture the DO. The DO is then maneuvered to a 330 km disposal orbit, where it is released.

For the purpose of this analysis, based on published proposals for EDDE, the system was assumed to be self-contained. That is, no external support hardware was required, and the quoted size and mass included all required subsystems, including ADR, propulsion, and DO capture mechanism. It is of note that EDDE is the only self-contained technology considered in this analysis. The fundamentally unique nature of EDDE makes it unrealistic to simply model it as a payload on an otherwise conventional spacecraft, as was done with the other technologies.

2.2.2.2 Laser Ablation Tug (LAT)

The LAT [33] features a pulsed laser that repeatedly ablates small portions of surface material from the DO, producing net thrust in a desired direction. Since this ADR technology ablates the surface of an attached DO, there is no need to carry a dedicated onboard propellant supply. Upon detaching from a DO, the LAT separates a small portion of the DO, which it keeps to use as propellant to reach its next target.

2.2.2.3 Conventional Tug

A conventional tug was also included in this analysis as a baseline ADR vehicle, against which to compare the other proposed ADR technologies. The conventional

tug is simply a spacecraft with a manipulator to grapple a DO, and a flight proven propulsion system to maneuver the DO into a disposal orbit. No additional ADR system is present, so the ADR system for a conventional tug is modeled as having no mass and requiring no power.

2.2.3   ADR Vehicle Design Optimizer

Vehicle design optimization software was developed to generate vehicles, each based upon a proposed ADR technology. A genetic algorithm was used to optimize vehicle designs, minimizing the financial cost per DO removed and the risk posed by debris removal. The properties listed in Table 2.3 were assumed for each ADR system. In the case of EDDE, actual thrust values were not available, so rated altitude and plane change rates were used instead, as listed in Table 2.3.

Table 2.3: ADR System Parameters.

ADR system	Circularizing Thrust	$\Delta\Omega$ Thrust	Deorbit Thrust	Self-Propelling?	Self-Contained?	Self-Grappling?
KSII	-	-	-	No	No	No
TRIS	-	-	-	No	No	No
GOLD	-	-	-	No	No	No
T. Tether	-	-	-	No	No	No
EDDE	4.4 m/s	1.4/day	4.4 m/s	Yes	Yes	Yes
LAT	0.035 N	0.035 N	0.035 N	Yes	No	No
Conv. Tug	-	-	-	No	No	No
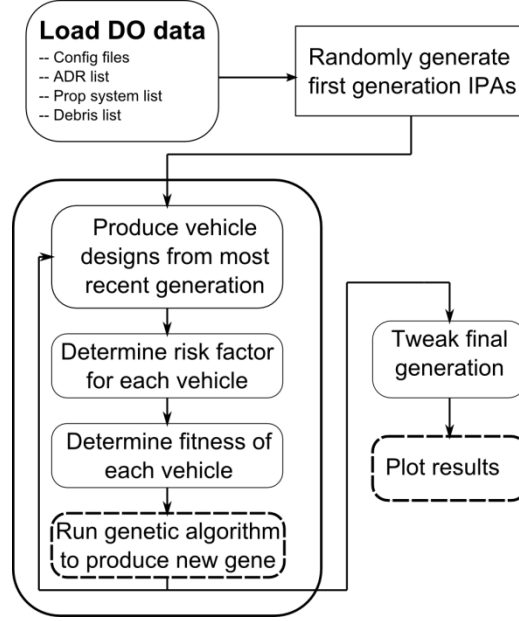
Figure 2.3: Top-level ADR design optimizer algorithm.

2.2.3.1 Vehicle Designer

Vehicle designs were generated as described below, with the top-level design optimization process as depicted in Fig. 2.3. The design of each vehicle was based on an input parameter array that serves as the genome for the genetic algorithm, described below. Each genome is composed of several input parameters (IP_i, where i is the input parameter in question). An example genome is shown in Fig. 2.4, and a brief description of each input parameter is given in Table 2.4. A listing of the potential values for each input parameter is given in Appendix A. IP_1 designates the ADR system a vehicle carries, and IP_2 designates the thruster to be used as the dedicated propulsion system (DPS). A key of potential options for IP_1 and IP_2 is given in Table 2.5. In some cases, multiple thrusters of a single type (e.g. ion

H M 10 B B B A B J

ADR System Thruster # of targets Circularization selector Draan selector Disposal selector Impulsive burns? Hold Short? #CAMs

Figure 2.4: Example input parameter array.

Table 2.4: Input Parameters.

Parameter	Description
IP_1	ADR system
IP_2	DPS
IP_3	Number of DOs removed by a single vehicle
IP_4	Determines whether ADR system or DPS is used for circularization (reboost)
IP_5	Determines whether ADR system or DPS is used for plane change
IP_6	Determines whether ADR system or DPS is used for DO orbit lowering
IP_7	Impulsive or low thrust trajectory?
IP_8	Phasing for conjunction avoidance
IP_9	Number of collision avoidance motors

engine) were considered as potential DPSs. In such cases, each potential thruster was given its own value for IP_2, and the range of values for each thruster type is given in Table 2.5. IP_3 designates the number of targets to be deorbited by a single vehicle, while IP_4, IP_5, and IP_6 are binary parameters that select whether the ADR system or DPS performs a given type of maneuver. In each case, 0 designates that the maneuver is performed by the DPS, and 1 designates that it is performed by the ADR system. If no thrust is specified for a given ADR system for a given

Table 2.5: Input parameter key for IP_1 and IP_2.

IP_1 Value	ADR system	IP_2 Value	Thruster Type
B	KSII	B-H	Bipropellant
C	Conventional Tug	I-O	Monopropellant
D	TRIS	P	Resistojet
E	EDDE	Q-R	Arcjet
F	GOLD	S	Pulsed Plasma Thruster
G	Terminator Tether	T-Z	Hall Effect Thruster
H	LAT	a-e	Ion Engine
		f-i	No DPS

maneuver type, the input parameter for that maneuver type will be forced to 0. IP_4 selects for circularization or orbit raising (depending on whether impulsive or low thrust) maneuvers, which return the vehicle to the orbit occupied by the DOs. IP_5 selects for plane change maneuvers. In the case of low thrust maneuvers, plane change is performed as part of the orbit raising and disposal maneuvers, so the parameter is ignored. IP_6 selects for disposal maneuvers, which lower the DOs perigee altitude to 200 km. A DO being removed by an orbital tender vehicle was considered removed upon attachment of the DP to the DO, so this parameter was ignored for orbital tender vehicles. IP_7 dictates whether maneuvers performed by the vehicle are impulsive or low thrust, IP_8 designates whether a vehicle should perform phasing conjunction avoidance while crossing high priority orbits (see risk factors section below), and IP_9 designates how many collision avoidance motors should be added to the vehicle.

An overall risk factor ORF was assigned to each vehicle produced. This was used to quantify the risk posed by each design to people and property in orbit and on the ground. r was determined through the combination of several factors influencing the risk of a given design. An in-depth discussion is provided in the risk factors section below.

Based on a given genome, individual vehicles were designed following the process shown in Fig. 2.5. A maneuver table was produced, detailing the ΔV required, the propulsion system used, and the mass of any object attached to (or removed from) the vehicle for each maneuver, from the last maneuver the vehicle produced to the first. The maneuver table produced was based on the mission profiles described in Fig. 2.1 and Fig. 2.2. For the purposes of this simulation, vehicle life was limited to fifteen years. A manipulator was added to vehicles for which the ADR system did not have self-grappling capability for grappling DOs. The payload mass for the vehicle was assumed to be the combined mass of the ADR system and manipulator, if present.

With the exception of self-contained ADR systems, the mass of the spacecraft excluding the mass of the DPS and electrical power system (EPS) was assumed to be 2.33 times the payload mass, based on historical data [34]. The total power requirement was defined as the greatest maximum power requirement among the ADR system, manipulator, or DPS. Note that this implies that the ADR system, manipulator, and DPS never operate at the same time. An additional load was added to this value for command and data handling and communications. This requirement was multiplied by a factor of 1.31 to account for losses within the
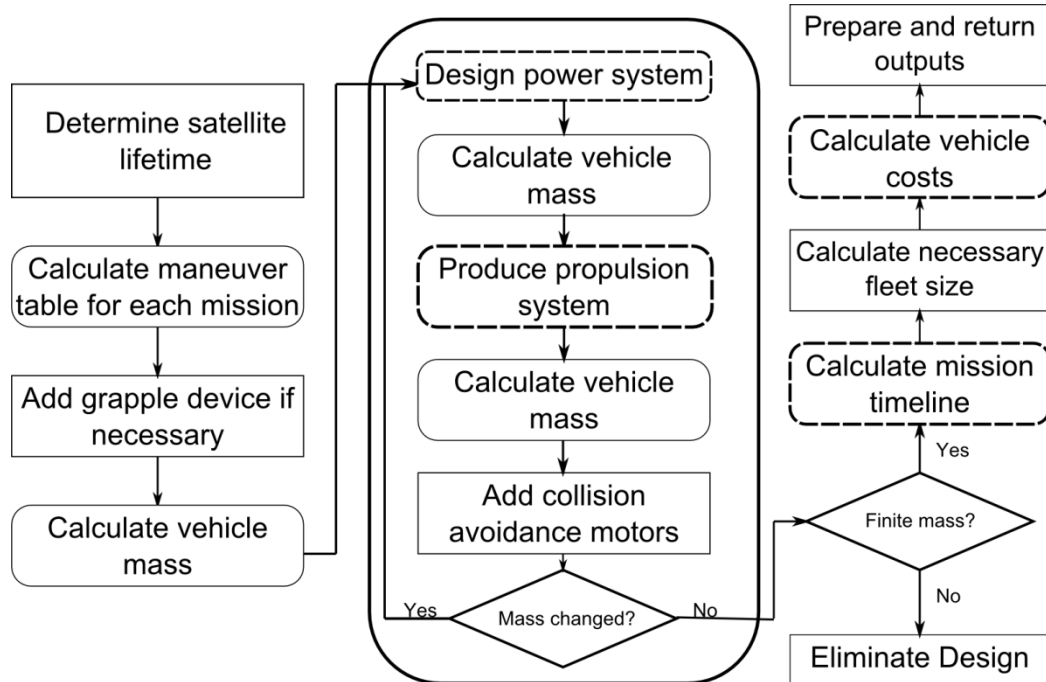
Figure 2.5: Individual vehicle design process.

EPS [17]. Based on this power requirement and the given DO orbit, an EPS was produced for the vehicle that included triple junction GaAs photovoltaic arrays for power generation.

A propulsion system was then produced based on the vehicle mass thus far and the vehicles maneuver table, following the process shown in Fig. 2.6. This included the mass of the DPS, propellant, and propellant tank. Collision avoidance motors were attached as dictated by the genome. The motors were designed to provide a ΔV of 0.3 m/s each, enough to lower the perigee of the orbit by 1 km. The vehicle designer was iterated until the total vehicle mass converged, or the mass exceeded existing or near future launch capability, assumed to be 70 metric tons to low Earth orbit [35]. Once the mass converged, a mission timeline was calculated based on
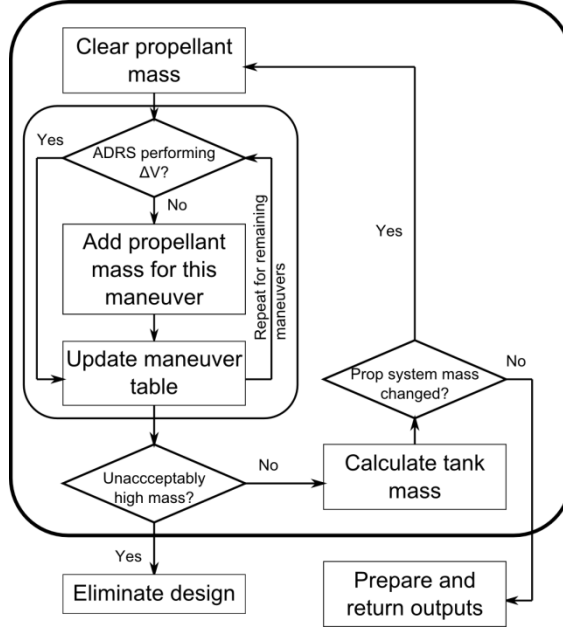
Figure 2.6: Propulsion system design process.

the maneuver times, with three days added per DO, dedicated to rendezvous and grappling. The required fleet size was then determined, ensuring enough vehicles to remove 100 DOs, at a rate of at least 10 DOs per year.

Development and production costs were determined in 2014 USD using the Spacecraft/Vehicle Level Cost Model [36]. Launch costs were determined based on published prices of actual launches on commercially available launch vehicles. Based on these, a linear fit of $C_{LV} = 0.0094m_{tot} + 18$ was developed to determine launch cost, where C_{LV} is the launch cost in millions of 2014 USD, and m_{tot} is the vehicle total mass in kg. For payloads that were known to be small enough and light enough to fit into a single slot on an EELV Secondary Payload Adapter (ESPA) ring [37], it was determined whether doing so would decrease the launch cost, assuming \$3M

per ESPA slot. The ADR vehicle was assumed to be launched on an ESPA ring when doing so was less expensive than the launch cost given by the function for C_{LV} above, and vehicles launched on an ESPA ring were assumed to be delivered directly to the orbit of the first DO to be removed.

2.2.3.2 Risk Factors

Each vehicle design was assessed to determine the overall risk it would pose to active hardware and human life, in orbit and on the ground. This risk factor roughly represents the expected value lost inadvertently as a result of a given ADR program, with units of active scientific spacecraft. For example, a system with $ORF = 0.5$ roughly corresponds to a loss of value equal to half the cost of a single scientific satellite mission over the course of the ADR program. While this comparison was used to develop much of the logic of the risk evaluation, it should only be considered valid for determining trends for comparing proposed ADR vehicles. It should not be assumed without future work that these numbers accurately denote the actual loss of value from execution of these programs. The remainder of this subsection details the basis for the formulation of ORF, the overall risk factor. ORF is the sum of two partial risk factors; the trajectory risk R_T and the technology development risk R_{TRL}.

R_T quantifies risk due to the trajectory of the ADR vehicles and DOs take in Earth orbit and during reentry. Specifically, it addresses how these trajectories cross the orbits of operational satellites as well as the uncertainty in potential ground

impact locations of the DOs. R_T represents value lost directly through damage caused by the debris removal program. A system was considered high risk if it could not perform a reentry targeting a safe drop zone on the surface of the Earth. It was considered medium risk if it was not high risk but could cross the orbit of a high priority spacecraft, such as a manned spacecraft, and low risk if it was neither high nor medium risk. An entry was considered targeted if it could be conducted within three orbits from a low (disposal) orbit, after holding in a higher orbit for a period of at least a week. It was assumed that variations in the atmosphere below 200 km make orbital decay unpredictable once an object reaches this region.

An entry simulation including an atmospheric model was implemented to determine whether or not a given ADR system was high risk or medium risk. An example entry profile is shown in Fig. 2.7. In the figure, each of the horizontal bars indicates a simulated high priority orbit. The beginning of targeted reentry operations is indicated where the rate of altitude loss decreases substantially, around 334 days in Fig. 2.7, indicating that the vehicle has halted orbit lowering operations. After the Earth has rotated such that the DO orbit passes over an acceptable drop zone, the ADR system is re-activated for a rapid reentry. Entry plots for each ADR system are given in Fig. 2.8, with the exception of Terminator Tether. This exception is due to Terminator Tether's ability to retract for phasing, collision avoidance, and targeted reentry. Such an ability removes the need and benefit from performing such an atmospheric simulation at this design phase. In the simulations performed for this work, the orbits of the NASA A-Train, the Hubble Space Telescope, and the International Space Station (ISS) were included as high-priority orbits, repre-
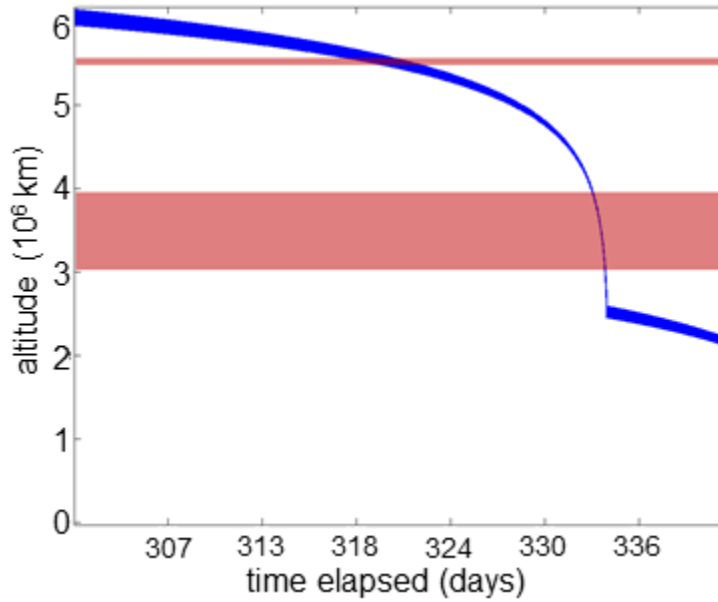
Figure 2.7: Example targeted deorbit profile.

sented by horizontal bars. It should be noted that the actual collision avoidance zone around the ISS orbit is much narrower in altitude than the bottom bar on the plot, but the ISS orbit is allowed to vary within this bar over time. These orbits were arbitrarily selected for this analysis as a representation of elevated risk altitude bands that a DO may pass through as a result of ADR operations. The goal is not to indicate that these objects are actually those whose orbits would be considered high-priority. In an actual debris removal program, the number of orbits and selection of specific objects to avoid would likely be different, involving a number of factors such as the number of satellites affected in a specific orbital band.

The requirement was added that the deorbit time for a single object be limited to one year. As a result, some DPs were scaled up to ensure deorbit within this
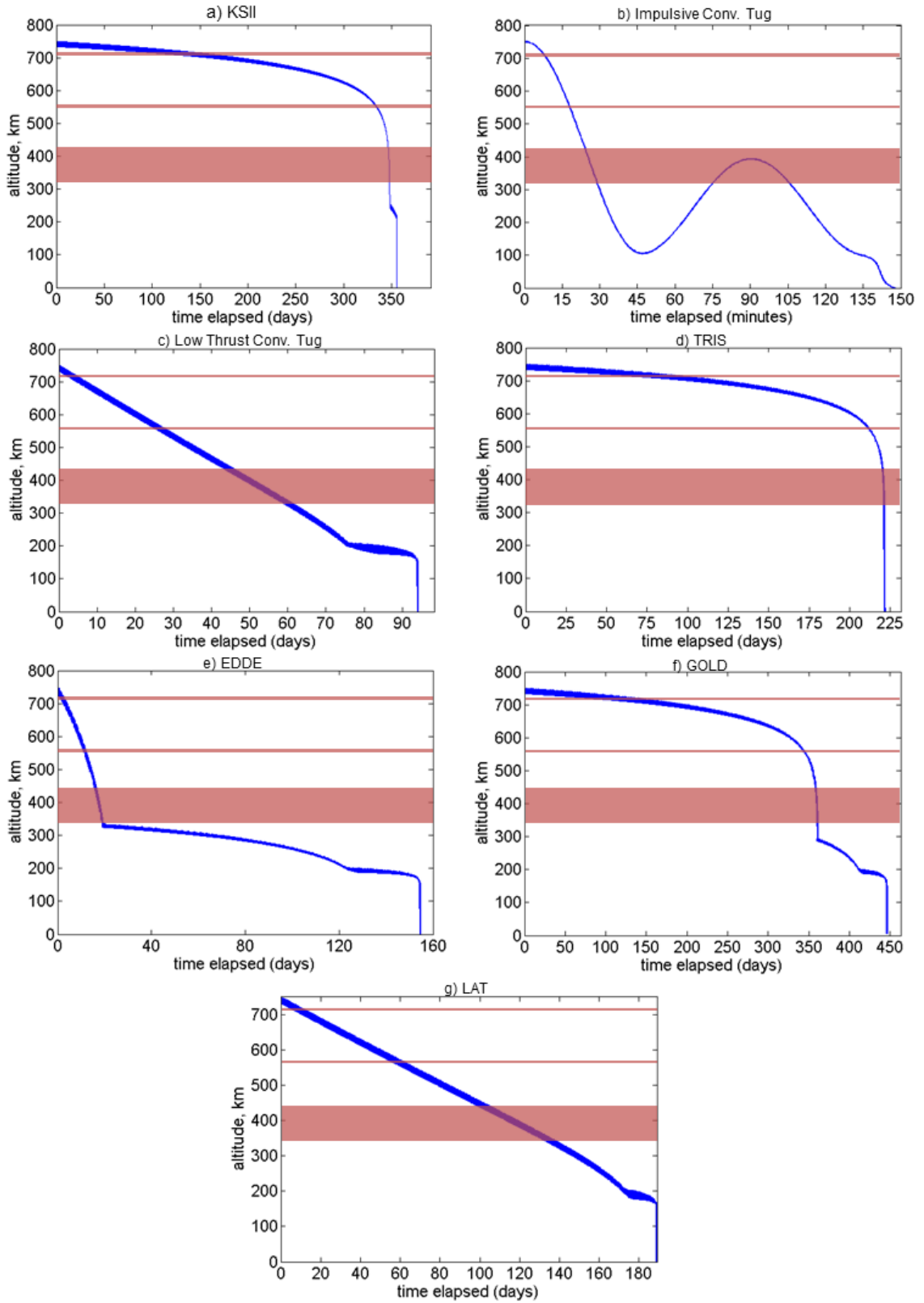
Figure 2.8: Entry profiles based on ADR system and atmospheric simulation.

time frame. The values provided in Table 2.1 take this scaling into account. As an example, KSII was scaled up from 9 m² to 1000 m² in order to meet the one year deorbit requirement, increasing the systems mass from 15 kg to 74 kg. This is a highly optimistic scaling, ignoring many of the complexities associated with a device of the required size for the intended debris removal. However, as will be shown below, even these scaled versions of DPs do not appear on the Pareto front, so the oversimplifications made do not have a meaningful impact.

KSII can perform active attitude control using magnetic torque rods. It was therefore assumed that its gossamer sail can be turned edge on to the direction of travel, reducing the aerodynamic cross section to that of the DO. This ability could be used to dramatically slow the DOs descent, allowing it to be parked in a low orbit (200-300 km). The sail can later be returned to its original attitude, allowing for targeted reentry. For KSII, crossing the A-train will require one to two months, creating a risk of a conjunction between a DO being deorbited and a high-value observatory. Therefore, KSII is assessed as medium risk. GOLD has the ability to partially deflate its spherical envelope at lower altitudes. This causes the envelope to assume an ellipsoidal shape, decreasing its aerodynamic cross section, and slowing orbital decay. The envelope can then be re-inflated to the original cross section, which allows for targeted reentry. GOLD is therefore assessed as medium risk. TRIS is assumed to have no actuation capability after deployment. It is therefore unable to perform targeted reentry, and assessed as high risk.

For conventional tugs, the ADR specific risk is a function of the propulsive capability of the DPS. This splits these vehicles into two categories: those that

perform impulsive maneuvers for deorbit, and those that perform non-impulsive low thrust maneuvers for deorbit. In the former case, it is assumed that the vehicle performs a 175 m/s braking maneuver while grappling the DO, releases the DO, and immediately performs a 175 m/s recircularization maneuver. This V places the debris on a trajectory where it will be deorbited within three orbits, allowing for targeted reentry and avoidance of high value orbital objects. Therefore, the impulsive conventional tug is assessed as low risk. The low thrust conventional tug applies a continuous retrograde thrust to the DO until it reaches a 200 km orbit, at which point it disengages and raises its own orbit, and the DO is deorbited by aerodynamic drag within a month. Since the time of terminal entry cannot be predicted within a resolution of a few orbits, targeted reentry is not possible, and therefore a low thrust conventional tug is assessed as high risk.

The LAT is stated as capable of performing a ΔV of 306 m/s, over 30 days while attached to a 300 kg DO [33], reducing its orbital altitude below the ISS. It was assumed that this was accomplished through constant low thrust, resulting in a thrust of 0.035 N. The LAT can also halt orbit lowering to avoid high value spacecraft while passing through their orbit.

Given EDDEs maneuvering capability of 380 km per day in the orbit of the DOs while not carrying a DO [32], it is expected that EDDE can lower the orbit of a 1400 kg DO by approximately 20.5 km per day. However, neither EDDE nor the LAT can perform a targeted reentry without themselves entering the atmosphere. Therefore, both are assessed as high risk.

Trajectory risk was defined as

$$R_T = (N - n_{CAM}N_F)aR_M + NR_H \qquad (2.1)$$

where N is the total number of DOs that an ADR program is to deorbit, and n_{CAM} is the number of collision avoidance motors attached to each vehicle, detailed below. N_F is the number of ADR vehicles involved in the debris removal program. For any medium or high risk ADR system, R_M, representing the risk of collision with an active spacecraft, was set to 10^{-3}. This is derived from the fact that 1 in 1000 is considered the threshold of acceptable risk of collision for a conjunction involving an active satellite. That is, any higher risk of collision would warrant performing a collision avoidance maneuver [38]. It was therefore concluded that a loss of value of one thousandth the cost of a NASA robotic spacecraft is considered acceptable, per conjunction. It is required that the risk of human casualty from any deorbit activities be no greater than 1 in 10,000 [39]. Due to the size and structure of the DOs to be deorbited, any high trajectory risk system, which does not possess the ability to perform controlled entry of DOs, is assigned a value of 10^{-2} for R_H, the lost value associated with harm to people and objects on the ground. This is based on the fact that acceptable risk of collision with a robotic spacecraft is ten times as great as acceptable risk for collision with ground objects. For medium and low trajectory risk systems, R_H was set to 0, indicating that targeted DO reentry assumes no risk to people or property on the ground. For low trajectory risk systems, R_M was also

set to 0, indicating that the ADR system includes the capability to avoid collisions with high priority objects on orbit.

A parameter (a) was included to account for the risk that debris removal poses to any active satellite or other large DO crossing or nearing the orbit of the object being removed. A destructive collision was assumed if this object came within a keep-out zone extending 200 m in every direction from the structure of the ADR system, ADR vehicle, or DO being deorbited, based on the keep-out sphere enforced for the ISS [40]. (a) was defined as

$$a = \frac{A_{ADR}}{A_{DO}} \tag{2.2}$$

where A_{ADR} is the destructive collision cross section of the mated stack, and A_{DO} is the destructive collision cross section of the DO alone. For tugs, A_{ADR} includes the body of the tug and the geometry of the DO. For tender vehicles, A_{ADR} includes the geometry of the deployed DP and DO. Destructive collision cross sections are listed for each ADR system and for an unmitigated DO in Table 2.6, along with the corresponding values for (a). It should be noted that GOLD and Terminator Tether do in fact produce an increased cross section when deployed. However, GOLD claims that an impact would not be destructive for the impacting object, and Terminator Tether can be rapidly retracted to avoid a collision. Therefore, these systems are assessed as having the same destructive collision cross section as the unmitigated DO.

Table 2.6: Destructive collision cross sections.

ADR system	Cross Section	a
Unmitigated DO	129,000 m2	1
Conventional Tug	129,000 m2	1
KSII	151,000 m2	1.17
TRIS	156,000 m2	1.21
EDDE	1.76 x 106 m2	13.6
GOLD	129,000 m2	1
Terminator Tether	129,000 m2	1
LAT	129,000 m2	1

In order to avoid an impending (within a few orbits) conjunction with another orbiting object, the vehicle designer contains the option for an ADR vehicle to carry one or more collision avoidance motors. These are sized by the vehicle designer to provide enough impulse to lower the perigee of the vehicle by 1 km. Adding these motors mitigates the effect of R_M by eliminating the risk of collision with some number of active spacecraft. Each motor is assumed to eliminate the risk that a single DO will collide with an active satellite. Therefore, the maximum number of collision avoidance motors for a spacecraft was set as the number of DOs that a single vehicle in the program is designed to remove.

The total trajectory risk for a given ADR system was determined as the sum of the total risk to objects on the ground and the total risk to satellites of interest in orbit. Total risk to objects on the ground is determined by multiplying R_H by N. Total risk to orbits of interest is similarly determined by multiplying R_M by the number of DOs deorbited without some collision avoidance mechanism. In the current iteration, the only collision avoidance mechanisms are the collision avoidance

motors described above, so the number of DOs deorbited without some collision avoidance mechanism is $N - n_{cam} \ N_F$. R_M is also multiplied by (a) to account for potentially increased risk of collision with other satellites due to increased cross section.

A technology development risk factor R_{TRL} was included to account for uncertainty in the performance and reliability of ADR technologies that are not yet flight proven. The technology readiness level (TRL) assumed for each ADR system is given in Table 2.7, based on NASA TRL definitions [41].

Table 2.7: ADR system TRLs.

ADR system	TRL
Conventional Tug	6
KSII	5
TRIS	6
EDDE	5
GOLD	6
Terminator Tether	6
LAT	5

This risk factor accounts for potential cost and schedule overruns due to a lack of current technological maturity of systems involved in a vehicle design. Cost overruns are assessed as lost value, in order to equate with risk due to damages outlined above. A cost growth value was determined as a function of a cost correction factor f_C [42] and the expected ADR system and grapple mechanism development cost. This factor was normalized by c_{sat}, the expected cost of an Earth orbiting scientific observatory, assumed to be \$672M. Bus development cost growth was only accounted for if an ADR system was self-contained. That is, if the vehicle designer

49

was designing a bus for the ADR system, was assumed that the bus was developed with flight-proven technologies. For self-contained ADR systems, the TRL of the bus was determined based on the spacecraft design details given by the author for that ADR system. A risk factor was also added to account for the expected schedule slippage based on TRL. A relative schedule slippage

$$RSS = 8.29e^{-0.56(WTRL)} \tag{2.3}$$

was assessed based on the work of Dubos, Saleh, and Braun [43], where WTRL is the weighted sum of the TRL and development cost of each subsystem, divided by the total development cost. To determine WTRL, the entirety of the spacecraft, with the exception of the grapple mechanism and ADR system, was considered to be a single subsystem with a TRL of 9 for non-self-contained systems. For self-contained systems, a TRL was determined based on provided details, with the relative schedule slippage being based on the lowest TRL subsystem. To determine the total schedule slippage, this relative schedule slippage was multiplied by an assumed development time of five years. The main risk associated with schedule slippage is that additional catastrophic collisions will occur in low Earth orbit due to the unmitigated debris during the schedule delay. This risk is assumed to result in an additional seven collisions over the next two hundred years per forty years of schedule slippage [9]. A nominal five year development schedule is assumed for a given vehicle. Therefore, the absolute schedule slippage for this program is determined by multiplying the relative schedule slippage by five. Multiplying

the above collision rate by the absolute schedule slippage results in a number of additional collisions equal to 7/8 times the relative schedule slippage. Therefore, the total risk factor from technology readiness is

$$R_{TRL} = \frac{[\Sigma(f_c - 1)c_{dev}]}{c_{sat}} + \frac{7}{8}RSS = \frac{c_{ov}}{c_{sat}} + \frac{7}{8}RSS \tag{2.4}$$

The final overall risk factor is then

$$ORF = R_T + R_{TRL} \tag{2.5}$$

2.2.4 Genetic Algorithm

An initial generation of vehicles was produced based on random genomes. A genetic algorithm was implemented to produce successive generations of designs. The process followed by the genetic algorithm is shown in Fig. 2.9. To produce a new generation, a fitness score is assigned to each member of the current generation. The fitness function, determined heuristically, is given in Eq. 2.6:

$$f_r = [10^{c_{DO}}(t_{PO})(ORF^3)]^{-1} \tag{2.6}$$

Vehicle fitness is based primarily on the cost per DO removed, C_{DO}, and the overall risk of the ADR program, ORF. There is also some dependence on the time per DO removed per ADR vehicle, t_{PO}, added to prevent designs with unrealistically high times per DO from achieving a high fitness score. Any genomes that produce
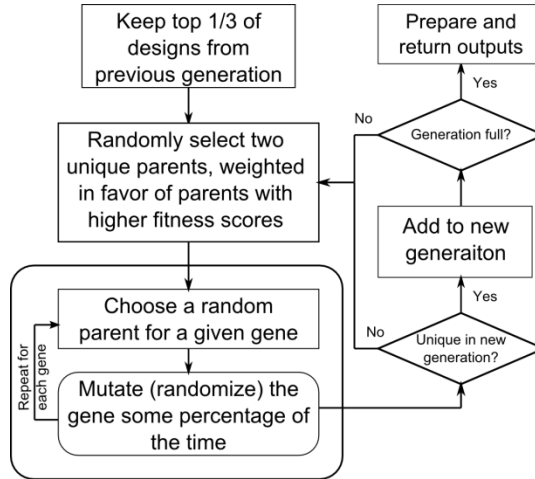
Figure 2.9: Genetic Algorithm Process.

more massive vehicles than can be launched are eliminated, regardless of their f_r, as well as any genomes for which the designs cost per target is more than two standard deviations above zero. Fitness scores are then normalized, such that the sum of all fitness scores is one. These normalized fitness scores (f_N) are then used to determine the parent designs for the new generation.

The 1/3 of designs with the highest fitness scores in the current generation are added to the next generation without modification. This ensures that the top performing designs are preserved for the next generation, even if by chance they are not selected as parents for the new generation, or do not produce as high performing child designs in the new generation. The remaining 2/3 of the new generation are produced through combinations of two parents from the current generation. Parents are randomly selected, with selection weighted in favor of designs with higher f_N. For each input parameter for the child genome, one of the two parent genomes is

chosen at random, and that input parameter is inherited from the chosen parent. There is also a 3% chance that a given input parameter will be mutated for the child genome. In such a case, the childs input parameter is not based on either parent, but is randomly assigned, and as a result can be any valid value. This genetic algorithm is utilized to produce ten successive generations, with the goal of a more fit set of designs in each successive generation. Ten generations were used, as this proved sufficient for Pareto-optimal designs to converge and improvement to cease.

2.2.5 DO Population Selection

Liou [9] categorized the 500 objects in LEO with the highest mass-collision probability products by their inclination and orbital altitudes. The majority of these objects fall into about eight inclination belts, and include both defunct satellites and spent launch vehicle upper stages. Each accounts for approximately half of the 500 objects, with the highest mass and collision probability products in LEO [44]. Defunct satellites present unique challenges to remove. The original owner or operator of the satellite may have reservations about it being visited and removed from orbit by another vehicle, even if it is defunct. By contrast, spent upper stages usually do not have the same level of restriction placed on their removal by the original owner. From a rendezvous and capture point of view, it is far more likely to find nearly identical upper stages in similar orbits within LEO than to find nearly identical satellite vehicles. Therefore, it is desirable to focus on deorbiting launch vehicle upper stages rather than spacecraft.

Several of the inclination belts described by Liou are composed almost exclusively of expended SL-8 rocket bodies, so the debris population considered in this study was modeled on this group of DOs. Based on this object group, the model debris population was assumed to comprise 1400 kg objects in 750 km circular orbits, each with a 74 degree inclination. The objects were assumed to be cylinders 2.4 m in diameter and 6 m in length [45]. The distribution of right ascensions of the model DOs was taken from two-line element (TLE) data for SL-8 rocket bodies at 74 degrees inclination and with semi-major axes of approximately 750 km altitude. For a given number of targets visited by a single vehicle, the total $\Delta\Omega$ for a set of targets was determined by finding the group of that number of targets within the smallest $\Delta\Omega$ band. The $\Delta\Omega$ between two consecutive targets was then assumed to be the average $\Delta\Omega$ between targets within the band.

2.3   Results and Analysis

The vehicle design optimizer was run for three test scenarios; a primary scenario, a solar max scenario, and an orbital scrap yard scenario. In the solar max scenario, debris removal is assumed to occur at solar max, enhancing the effect of aerodynamic drag, and therefore lowering the required size of any aerodynamic decelerator device. For this scenario, the mass of these systems was scaled by a factor of approximately 0.8 to account for the reduced surface area necessary to complete deorbit within one year of device activation. Placing debris in a scrapyard rather than deorbiting it allows the material to potentially be re-used in orbit, or to be

deorbited in a target manner at a later date. This consolidates multiple DOs in one place, reducing the overall risk of collision in a manner similar to deorbit. It also allows low thrust tugs to carry the DOs all the way to their final orbit, compared to the primary scenario, where they must separate from the DOs in a low orbit, allowing atmospheric drag to perform the final deorbit.

2.3.1 Baseline and Solar Max Scenarios

The results for the baseline and solar max scenarios are plotted to in Fig. 2.10 and Fig. 2.11 respectively, based on cost per DO removed and overall risk factor. The resulting Pareto front, the curve containing the leading non-dominated designs, is given in each of these figures. Approximate details of a design from each of the leading groups on the front are given in Table 2.8 and Table 2.9, respectively, for each scenario. The listed DPS mass includes all thrusters and propellant tanks, but not propellant itself. The listed EPS mass includes the mass of solar arrays, batteries, and power regulation and distribution systems. Available information for EDDE is for a self-contained spacecraft, rather than simply for the ADR system, and so the EDDE ADR system was assumed to be self-powering, as well as having built-in capability for DO grappling. The ADR system, structure, and avionics mass accounts for all vehicle systems not included in another group in this table.

Table 2.8: Leading Vehicle Designs - Baseline Case.

ADR system	genome	DPS mass	Propellant Mass	EPS mass	ADR system, structure, and avionics mass	Total mass	Time per DO removed
EDDE	ES41 BBBA Bp	-	-	-	80 kg	87 kg	33 days
LAT	HW14 BBBA AL	-	-	200 kg	285 kg	490 kg	360 days
T. Tether	GF20 AAAB AC	100 kg	3200 kg	370 kg	1500 kg	5200 kg	4 days
Conv. Tug	BF7 AAAB AA	90 kg	3000 kg	340 kg	190 kg	3600 kg	4 days

Table 2.9: Leading Vehicle Designs - Solar Max Case.

ADR system	genome	DPS mass	Propellant Mass	EPS mass	ADR system, structure, and avionics mass	Total mass	Time per DO removed
EDDE	EF39 BBBA Aj	-	-	-	80 kg	86 kg	32 days
LAT	Hi13 BBBA Bl	-	-	200 kg	290 kg	490 kg	350 days
T. Tether	GE13 AABB AJ	40 kg	1400 kg	360 kg	1000 kg	2800 kg	4 days
Conv. Tug	BG6 AAAB AA	80 kg	2700 kg	340 kg	190 kg	3300 kg	4 days

The Pareto front is divided into three distinct groupings in the baseline scenario, each comprising a single ADR system. No conventional tugs exist on the front, indicating that all other designs presented in Table 2.8 and all designs in Fig. 2.10 achieve better performance than a baseline conventional tug using all proven technology. EDDE was the lowest cost design by an order of magnitude, but also had the highest risk among all groups on the front, with an $r \approx 3$. The LAT carried approximately 40% the risk of EDDE in this case, but had a financial cost nearly an order of magnitude higher than EDDE per DO removed. Terminator tether had substantially lower overall risk factor than the LAT and EDDE, at a cost of approximately twice that of the LAT per DO. The conventional tug presented in Table 2.8 had comparable risk to the Terminator Tether based vehicle on the front, but carried a cost per DO removed that was approximately 30% higher than that of Terminator Tether. Risk parameters of the designs described in Table 2.8 are given in Table 2.10 and Table 2.11. Note that a negative cost overrun in Table 2.11 corresponds to an anticipated savings compared to the calculated system development cost. The LAT and EDDE were both considered high risk with regard to the ADR system specific risk multipliers, and the Terminator Tether on the front, as well as the conventional tug were both considered low risk. The inability of EDDE and the LAT to send a DO on a targeted reentry is a substantial risk, and is the primary reason for the large difference in the value of r for EDDE and the LAT, and for that of Terminator Tether and the conventional tug. In order for these systems to be considered for flight, the risk of an untargeted reentry must be accepted, or fur-
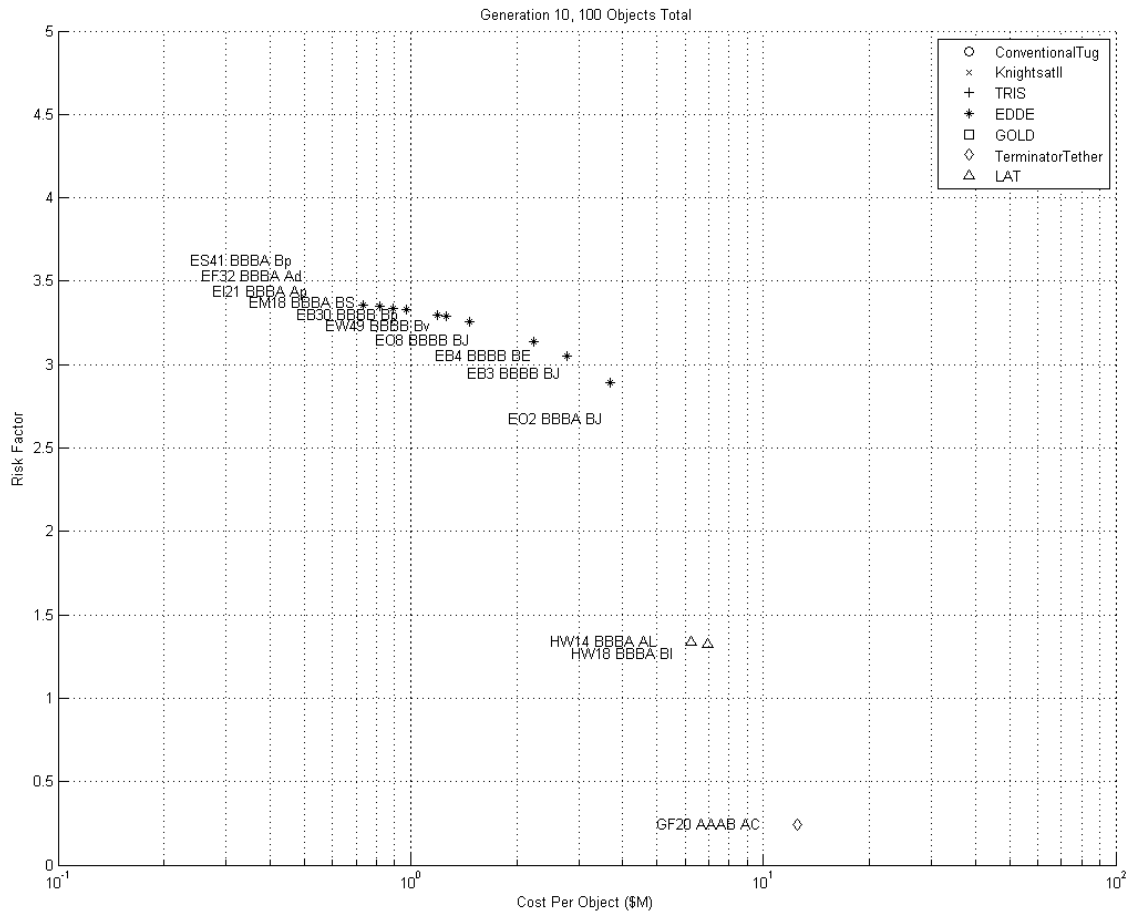
Figure 2.10: Leading vehicle designs based on risk factor and cost per object.
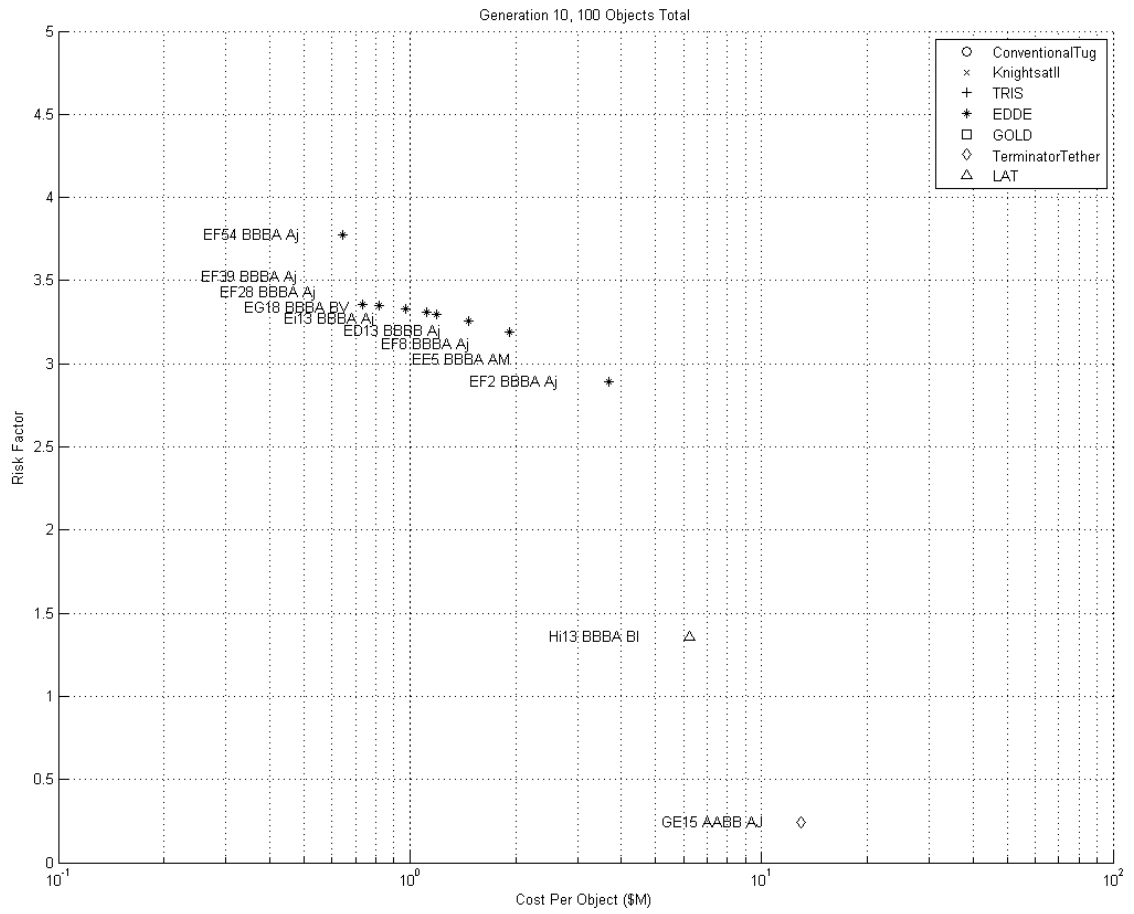
Figure 2.11: Leading vehicle designs assuming deorbit at solar max.

ther risk mitigation measures must be developed. The alternative orbital scrapyard scenario is considered below as a potential method of avoiding this risk.

Table 2.10: Trajectory risk parameters for leading designs.

ADR system	R_H	R_M	n_{cam}	N_F	a	R_T
EDDE	10^{-2}	10^{-3}	42	4	13.64	1.0
LAT	10^{-2}	10^{-3}	11	10	1	0.9
T. Tether	0	0	2	5	1	0
Conv. Tug	0	0	0	15	1	0

Table 2.11: Technology development risk parameters for leading designs.

ADR system	c_{ov}	RSS	R_{TRL}
EDDE	$14.7M	2.7	2.4
LAT	-$1.04M	0.50	0.44
T. Tether	-$4.51M	0.28	0.25
Conv. Tug	-$4.51M	0.28	0.25

Table 2.12: Objective values for leading designs.

ADR system	r	Cost per DO removed
EDDE	3.4	$0.73M
LAT	1.3	$6.2M
T. Tether	0.25	$13M
Conv. Tug	0.25	$14M

The difference in ORF between the LAT and EDDE is primarily a result of EDDE's low technological maturity compared to the LAT. While both debris removal methods are considered TRL 5, EDDE is designed with other subsystems, such as proposed terrestrial solar panels. Such subsystems are of lower TRL than

61

the other vehicles on the front, which use more conventional spacecraft busses with existing technologies. As a result, the EDDE vehicles on the Pareto front have a WTRL of 5, while all other vehicles on the front have a WTRL of 7. This difference results in a threefold increase in schedule slippage, increasing R_{TRL} by approximately 2.4. As a result, EDDE has the highest overall risk factor of any design evaluated, due to its low thrust nature and low technical maturity of many subsystems required. However, its lightweight, propellantless design also enables it to remove DOs at around 10% the financial cost per object of any other vehicle on the front. This is possible since EDDE has a much lower dry mass than any other design on the front, due largely to its use of many technologies that are far lower mass than their current state of the art space-grade counterparts. Using these advanced technologies affords EDDE a far lower mass than any other vehicle considered, leading to both a lower development cost and lower launch cost.

The LAT also benefits from a reduced launch mass, due to its essentially propellantless design. However, the LAT is built on otherwise existing satellite technology. As a result of these two factors, the estimated cost per DO of the LAT is substantially lower than the other vehicle designs on the front, but is closer to them than to EDDE.

It is of note that no aerodynamic decelerators appeared on the Pareto front, even in the solar max scenario. The only DP-based vehicle to appear on the front was a single Terminator Tether design, propelled by a high-thrust bipropellant rocket engine. Upon further investigation it became clear that this was the result of a limitation in the number of DOs reachable by a single spacecraft due to additional

mass required to reach each DO. All DP-based designs (as well as the conventional tug) utilize a propulsion system for which all propellant must be carried at launch. This leads to an exponential relationship between DOs per vehicle and vehicle mass, resulting in vehicles with prohibitively high mass for more than approximately 7 DOs per vehicle. In each of these cases, the majority of this mass results from propellant required for plane change. The remaining mass increase per DO is due to additional propellant for orbit lowering for the conventional tug, or the mass of DPs for DP-based vehicles. As a result of these factors, only a single design from this group appeared on each Pareto front. In all scenarios this design was the most expensive, but also lowest risk design on the front.

It should also be noted that of vehicles produced for the final generation of each ADR system, almost no low thrust, high I_{sp} DPSs were used, and none were present on the vehicles on the Pareto front. At first glance it may seem that a high I_{sp} electric propulsion system could help mitigate the prohibitive propellant requirements to visit a large number of DOs with a single vehicle. However, the low thrust nature of such propulsion systems imposes its own limit on the rate at which an ADR vehicle can visit DOs. As a result, much larger fleets of vehicles are required to maintain the required removal rate of 10 DOs per year, resulting in a somewhat lower optimal number of DOs per vehicle than a chemical thruster based vehicle. This primarily acts to drive up the total production cost for these programs, resulting in a higher cost per DO than those programs utilizing high thrust chemical thrusters.

The cost breakdown for each of the designs listed in Table 2.8 is given in Table 2.13. Note that the total development cost listed includes overhead costs in addition to the ADR system and bus development costs. The development and production costs are fairly similar for the LAT, Terminator Tether, and conventional tug. The ADR system development costs are similar among all designs on the front. However, since the entire spacecraft for EDDE is contained within the ADR system, the mass used for ADR system costing relations was the total mass of the vehicle. Therefore, the actual ADR system production and development costs for EDDE are assumed to be lower. The launch cost for EDDE is also an order of magnitude lower than other systems on the front, due in large part to the fact that EDDE is small and light enough to launch in an ESPA slot. This decreased mass is also responsible for a dramatic reduction in development and production costs, as the entire EDDE vehicle is similar in mass to the ADR system alone on the other vehicles. The cost and risk of each of the designs in Table 2.8 is shown in Table 2.12.

Table 2.13: Cost breakdown for Pareto front designs.

ADR system	ADR system development ($M)	Bus development ($M)	Total development cost ($M)	ADR system first unit ($M)	Bus first unit ($M)	Total first unit cost ($M)	Launch cost ($M)
EDDE	22.5	-	44.6	7.68	-	7.68	3
LAT	34.0	86.8	206	10.7	17.8	28.5	22.6
Conv. Tug	22.6	132	258	7.68	29.5	37.2	51.8
T. Tether	35.9	138	289	11.4	31.2	42.6	66.4

2.3.2   Orbital Scrapyard Scenario

An alternative orbital scrapyard scenario was considered in an attempt to mitigate the risk posed by uncontrolled reentry of debris removed by the orbital tugs. In this scenario, each orbital tug moves all DOs to a single orbital scrapyard. This scrapyard was positioned in a circular orbit at an altitude of 600 km and with an inclination of 74deg, with its right ascension centered within the band of orbits of the target DOs for that vehicle. Relative nodal precession between this scrapyard and the DOs was not considered. It was assumed that the orbit for the scrapyard was selected to minimize the risk of collision with other spacecraft and debris, while remaining easily accessible from the simulated debris belt. Use of this alternative methodology was assumed to reduce the trajectory risk of low thrust orbital tugs from high risk to medium risk, since an uncontrolled reentry no longer occurs. RL and RH were therefore set to 0 for low thrust tugs. Orbital scrapyards are an untested mission architecture, with no known proof of concept having flown at the time of this writing. Therefore, in this scenario, the ADR system of any low-thrust tug is assumed to be TRL 2.

The results of this scrapyard scenario are given in Table 2.14 and Fig. 12. In this scenario, EDDE appears to have increased in cost, while decreasing in ORF. The plane change required for EDDE to move DOs to the plane of the scrapyard now dominates time per object required. As a result, a larger fleet of vehicles is required to meet the required removal rate of 10 objects per year, raising the cost per DO removed for EDDE. The decrease in EDDEs overall risk factor is due to the

66

elimination of uncontrolled reentries for DOs, as well as crossings of high priority orbits. As a result, EDDE now has an expected cost overrun of \$34M and schedule slippage of 13.5 years. While the overall TRL of EDDE has decreased, substantially increasing R_{TRL}, ORF has decreased due to a near elimination of the R_T in this scenario. The LAT has increased in cost in this scenario, though not profoundly. Unlike EDDE, ORF has actually increased for the LAT in this scenario. The LAT spacecraft utilizes conventional subsystems with the exception of the ADR system. As a result, it suffers from a greater change in TRL between scenarios than EDDE, leading to ORF increasing. Like EDDE, the LAT now requires a larger fleet size to meet the DO removal rate requirement due to the large plane change required. This is almost exclusively responsible for the cost increase of the LAT. Terminator Tether was unaffected, since as a DP, its concept of operations was unchanged in this scenario.

Table 2.14: Cost breakdown for Pareto front designs, Orbital Scrapyard Scenario.

ADR system	ADR system development ($M)	Bus development ($M)	Total development cost ($M)	ADR system first unit ($M)	Bus first unit ($M)	Total first unit cost ($M)	Launch cost ($M)
EDDE	EB14 BBBA AO	-	-	-	80 kg	82 kg	191 days
LAT	HB7 ABBA BE	100 kg	115 kg	200 kg	290 kg	710 kg	580 days
T. Tether	GF20 AAAB BP	100 kg	3200 kg	370 kg	1500 kg	5200 kg	4 days
Conv. Tug	BE4 AAAB BC	80 kg	2800 kg	340 kg	190 kg	3400 kg	4 days

2.3.3 Additional Options

No aerodynamic drag based designs appeared on the Pareto front, even in the case where deorbit is performed at solar max. These designs did appear in the results, however both r and financial cost were higher than that of the conventional tug. It is possible that the cost of these systems as well as that of Terminator Tether could be lowered such that they are competitive with the remaining designs on the front by attaching their DPs to launch vehicle upper stages and spacecraft prior to launch. The DP could then be used as a simple, propellantless deorbit device at end of life for a spacecraft or after completing orbital delivery for spent upper stages. Treating a DP as a scientific instrument and applying the Spacecraft/Vehicle Level Cost Model, the development and first unit production costs are given in Table 2.15. Assuming a Terminator Tether design as described in this paper is used for 100 deorbits, with the development cost spread evenly across all DOs deorbited, and applying an 80 percent learning curve, on average such a device will cost \$1.4M per launch. Assuming \$8,000 per kg for launch on a Kosmos 3M [46], the rocket whose upper stages are used as model DOs in this analysis, the portion of the rockets payload lost to the DP would be approximately \$225,000 in value. Therefore, this method of DO deorbit can be assessed at a cost of approximately \$1.6M per DO. As discussed earlier, the ADR specific risk and destructive collision cross section ratio are both minimized for Terminator Tether. Since the device would only have to remain on orbit for the duration required to deorbit a single DO, the required lifetime would not be a concern with regard to risk factors, as defined here. Therefore, attaching
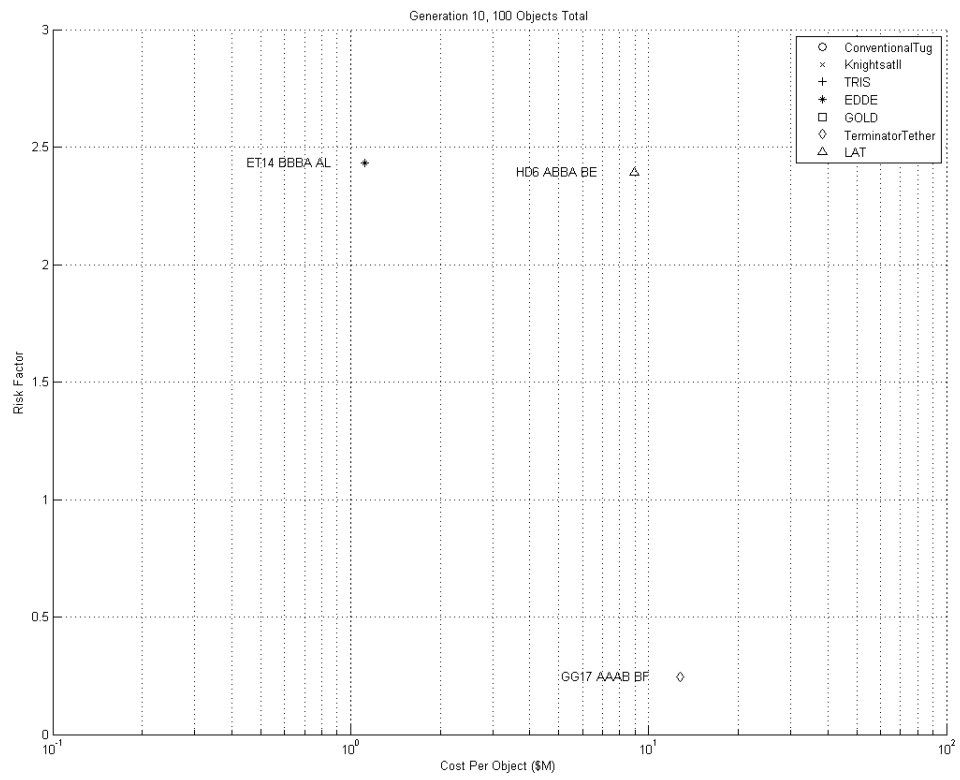
Figure 2.12: Leading vehicle designs assuming use of orbital scrapyards.

a DP prior to launch would provide an ADR method with costs competitive with EDDE, at substantially lower risk.

Table 2.15: DP development and first unit costs.

ADR system	Development cost ($M)	First unit cost ($M)
KSII	22	7.3
TRIS	26	9.3
GOLD	21	7.0
Terminator Tether	13	3.7

2.3.4   1D Cost Function Evaluations

In an attempt to achieve a clear ranking of Pareto-optimal vehicle designs, a comparison was performed by using a cost adjusted by r as a single, one-dimensional figure of merit. This adjusted cost per object c_a was determined as indicated in Eq. 2.7:

$$c_a = C_{DO} + \frac{r}{N}c_{sat} \tag{2.7}$$

In essence this adjusted cost assumes that a debris removal program, if implemented, must pay for any damages resulting from debris removal operations in addition to other program costs. The fitness function was changed to

$$f_r = \frac{1}{c_a} \tag{2.8}$$

and all scenarios were re-evaluated using this new fitness function. The results of these runs are given in Fig. 2.13, Fig. 2.14, and Fig. 2.15.

71

Figure 2.13: Leading Vehicle Designs - Baseline Scenario - Adjusted Cost
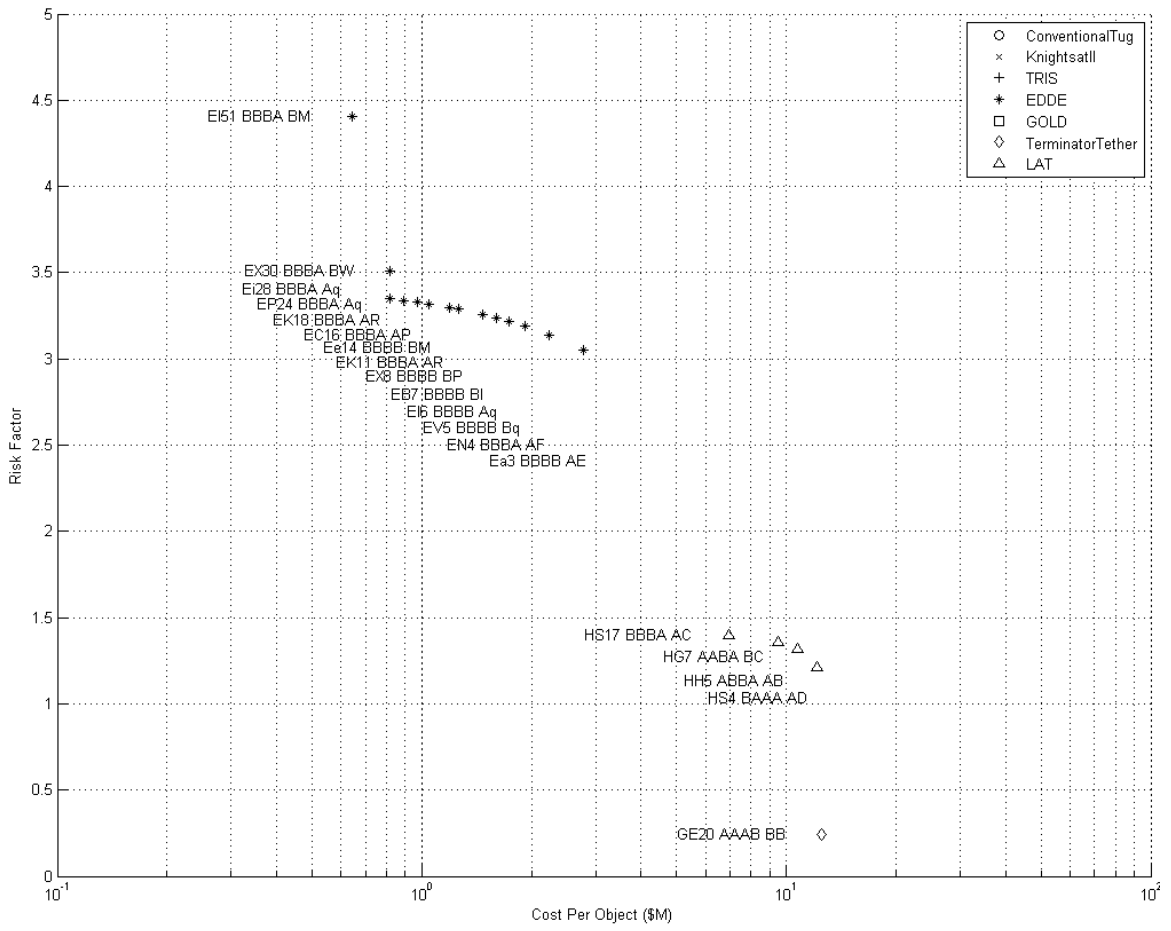
Figure 2.14: Leading Vehicle Designs - Solar Max Scenario - Adjusted Cost
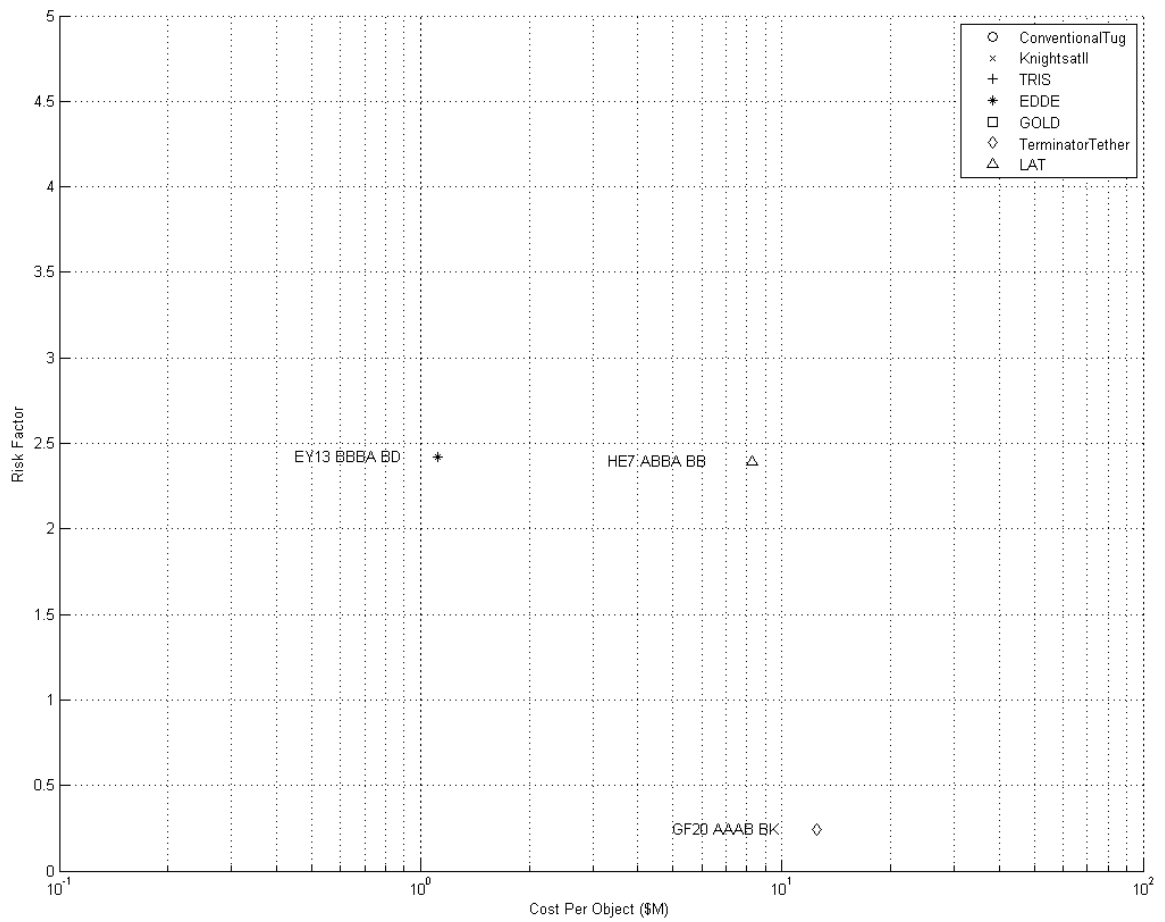
Figure 2.15: Leading vehicle designs assuming use of orbital scrapyards (adjusted cost).

The designs listed in these figures bear a strong resemblance to those in Fig. 2.10, Fig. 2.11, and Fig. 2.12. A list was produced, ranking designs by c_a. The lists for all three scenarios were combined, with the results presented in Table 2.16. Designs that are in the same group of the Pareto front, such as all of the LAT designs in Fig. 2.13, are assumed to be variations of the same vehicle design, and therefore only the design with the lowest adjusted cost in each group is presented in Table 2.16. Groups of designs have also been combined from Fig. 2.13 and Fig. 2.14, since, as with the original cost function, no aerodynamic decelerators appeared on the front in either scenario, and therefore the difference in the two scenarios is not expected to have an influence on vehicle designs.

All designs listed in Table 2.16 have an adjusted cost within a factor of no more than 1.75 of each other. Due to the uncertainty in the exact relationship of risk and cost, all of the designs presented in the table should be considered of equal merit. All warrant further investigation moving forward, likely making a final decision using additional criteria not considered in this work.

Table 2.16: Leading vehicle designs based on adjusted cost.

Genome	ADR system	Scenario	Total mass	Time per DO removed	ORF	Cost per DO removed	Adjusted cost per DO removed
GF20 AAAB BK	T. Tether	Scrapyard	5200 kg	4 days	0.25	$12.5M	$14.1M
HS17 BBBA AC	LAT	Standard/Solar Max	490 kg	419 days	1.4	$7.0M	$16.3M
EY13 BBBA BD	EDDE	Scrapyard	81 kg	173 days	2.4	$1.1M	$17.4M
EQ1 BBBB Ae	EDDE	Standard/Solar Max	85 kg	4 days	2.4	$6.4M	$22.4M
Ei28 BBBA Aq	EDDE	Standard/Solar Max	87 kg	32 days	3.3	$0.82M	$23.3M
HE7 ABBA BB	LAT	Scrapyard	590 kg	533 days	2.4	$8.3M	$24.4M

2.4   Summary

The current debris population in low Earth orbit has reached a point where, even with no new satellite launches, it will grow due to collisions between existing on orbit objects. The present work detailed an investigation of leading designs under consideration for orbit based removal of low Earth orbit debris. Designs were evaluated in three scenarios; a standard scenario, where all DOs are deorbited, a solar max scenario, where aerodynamic decelerators are reduced in mass under the assumption that debris removal occurs at solar max, and an orbital scrapyard scenario, where low thrust tugs gather all DOs in a scrapyard rather than directly deorbiting them. Designs in each scenario were evaluated based on their financial cost per object removed and a programmatic risk factor. In each scenario, Terminator Tether, LAT, and EDDE designs appeared on the final Pareto front, with each grouping of Pareto-optimal designs within the design space based around one of these technologies. The conventional tug exhibited very similar performance to Terminator Tether, although it did not actually appear on the front. However, due to the conventional tugs proximity to the front, its performance is considered essentially equal to Terminator Tether within the scope of this study, and therefore it warrants further investigation.

The benefit of propellantless vehicle designs (the LAT and EDDE) is evident from this study, with all but the most expensive Pareto-optimal programs being designed around such technologies. The fact that these vehicles need not carry all propellant for their mission at launch allows them to remove a large number of DOs

without becoming prohibitively massive. Additionally, of the designs on the front that utilized a dedicated propulsion system, none used a high I_sp electric propulsion system. This is due to the larger fleet size that would be required as a result of the large time per DO resulting from the low thrust nature of these systems.

The absence of aerodynamic decelerator based designs on the Pareto front indicates that these devices are currently of too great of a mass to achieve comparable performance to the Pareto-optimal designs. Not only must these vehicles carry all mission required propellant at launch, but they must also carry a number of DPs equal to the number of DOs they are to remove. In all aerodynamic decelerator cases, this mass, combined with the production costs of the DPs, raised the cost per DO for each of these systems substantially beyond that of Terminator Tether and the conventional tug. These methods of debris removal may still prove beneficial if attached to satellites and launch vehicle upper stages prior to launch. The system could then passively deorbit an upper stage without the expense and complication of sending a dedicated ADR vehicle. Further investigation should be performed to refine this option, and to determine under what conditions it may be the preferred method of debris removal.

Based on the above work, the Electro-Dynamic Debris Eliminator, the Laser Ablation Tug, a passive electrodynamic drag tether such as Terminator Tether, and a conventional tug utilizing an impulsive chemical propulsion system should be considered for further analysis. Additionally, other passive decelerator technologies, while not as high performance as the aforementioned systems when delivered by space based systems, may be useful for deorbiting future orbital objects (satellites

and launch vehicle upper stages) if attached before launch. The final design that should be developed for debris removal will depend on the results of this future analysis. In addition, the risks to people and infrastructure, both on orbit and on the Earth, must be weighed with the added financial burden of a lower risk system, and a decision made as to what level of risk is acceptable to avert the impending risk of an ablation cascade.

Chapter 3: The General Static CR Model

3.1 Overview

This chapter lays out the basic form of the CR model, around which remainder the framework is built. This form of the model addresses systems where all components are assumed to be in a steady state. In these systems resource flows are constant. It is therefore sufficient to analyze such a system at a single point in time.

The static CR model is not sufficient to model most spacecraft, where component behavior changes over time. However, it is beneficial to introduce as many concepts of the CR model and framework as possible in the context of a static design problem. The design of a lighting system is used as an example in this chapter to help describe the static CR model. Later chapters will detail the necessary additions to extend the framework to dynamic problems like spacecraft design.

3.2 Component Definition

As has been stated, the CR model takes a complex system and models it as a collection of components and resources flowing between them. Each component may

Figure 3.1: Component resource flow example. The lamp shown is a sink for electrical power, and a source for light and heat, each of the quantities shown in the figure.

be a source, sink, or store for some given number of resources. For each resource for which it is a source, it produces some amount of that resource. For each for which it is a sink, it consumes some amount of that resource. Stores will be discussed briefly at the end of this chapter, and will be discussed in more detail in the context of the dynamic CR model. As an example, consider a 60 W incandescent lamp. A resource flow diagram for such a component is given in Fig. 3.1. This component involves three different resources; light, heat, and electrical power. It is a sink for electrical power, requiring some (assumed constant) wattage to operate. It produces 15 lm/W of light, totaling 900 lm at 60 W. This corresponds to an efficiency of 2.2% [47]. We assume that all losses are thermal, so the lamp produces 58.7 W of heat.

Components are separated into classes by their function, and further subdivided into subclasses by similar operating principles. Components of a given class serve the same function in the system. That is, they are a source or sink for a given set of resources. Maintaining the above example, consider the design of a lighting system, as shown in Fig. 3.2. Two classes are included in this system; lamps and power sources. Lamps sink electrical power and produce heat and light. Power sources produce electrical power. In this example, light and heat are edge resources.
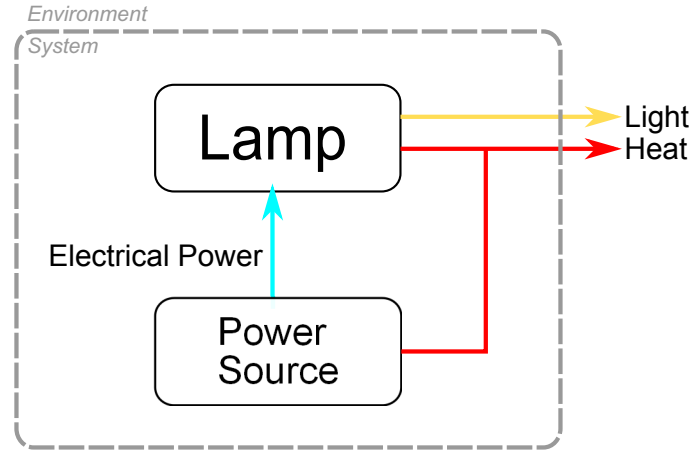
Figure 3.2: Lighting system example. This simple example contains two top-level component classes; lamps and power sources.

Each component class can contain multiple subclasses. Components within a given class are grouped into subclasses by similar manner of operation. Doing so allows a similar component-level model to be used for all components of a subclass, only changing the values of variables in the model. In this example, incandescent lamps, fluorescent lamps, and LED lamps may each be their own subclass of the lamp class.

The resource flow for the incandescent lamp subclass would then be defined in equations 3.1, 3.2, and 3.3:

$$P_{in} = P_{op}[\text{W}] \tag{3.1}$$

$$L_{out} = \lambda_{lm} P_{in}[\text{lm}] \tag{3.2}$$

$$H_{out} = (1 - \eta_{lamp}) P_{in}[\text{W}] \tag{3.3}$$

where P_{in} is the power consumed, P_{op} is the required operating power of the component in W, L_{out} is the light produced, λ_{lm} is a conversion factor from electrical power to light, H_{out} is the heat produced, and η_{lamp} is the efficiency of the lamp. Maintaining the assumption that all energy entering the lamp is converted to either light or heat, it is possible to equate λ_{lm} and η_{lamp}, but they will both be kept as separate properties for simplicity of the example. P_{in}, L_{out}, and H_{out} are the resource flows to and from the component. The goal of the component class (and subclasses, where applicable) is to determine the resource flows of the component as functions of the remaining properties. The values of these component parameters are defined for each specific component. The component parameters for all components of a given subclass are compiled into a component library for that subclass.

Component parameters can either be fixed, appearing as a constant for each entry in the library, or genetically determined, in which case the range of possible values is described in the component library. Allowing for components with genetically determined parameters gives the framework the ability to handle some design aspects of individual components. This distinction enables the framework to propose and optimize its own components for subclasses in which component behavior can be analytically described. It is envisioned (and is certainly the case in the spacecraft design problems of interest to the author) that systems may exist that contain "off the shelf" components, which will henceforth be referred to as "real" components. However, the ability to propose new or custom components may be desirable. These will henceforth be referred to as "notional" components.

This is indeed the situation in current practice integrated space mission design. Previously flown components are used where possible, and where they efficiently fulfill a given role, but new components are also developed for a new spacecraft. At this proposal-level mission design, novel components are often modeled by interpolation and regression of data from existing components, as well as with analytical models. The goal of variable component parameters is to allow the CR model to handle and replicate this capability.

As an example, consider a high gain parabolic antenna (HGA) for a spacecraft. The gain of the antenna is defined as

$$G = 10 Log_{10} \left(\frac{4 \pi e_A A}{\lambda^2} \right) \text{[dBi]} \tag{3.4}$$

where e_A is the antenna efficiency, A is the aperture area of the antenna in m^2, and λ is the wavelength of the transmitted signal in m. The mass of the antenna is defined as

$$m = \rho A \text{[kg]} \tag{3.5}$$

where ρ is the areal density of the antenna, in kg/m^2. The values of e_A and ρ will be a function of the antenna material and construction, accounting for factors that cannot be modeled analytically in a simple way. λ is determined by the incoming signal from the spacecraft's transmitter, which would be considered a resource for which an antenna of this class is a sink. A is defined by the designer, and drives the gain and mass properties given eqs. 3.4 and 3.5. An entry in the component library

for notional parabolic antennas would then contain constant component parameters for e_A and ρ, and the range of reasonable values for A, or more likely, r, defining $A = \pi r^2$. r would then be determined by a component genome, discussed in more detail in Chap. 4.

To summarize, all components within a given class or subclass exist as a listing of parameters in the component library for that class or subclass. The class or subclass then models the resource flows of the component as a function of its component parameters. These resource flows then describe the interactions of the component with the rest of the system. Fig. 3.1 illustrates the calculated resource flows for a component with $P_{op} = 60$ W, $\lambda_{lm} = 15$ lm/W, and $\eta_{lamp} = 0.022$, based on [47]. By constructing a system from combinations of components and analyzing the resource flows between them, the CR model is able to determine the behavior, performance, and feasibility of the system as a whole.

3.3 Resource Analysis

Following the procedure from the previous section, one is left with a series of components, each producing and consuming known quantities of given resources. Analysis of these resource flows between components serves as the system-level simulation for the CR model. This ultimately leads to an ability to assess the performance and feasibility of whole systems, allowing generalized analysis of multiple design options for a given design problem.

Two types of resources exist within the CR model; internal resources and edge resources. Internal resources flow between components of the system, and must be balanced, as described below. Edge resources flow between the system and its external environment. In the static CR model, edge sources can supply a resource flow into the system at a constant rate, and edge sinks can consume some flow produced by the system at a constant rate. Either of these rates may be finite or infinite by convention. In the case of infinite edge resources, the amount of a given resource flowing to or from the environment is tracked. These tracked values may then serve as figures of merit for determining the performance of the system. In our lighting system example, objectives may be to maximize the amount of light produced and minimize the heat produced by the system. Light and heat are edge sinks, produced within the system and sunk to the external environment. It is not a requirement that edge resources are the only figures of merit in the design problem. Additional objectives in this design problem may be to minimize the mass or minimize the financial cost of the system.

The power of the CR model is that constraints can be naturally handled through resource flows. The net flow of each resource is constrained to be greater or less than some constant value. In most cases this constant ends up being zero. That is, a resource is constrained simply to have a surplus or deficit across the system. For the lighting system, the driving feasibility constraint is that the power sources produce at least as much electrical power as the lamps consume.

Usually an objective value is determined by summing the value of a given property across the system. For non-resource figures of merit such as mass and

cost, this is straightforward. Property values are directly summed across all system components. For resource tabulation, the process is a little more involved. For a given design problem, a resource relation

$$\delta_i = \Sigma_{i,source} - \Sigma_{i,sink} \tag{3.6}$$

is defined for each resource i, where $\Sigma_{i,source}$ is the total amount of resource i produced across all components of the system, and $\Sigma_{i,sink}$ is the total amount of resource i consumed across all components of the system. For each resource, δ_i is constrained to be greater than or less than some constant, often zero. This implies a desired surplus (for $\delta_i > 0$), or deficit (for $\delta_i < 0$) of a given resource. This concept is then the heart of the CR model.

A complex system can be decomposed into a series of components, each of which produce and consume certain resources at a given rate. Most constraints on the system can be handled by balancing this resource flow across the system. In the lighting system example there is only a single internal resource - electrical power. As discussed above, we wish to constrain the problem, ensuring that at least as much electrical power is available as is consumed within the system. Therefore,

$$\delta_P > 0, \tag{3.7}$$

where δ_P is the resource relation for electrical power within our system.

The final topic to discuss regarding resources in the static CR model is the concept of resource conditioning. A resource may have properties associated with it besides its flow rate. As a result, multiple versions of the same resource may exist within the system. In our example problem, voltage may serve as a condition on electrical power flow. It is possible to have a power source that produces power at one voltage, and a lamp that requires power to be supplied at another voltage. For all intents and purposes, flows of the same resource with different conditioning function as separate resources altogether. Resource conditioning serves as an added layer of complexity that may or may not be necessary for analysis, depending on the problem at hand.

The main purpose in organizing resources in this way is to facilitate compatibility checking between sources and sinks of a given resource within the system. Versions of the same resource with different conditioning can simply be summed to a single value, ignoring any compatibility issues at this stage of analysis. Alternatively, they can be treated as completely separate resources, or some conversion penalty can be imposed to convert from one conditioning to another. In the case of the former, additional components could be added to the system that perform conversion. For example, a transformer can be added to convert from power produced at one voltage to power consumed at another voltage.

3.4   The Quasi-Static CR Model

One extension to make to the static CR model is to introduce components with stores, as alluded to earlier, to the model. A store is a type of component that contains a finite internal reservoir to cache a particular resource. A store operates as either a source or sink, depending on other resource flows within the system. In the lighting system problem, a possible example would be to express batteries as a subclass of power sources. A battery starts fully charged (that is, with its electrical power reservoir full). It operates as a source, providing electrical power to other components within the system. One common use of stores is to handle component lifetime constraints, especially when those lifetimes may be tied to some other resource flow. For example, a lamp may only be able to produce some amount of light before it is expended. In this case, the lamp can be considered a store for component lifetime, which depletes at some rate per light produced.

The model is no longer truly static, since resource relation violations may occur when stores are depleted. The model is still quasi-static, with the system still operating in steady state until a store is depleted or filled. This implies the resource flow of the system does not change during operation, so stores operate as either a source or a sink, but never both in the same simulation. Assuming stores are utilized, they will at some point be either expended (if operating as a source) or completely filled. At this point, they no longer function as a store for that resource in the system. The elapsed time at which this happens is tracked, and the resource flow of the system subsequently changes. If any resource relations are violated as

a result, the simulation ceases, with the total simulation time elapsed noted. This simulation time then becomes a figure of merit, which may be used as an objective, or as an input to some more complicated objective function.

It may be evident at this point that there is a potential for modeling more complicated systems with time varying resource flow, due to operational changes or environmental changes external to the system. In such cases, stores may operate as either sources or sinks at different points in time depending on the state of the rest of the system. In the lighting system example, a battery may provide power from its internal reservoir until power is expended, but may then be recharged by an external power source, which, if necessary, may power other components of the system simultaneously. Most of the problems of interest to the author are of this more complex, dynamic nature. They will be addressed in full detail in the following sections on the General Dynamic CR model.

Chapter 4:   Optimization with the CR Model

4.1   Overview

The motivation behind the CR model is to facilitate automated design opti-

mization of a wide class of complex systems built from discrete components in a

very uniform manner. The CR optimization problem can be generally stated as

$$
\begin{aligned}
\min \quad & F(\boldsymbol{C}, \boldsymbol{x}) \\
\text{s.t.} \quad \delta_i \ & \geq \ k_i \\
\delta_j \ & \leq \ l_j \\
\forall i \ & \in \ \{1, ..., M\}, \\
j \ & \in \ \{1, ..., N\}
\end{aligned}
\tag{4.1}
$$

where each δ_i is a surplus constraint and each δ_j is a deficit constraint, and k_i and l_j

are a series of constants. For surplus constraints, the requirement is that more of the

resource associated with that relation is produced than consumed across the system.

For deficit constraints, the opposite is true. M and N are the total number of surplus

and deficit constraints, respectively. $\boldsymbol{C}$ is the set of all components comprising an

individual design, and $\boldsymbol{x}$ is the vector of system-level variables beyond component

selection. $F(\boldsymbol{C}, \boldsymbol{x})$ is the objective function, which varies with the specific design problem. In words, the problem can be stated as follows: find the combination of allowable components and system-level design variables that optimize objective performance while meeting all required resource flows, ensuring proper functioning of the system.

A specialized GA detailed in this chapter, was developed to perform this optimization. A GA was selected for its ability to perform more complete design space exploration simultaneously compared to other metaheuristic optimization algorithms. This is due to the way it produces entire generations of design options spanning a trade space. The penalties for increasingly large numbers of variables are also much lower for GAs than many other optimization techniques. This makes them well-suited for problems with a large or variable number of design parameters. As was discussed in the introduction, substantial literature already exists for handling variable-size problems with GAs.

Metaheuristic algorithms do not rely on any analytical knowledge of the problem for optimization. This makes them well suited for multidisciplinary problems. In these problems, the relationship between the design variables and objective functions is complex, and may be iterative or even transcendental. GAs in particular are well-suited for combinatorial problems with discrete variables, like component selection problems [19]. Furthermore, there is an extensive history of applications of GAs for multiobjective design space exploration problems [19, 21, 48, 49], the role this work seeks to fill.

An overview of GAs in general can be found in Chap. 1. The remainder of this section will focus on the particulars of the GA implementation developed for this dissertation. Unlike most other GAs, this implementation utilizes a variable length genome. Each gene of the primary genome corresponds to a component present in the system. Enabling the genome length to vary across population members and from parent to child allows the algorithm to naturally vary the number of components in a design.

4.2   The VEGA Genome

A variable length chromosome is utilized to maintain the greatest generality possible. It naturally allows the number of components present in a system design to vary within a given design problem. The VEGA genome is separated into three levels, summarized in Table 4.1, with a simplified satellite genome example given in Fig. 4.1:

Table 4.1: Various levels of the VEGA genome.

Genome level	Description
0	System-level genes
1	Primary genome/component selection genome
2	Component-level genome

The Level 1 (L1) genome, or system-level genome, accounts for problem-specific design parameters. These parameters cannot be tied to a given component. They drive the behavior of the system as a whole. For example, consider a spacecraft
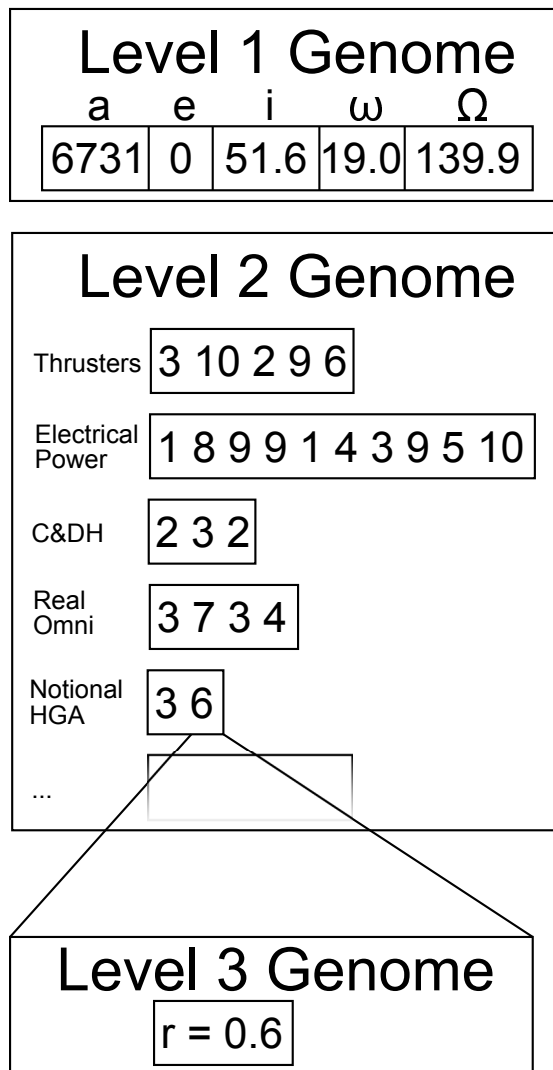
Figure 4.1: Simplified genome for a spacecraft design. The L1 genome specifies the orbit in which the spacecraft will operate. The L2 genome specifies the components that comprise the spacecraft, and is separated into chromosomes based on component class. The final chromosome displayed is for notional HGAs, described to some extent in Chap. 2. For one of these, the L3 genome is displayed, specifying the radius of the antenna.

design. The orbit in which a spacecraft is operating has a strong influence on its performance and requirements. Several orbit options may be available for a given mission. This may consist of a number of discrete orbits. Alternatively, the orbital parameters may exist as continuous variables to be optimized in the design problem. In both cases, the orbit would be determined using genes in the L1 genome.

The goal of VEGA is to support a system design optimization framework that is as general as possible. Contrary to this, the L1 genome is very problem specific. Much of the purpose of the L1 genome is to encapsulate any necessary design variables specific to the problem at hand, passing them to the simulation. Therefore, for a specific design problem, the user must specify the sequence of L1 genes. Some additional information about each gene, based on whether it is discrete, or continuous is also required. For discrete genes, the user can either specify a list of all possible values, or a range within which any integer value is acceptable. For continuous genes, the user simply specifies the bounds for possible values. Then, for a given individual, the L1 genome will then be passed with the system object to the system-level simulation.

The Level 2 (L2) genome is the most critical portion of the genome, and is always included. It dictates which components are present for a given individual. The L2 genome is segmented into "chromosomes" by component class and subclass. Crossover is then performed separately between corresponding chromosomes. The reason for this segmentation is related to how the variable length crossover operator functions. Its purpose will become evident in that section. Within each chromosome, the value of each individual gene references a component in the component library
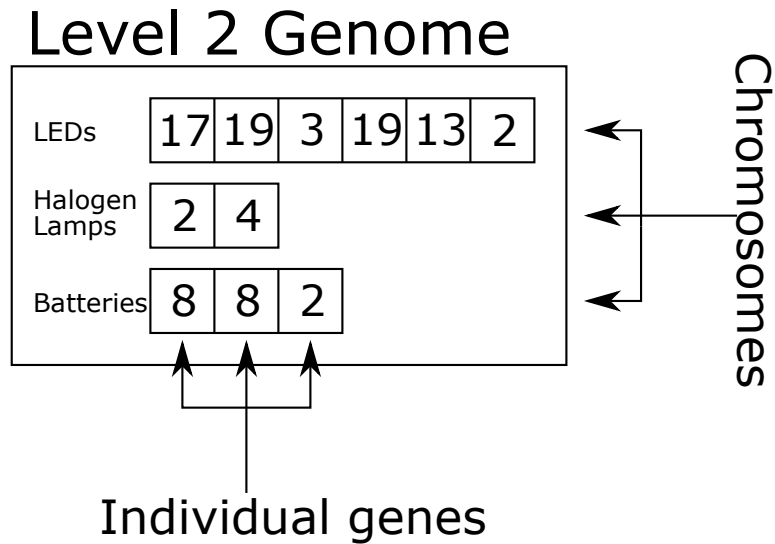
Figure 4.2: L2 genome for lighting system example, containing three subclasses; halogen lamps, LED lamps, and batteries. Each line is a chromosome, representing the components present from a given subclass. Within each line, each number is an index in that subclass' component library, and represents an individual component. The number of genes in each subclass is randomly determined, and can vary from individual to individual within a population.

for the corresponding subclass. The L2 genome is integer coded, with the range for a given chromosome being $[1, i_{max}]$, where i_{max} is the maximum index in the subclass library for that chromosome, equal to the number of component entries in the library.

The L2 genome is of variable length, with each gene representing the index of a component in the component library. Repeats are allowed within a chromosome, simply implying multiple copies of a component exist within the system. It is possible for these copies to have differing L3 genomes, discussed below, meaning that the two "copies" exhibit dissimilar behavior within the system. Fig. 4.2 presents a diagram of a hypothetical genome for our lighting system example.

In order to initialize the first generation of designs for an optimization run, it is necessary to randomly determine all chromosomes of the L2 genome. This involves randomly determining both the number of components and selection of components present. The latter is straightforward once the former is accomplished. For the former, a set range on the number of components in each class is used to generate the initial population. By default, the range on number of components for a given subclass is [0, 10], but this starting range can be user defined as well. As will be discussed, this is simply used to bound the genome size of the initial population, and has little bearing on the final chromosome length to which the GA converges.

The final remaining portion of the genome is the Level 3 (L3) or component-specific genome. The L3 genome exists to support notional component subclasses, where component behavior is a function of some number of selectable options for a given component. For notional components, analytic relations exist for defining components as a function of some number of parameters. The encoding of L3 genes is therefore specific to each component class which utilizes them. It is implicitly defined through the component class model on a case-by-case basis.

L3 genes are created when a component is first initialized. This usually occurs when randomly generating the first generation of designs. The values of the L3 genes for the given component are randomly determined as well. The component is essentially "fixed" at this point, maintaining the same L3 genome as it is inherited from generation to generation. There is still the potential for the L3 genes to mutate each time the component is inherited. Therefore, it is still possible that an L3 genome may vary over the multiple generations of an optimization run.

4.3 The Variable Length Crossover Operator

Considerable effort in the development of this GA entailed the design of the variable length crossover operator, which allows the GA to vary and optimize the number of components included in a system as part of its regular iteration. This section is therefore included, and focuses solely on the discussion of that effort. The overall operation of our GA implementation will be detailed in the following section.

In order to utilize a GA with a variable length genome, special considerations must be made in the algorithm's crossover operator. The crossover operator developed for this work draws heavily from that proposed by Ting et al. [25]. It is largely what Ryerkerk et al. refer to as a cut and splice crossover [15], but includes some design philosophies of their synapsing variable length crossover. In the latter, the genome is grouped or "synapsed" by identifying common substrings in both parents, aligning those, and then performing n-point crossover, with the crossovers inserted within the synapsed portions of the genomes.

The encoding scheme for VEGA presents a straightforward method for a process similar to synapsing the genome - grouping it by chromosomes. The genome is in fact already grouped into chromosomes in this way. VEGA matches corresponding chromosomes of the L2 genome from each parent, then performs a cut and splice crossover for each chromosome. The cut and splice crossover operates in essentially the same way as an n-point crossover. The difference is that, rather than inserting the crossover points at the same random location in both parent genomes, they are inserted at different random locations in each parent genome. This is illustrated in
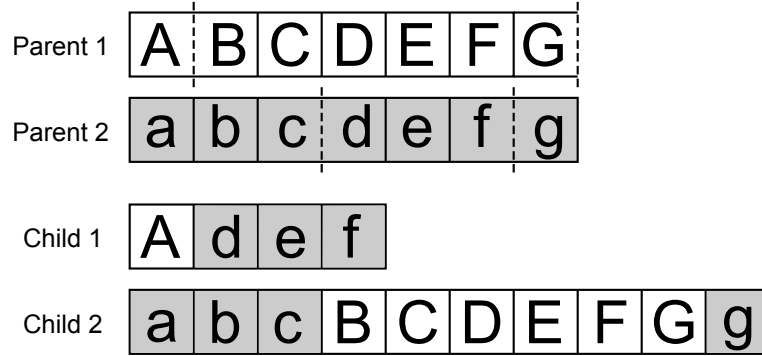
Figure 4.3: Cut and splice crossover. The example provided here is for a two-point cut and splice crossover. Note how this operator varies the chromosome length.

Fig. 4.3. Each child inherits genes from the corresponding parent (Child 1 from Parent 1, Child 2 from Parent 2) until a crossover point is reached on each parent genome. Both children then flip, inheriting genes from the other parent, continuing this process, flipping between parents at each crossover point until all genes in both parent chromosomes has been assigned to the child genomes. For VEGA, a single-point cut and splice crossover is used for each chromosome.

A similar component crossover (SCC), also proposed by Ryerkerk et al. [15], was considered. The concept of SCC is to find pairs of similar components between the parent genomes. That is, components which serve the same role in their respective designs. Each component in one parent genome is compared to each component in the other parent genome. Each pair is assigned a similarity, or, in the case of [15], a dissimilarity. Ryerkerk et al. defined this dissimilarity as

$$D = \frac{1}{n} \sum_{i=1}^{n} \frac{|C_{1i} - C_{2i}|}{\sigma_i} \qquad (4.2)$$

99

where C_{1i} and C_{2i} are the values of the ith parameter of the two components being compared, σ_i is the standard deviation in the ith parameter over the entire population, and n is the number of parameters. Some threshold of dissimilarity is defined, 0.5 in the case of [15]. Any component pairs with a dissimilarity less than this value are considered similar. Once the dissimilarity between all components has been calculated, the most similar pair is placed in the genome. The next most similar pair of the remaining components is then placed in the genome, and this process repeats until the threshold of dissimilarity is reached. The genome up to this point is of fixed length, since only pairs of components from each parent have been added. The remaining components (the dissimilar components) are added to the genomes of their respective parents as is. A standard n-point crossover is then performed on the similar portions of the genomes, and a cut and splice crossover is performed on the dissimilar portions of the genomes.

The similar component crossover developed for VEGA was inspired by this one, but operates somewhat differently. The similarity evaluation is somewhat more involved than that outlined above. This was necessary due to differences in the genome encoding scheme. Usually (except in the case of notional components), there is only a single parameter in the genome for each component. That parameter is simply a reference to an index in a component library. The measure of functional similarity in the CR model is the extent to which two components' resource flows are the same. For VEGA, a value for similarity was determined, rather than dissimilarity. This similarity was defined through the following derivation. Let the resource similarity

be defined as

$$S_i^j = \min \left[\frac{r_{iA}^j}{r_{iB}^j}, \frac{r_{iB}^j}{r_{iA}^j} \right] \tag{4.3}$$

where S_i^j is the similarity of the ith resource present in the two components, with either $j = I$, implying this is a resource flowing into the component (a resource for which the component is a sink), or $j = O$, implying this is a resource flowing out of the component (a resource for which the component is a source). r_{iA}^j and r_{iB}^j are the corresponding resource flows of the components being compared. Expressing S_i^j in this way means that its value will always be between 0 and 1, with 0 implying the resource flow is only present on one of the two components (completely dissimilar) and 1 implying the same flow of that resource on both components (completely similar). The similarity of all resource flows present in the components is then averaged to determine the overall source and sink similarities for the pairs:

$$S^j = \sum_{i=1}^{n} \frac{S_i^j}{n} \tag{4.4}$$

Finally, the overall similarity is defined as the average of the overall source similarity and overall sink similarity:

$$S = \frac{S^O + S^I}{2} \tag{4.5}$$

S is determined for each pair of components within a given chromosome of the two parent designs. The threshold of similarity was defined as 0.5. Any components with similarity greater than this threshold that are considered similar. As in [15], pairs of components are added to the similar portion of the genome until the highest

101

similarity of remaining possible pairs is less than the threshold value. Crossover is then performed in the same manner as in [15].

Ultimately, SCC was not adopted for VEGA, which continued to use the simple cut and splice crossover, based on performance with a preliminary test scenario. The design problem of this test case was to design a table to hold a given payload mass. This problem will be discussed in full detail in the next chapter. The specific reason for this abandonment is that SCC and cut and splice were found to produce comparable results, but SCC required much higher computation time to achieve these results. This additional computation time was required to calculate S for each pair of components for each pair of parents during recombination, a problem which is $O(mn^2n)$ (this is actually slightly pessimistic, due to similarities only having to be calculated by chromosome, but is still of the right order). In the table test problem, designs in the initial generation had an average of 16-18 components, with an average of two resources per component, requiring approximately 600 resource similarity evaluations per set of parents. The problem used a generation population size of 500. 30% elitism was used, "cloning" the 150 most fit population members to the next generation. The remaining genomes for each new generation were produced through genetic crossover, requiring 175 pairs of parents to produce 175 pairs of children. As a result, approximately 150,000 resource similarity evaluations were required for each new generation.

After substantial optimization of the SCC, the GA still took three times as long to run as when using the cut and splice crossover. Fig. 4.4 shows the performance of the GA using the cut and splice crossover. Fig. 4.5 shows the performance of the
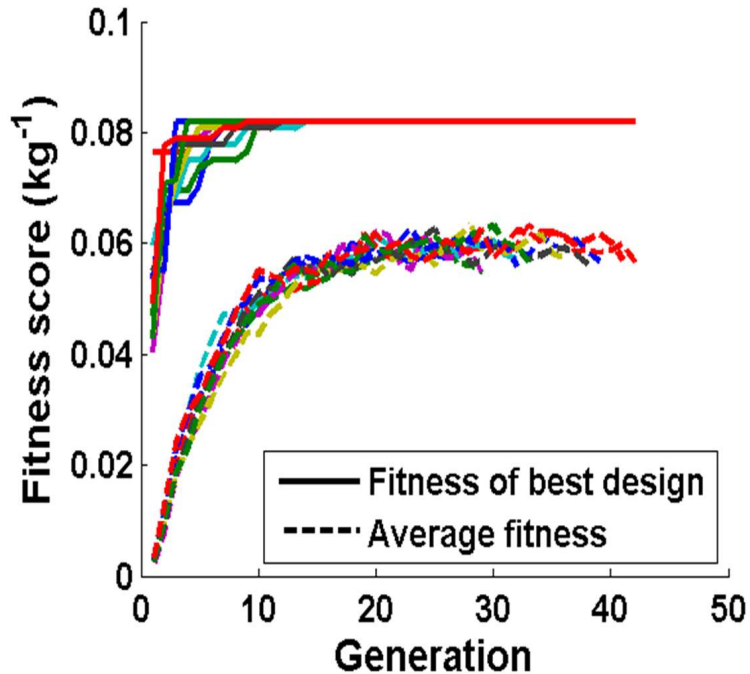
Figure 4.4: VEGA performance using cut and splice crossover.

GA using the SCC, which has been superimposed on the results from Fig. 4.4. As can be seen, the cut and splice operator did not produce substantially better results. Additionally, this was for a fairly simple test case, with most designs in the initial population containing less than twenty components. For a more complex problem like spacecraft design, the number of components per design would be expected to be substantially larger. An increase in the number of components corresponds to a quadratic increase in the number of resource similarity evaluations. For these reasons, similar component crossover was not developed beyond this point, and the cut and splice crossover has been used for all following VEGA optimizations presented in this work. Sometimes the simplest solution is the correct one.
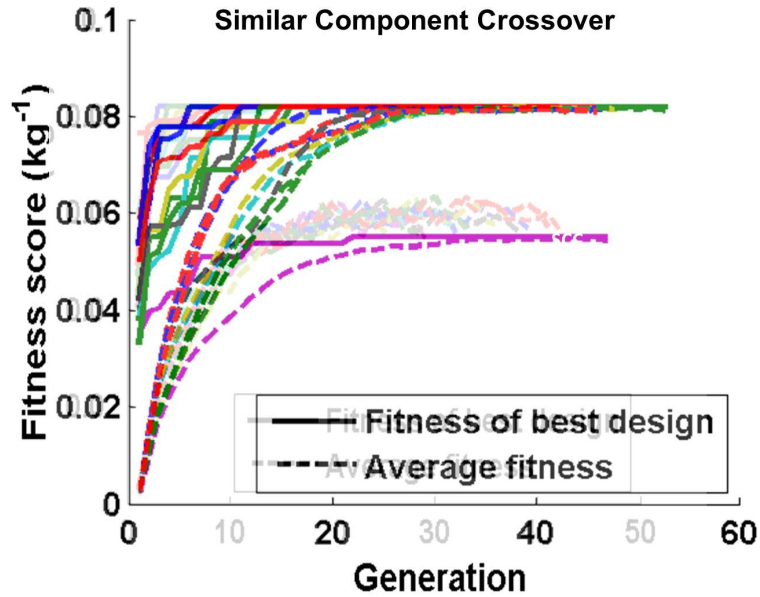
Figure 4.5: VEGA performance using similar component crossover. For comparison, the results from Fig. 4.4 are superimposed, faded, on this plot.

4.4   VEGA Operation

The general operating process of VEGA is the same as that of a traditional GA, as depicted in Fig. 1.1, repeated here as Fig. 4.6 for reference. The algorithm begins by randomly generating the initial population. The fitness of each individual in the population is evaluated as a combination of user-specified objectives. A new generation is produced from the current one through genetic selection variable length crossover, and possible mutation. The process then repeats starting again with fitness evaluation for the entire generation, iterating successive generations until some stopping condition is reached. The remainder of this section will discuss each of these steps in detail.
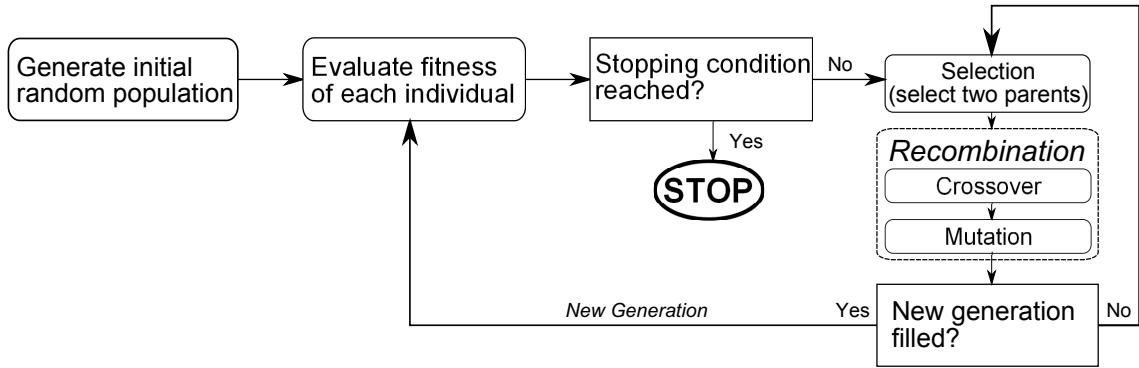
Figure 4.6: Genetic algorithm process. The algorithm is initialized with a population of random individuals. For each generation, the fitness is evaluated, and parents are selected from the population. Recombination produces child genomes from the parent genomes, populating the next generation. This process iterates over successive generations until some stopping condition is reached.

4.4.1 Initialization

The first step of any genetic algorithm is generating the starting population of designs. In VEGA, this involves randomly generating all levels of each individual in the population. Randomization of the L1 genome is straightforward; each gene is either a random discrete value, or a uniform random integer or real number within a given range. For the L2 genome, a chromosome is generated for each component sub-class included in the simulation. The number of components is randomly chosen within a given seed range specified by the user, with a minimum number of components $n_{i,min}$, and a maximum number of components $n_{i,max}$ in the class. Default values are $n_{i,min} = 1$ and $n_{i,max} = 10$.

The CR model is then created for each individual in the initial population. Each gene value references an entry in the component library for the corresponding

class. The component properties are supplied from the library, and the component is created following the class model which describes the class. If the class uses an L3 genome, it is randomly generated following the encoding scheme for the class, and embedded in the component object. Based on the component properties and a potential L3 genome, the class model simulates the component, returning the resource flows into and out of the component.

4.4.2   Fitness Function Evaluation

A genetic algorithm like VEGA works to maximize the value of the fitness function, which must incorporate all objectives and constraints. Constraints are represented by three penalty functions. Q_r corresponds to resource constraints, Q_q to component quantity constraints, and Q_u to user-specified constraints, which can be further subdivided into problem constraints and component level constraints.

The intent behind the CR model is that resource constraints can implicitly handle nearly all constraints in the addressed class of design problem. As a result, they are expected to form the bulk of constraints for most design problems. Resource constraints are defined based on the resource relations δ_i, as defined in Eq. 3.6. For each resource i present in the system, there exists a resource constraint

$$\delta_i \geq K_i \tag{4.6}$$

or

$$\delta_i \leq K_i \tag{4.7}$$

where K_i is some non-negative constant value. Whether Eq. 4.6 or 4.7 is used, as well as the value of K_i, are specific to the design problem. Usually, K_i is zero. In this case, Eq. 4.6, which we call a surplus constraint, simply states that the system must produce at least as much of that resource as it consumes. Eq. 4.7, which we call a deficit constraint, conversely states that the system must consume at least as much of that resource as it produces.

A linear penalty is imposed for any resource constraints violated, defined as

$$
q_{r,i} = \begin{cases} \max\left[\left(\frac{\delta_i - K_i}{\Sigma_{i,sink}} \right), 0 \right] & \text{if surplus constraint} \\[2ex] \max\left[\left(\frac{K_i - \delta_i}{\Sigma_{i,source}} \right), 0 \right] & \text{if deficit constraint} \end{cases} \tag{4.8}
$$

Note that for any constraints not violated, the nonzero term in the maximization will be negative, so $q_{r,i}$ will equal 0 for any constraints not violated. Q_r is then defined as

$$
Q_r = \sum_{i=1}^{N} q_{r,i} \tag{4.9}
$$

where N is the total number of resource constraints.

While it is not anticipated to see heavy use, functionality is included for component quantity constraints, allowing the user to specify a range of the acceptable number components for each sub-class. This does have some specific uses for spacecraft design. The most common is in the problem statement of spacecraft design itself, which can be stated as follows. Some number of payloads have been developed (scientific instruments, transponders for communications satellites, imagers for military surveillance, etc.), and have associated with them an environment in which they

are intended to fly. The goal of the design problem is to design a spacecraft which always includes the payloads, and returns some amount of scientific data (modeled as a resource or series of resources). In many cases, the instruments will have been predetermined, so the same instruments should be included in all designs. Within the CR model, each instrument is represented as a component, all feasible designs must contain a given quantity of all instruments (usually one of each).

Consider another very specific spacecraft design example: the use of a radioisotope thermoelectric generator (RTG) to provide electrical power. The production rate for the nuclear fuel required for RTGs is very low [50]. As a result, only a small number of RTGs (often only one) are available for use on specific classes of missions [51,52]. As should be evident, there is a desire in this case to constrain the design optimization problem to using no more than the available quantity of RTGs in any given design.

Component quantity constraints are indicated at class level. If the quantity of components from a given class is constrained, it is constrained to the seed range for that class used for initialization. The constraints

$$n_{i,min} - N_i \leq 0 \tag{4.10}$$

$$N_i - n_{i,max} \leq 0 \tag{4.11}$$

are imposed, where N_i is the number of components from class i included in the design at hand, $n_{i,min}$ is the minimum number of components included from class

i, and $n_{i,max}$ is the maximum number of components included from class i. The penalty

$$q_{q,i} = \max\left[0, \left(1 - \frac{N_i}{n_{i,min}}\right), \left(\frac{N_i}{n_{i,max}} - 1\right)\right]^2 \tag{4.12}$$

is imposed, producing a nonzero penalty if either (4.10) or (4.11) is violated. Note that (4.10) and (4.11) are mutually exclusive, never being active simultaneously. Q_q is then defined as

$$Q_q = \sum_{i=1}^{N} q_{q,i} \tag{4.13}$$

where N is the total number of component classes included in the design problem.

Q_u remains as a catch-all for any user-specified constraints. Component level constraints are included in the appropriate component class, and inherited by any design which contains components from that class. System level constraints are specific to the design problem at hand. As such, the form of any such constraints is not discussed further here. The final total penalty value is then defined as

$$Q_{tot} = p_r Q_r + p_q Q_q + Q_u \tag{4.14}$$

where p_r and p_q are penalty weight values.

The fitness of a given design for single objective problems is defined as

$$F = \begin{cases} f - Q_{tot} & \text{if maximization problem} \\ \\ -f - Q_{tot} & \text{if minimization problem} \end{cases} \tag{4.15}$$

where F is the fitness of the design, and f is the value of the objective function. For multiobjective design problems, a non-dominated sorting scheme similar to NSGA-II [23] is used. The population of feasible designs is ranked by their level of domination, that is, how far a given design is from Pareto-optimality in the population. All designs on the Pareto front are assigned rank 1. The Pareto front is then removed from the population and all designs on the new Pareto front are assigned rank 2, and so on, until all designs have been ranked. Within a given rank, a crowding distance is calculated between each design and its neighbors. Designs within a rank are then sorted from lowest to highest crowding distance. That is, designs are considered more fit the further they are from all other designs. In this way the GA favors uniqueness within a Pareto front. This encourages an even spread of designs along the Pareto front, more completely exploring the design space. Finally, all infeasible designs are ranked from smallest Q_{tot} to largest, and are placed on the list of designs after all feasible designs.

The result is a ranked list, representing the fitness of each design. The higher on the list a design appears, the more fit is. The form of this list means that the following statements are true, giving some insight into the goals of the GA. Any designs of a given Pareto rank will be higher than any design of a lower rank (the less dominated design will have a greater fitness). Within a given rank, the most unique designs will have the greatest fitness, encouraging the algorithm to explore along the Pareto front. A feasible design will always be of greater fitness than an infeasible design. Finally, for any two infeasible designs, the more feasible one will have the greater fitness.

4.4.3   Selection

The first step in the VEGA selection is the process of elitism. The idea behind elitism is to select the most fit designs, and "clone" them unmodified to the next generation. This is to ensure that the best performing designs are not inadvertently discarded through random chance during the remainder of selection, outlined below, and crossover. An elite cutoff value is selected - in the case of VEGA a value of 0.3 is used - and that portion of the current generation with the highest fitness values is cloned into the next generation.

Tournament selection is used for selecting parent designs. This selection operator was chosen as it naturally facilitates use of NSGA-II as a multiobjective fitness function, and has similar performance on single objective problems to roulette wheel selection [53, 54]. With tournament selection, some number of individuals equal to the tournament size are chosen at random from the population for each parent, and grouped together into a tournament. The individual with the highest fitness value within each tournament is chosen as a parent.

Tournament selection avoids a trap that other selection operators such as roulette wheel selection are often prone to too strongly favoring the most fit designs in the population. This can occur when a small number of individuals in a new generation exhibit some new improvement, causing a substantially superior objective performance. In these situations, selection operators like roulette wheel selection can too strongly favor these designs with much higher fitness. As a result, the genetic diversity of the population diminishes.

4.4.4 Recombination

Once two parents have been selected, recombination, including crossover and mutation, is performed between them to produce two child designs for the next generation. Recombination is repeated with pairs of parents until the next generation is full. The mutation probability P_M of any gene was set to 1% across all levels of the genome. Recombination is performed separately on each level of the genome.

For the L1 genome, uniform crossover is performed, with a crossover rate of 50% (equal likelihood of inheritance of each gene from each parent). In the case of a mutation, a random value is selected for the gene following the same process used for initialization of the L1 genome, described above.

For the L2 and L3 genomes, the variable length crossover described earlier in this chapter is performed. The crossover is essentially a cut-and-splice crossover [15]. If an L2 gene mutates, a new gene is selected following the same procedure used for initialization of the L2 and L3 genomes, described above. When a component with L3 genes is inherited from a parent, each L3 gene may also mutate. If this occurs, new values are selected for that gene following the same procedure used for initialization.

Finally, once the child genomes have been defined, new CR models are created using the child genomes, which are added to the population for the new generation.

4.4.5 Stopping Conditions

The selection and recombination processes outlined above are repeated until the new generation is full (i.e. of the defined generation size). The fitness of all individuals in the new population is then evaluated. At this point, stopping conditions are checked. For a single objective problem, the primary stopping condition is a lack of improvement in objective value for a given number (ten by default) of concurrent generations. As a secondary stopping condition, the algorithm will terminate after some maximum total number of generations. For multiobjective problems, the stopping conditions are convergence of the maximum niche count across the Pareto front [55] and that the utopia point has not moved, both over the last ten generations. The first check is an indicator that the GA has finished exploring along the Pareto front. The second one is a backup check that the Pareto front as a whole has stopped improving. This is particularly relevant when, due to the nature of the design space, the Pareto front is sparse, and crowding is immeasurably low amongst Pareto-optimal designs.

This compound Pareto front is determined by taking the union of the Pareto front of each generation, and then taking the Pareto front of that set. In practice, this is achieved by maintaining a persistent, overall Pareto front. This compound front is initialized as the Pareto front of the first generation. The Pareto front of each subsequent generation is then combined with the compound Pareto front. The Pareto front of that compound set is adopted as the new compound Pareto front.

If the stopping conditions are met, VEGA returns the final results. In the case of a single objective problem, the final results consist of the final generation of designs, as well as the most fit design for each generation. For multiobjective problems, the final results contain the entire final population of designs, as well as the compound Pareto front.

Chapter 5:   The General Static CR Model: An Example

5.1   Overview

This chapter considers an example use case of the static CR model and associated framework. The problem considered is one of the simplest possible while still describing and demonstrating this framework. Specifically, the problem is to design a table to hold a fixed payload. This table problem was used for testing and evaluation of the CR model and framework due to its simplicity. Only a small number of component classes are required, and an analytical solution for the global optimum is fairly straightforward. This is true for both the single objective of mass minimization and the multiobjective problem of minimizing both mass and the number of components.

This discussion includes problem setup, the overall layout of the CR model used, and the specific details of that model. These include definitions of the component classes used, and discussion of the objectives and constraints of the problem. Finally, we derive the theoretical optimal solution, and compare this to the results obtained with VEGA. A listing of component parameters for this example can be found in Appendix B.

5.2   The Table Problem

The problem detailed here is the design of a structure to hold a fixed payload of 100 kg at a fixed height of 0.75 m above the ground. A table is composed of surfaces and supports (i.e. legs). A surface carries the weight of the payload, transferring it to the supports. The supports are of a fixed height defined by the problem statement and transmit the load to the ground. The failure mode considered for the table surface is simply failure to support more than a manufacturer supplied maximum weight. The failure mode considered for the supports is Euler buckling [56]. The general single-objective problem statement is then:

$$
\begin{aligned}
\min_{\mathbf{G}} \quad & m(\mathbf{G}) \\
\text{s.t.} \quad F_{max} \ \geq\ & 981\text{N} \\
\sum_{i=1}^{N} P_{cr,i} \ \geq\ & 981\text{N} + m(\mathbf{G}_{surf})g
\end{aligned}
\tag{5.1}
$$

where $\mathbf{G}$ is the genome, and $m(\mathbf{G})$ is the total mass of the system. $m(\mathbf{G})$ is calculated by summing the mass of all components which comprise the system. It is therefore a function of the genome. Similarly, $\mathbf{G}_{surf}$ is the surface chromosome of the genome. $m(\mathbf{G}_{surf})$ is therefore the combined mass of all surfaces included in the individual. F_{max} is the maximum weight that can be supported by the table surface, and $P_{cr,i}$ is the critical load for Euler bending of the ith support of N total supports.

In other words, the problem is to determine the genome (and therefore system design) that minimizes the total mass of the system, while ensuring that no failure modes of individual components are reached. These constraints will be detailed in the description of the component classes below. Hopefully this helps demonstrate some of the power of the CR model, allowing open-ended multiobjective design optimization when even the constraints are not fixed, but may change depending on the number and configuration of components. We will now discuss the conversion of this somewhat conventional minimization problem formulation to a CR optimization problem.

5.3   The CR Model

This problem contains three component classes; payloads, table surfaces, and supports. The resource flow diagram for the system is as shown in Fig. 5.1. The payload "produces" its weight as a resource. This payload weight is then sunk by the surface components, which convert it to internal load. They source this internal load, adding their own weight. This internal load is then sunk by the supports, converting it to reacted load and adding their own weight. Reacted load is an edge resource, dissipated out of the system through reaction forces with the ground.

5.4   Component Classes

All components considered fall under one of three classes; payloads, surfaces, or supports. All components have some mass m as a property, which will be used
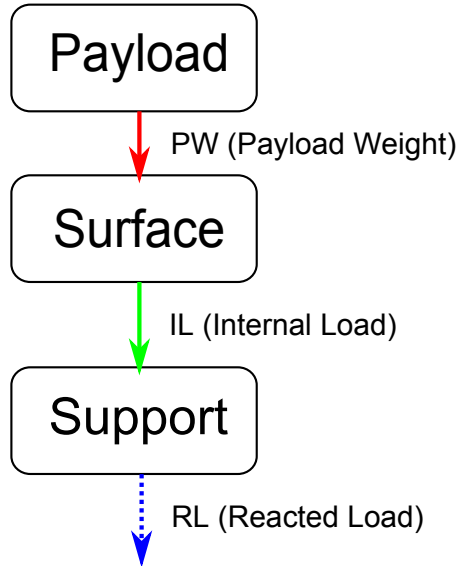
Figure 5.1: Resource flow diagram for the table system. Resources with dashed lines represent edge resources. Resources with solid lines represent internal resources.

in the objective functions. A listing of the parameters for components of each class can be found in Appendix B.

5.4.1 Payload

A single payload, with a mass of 100 kg as defined in the problem statement, is included in the class. Mass is the only parameter for a payload in this problem. The payload sources payload weight, defined by

$$PW_{out} = mg \tag{5.2}$$

where g is gravitational acceleration, assumed to be 9.81m/s^2. Given these parameters, $PW_{out} = 981\text{N}$.

5.4.2 Surfaces

Surfaces transfer the load to the supports. They sink payload weight and source internal load. The sourced internal load includes the sunk load as well as the weight of the surface itself. The maximum payload weight L_{max} a surface can sink is assumed to be provided by the manufacturer. It is therefore considered to be a component parameter. The list of all component parameters for surfaces is given in Table 5.1. Note that not all parameters are used for determining resource flows.

Table 5.1: Component parameters for surfaces.

Parameter	Description
L_{max}	Maximum payload weight that can be sunk
m	Component mass
l	length of surface
w	width of surface
t	thickness of surface

Some are tracked solely for possible use in objective functions and constraints. The resource flows of surfaces are defined by Eqs. 5.3 and 5.4.

$$PW_{in} = L_{max} \tag{5.3}$$

$$IL_{out} = PW_{in} + mg \tag{5.4}$$

A surface consumes an amount of as much payload weight as remains, up to its maximum rated weight. It passes this weight to the supports along with its own weight, producing an amount of internal load equal to the consumed payload weight plus its own weight. Note how the flow of a given resource to or from a component

119

can be a function of other resource flows to or from a component. For this problem, the resulting behavior is straightforward and trivial. However, this will lead to some interesting implications later for more complicated problems, particularly dynamic problems like spacecraft design.

5.4.3   Supports

The support class contains two subclasses; one containing real support cross sections and one containing notional cross sections. For real cross sections, all parameters are defined in the component library. For notional cross sections, some parameters are genetically determined with an L3 genome. Both subclasses describe supports of a constant cross section, extruded for a length of L. For this problem, L is set to 0.75 m.

Real supports have a known cross section and material, allowing their behavior to be determined in a simple fashion with a small number of parameters. Notional supports, on the other hand, have their cross section defined individually using L3 genes. As a result, many mechanical properties that can be simply specified for a real support must be calculated for each notional support in a design.

All supports sink some amount of internal load determined by their physical properties and source some amount of reacted load, an edge resource which is transmitted out of the system. The amount of internal load sunk by a support is the maximum possible without causing Euler buckling [56]. The amount of reacted load sourced is equal to the amount of internal load sunk plus the weight of the support

itself. The support resource flows are defined by

$$IL_{in} = \frac{\pi^2 IE}{(KL)^2} \qquad (5.5)$$

$$RL_{out} = IL_{in} + mg \qquad (5.6)$$

where I is the area moment of inertia of the support, E is its modulus of elasticity, and K is the effective length factor. K is set to 2, since the supports are assumed fixed to the surface at one end and free at the other end. m is the mass of the support. E is a material property of the support, defined as a component parameter in all cases. I and m, being functions of the support cross section, are defined differently based on subclass. Their formulations for each subclass are described below.

5.4.3.1 Fixed Geometry (Real) Supports

All fixed geometry supports have a fixed cross section and material known a *priori*. Their behavior can therefore be fully modeled with the parameters given in Table 5.2. Using these parameters, IL_{in} is defined by Eq. 5.5. RL_{out} is defined by Eq. 5.6, where $m = \lambda L$.

Table 5.2: Component parameters for fixed geometry supports.

Parameter	Description
I	Area moment of inertia
E	Modulus of elasticity
λ	Linear density

5.4.3.2 Notional Supports

The notional support class allows the framework to propose new cross sections other than those specified in the real support component library. Each entry in the notional support library contains material information for different potential support materials, as well as the range of acceptable values for the genetically determined parameters. The material parameters are outlined in Table 5.3 and the genetically determined parameters are outlined in Table 5.4. The values of these parameters for each component included in the notional support component library are given in Appendix B.

Table 5.3: Material parameters for notional supports.

Parameter	Description
E	Modulus of elasticity
ρ	Volume density

Table 5.4: Genetically determined parameters for notional supports.

Parameter	Description
Cross Section	Selector for either rectangular or elliptical cross section
r_1	Axis 1 of support
r_2	Axis 2 of support
t	Thickness of support cross section

The support cross section is defined through the L3 genes associated with the component. More complex cross sections could be proposed through some specialized code similar to that presented by Kim and de Weck [57]. A component could

then be produced matching the prototype for a real support. I and λ would be numerically determined based on the cross section developed. Due to the complexity involved with generating these, they should not be modeled as having L3 genes except under very specific circumstances. Specifically, unless the exact cross section created can be easily reproduced with meaningful input variables which could be optimized by the GA (something directly guiding the cross section, as opposed to a random seed value). In such a case, this complex analysis would have to be repeated for each crossover involving a component from this class. As may be evident, this process would likely introduce substantial upfront computational cost to randomly generate cross sections and determine their structural properties. This would likely involve a separate inner optimization problem for more complex geometries.

To maintain the simplicity of this case study, the geometries possible with notional supports were limited to simple rectangular and elliptical tubes. These geometries are simple enough to warrant optimization within VEGA through the use of L3 genomes. For rectangular cross sections, the outer base and height lengths are defined by Eqs. 5.7 and 5.8, respectively:

$$b = 2\min(r_1, r_2) \tag{5.7}$$

$$h = 2\max(r_1, r_2) \tag{5.8}$$

The cross-sectional area is then defined as

$$A = bh - (b - 2t)(h - 2t) \tag{5.9}$$

which can be simplified to

$$A = 2t(b + h) - 4t^2 \tag{5.10}$$

and I is defined as

$$I = \frac{hb^3}{12} - \frac{(h - 2t)(b - 2t)^3}{12} \tag{5.11}$$

For elliptical cross sections, the semimajor and semiminor axes are defined by Eqs. 5.12 and 5.13, respectively:

$$a = \max(r_1, r_2) \tag{5.12}$$

$$b = \min(r_1, r_2) \tag{5.13}$$

The cross sectional area is then defined as

$$A = \pi(ab - (a - t)(b - t)) \tag{5.14}$$

which can be simplified to

$$A = \pi t(a + b - t) \tag{5.15}$$

and I is defined as

$$I = \frac{\pi}{4} \left(ab^3 - (a - t)(b - t)^3 \right) \tag{5.16}$$

In either case, the support's mechanical properties can now be defined as functions of above properties. The linear density is defined as

$$\lambda = \rho A \tag{5.17}$$

and the resource flows are determined in the same way as for real supports.

5.5 Constraints

5.5.1 Resource Relations

For this case study, the two internal resource relations should be negative:

$$\delta_{PW} < 0 \tag{5.18}$$

$$\delta_{IL} < 0 \tag{5.19}$$

When these circumstances are met, the system has adequate capability to handle the full payload weight, and the supports have adequate capability to handle all load being transmitted from the surfaces. The resource relation is also negative for reacted load, the sole edge resource in this problem:

$$\delta_{RL} < 0 \tag{5.20}$$

This implies that all load can be transmitted to the ground (out of the system). However, the ground is assumed to sink an infinite amount of reacted load, with the total amount of reacted load (the weight of the table plus payload) being tracked.

This is, by intention, an extremely simplistic design problem, allowing the reader to focus their attention on the framework developed, without having any intricacies of the specific problem to worry about (that will come later with the spacecraft design problem). For a more complex design problem like spacecraft design, resources may not flow directly from one class to another. Based on this problem, it is easy to assume that all resources flow in a single line from one class to another. In general, however, resources do not flow linearly, and do not necessarily

all "flow down" from "left to right" from some initial set of classes to successively downstream sets of classes. Much of the power in the CR model arises from its ability to decompose a system in a way where individual components can be separately analyzed, and sources and sinks can be simply tallied and compared among all relevant system components.

5.5.2 Component Quantity Constraints

The sole component quantity constraint in this problem is that there is a single payload:

$$n_{payload} = 1 \tag{5.21}$$

This is a common situation across many design problems, certainly the spacecraft design problem. Some "payload" component exists, and the rest of the system exists to support that component or group of components. For a scientific spacecraft design, for example, often a principal investigator proposing a mission has a specific instrument or set of instruments they want to fly, and know a specific quantity (usually one) of each that they wish to fly. In other cases, the principal investigator may be satisfied with different combinations of instruments, as long as certain science data return requirements are met. This will be discussed more in later chapters.

5.6 The Table Optimization Problem

We have now established the CR model for this design problem and added all of our constraints. Our objective is to minimize the total mass of the system. A mass has been defined for components of each class. Our objective is therefore to

minimize the sum of all of these defined masses, with the exception of the mass of the payload itself:

$$M(\boldsymbol{C}) = \sum_{i=1}^{system} m_i \qquad (5.22)$$

We can now define the CR optimization problem for this design scenario:

$$
\begin{aligned}
\min \quad & M(\boldsymbol{C}) \\
\text{s.t.} \quad & \delta_{PW} \leq 0 \\
& \delta_{IL} \leq 0 \\
& \delta_{RL} \leq 0 \\
& n_{payload} = 1
\end{aligned}
\qquad (5.23)
$$

5.7   Results

5.7.1   Theoretical Optimum

A single 100 kg payload is included, as dictated by the problem statement. For all surfaces included in the surface library, L_{max} is 500 N, and therefore so is PW_{in}. For the specified payload, $PW_{out} = 981$ N, so two surfaces must be present to fulfill the resource relation $\delta_{PW} \leq 0$. All surfaces considered sink the same payload weight, so two copies of the lowest mass option must lead to the optimal solution. They both contribute the least mass to the system, and, as a result, produce the least amount of internal load. The lowest mass surface available, Surface1, has a mass of 5.92 kg. With our surfaces selected, we can now determine the total amount of internal load produced. Following Eq. 5.4, each surface produces an internal load of 558 N. The total internal load is therefore $\Sigma_{IL,source} = 1116$ N.

Determining the optimal number of supports analytically is slightly trickier. Of the real supports considered, the RealSupoprt6, the option with the lowest λ, had $IL_{in} = 765$ N. Therefore, a single RealSupport6 is insufficient to sink the internal load produced across the system. Two would be sufficient, however their combined mass would be greater than a single RealSupport4, the next lowest λ real support. For a single RealSupoprt4, with a mass of 0.56 kg, $IL_{in} = 5460$ N, more than sufficient to ensure compliance with the Eq. 5.19.

For a notional support, two factors drive the optimal support; minimization of the support's own mass, and maximization of its buckling load. Given Eq. 5.17, mass of the support is minimized when the cross sectional area of the support is minimized. IL_{in} is maximized when I and E are maximized. E is a material property, and is independent of cross sectional area. I, on the other hand, is a function of the cross section. For a given cross sectional area, where the support can buckle along the weakest axis in the plane of its cross section, the strongest cross section is an infinitely thin circular tube [56]. For practical purposes, we limit the minimum thickness of notional supports to 1 mm. Given this, the fact that the cross section is circular, implying $r_1 = r_2 = a = b = r$, and assuming thin walled tubes, Eq. 5.15 reduces to

$$A = 2\pi r t \tag{5.24}$$

and Eq. 5.16 reduces to

$$I = \pi r^3 t \tag{5.25}$$

Combining the objective to minimize mass with the objective to maximize strength, we wish to maximize I/A, as a sort of strength to weight ratio:

$$I/A = \frac{r^2}{2} \tag{5.26}$$

It can be seen that this quantity is maximized when r is as great as possible. For practical purposes, r was limited to be no greater than 1m, ensuring that no supports were substantially larger than the table surface. This gives an optimal cross section with $A = 0.0063\text{m}^2$ and $I = 0.0031\text{m}^4$. The optimal support, assuming a single support is sufficient in some case, is the one with the lowest mass (which will be implied for a fixed cross section by lowest ρ) which can sink an internal load of 1116 N. The lowest density support material considered is 6061 aluminum, with a support mass of 12.7 kg at the specified dimensions. For 6061 aluminum, $E = 6.9(10^{10})\text{Pa}$. This leads to the specified support having a capability to sink $9.5(10^8)\text{N}$, far beyond the internal load produced in the system. Due to the finite minimum thickness of the support, it is possible to decrease the radius of the support, decreasing I/A, but simultaneously decreasing the cross sectional area. Rearranging Eq. 5.5 to solve for I,

$$I = \frac{I L_{in}(KL)^2}{\pi^2 E} \tag{5.27}$$

which, for 6061 aluminum, leads to a required $I = 3.69(10^{-9})\text{m}^4$. Using Eq. 5.25, this results in $r = 1.1\text{cm}$, which in turn leads to an area of $6.6(10^{-5})\text{cm}^2$, and a mass of 0.13kg. This is less than the mass of a single RealSupport4, and is therefore the minimum mass support.

This solution produces the bill of materials outlined in Table 5.5, leading to a theoretical minimum mass of 11.97 kg.

Table 5.5: Bill of materials for the theoretical minimum mass table.

Component	Quantity	Mass (kg)
Payload	1	0
Surface1	2	5.92
6061 AL support	1	0.13
Total	-	11.97

5.7.2   CR Framework Optimal Result

The table optimization problem was set up using the CR model and framework, and optimized with the parameters listed in Table 5.6. Any parameters not listed have their default values discussed above. Over ten trials, the CR framework

Table 5.6: Tuning parameters used for the table problem in VEGA.

Parameter	Value
Population Size	500
Elite Fraction	30%
Mutation Rate	1%

converged in eight cases to an optimal design with a mass of 12.4 kg, coming within 4% of the theoretical optimum. In the remaining two cases an optimal design with a mass of 12.9 kg was achieved, within 8% of the theoretical optimum. The convergence of the fitness values are given in Fig. 5.2. For each design, the fitness score is expressed in this figure as -1 times the combined mass of the payload and table. The difference between the 12.4 kg tables and the theoretical optimum was in the
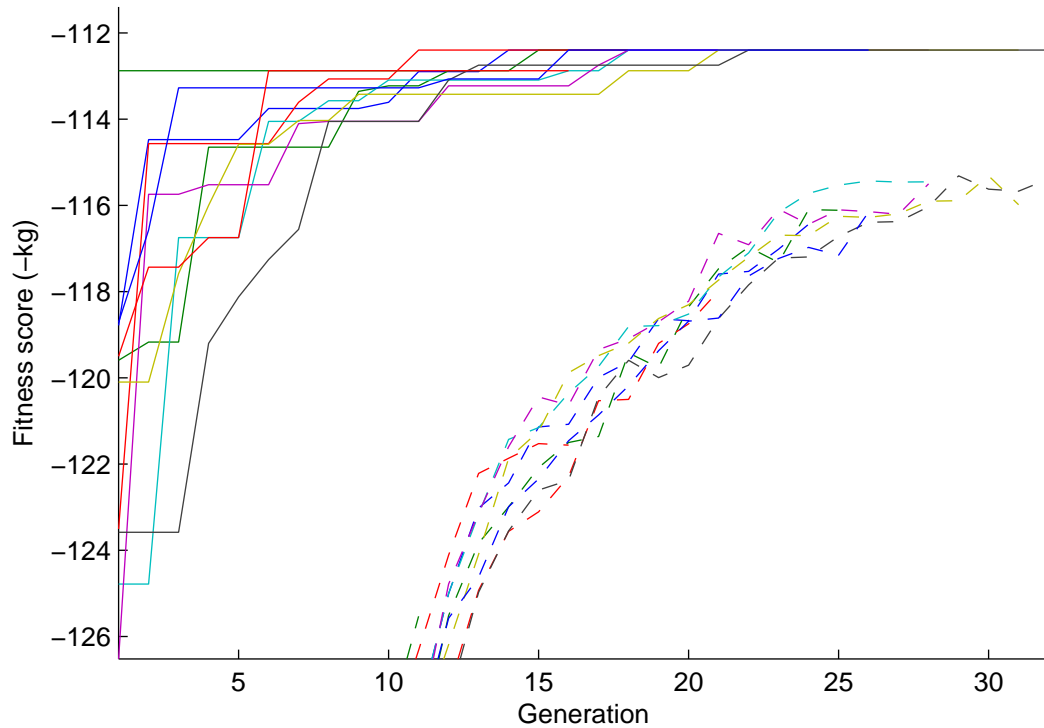
Figure 5.2: Fitness evolution for the table design problem. Ten trials are shown. A solid line represents the fitness score of the most fit individual in each generation, and a dashed line represents the average fitness of the whole generation, with solid and dashed lines of the same color corresponding to the same trial.

supports used. While the theoretical optimum utilized an optimal notional support, as discussed above, the genetically determined optimum in each case utilized Real-Support4, the optimal real support. The design achieved in the 12.4 kg cases is in fact the optimal design, should the notional support subclass be removed from the problem.

The framework therefore seems to show a behavior of favoring "real" components over notional ones when both serve the same role. This is likely due to the

fact that the available real components have already been independently optimized. Conversely, the notional components start with random internal design parameters, and must be optimized by VEGA over the course of the overarching design optimization. However, in the presence of better performing real components, VEGA will quickly eliminate the yet-to-be-optimized real components.

This demonstrates a need for some important considerations. VEGA is designed to address a component selection problem. It is not intended to perform "local" optimization within a single component or subsystem. It may be possible to pair it with an additional, dedicated component optimization step, but this must be weighed against the increased computational cost. When a real and notional class exist that serve the same purpose, the design optimizer will often favor real components. Usually this occurs when a very specific combination of L3 genes is required for component optimality. Therefore, the number of variables in any component's L3 genome should be limited to the minimum, and the components "pre-optimized" with reasonable simplifying assumptions. In this table design problem, for example, the assumption could be made that thin walled tubes are used, perhaps setting $t = \frac{\max[r_1, r_2]}{10}$. Further, it has been analytically shown that optimal supports will be those with $r_1 = r_2$, since buckling will occur along the lowest I axis. These considerations reduce the number of L3 genes from four to two, increasing the probability that random combinations of genes will lead to more optimal supports than the real supports.

Additionally, increasing the mutation rate of L3 genes could favor more rapid identification of viable notional components, although this comes at a cost in other

performance areas. What is better is to consider the notional components essentially fixed when they are created. It should not be assumed that VEGA will optimize individual notional components. Their genetic parameters should be carefully chosen to encourage viability with this consideration in mind.

Conversely, this behavior of favoring "off the shelf" components may actually be desirable, particularly in the realm of spacecraft design. There is often a lower cost, financially and in other ways, in using off the shelf components.

This behavior illustrates an important aspect of automated design optimization. Such tools are useful for trade space exploration in general, allowing one to compare a number of design options. However, they do not necessarily produce a truly optimal design or make all necessary considerations for a design proposal. For the foreseeable future, it will be necessary to perform human-based tuning and refinement of the design options chosen from the trade space.

Chapter 6:   The General Dynamic CR Model

6.1   Overview

This chapter extends the CR model developed thus far to handle systems whose behavior varies with time. This is important, since the vast majority of spacecraft design problems do have a changing behavior with time. In orbit of any planetary body, the resource flows of the spacecraft will change over the course of an orbit. Even for missions which do not orbit a planetary body, there will generally be a number of mission phases, each with their own spacecraft behavior.

In the dynamic model, we must account for a system which must respond to an external environment which changes over time. This will be accomplished by evaluating the state of the system at a number of discreet timesteps. The environment will be expanded in scope, with edge flows, as well as other environmental properties, taking on given values for each timestep. Then, within each timestep, the system can be viewed as static (or at least quasi-static), and can be evaluated following the logic already outlined, with a few additional considerations which will be detailed in this chapter. After the simulation (iteration of evaluation through all timesteps) is complete, we can assess penalties and determine objective values for a given de-

sign, for use in optimization. Penalty values are determined for each timestep, with penalties across all timesteps summed to determine the entire penalty.

There are a few key differences from the static CR model. For the dynamic model, the environment has been developed into its own component-like object. The environment is modeled as a sort of quasi-component, with its own sources and sinks, whose properties are allowed to change over time. A more involved simulation of the system over the period of evaluation/interest (henceforth referred to as the simulation window) is now required. Within this simulation, each timestep has a set duration. Each timestep is evaluated essentially using the static CR model. Rather than having a fixed amount of flow for each relevant resource, each component now has a flow **rate** for each relevant resource. As a result, all net flows, which were total flows in the static CR model, are now flow rates, assumed constant over the duration of each individual timestep. Therefore, the total net flow over a given timestep is determined by multiplying the net flow rate by the duration of the timestep. Additionally, the environment is now referenced by all components, containing properties in addition to edge flows that can change over time. All actual system components (not including the environment) must then obey the following rules:

1. A component's external behavior is entirely captured by the resources flowing to and from it.

2. If a component is not a store, its behavior within a given timestep is dependent solely on the environment. It does not depend on any internal net flows or on the state of any other components.

3. If a component is a store, its state may additionally be a function of the net flow of that resource, with the order of flow with stores determined by a priority for each reservoir. Otherwise it must follow the above rules.

The simulation proceeds following the general algorithm outlined below:

```
while !simComplete
   step environment forward
      timestep++
      if timestep > final timestep
         simComplete = true;
      else
         simulation time += duration(timestep)
         update all edge nodes
         if simulation time > maximum simulation time
            simComplete = true;
         else
            simComplete = false;
         end
      end
   end
   if !simComplete
      update resource flows for sources and sinks
      tabulate net flows
      update resource flows for stores
      calculate resource relations for this timestep
   end
end
apply constraints to design
determine fitness of design
```

There may be additional steps, particularly within the operation of the environment, depending on the problem at hand. Later chapters, will outline the specific

136

environment used for spacecraft design for this work. A complete source code for the framework, including this simulation, will be published upon completion of scouring of proprietary and privileged data.

6.2 The Environment Object

The behavior of the environment is largely dependent on the design problem at hand. Just as the resource flows of a component are driven by the internal models specific to that component class, the edge flows of the environment are driven by time-varying models of the environment specific to the design problem. These models set fixed values for each resource flow at each timestep. The system can therefore be analyzed at a single snapshot in time to determine its feasibility and performance. Analysis that is essentially identical to that of the static CR model is performed at each timestep. The biggest differences are that all component behaviors may be a function of a number of environment parameters, and that the state of reservoirs carries over from one timestep to the next. After the simulation is complete, the penalty values from each timestep are summed, providing a total penalty value for any infeasible design. Objective functions are then evaluated following the same scheme as in the static CR model.

The biggest difference between the static and dynamic CR models is the treatment of the environment external to the system. In the static CR model, the environment was treated simply as a set of steady state edge nodes. In the more general dynamic CR model, the system may not be in steady state throughout the

simulation window. Thus, in the static CR model, the environment contains its own models and additional properties which may act as inputs to the component level simulations. In general, an environment object must include three sets of information at any given timestep; nodes for all edge flows, at the current timestep i, and the duration of the current timestep Δt_i.

Just as the component classes will be different for each design problem, so too is the structure of the environment different for each design problem. The level of complexity is similarly variable, as chosen by the user. Consider an extension of the lighting system design problem from Chap. 3. Let us say that this is a solar powered lighting system, designed to collect and store energy while illuminated, and then supply power to the lamp when the system is unlit. The CR diagram for the system, originally presented as Fig. 3.2, is shown here in Fig. 6.1, modified for treatment as a dynamic system. As before, boxes in the diagram within the system represent components, and the "environment" box outside the system represents the environment object.

Lines connecting components to the environment are not the only information about the environment available to a given component. For example, within a given timestep, the lamp's mode is determined by the state of the sunlight resource, even though sunlight does not flow directly to the lamp. One may intuitively draw the conclusion that the power source could supply power to the lamp when unlit, and based on this electrical power flow the lamp could turn on. This is the straight-forward description of what is physically happening in the system. However, this would require that the lamp's behavior be dependent on the state of other compo-
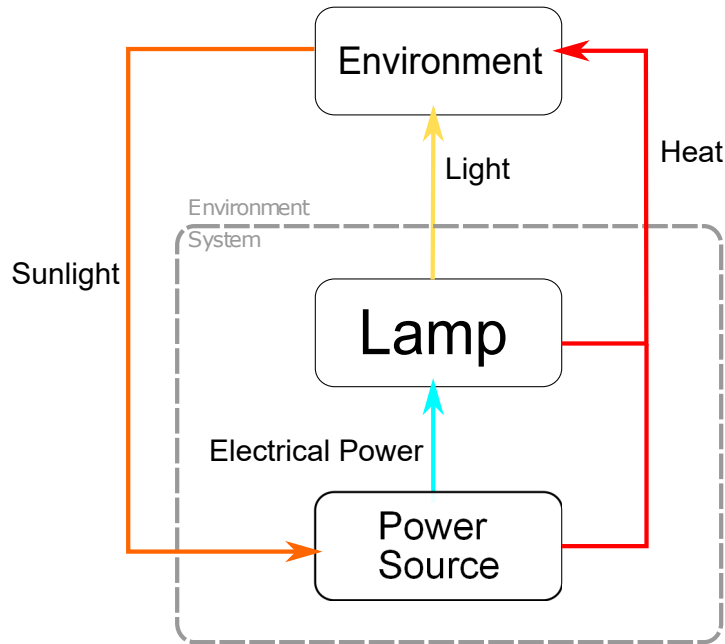
Figure 6.1: Revised, dynamic lighting system example. The environment is now a standalone object, with three edge flows with the system.

nents within the system, indirectly, through resource flows. For reasons that will be discussed in section 6.3, the rules listed in section 6.1 must be imposed. As a result (and to preserve generality), the state of the lamp cannot depend on the power generation state of the power source. Instead, the lamp will be in an "off" state whenever the flowrate of sunlight from the environment is above some critical level, and will in an "on" state at all other times.

6.3 Dynamic Resource Flows

In dynamic CR problems, having a component's behavior be a function of it's resource flows leads to two coupled issues; it can lead to transcendental loops, and the flow state of the system becomes ambiguous, potentially dependent on the
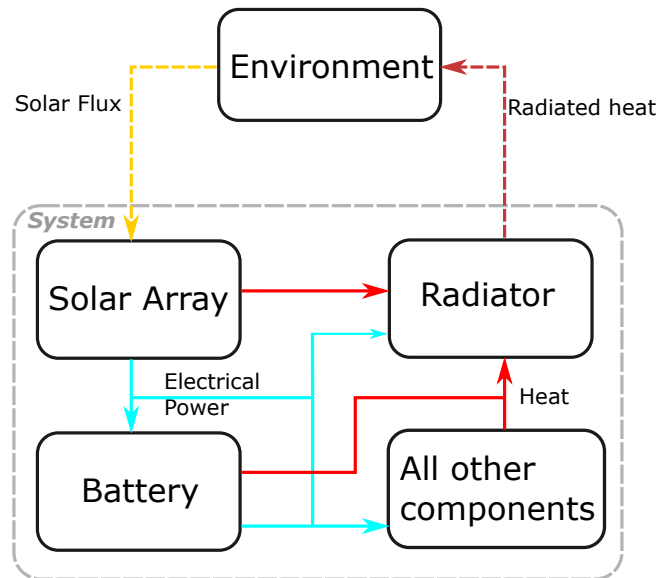
Figure 6.2: An extremely simplistic spacecraft system. All components other than solar arrays, radiators, and batteries are lumped together. They are assumed to simply consume electrical power and produce heat.

order in which components are updated. Consider, as an example, a most simplistic spacecraft design, shown in Fig. 6.2. Solar arrays produce electrical power and heat, both linearly proportional to the flow of solar flux from the environment. Radiators consume heat produced within the system and radiate it to the environment. They are assumed to require an amount of electrical power proportional to the heat rejected to operate. Batteries are a store, consuming any excess electrical power surplus to fill their electrical power reservoirs, and supplying electrical power from their reservoirs to close any deficit. In either mode, batteries produce heat proportional to their electrical power flow rate. All other components are lumped together, and assumed to consume electrical power and produce heat. Other aspects of their behavior are not relevant to this example. At this point, a few of issues

may be apparent. The order in which components update now matters. The mode in which batteries operate, and the flow rate of heat from them, is a function of the net electrical power flow. The amount of electrical power consumed by the radiator is dependent on the heat it is rejecting. The state of each battery and radiator is dependent of the net resource flows through the system. The relevant net flows for each component cannot be known until the other is fully simulated. Thus a sort of "transcendental loop" forms, where the state of multiple components are dependent on each other. None can be simulated until they are all simulated.

A few potential solutions exist to solve this problem. Timesteps can be held to sufficiently short duration that each component's state can be solved using the net flows from the previous timestep, without a significant accumulation of error. Alternatively, the states of any components in transcendental loops can be iteratively solved, continuing to update the state of all components in the loop until each of their states is stable. Both of these options were avoided, as, depending on the particular design problem, they have the potential to become very computationally intensive. In the dynamic CR model, the problem is solved by imposing rules two and three listed in section 6.1. Applying rule #2 to radiators, radiators will be assumed to operate at a set power level, consuming heat from the system at a given time. The net flow of heat can then be constrained to be less than 0 within the system. That is, those components which consume heat must always have the capacity to consume at least as much heat as is being produced for the system to be considered feasible. The state of radiators are now only dependent on the environment (through their

internal models, which account for the background temperature of the environment to which they are radiating).

Applying rule #3 to stores, we see that their state is still dependent on internal net flows. Therefore, their behavior (at least the portion involving their reservoirs) must be determined after the state of the rest of the system is determined. Once the rest of the system has been simulated, we can determine if we have an electrical power surplus or deficit, and update the state of the batteries accordingly. There is still the possibility that the state of some store may rely on the state of another store. When a reservoir updates, it may change the state of its component, altering additional net flows within the system. Since all non-reservoir components in the system adhere to rule #2, this only affects other stores. Therefore, a priority must be assigned to each reservoir, used to determine the order in which they update. Priority may need to be carefully chosen by the user to ensure realistic simulation.

Ultimately, an end user should be able to use a design tool powered by this framework without intimate understanding of the framework itself. As will be detailed below, reasonable options for spacecraft design are chosen for many properties of the dynamic CR framework. Other values for these properties may be better suited for other design problems. It is also of note that adherence to the rules discussed here does mean that the dynamic CR model may be conservative, not accurately predicting the optimal behavior of the system throughout the simulation. The dynamic CR model can confirm feasibility of a given design, but as a result of conservatism, under the right circumstances a design found to be infeasible by the dynamic CR model may in fact be feasible.

6.4 Stores in dynamic simulations

In the quasi-static CR model, net flows were still of a constant amount of each resource. If, before considering stores, any resource relations were violated, it was sufficient simply to check if stores had the capacity to, based on their initial state, consume any undesired surplus or supplement a flow to close any undesired deficit for a given resource. In the dynamic CR model, resource flows are really flow **rates**. Additionally, stores contain some internal reservoir, which can be drained and replenished over time. We must do two things when evaluating resource flows with stores. first, we must take the net flow rate, and factor in the duration of the timestep to determine the **total** resource deficit and surplus. Second, if the state of a store's reservoir has been updated by a deficit or surplus, that state must persist from one timestep to the next.

Consider the second consideration first. For each resource j for which a component is a store, it contains a reservoir with, at any point in time, a current fill level f_{cj}. The fill level is bounded by a maximum fill level $f_{max,j}$ and minimum fill level $f_{min,j}$. All stores are initialized as either full $f_{cj} = f_{max,j}$ or empty $f_{cj} = f_{min,j}$. The fill level of the reservoir can then vary between $f_{min,j}$ and $f_{max,j}$ over the duration of the simulation.

The general logic for stores within a given timestep is as follows. It is assumed, as described in section 6.1, that initial net flows δ_{j0} have already been tabulated based on all sources and sinks in the system. For each δ_{j0} there is an associated

resource relation of the form of either Eq. 4.6 or 4.7. With stores, the desire is to drive this net flow rate towards the "ideal" value, K_j, i.e.,

$$\delta_j = K_j \tag{6.1}$$

The remaining question is, if multiple stores exist for a given resource, in what order should they be updated? It is possible to have multiple component classes in a design which contain a reservoir for the same resource. The rate at which resources flow to or from a reservoir could affect the overall state, and therefore other flows of the component. Without knowing specific details of the component classes involved, it cannot be known what these ripple effects may be. To solve this issue, each component class containing a store was assigned a priority. Within a given class, priority order is determined by the order in which components appear in the chromosome for that component class. Stores are then evaluated in order of descending priority (from highest priority to lowest priority).

Within a given timestep, flow into or out of any store is as follows. For a given resource i, define the resource flow gap γ_j as

$$\gamma_j = \delta_{j0} - K_j \tag{6.2}$$

such that $\gamma_j > 0$ implies a surplus, and $\gamma_j < 0$ implies a deficit. γ_j should be driven towards 0 through the use of stores. For a given store for resource j, the total resource gap over the timestep j, $\Gamma_j = \gamma_j \Delta t_i$, is calculated. The fill is then updated based on Γ_j:

$$f_{cj} = f_{cj} + \Gamma_j \qquad\qquad (6.3)$$

If, after doing this, f_{cj} is beyond the bounds $f_{min,j}$ and $f_{max,j}$, it is set to the closer bound, and Γ_j is set to the remainder between f_{cj} and that bound. If f_{cj} is within bounds, Γ_j is set to 0. As long as Γ_j is nonzero, the framework continues moving through the list of available stores. Finally, the remaining net flow after considering all stores is averaged over the duration of the timestep. That is, after achieving $\Gamma_j = 0$ or exhausting all available stores, γ_j is set to $\Gamma_j/\Delta t$. From the change in f_{cj} over Δt, a flow rate into the store can be determined. It is then possible for this flow with the store to modify the state of the component. For example, considering a battery as a store, charging or discharging a battery will generate heat proportional to the power level at which the battery is charging or discharging.

6.5   Module Components

In certain complex cases, including satellite design, it becomes necessary to consider interoperation between what would otherwise be considered separate components. For example, consider a spacecraft transmitter and antenna. Physically, they are separate components. Within the CR model, an antenna would sink a signal, radiating it as a telemetry stream to the environment. The transmitter would sink data, and source a signal (modulating the data onto a signal to be transmitted). However, the properties of the signal radiated by the antenna will be a function of the input signal from the transmitter, depending on the power level and frequency

of the signal to determine the radiated power and gain of the antenna. Thus their behavior cannot be independently modeled. The state of the antenna depends on the properties of the internal signal flow. This violates rule #2 of the dynamic CR model.

The solution adopted is the introduction of a new concept to the CR model: the module component. Modules function externally as a single component. A module as a whole must follow the same rules as any other component class. Internally, they appear as their own quasi-systems. They behave in a similar manner to a CR-modeled system. They are similarly organized, constructed out of subcomponents of varying classes. When present in CR optimization problems, modules feature an L3 genome which resembles a CR system's L2 genome, defining their internal subcomponents. It contains a chromosome for each subclass of the module, and contains all subcomponents as child objects. The module initializes in a similar way to a proper system, populating components class by class based on its genome. Specific module classes may define additional properties. For modules in general, the only additional property is mass, which, unless otherwise noted, is assumed to be the sum of the mass of its subcomponents. For an example of a module and its subclasses, see section 7.4.3 for a full discussion of an RF subsystem modeled as a module.

6.6   Summary

This chapter has extended the static CR model to handle the design of systems whose behavior changes over time, creating a dynamic CR model and simulation framework. In the static CR model, the environment was merely a set of sources and sinks (nodes) for edge resources. In the dynamic CR model, the environment has been extended into a component-like object which not only contains edge nodes, which now may change over time, but also contains additional properties specific to the problem at hand. Resource flows have changed from fixed quantities of resources produced and consumed by components to flow rates, over a variable timestep, with time dictated by the environment object. In the static CR model, system objectives and constraints could be evaluated merely considering fixed properties of the system components, and by balancing the resource flows at a fixed point in time. In the dynamic CR model, this resource balance still occurs, and components still have the same sort of additional properties for objective function evaluation. However, the resource balance must now be performed at each timestep of the simulation, with considerations made to avoid ambiguous flow behavior, such as resource flow loops. With this more complex treatment of resource flows, we have extended stores from their rudimentary existence in quasi-static CR problems. Stores now track their internal state from one timestep to the next, and use a somewhat modified component update logic from the quasi-static case.

Unfortunately, with this added complexity, a significant amount of problem specific work must be performed to craft an environment for each design problem.

The following chapter presents a general form of an environment object which may be applied to a wide range of spacecraft design problems. While specialized portions of the model are now required which specific to the design problem, A dynamic model that is still general enough to, without modification, address a wide range of spacecraft design problems may be developed.

Chapter 7: The Dynamic CR Spacecraft Design Framework

7.1 Overview

The discussion of the CR model thus far is generally applicable to any system that can be modeled as a collection of components and resources flowing between them. However, the goal of this dissertation is to develop a framework for to facilitate satellite design and trade space exploration. Chap. 2 discussed one case study, LEO ADR. An additional, somewhat simpler problem is the design of an Earth observing cubesat on a fixed orbit. Addressing these design problems through application of the CR model will serve as a proof of concept and validation of the model.

This chapter discusses the specifics of spacecraft design using the dynamic CR model. The discussion will remain as general as possible. The specifics of the General Evolutionary Spacecraft Design Analyzer (GESDA) described here, powered by VEGA and the CR model, are therefore applicable to a wide range of spacecraft design problems. For this dissertation, the scope was limited to Earth orbiting satellites, and separated into two cases. The first models a "simple passive" satellite that is assumed to be on a fixed orbit. In this context, "passive" means that the spacecraft does not interact with its environment (except in the context of edge flows and reading the state of environment properties). This includes those mission

types within the range of applicability of the GINA model, such as communications satellites, Earth observation satellites, and scientific missions in a fixed orbit.

The second model is an extension of the first, capable of modeling an "active" satellite, where the satellite is expected to maneuver and/or interact with its environment. Even if the spacecraft is "active" (e.g. with a radiating antenna or laser altimeter) these spacecraft do not change the state of the environment, or their own structure over the simulation window. By contrast, active satellites either maneuver or physically interact with their environment. Examples of such missions include ADR missions, interplanetary sample return and surface missions, robotic satellite servicing.

Specific examples of applications of the simple and complex satellite models will be presented in Chap. 8 and 9, respectively. Chap. 8 will validate the simple satellite model, comparing a design for an Earth imaging cubesat to a Dove cubesat developed by Planet Labs [58]. Ultimately, Chap. 9 will validate the GESDA and the complex satellite model by revisiting the LEO ADR study of Chap. 2, this time performing the vehicle design using GESDA. In both cases the results obtained with GESDA are validated through comparison to previous data from the missions/studies they are replicating.

7.2   Resource Flow for Spacecraft Design

The general CR model for spacecraft design is as shown Fig. 7.1.
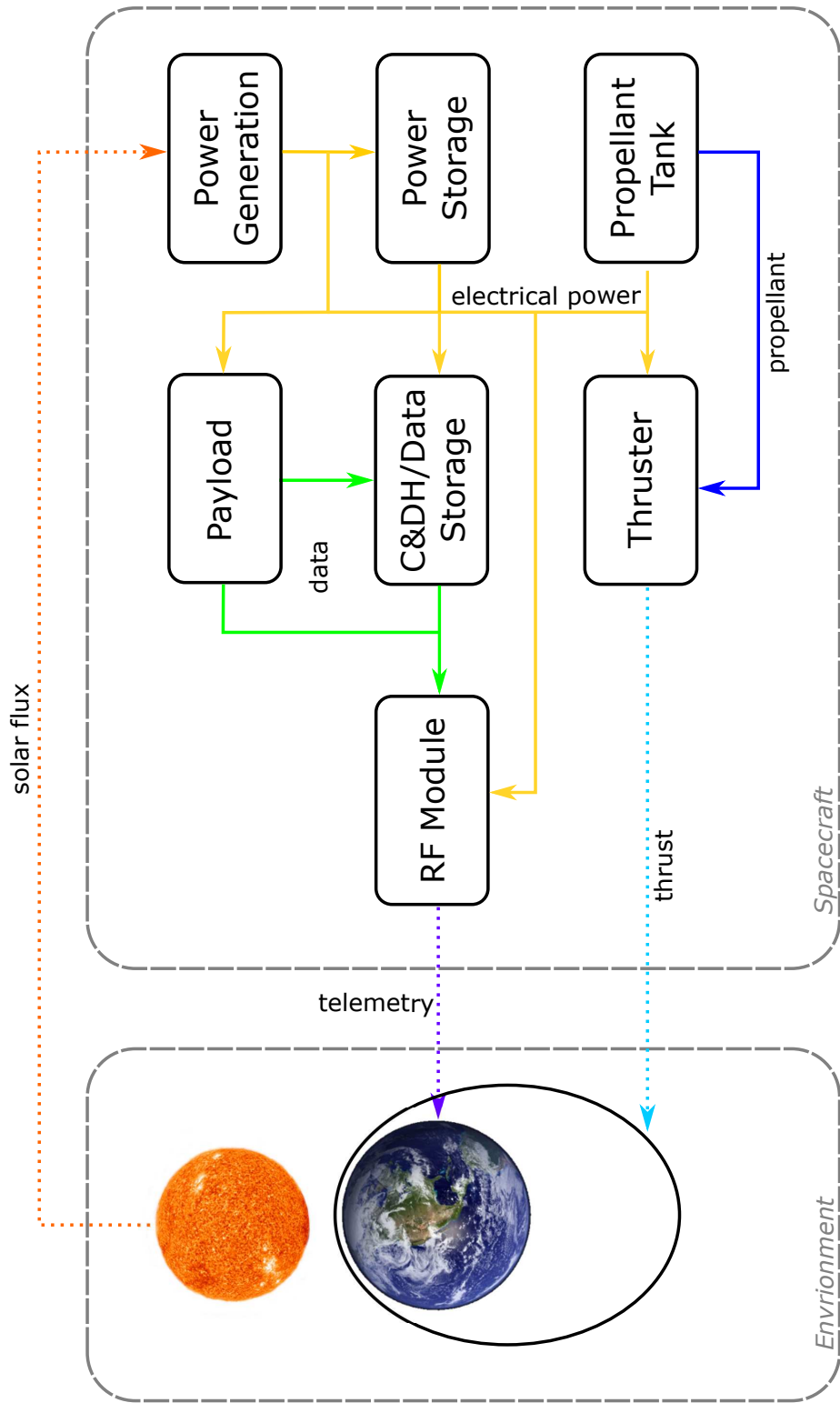
Figure 7.1: The CR flow diagram for generalized spacecraft design.

The topology shown is for an active spacecraft. The topology is essentially the same for a passive spacecraft, with the exception that the thruster and propellant tank classes may not be present. They may be required for a passive spacecraft if attitude control requirements are under consideration (they were not in the scope of this work), in which case they could be re-added to the CR model. Three internal resources, data, electrical power, and propellant, and three edge resources, solar flux, telemetry, and thrust, are present in this problem. Their resource relations are as given below, respectively:

$$\delta_{data} < 0 \tag{7.1}$$

$$\delta_{power} > 0 \tag{7.2}$$

$$\delta_{prop} > 0 \tag{7.3}$$

$$\delta_{solflux} \geq 0 \tag{7.4}$$

$$\delta_{tlm} < 0 \tag{7.5}$$

$$\delta_{thrust} < 0 \tag{7.6}$$

The payload produces some amount of data throughout the simulation, and Eq. 7.1 results from the constraint that the spacecraft must be able to handle all data produced by the payload. Eq. 7.2 results from the constraint that the spacecraft must be able to supply at least as much power as it is consuming at any given point. Eq. 7.3 results similarly that the spacecraft must be able to supply propellant at a

rate sufficient to feed any active thrusters. Data flow is measured in bits per second, power flow is measured in W, and propellant flow is measured in kg/s.

The issue of interoperability arises with the flow of power and propellant throughout the system. A power source will supply power within a certain voltage range, and all power sinks will require power within a certain voltage range. Thrusters are designed to use a given mix of propellants, and any tanks onboard must supply the *proper* propellant to a given thruster. For electrical power, a survey of spacecraft components, conducted to populate the GESDA component libraries, revealed that voltages of spacecraft components are largely standardized to a small number of voltage ranges. Additionally, the voltage of power sources considered can be easily reconfigured through the wiring of battery and photovoltaic cells, changing the voltage and current output of the component without changing the power output. Therefore, it was assumed that the voltage ranges of individual components is beyond the scope of necessary considerations at this high level of spacecraft design, so interoperability of electrical power was not considered.

On the other hand, it is not uncommon for spacecraft to have multiple propellants onboard to support dissimilar thrusters with different propellant requirements. Therefore, the propellants shown in Table 7.1 were considered, each modeled as a separate resource. Table 7.1 also lists the density of all liquid propellants considered, and the molar mass of all gaseous propellants considered. Additional interoperability considerations beyond resource flows are required for certain components. These are covered by the inclusion of module components, which are discussed in section 7.4.

Table 7.1: Parameters of propellants considered.

propellant	phase	density (kg/L)	molar mass (kg/mol)
Monomethyl Hydrazine (MMH)	liquid	0.88	-
Nitrogen Tetroxide (NTO)	liquid	1.44	-
N_2H_4	liquid	1.02	-
Aerozine 50	liquid	0.903	-
Xenon	gaseous	-	0.131

The "flow rate" of solar flux is undefined in this context. The actual flux of solar radiation is a condition of the flow. The flow **rate** is essentially infinite (technically the power output of the entire sun), with the available flow scaled by the incident area of the system component in question. However, it is always the case that any nonzero solar flux should flow from the environment to the spacecraft. Eq. 7.4 handles this constraint, being satisfied as long as solar flux is not flowing from the spacecraft to the environment. Eq. 7.5 states that any ground stations receiving telemetry must be able to handle at least as much telemetry as the spacecraft is downlinking. Stated alternatively, Eq. 7.5 constrains the spacecraft to downlink no more data than can be consumed by ground stations. Similar to the reasoning behind Eq. 7.4, Eq. 7.6 implies that thrust should flow from the spacecraft to the environment, not the other way around. The units of solar flux are W/m^2, and data are bits per second. The edge resource "thrust" is a measure of ΔV. Its units are m/s. The flow rates of all environment nodes are infinite. As a result, the latter three resource relations are trivial.

The model topology presented here should be considered a general template for a spacecraft design, which can be used for a wide range of missions. However, the capability of the framework is not limited to this specific topology. Neither satellite design problem studied in this work uses all component classes defined in Fig. 7.1. Additional satellite design problems may require additional component classes and resources. These can be easily added for the problem at hand. To do so, the user must only specify the internal model for new component classes for determining their resource flows, and a resource relation for any new resources. For example, consider a trade study investigating how the use of a thermodynamic power generation subsystem (such as a space-based nuclear reactor, or sterling engine based solar concentrator), compared to conventional space-based power generation, such as photovolatic arrays (conventional solar panels). The design of the thermal management subsystem has a significant effect in overall system performance in the design space. One would introduce heat as an additional resource. For thermal stability, the spacecraft must be balanced such that it can always reject at least as much heat as it is producing. Therefore, the resource relation for heat would be

$$\delta_{heat} < 0 \tag{7.7}$$

In addition to being electrical power sources, these new power generation subsystems would also be heat sources. A new component class is then required that can act as a heat sink. One could introduce a "radiator" class, which would sink heat and electrical power at given rates. The electrical power sink rate would likely be

155

constant. Depending on the fidelity of the radiator class's internal model and of the environment, the heat sink rate may also be constant, or may be a function of the environment at the current timestep.

As can be seen in this example, no modification of the overall framework is required to introduce a whole new class of components. Resource flows are pooled between all components. This adds a layer of abstraction between all component classes, so the existing topology is essentially agnostic to the addition or removal of component classes. The only new information that is required is the internal model for the new component class and the resulting resource nodes.

7.3   The GESDA Environment

Typically, the environment must be purpose-built for the design problem at hand using the dynamic CR model. A generalized environment object was developed which could be used for any spacecraft design problem. For reasons that will be discussed in greater depth below, the nature of the environment is more complex for spacecraft which maneuver. This is because the simulation contained in the environment is of variable time, depending on how long it takes the spacecraft to complete each maneuver. For passive spacecraft, a much simplified environment can be used, which handles a simulation over a fixed time period, such as an integer number of orbits. The remainder of this section is therefore divided into two subsections, each covering a different spacecraft environment. The first is a passive environment, which has a much smaller, fixed size simulation window, but simulates

the environment at a higher fidelity. The second, based upon the first, simulates an active environment. It has additional functionality to handle a variable simulation window and maneuvers, but is lower fidelity to keep runtimes manageable for GA-based optimization. It is hoped that future computational advancements, along with a re-write of the simulation in a faster language than Matlab, will facilitate high fidelity active simulations. Section 7.3.1 lays the groundwork for the satellite environment in general, describing it up to the point necessary to simulate a passive spacecraft. Section 7.3.2 then discusses the changes and extensions necessary to the passive environment to simulate active spacecraft.

7.3.1 The Passive Satellite Environment

In general, the environment object is built around a simulated orbit or trajectory. External simulation or analysis is used to, determine the values of the parameters that drive environmental behavior at each timestep. For the work presented in this dissertation, external simulation was performed in the General Mission Analysis Tool (GMAT) to determine simulation step sizes, and available solar flux at each timestep. AGI's Systems Toolkit (STK) was used for communications access calculations. An additional, user defined dataset determines the observation windows in which the payload is active. In the case of multiple payloads, this dataset takes the form of a table with a column for each payload. The timestep and solar flux data from GMAT are concatenated with this payload scheduling data to create an input data file for environment creation. Table 7.2 gives the format of this simulation

157

data. The first column gives t_i, the elapsed time at which the timestep begins in

Table 7.2: Simulation data format.

t_i (s)	ϕ_{sol}	payload1	payload2	...
51.65	1.03	1	0	...

seconds. The second column gives ϕ_{sol}, the solar flux, normalized by the solar flux

at Earth, which is assumed to be 1367 W/m^2. The remaining columns are binary,

with 1 indicating a given payload is active, and 0 indicating it is not. A separate

file contains the access information from STK. This file lists communications passes

with user-selected ground stations.

At a given timestep i, the duration of the timestep Δt_i is determined as

$$\Delta t_i = t_i - t_{i-1} \tag{7.8}$$

therefore, the duration of the 0th timestep is undefined. $\Phi_{sol,i}$, the actual solar flux

at t_i is defined as

$$\Phi_{sol} = \Phi_{Earth}\phi_{sol} = 1367 \text{ W/m}^2\phi_{sol} \tag{7.9}$$

For downlink access, a list of terminals is supplied, along with the compatible

downlink bands, and G/T of each station in each band. An example communications

pass is given in Table 7.3: Terminals can either be ground terminals, such as SG1

at Svalbard [59], shown in Table 7.3, or space terminals, that is, relay spacecraft,

such as one of NASA's Tracking and Data Relay Satellites (TDRSS). If a given

timestep falls within a communications pass, the environment's link parameters will

158

Table 7.3: Example communications pass.

Ground Terminal - SG1		
t_i (s)	range (km)	elevation (deg)
897.855	2548.776	-21.746
957	2154.629	-22.095
1017.000	1769.16	23.36
1077.000	1412.368	26.035
1137.000	1114.424	30.526
1197.000	935.2109	35.271
1257.000	945.6845	34.966
1317.000	1140.528	30.089
1377.000	1446.413	25.793
1437.000	1806.806	23.29
1497.000	2193.794	22.132
1552.685	2565.077	21.843

be interpreted by linearly interpolating the range and elevation of the spacecraft.
Unless otherwise noted, the following parameters are used for link calculation across
all designs and possible orbits: the 6 dB Eb/No assumes Reed-Solomon(255,223)

Table 7.4: Link parameters assumed across all designs and orbits.

Bit Error Rate (BER)	10^{-5}
Eb/No	6 dB

encoding. For the purposes this work, this value was hard coded into the design
problems addressed. Future extensions of this work could consider the encoding
used as a design parameter, with multiple possible encoding schemes selected from
using an L1 gene. If multiple orbits are under consideration, a separate input data
file is created for each of them. If optimization is being performed, an L1 gene is

used to specify the orbit chosen for a given design, such that the selection amongst orbits under consideration can factor into the global optimization.

Since passive spacecraft do not maneuver, this covers the only two edge resources, solar flux and telemetry, as well as the additional environmental parameters for which payloads are currently operating. The flow rate of solar flux is infinite. The environment is assumed to provide an infinite flow of solar radiation over an infinite area, with the actual amount captured by a component determined by that component's area. The actual flux Φ_{sol} in W/m^2 is captured in the conditioning of the environment's solar flux source. Similarly, the flow rate of telemetry is negatively infinite. That is, the environment has an infinite capacity to sink telemetry from the spacecraft. However, similarly, the conditioning of the environment's telemetry sink provides the limiting factor on the actual rate at which telemetry is "dissipated" from the spacecraft. This is accomplished through link budged analysis, as will be discussed in section 7.4, using the range and G/T of the ground station being used and the transmitter properties of the RF module onboard the spacecraft. Binary properties exist within the environment object which update at each timestep with edge nodes, dictating whether or not each payload is active. In the next subsection, we will extend and modify this environment object to handle active spacecraft, with particular attention paid to LEO ADR spacecraft.

7.3.2 The Active Satellite Environment

The active satellite environment is fairly similar to the passive environment with two key differences; complex interactions with the environment, and a procedurally generated simulation. In terms of edge resource flows, the active satellite environment is similar to the passive satellite environment. The only change is the addition of a ΔV store. The simulation is procedurally generated, as discussed below, based on the completion of scheduled maneuvers. This ΔV store contains the remaining ΔV that must be completed for a given maneuver. Once the store is "depleted", the simulation can move on to the next maneuver at the next procedural update.

More complex interactions between the spacecraft and the environment are required than for a passive satellite, largely tied to performing maneuvers. For example, an ADR spacecraft must rendezvous with, capture, and potentially reposition a debris object. These complex interactions have complex (and coupled) implications on the behavior of the spacecraft. A spacecraft's mission, generally speaking, can be considered to start from an initial orbit, and maneuver in such a way to arrive at a number of waypoints, potentially with different operating modes driven by the payload and mission at and around each waypoint. The logistics of travel between these waypoints is dependent on the capabilities of the spacecraft, which will vary based on the configuration of onboard components. Especially when this framework is being used for optimization, multiple spacecraft may be under evaluation with no a priori knowledge of spacecraft configuration. In particular,

the configuration of the propulsion system affects the time required to complete a maneuver, and whether it is more prudent to accomplish an orbit change with low thrust or impulsive maneuvers.

Components cannot know information about each other's states. Therefore, the environment must provide information on the particulars of a maneuver to be performed, and somehow coordinate between an unknown set of propulsion systems that may be active simultaneously. For active spacecraft in GESDA, the maneuver type (whether maneuvers are impulsive or low thrust) is dictated by an L1 gene. A ΔV table, a list of maneuvers to be completed are then specified by the user in each case. For each trajectory being considered, two ΔV tables are required. One for maneuvering with low thrust, and one for maneuvering impulsively. The format of the table is given in Table 7.5. Each line of the ΔV table contains the magnitude

Table 7.5: ΔV table format.

ΔV (m/s)	t_{wait} (orbits)	mass increment	thruster class	maneuver type
175	48	1	thruster	raise orbit

of the ΔV being performed, a minimum wait time between maneuvers, a mass increment, thruster class, and maneuver type. The ΔV itself is self-explanatory.

The wait time indicates some period of time expressed in orbits in the active satellite case considered. This wait time is assumed to include the time the maneuver is actually being performed. The wait time sets a repetition counter r, stored as a property of the environment. r decrements for each orbit procedurally added to the simulation.

The mass increment indicates that some mass should be added or subtracted from the spacecraft at the end of the maneuver. For orbital debris removal, for example, this could be the addition of a debris mass after completing rendezvous, or, in the event of a negative increment the jettisoning of a debris object, spent stage, or some other mass from the spacecraft. The units and amount of mass that comprises a mass increment is specific to the design problem, so a property exists within the payload component class to set it. For example, if a spacecraft is grappling a 1000 kg mass at the end of a maneuver, a mass increment of 1 in the ΔV table means that the spacecraft's mass would be increased by 1000 kg in the simulation. A mass increment of -1 means that the spacecraft's mass would be decreased by 1000 kg in the simulation.

The thruster class indicates what component class performs the maneuver. For example, a mission may perform large maneuvers with a low thrust electric propulsion system, while performing proximity operations or terminal guidance with impulsive thrusters. In the LEO ADR case considered in this work, electric and chemical thrusters were all placed in a single thruster class, but some of the payloads could perform maneuvering. In this case the possible values for the thruster class were "thruster" and "payload", with selection for each maneuver type performed through L1 genes.

The maneuver type indicates what type of maneuver is being performed. This may place restrictions on some components in the system, or, in the case of very advanced design problems, indicate the operating mode of the spacecraft (e.g. commissioning, cruise, science flyby, etc. for a planetary science mission). It is redundant

in the LEO ADR problem with information already provided by the thruster class, but is included to preserve generality.

Active spacecraft simulations are by necessity much lower fidelity than passive spacecraft simulations. As will be discussed in the following chapters, the passive satellite design problem contained on the order of 100 timesteps, over a period of approximately two orbits, with each timestep on the order of minutes. By contrast, each timestep for the active satellite design problem considered (LEO ADR) covered half an orbit. Despite this, many of the dynamic simulations contained thousands of timesteps, spanning weeks, months, or in some cases years. For a passive satellite, it is likely sufficient to study a small number of orbits to gage the performance of a given design. For active spacecraft, especially simulations where spacecraft maneuvering is a substantial part of the mission, a much larger portion of the mission must be considered. For the case of LEO ADR, for example, the assumption was made for simulation purposes that the spacecraft remained on a closed orbit of fixed radius and inclination. More specifics on that will be discussed in Chap. 9.

Using the ΔV table, the environment procedurally generates a simulation from a set of templates for each maneuver, continuing to append future timesteps as the simulation progresses. Each template is a set of simulation timesteps, specifying all pertinent environmental parameters, which may be repeated until a maneuver is complete. Due to this repetition, it is useful to consider the template as, for example, containing simulation information for a single orbit. If additional orbits are needed to complete a maneuver, they can be procedurally added to the simulation with

these templates (hereafter simply referred to as orbits). The process repeats with the next maneuver following the logic outlined in Fig. 7.2.

The environment, as constructed, could potentially utilize a separate orbit template associated with each maneuver. However, within the scope of the active mission considered in this work, it was deemed reasonable to assume an unchanging environmental conditions from one orbit to the next, unless otherwise noted. Thus, in Chap. 9, a single orbit template was used for the entire simulation.
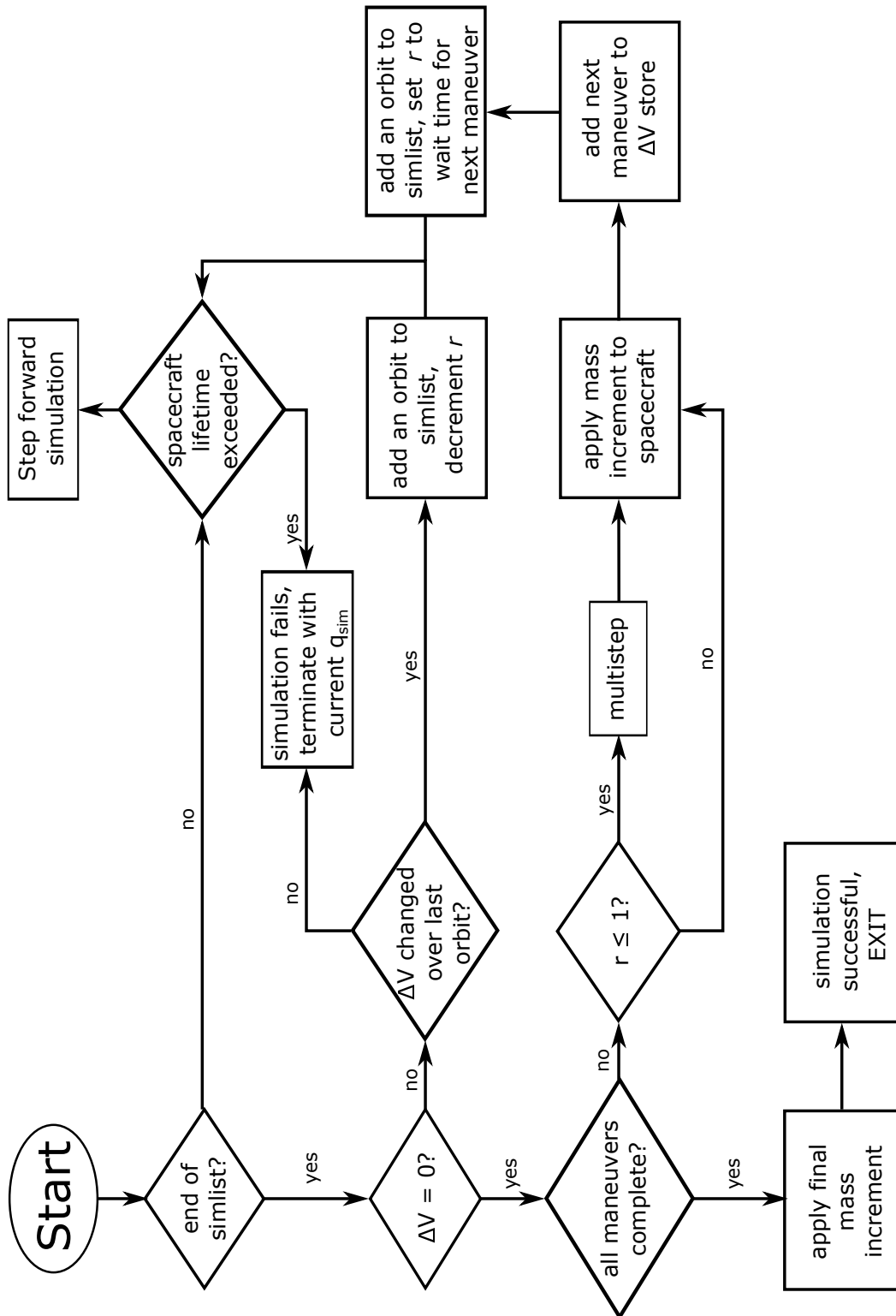
Figure 7.2: The CR flow diagram for generalized spacecraft design.

The simulation list (or simlist for short) is the list of timesteps in the simulation. It is the simlist that is procedurally updated with new timesteps based on the logic in Fig. 7.2. Each line of the simlist corresponds to a single timestep in the simulation.

The simulation is initialized with one orbit in the simlist, during which no maneuvering occurs. The process detailed in Fig. 7.2 is then executed every time the environment steps forward to the next timestep. Simulation time is limited to a maximum set in the environment, corresponding to the design lifetime of a spacecraft. If, at any time, the spacecraft lifetime is exceeded, the simulation fails, terminates, and a constraint violation is marked for the spacecraft failing to complete the mission. The penalty for constraint violation is weighted by the portion of the simulation completed, defined as

$$q_{sim} = \frac{N_{complete} + \Delta V_{i,complete}/\Delta V_{i,tot}}{N_{tot}} \tag{7.10}$$

where $N_{complete}$ is the total number of maneuvers (lines of the ΔV table) that have been completed, $\Delta V_{i,complete}$ is the amount of ΔV completed of the maneuver where the simulation failed, $\Delta V_{i,tot}$ is the total ΔV for the maneuver where the simulation failed, and N_{tot} is the total number of maneuvers. In other words, the penalty is the fraction of maneuvers that have been completed, including the partial completion of the maneuver being performed when the simulation failed. This is considered a user defined penalty function to fit within the existing CR framework.

The first check on an environment update is whether or not the simulation has reached the end of the simlist. If it has not, and the spacecraft lifetime has not been exceeded, the simulation steps forward to the next timestep, and proceeds to update the state of all system components. If the simulation has reached the end of the simlist, more orbits may need to be added to the simlist if the current maneuver is incomplete, or if it is complete but there are additional maneuvers to perform.

If the current maneuver is not complete, the environment checks whether or not the fill level of the environment's ΔV store has changed over the last orbit. Essentially, this is a check to determine if the spacecraft's propulsion system is functioning. If the ΔV remaining in the current maneuver does not change over an entire orbit, then it can be assumed the spacecraft cannot proceed any further in the mission, since orbits are repeated until the maneuver is complete. This triggers a simulation failure, terminating the simulation with a penalty value q_{sim}, as given by Eq. 7.10.

If the ΔV has changed over the last orbit, then the propulsion system is still functioning, and an additional orbit is added to the simlist to continue performing the maneuver. If the repetition counter r is nonzero, it is decremented, counting the new orbit as part of the wait time for the current maneuver.

If the current maneuver is complete, the environment checks whether or not there are remaining orbits as dictated by r. If r is nonzero, the environment performs a "multistep." If performed, a multistep, detailed below, simulates a single orbit, then multiplies the results by r to achieve the change in the system over multiple timesteps. Use of multisteps, as opposed to simulating multiple concurrent orbits

168

when the spacecraft is in steady state, avoids essentially re-solving the same static CR problem multiple times. For missions where maneuvers are separated by long wait periods, such as a spacecraft coasting on a phasing orbit, this reduces the computation time substantially.

A multistep starts by performing a single orbit of the template to be repeated. The total simulation time of this orbit t_r, as well as the total net flows of each resource over the entire orbit, is recorded. The individual states of non-store components need not be recorded outside the simulation. This is because those components' behavior is only a function of the current state of the environment. As a result, their state within a given timestep is (at least directly) agnostic to all past and future timesteps. Their behavior may be indirectly influenced by past timesteps if any parameters within the environment convey information from past timesteps.

Once this single orbit has been simulated, the total simulation time elapsed over the multistep

$$\Delta t = t_r r \tag{7.11}$$

is determined, and added to the elapsed simulation time. Similarly, the fill level of each store is updated by multiplying the net flows of each resource by r:

$$\delta_{i,tot} = \delta_i r \tag{7.12}$$

and negotiating these net flows to the stores following the same logic described in section 6.4. Penalties are then determined for any resource relation violations, again

multiplied by r:

$$q_{r,multi} = q_{r,orbit}r \tag{7.13}$$

Finally, the current timestep of the simulation is incremented by the number of timesteps per orbit times the number of repetitions:

$$i = i + \Delta i_{orbit} \tag{7.14}$$

r is then set to 0 and the multistep is complete. For a full implementation of this multistep procedure, as well as the active environment update process, see the `multistep` and `stepForward` methods of the environment object in the `LEO_ADR_Base_Final` project in [PUBLISHED CODE].

Additionally, a special propulsive multistep can be inserted in the middle of a maneuver, achieving similar benefits for low thrust maneuvers which occur over many orbits. However, validity of the propulsive multistep depends on the nature of the problem at hand, so it is not included in the standard active satellite environment. It will be discussed further in the context of the LEO ADR problem, for which it was implemented.

Regardless of whether or not a multistep is performed, a maneuver is considered complete when the environment's ΔV reservoir becomes empty and $r = 0$. At the end of the maneuver, any mass increment for that maneuver is applied to the spacecraft. The next maneuver is then added to the environment's ΔV reservoir, an orbit is added to the simlist, r is reset to the wait time for the next maneuver, and

the simulation proceeds. Once all maneuvers are complete, the simulation performs any final mass increment, and exits successfully.

7.4 Spacecraft Component Classes

All component classes utilized within this framework, along with their sub-classes, are detailed in this section. Payloads, while discussed in general here, are more mission-specific (in fact, one could say that they are fundamentally what differentiates different missions). Therefore, general aspects true of payloads across missions are discussed here, with a more detailed discussion of the mission-specific aspects each payload described in the chapters for their missions.

As discussed above, additional component classes can be added for enhanced fidelity, and to model more complex mission types. Additionally, the internal models for the spacecraft described here should be considered rudimentary, to allow a proof of concept of the CR model and framework. This may be sufficient for many analyses, while being simplistic for others. The scope of this work is system-level evaluation, and proof-of-concept of the framework. As will be demonstrated in later chapters, the fidelity of these component-level models proved sufficient to validate the framework in the design problems considered.

All spacecraft components are assumed to have a TRL. If TRL is not specified for a component, the component is assumed to have a TRL of 6. Additionally, all components are expected to have an associated mass.

The remainder of this section is organized by component class. Each component class may have subclasses, which, where applicable, will also be listed. Accompanying each component class is a resource flow diagram for the component, which specifies the sources, sinks, and stores for the component class, as well as any environmental parameters affecting the component's state. Sources and sinks are differentiated by the direction of resource flow, as indicated by the arrows. Stores are indicated by a T-junction of the resource(s) for which they are a store, much like a "water tower" that can act as a buffer when there is a deficit or surplus of a resource. Edge flows to or from the component are represented by dashed lines crossing the component/environment boundary. For a complete list of component properties for each component class, see Appendix C.

7.4.1 Payloads

The central component around which the spacecraft is constructed is the payload. The payload is by nature very mission specific, so it is only discussed generally here. Specific details of the payload for each design problem considered will be detailed in their respective chapters. The payload can exchange mass with the environment, as discussed in the context of mass increments in section 7.3.2. If positive, this accounts for things like capture or docking of another object. If negative, it may account for release or unlocking, or additionally a jettison or staging event.

A property in the environment indicates whether or not the payload is active. If active, the payload consumes electrical power and produces data at a constant
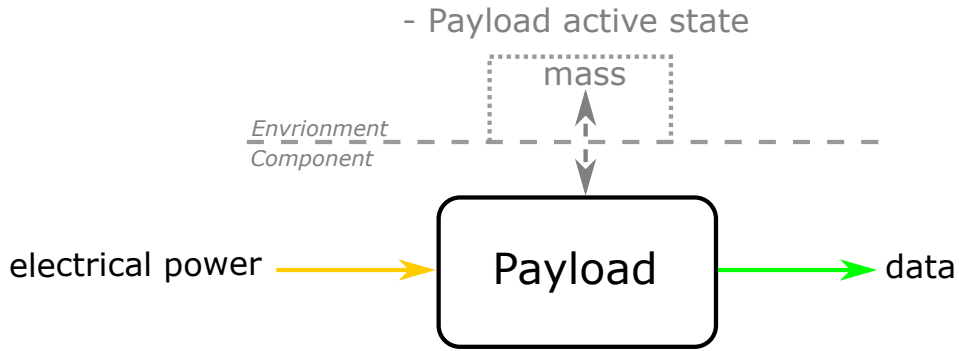
Figure 7.3: Payload resource flow diagram.
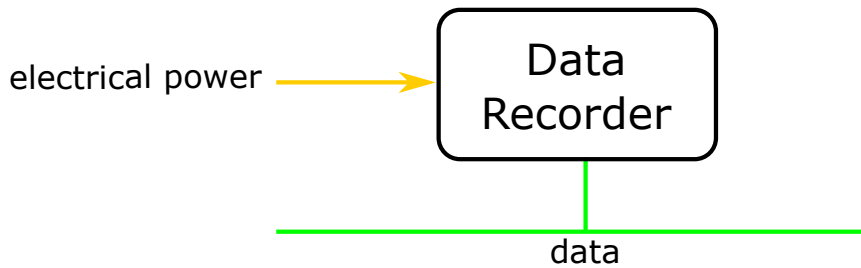
Figure 7.4: Data recorder resource flow diagram.

rate. If not active, it has no resource flows. In both of the spacecraft design problems considered in this dissertation, the payload was assumed to always be active, so this environment was essentially unused.

7.4.2 Data Recorders

By default, GESDA contains a C&DH/Data Storage class, known as the Data Recorder class. Within the scope of the simulation implemented, the purpose of this component class is merely to act as a data store. Relevant properties for

the simulation of this component class are as detailed in Table 7.6. All properties

listed in the table are properties of components of the class. For data recorders,

Table 7.6: Data recorder properties.

property	description	units
P_{req}	operating power	W
C_{data}	data capacity	b
R_{read}	data read rate	bps
R_{write}	data write rate	bps

$f_{min,data} = 0$ (the minimum fill level of a data store is 0 b), and the $f_{max,data} = C_{data}$

(the maximum fill level of the data store is the component's data capacity). Within

GESDA, data recorders are assumed to only consume power when reading or writing

data. Therefore their state does not change during the regular component update.

Only on the store update step.

When, $\delta_{data} > 0$, there is a surplus of data, the data recorder sinks data,

assuming its data reservoir is not full. The component level simulation for a data

recorder sinking data follows the process shown in Fig. 7.5. The update returns

r, the remaining portion of δ_{data} that could not be consumed by the component,

and the time t_{active} it spent during the timestep sinking data up to a maximum of

Δt_i, the length of the current timestep. A check is first performed to ensure the

component's data reservoir is not already full ($f_{c,data} = f_{max,data} = C_{data}$). If it is,

null outputs indicated in Fig. 7.5 are returned. $t_{active} = 0$ indicates the component

was not active during the timestep, and $r = \delta_{data}$ indicates no change in the net

flow performed by the component. If the reservoir is not full, the data flowrate r_b

174
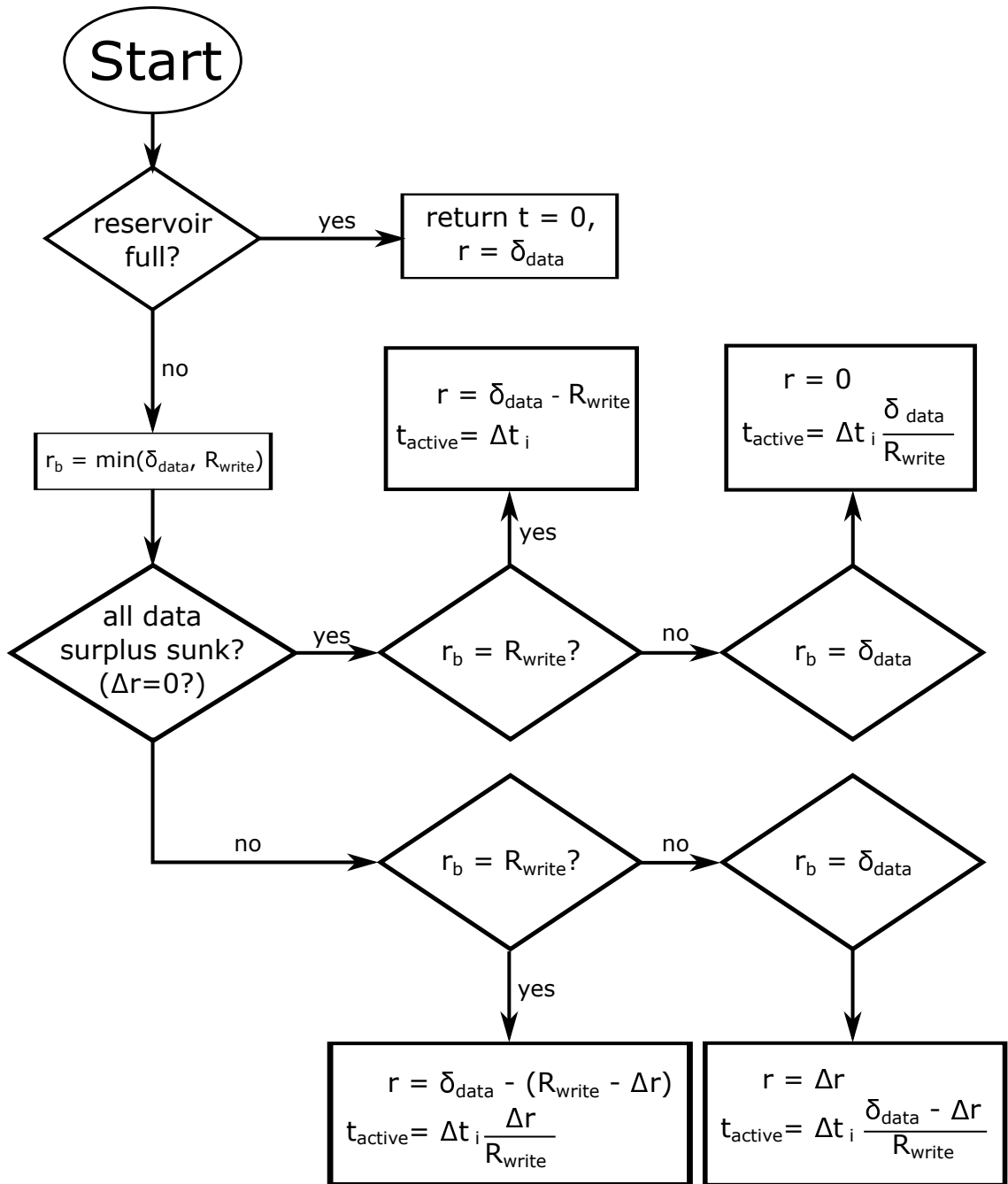
Figure 7.5: Data recorder store update process for data surplus.

into the component is set to the minimum of δ_{data} and R_{write}. In the case of the former, the maximum write rate to the component is greater than the net flow rate of data, so all data surplus can be captured by this component. In the case of the latter, the data flow into the component is write-limited, so the component alone will not be sufficient to sink the net data flow. The remainder r of the net flow will be returned, potentially to be sunk by other stores.

The above is true assuming $f_{c,data} < C_{data}$. This may be true at the beginning of the timestep, but the component's data may still become full before the end of timestep. If this occurs, an additional remainder Δr must be added to r from above. For the purpose of calculating remaining r, the remainder of δ_{data} is averaged over the entire timestep. However, for the purpose of calculating power consumption of the component while writing, it is assumed to write at a rate R_{write}, for only a time t_{active}, which is some fraction of Δt_i.

The combination of r_b being set to either R_{write} or δ_{data} and whether or not the data reservoir becomes full during the current timestep produces four cases, all with different potential values for r and t_{active}. Fig. 7.5 gives the logic for selecting the proper case, and the values of r and t_{active} in each case.

When $\delta_{data} < 0$, there is a "deficit" of data. Physically, observing our general spacecraft topology in Fig. 7.1, this means that the spacecraft is transmitting data out of the system, and there is excess capacity to send any data in recorders. The recorder sources data from its reservoir until the deficit is eliminated or the reservoir is empty. The update returns r, the remaining capacity in δ_{data} after sourcing the component's data to the system, and the time t it spent during the timestep sourcing
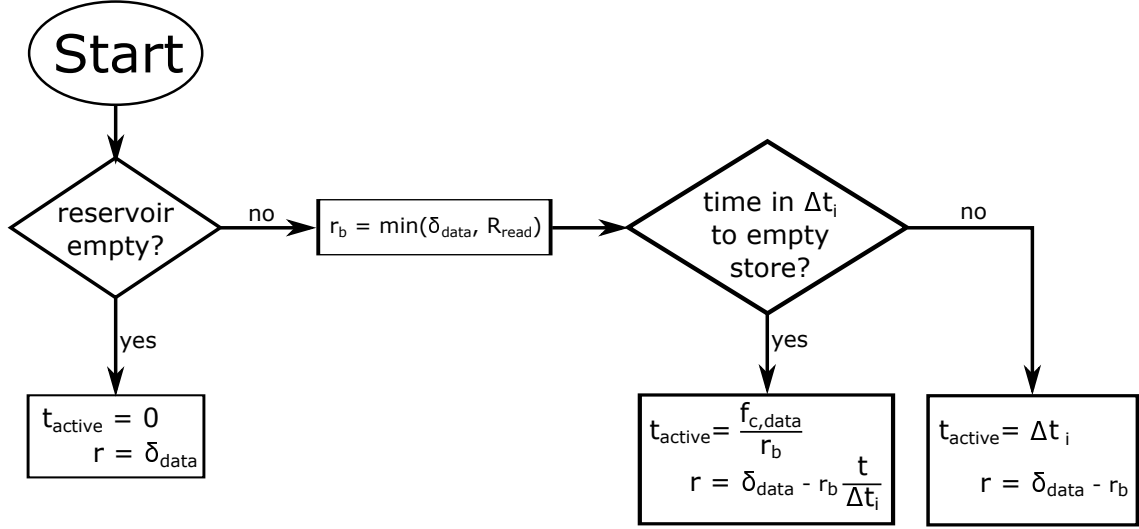
Figure 7.6: Data recorder store update process for data deficit.

data up to a maximum of Δt_i, the length of the current timestep. The process for this data sourcing mode is illustrated in Fig. 7.6.

The data flow rate r_b out of the recorder is set to the minimum of δ_{data} and R_{write}. If $r_b = \delta_{data}$, the flowrate is externally constrained by the capacity in the system to sink additional data. If $r_b = \delta_{data}$, the component is read limited (internally constrained). In either case, the following logic holds in terms of r_b.

If, at the rate r_b, the component has time to empty its reservoir, it does so in time

$$t_{active} = \frac{f_{c,data}}{r_b} \tag{7.15}$$

leading to a remaining net data flow

$$r = \delta_{data} - r_b \frac{t_{active}}{\Delta t_i} \tag{7.16}$$

177

In case where $t_{active} = \Delta t_i$, the component uses the full capacity δ_{data}, so $r = \delta_{data} - r_b$. The component will not be able to source all data stored data, only the portion $\Delta f_{c,data} = r_b \Delta t_i$.

A data recorder requires electrical power as long as it is sourcing or sinking data, at the constant rate P_{req}. With this in mind, the rate at which a recorder sinks electrical power is

$$P_{in} = P_{req} t_{active} \tag{7.17}$$

Given the appropriate definition of t_{active} for the current state of the data recorder, determined following the logic of this subsection, Eq. 7.17 holds regardless of the state of the component.

7.4.3 RF Modules

RF modules are the sole implementation of a module class within the design problems considered in this dissertation. The general resource flow of an RF module, as well as its interaction with the environment, is outlined in Fig. 7.7. RF modules contain two subcomponent classes; amplifiers and antennas. Amplifiers and antennas can themselves be broken down into subclasses which function the same externally, but are modeled differently internally. Amplifier subclasses include traveling wave tube amplifiers (TWTAs) and solid state transmitters. Antenna subclasses include low gain antennas (LGAs) and high gain antennas (HGAs). The hierarchy of RF modules, subcomponent classes, and subcomponent subclasses, is given in Fig. 7.8.
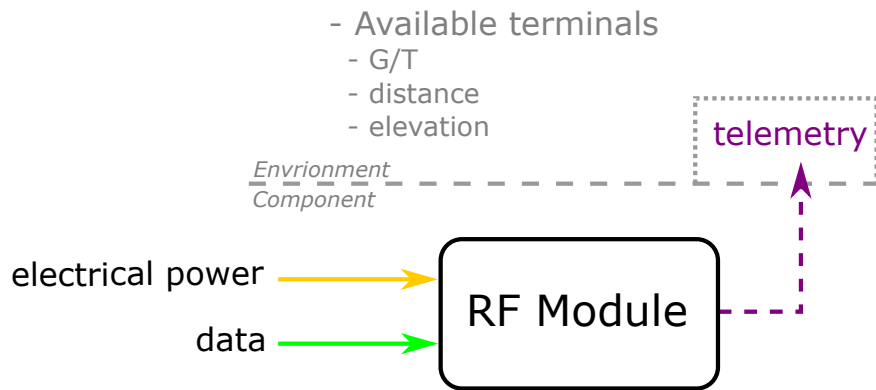
Figure 7.7: RF module resource flow diagram.
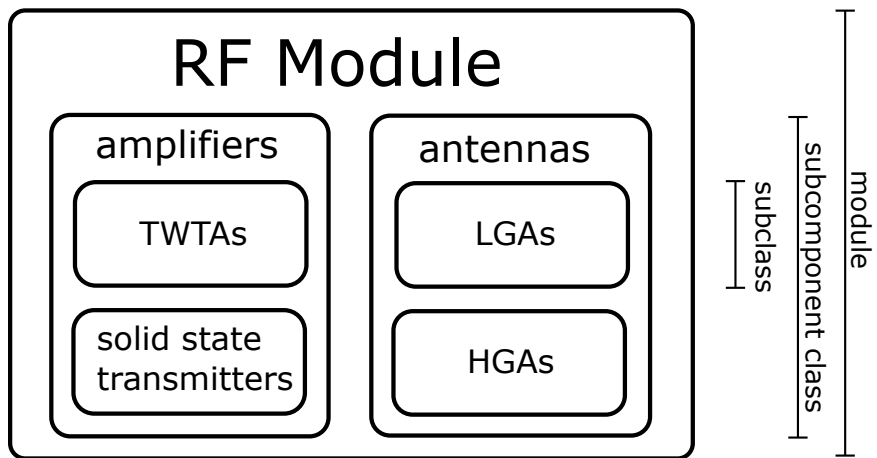
Figure 7.8: RF module subcomponent and subclass hierarchy.

The properties used in component level simulation of RF modules are determined as functions of subcomponent properties. They are given in Table 7.7, along with their description, the subcomponent class they are inherited from, and any units of the property. Note available stations is determined by line of site, and so is inherited from the environment, not a subcomponent.

Table 7.7: RF module properties.

property	description	inherited from	units
P_t	operating power	amplifiers	dB
G	antenna gain	antennas	dB
EIRP	effective isentropic radiated power	-	dB
f	carrier frequency	amplifiers	MHz
bands	communications bands compatible with the module	amplifiers	-
stations	stations currently reachable by the RF module	environment	-

The RF module update process is shown in Fig. 7.9. On a component update, the module loads the list of currently available stations, along with their properties, from the environment. If there is no line of sight to a ground station, all resource flows are set to 0. If there is at least one available ground station, the simulation proceeds to find a combination of amplifier and antenna that can close the link to an available station. Note that this process does not necessarily pick the optimal combination of amplifier and antenna within the RF module if there are multiple choices for either. This optimization is left to VEGA, which is performing the global optimization. The RF module simulation simply picks the first combination of an antenna and amplifier that can close the link to a visible station. If the link can be
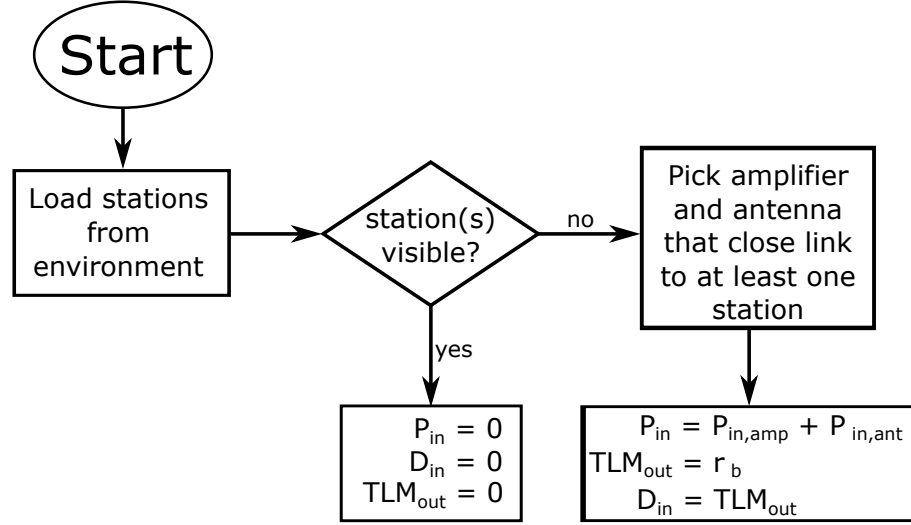
Figure 7.9: RF module update process=.

closed to multiple ground stations with the same antenna/amplifier combination, the link providing the highest data rate transmitted will be used. Closure of the link is determined by calculating the link budget with a given antenna and amplifier, defined by the following system of equations. The effective isentropic radiated power (EIRP) is

$$\text{EIRP} = P_t + G \tag{7.18}$$

where P_t is the transmitter power, in dB, and G is the antenna gain, in dB. The path loss is

$$L_p = 32.44 + \rho_{dB} + f_{MHz,dB} \tag{7.19}$$

where ρ_{dB} is the range to the station and $f_{MHz,dB}$ is the carrier frequency, in MHz, converted into dB [60]. $f_{MHz,dB}$ is assumed to be the maximum frequency that the amplifier can output. This assumption is a worst case scenario in this calculation,

maximizing path loss. The final bitrate transmitted, in dB, is then

$$r_b = \text{EIRP} + G/T - k_b - L_p - Eb/No \qquad (7.20)$$

where G/T is the gain-to-noise-temperature of the receiving station antenna, k_b is the Boltzmann constant, expressed in dB, assumed to have a value of -228.599 dB, and Eb/No is the energy per bit to noise power ratio.

Eq. 7.20 gives r_b, the rate at which data is transmitted to the environment. It therefore defines the telemetry flowrate out of the RF module:

$$TLM_{out} = r_b \qquad (7.21)$$

The RF module consumes data as fast as it can modulate it for transmission as telemetry. Therefore the sink rate of data is equal to the source rate of telemetry:

$$D_{in} = TLM_{out} \qquad (7.22)$$

Finally, the operating power for the RF module is the sum of the operating power of the active antenna and amplifier:

$$P_{in} = P_{in,ant} + P_{in,amp} \qquad (7.23)$$

The remainder of this subsection details the inner workings of the antenna and amplifier subcomponent classes, giving insight into how P_t and G are determined.

7.4.3.1 Amplifiers

Each amplifier has a minimum and maximum output frequency for its carrier signal, f_{min} and f_{max} respectively. These can be user specified in the component data. Alternatively, a number of compatible IEEE radio frequency bands may be specified [61]. If bands are specified, f_{min} and f_{max} are set to the outer bounds of the union of the compatible bands.

For TWTAs, the input parameters given in 7.8 were specified for each component in the TWTA component library. For a full list of components considered, see Appendix C. η_T then defines the amplifier's output power:

Table 7.8: TWTA input parameters.

property	description	units
f_{min}	minimum carrier frequency	Hz
f_{max}	maximum carrier frequency	Hz
$P_{in,amp}$	amplifier input power	W
η_T	amplifier efficiency	-

$$P_t = \eta_T P_{in,amp} \tag{7.24}$$

Solid state transmitters may have f_{min} and f_{max} directly specified, or may use IEEE bands. Within the scope of this dissertation, a solid state amplifier module was considered synonymous with a solid state amplifier. Table 7.9. The key difference between the treatment of TWTAs and solid state amplifiers is that P_t is directly specified as an input parameter for solid state amplifiers rather than being calculated

with a specified efficiency. Additionally, solid state amplifiers specify a maximum

data rate, which cannot be exceeded even if link budget analysis would allow it.

Table 7.9: Solid state amplifier input parameters.

property	description	units
f_{min}	minimum carrier frequency	Hz
f_{max}	maximum carrier frequency	Hz
bands	compatible IEEE radio bands	-
$P_{in,amp}$	amplifier input power	W
P_t	amplifier output power	W
$r_{b,max}$	max data throughput rate	bps

7.4.3.2 Antennas

Table 7.10 gives the input parameters for LGAs. The only real internal logic

rather than encapsulating these parameters, accessible to the RF module, is that a

check is performed to ensure that there is a range of interoperability between carrier

wavelength of the amplifier and antenna. If there is not a range of interoperability,

a component level constraint violation is noted, to be used in feasibility analysis and

penalty calculation on the spacecraft level.

Table 7.10: LGA input parameters.

property	description	units
f_{min}	minimum carrier frequency	Hz
f_{max}	maximum carrier frequency	Hz
G	antenna gain	dB
$P_{in,ant}$	antenna input power	W

Table 7.11 gives the input parameters for HGAs. In comparison to LGAs, the

Table 7.11: HGA input parameters.

property	description	units
G_{nom}	nominal antenna gain	dB
λ_{nom}	nominal wavelength	m
d	antenna diameter	m
$P_{in,ant}$	antenna input power	W
BW	half power beamwidth	deg

gain now becomes a nominal gain G_{nom}, with G being sensitive to the wavelength of the carrier. f_{min} and f_{max} are set to $\pm 5\%$ of the nominal carrier wavelength λ_{nom}:

$$f_{min} = 0.95 \frac{c}{\lambda_{nom}} \tag{7.25}$$

$$f_{min} = 1.05 \frac{c}{\lambda_{nom}} \tag{7.26}$$

where c is the speed of light, assumed to be 3×10^8 m/s. While the actual gain G is not necessarily equal to G_{nom}, it is assumed to be so. This is because the frequency range has been bounded based on the nominal wavelength of the antenna, so component level constraints on the carrier frequency should ensure that $\lambda \approx \lambda_{nom}$. Pointing requirements were considered beyond the scope of this work, since attitude control is not modeled. However, for future use, beam width was allowed as an input parameter, and, if unspecified, was calculated for HGAs:

$$BW = 70 \frac{\lambda}{d} \tag{7.27}$$

where λ is the actual wavelength of the carrier.
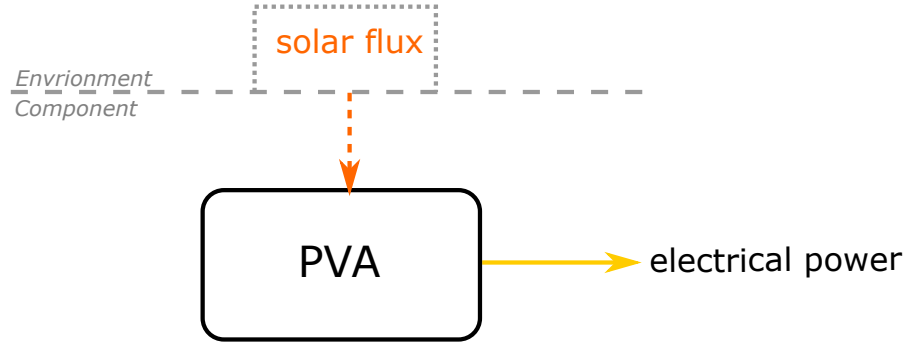
Figure 7.10: PVA resource flow diagram.

7.4.4 Power Generation

The only power generation type considered was photovoltaic arrays (PVAs). Future work can investigate use of alternative power generation, including other forms of solar power, radioisotope power sources, and fusion and fission reactors. The resource flow for a PVA is given in Fig. 7.10, and their input parameters are given in Table 7.12. PVAs are perhaps the simplest component class considered.

Table 7.12: PVA input parameters.

property	description	units
A	solar array area	m^2
η_{PVA}	effective efficiency	-

They sink solar flux Φ_{sol} from the environment at a fixed rate per unit area, and have some total solar flux consumed over a set area. Their output power is then
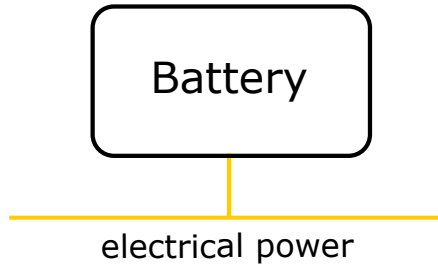
Figure 7.11: Battery resource flow diagram.

this total flux over a given area:

$$P_{out} = \eta_{PVA}\Phi_{sol}A \qquad (7.28)$$

Φ_{sol} is assumed to be 1367 W/m^2 at Earth, and is scaled by the environment based on that value. Therefore, P_{out} is in W. A is assumed to be only the area producing power. η_{PVA} is an **effective** efficiency, accounting for non-power producing portions of the panel area.

7.4.5 Power Storage (Batteries)

In GESDA as modeled, power storage is accomplished with batteries. The resource flow for batteries is given in Fig. 7.11, and their input parameters relevant to modeling their behavior are given in Table 7.13. Cell chemistry is used to determine the charge and discharge efficiency of batteries η_c and η_{dc}, respectively. For simplicity, in the design cases considered, η_c and η_{dc} were set to 1 (considered

Table 7.13: Battery input parameters.

property	description	units
cell chemistry	battery cell chemistry	-
Q_{max}	capacity	Wh
r_{sd}	self-discharge rate	%/day
η_c	battery charging efficiency	-
η_{dc}	battery discharge efficiency	-

a reasonable approximation at this design stage, assuming a lithium ion or lithium polymer cell chemistry, which all batteries considered were). Consideration of non-unity values for η_c and η_{dc} is included in the model for generality. A nominal depth of discharge of 20% was set for batteries. On the regular component update, self-discharge is applied to the battery:

$$f_{c,i} = f_{c,i-1}(1 - r_{sd})^{\Delta t_i / 86400 \text{ s}}$$ (7.29)

where $f_{c,i}$ is the fill level of the battery's electrical power reservoir at the current timestep (after applying self-discharge), $f_{c,i-1}$ is the fill level before applying self discharge, and Δt_i is the duration of the timestep. Eq. 7.29 takes the self discharge rate in %/day, converts it to percent over the duration Δt_i, and applies it to the battery fur the current timestep. The remainder of battery functionality occurs during the store update step of the simulation.

When $\delta_{power} > 0$, there is a surplus of electrical power in the system, and the battery will charge. Some power will be lost during charging for $\eta_c < 1$. To increase the energy stored in the battery by Δf_c, the battery must actually sink amount of

energy equal to $\frac{\Delta f_c}{\eta_c}$. To account for this, when sinking power to the battery, the power available to the reservoir is considered to actually be $\eta_c \delta_{power}$. The remainder r of δ_c not sinked by the battery is then calculated as follows. Consider η_c to be due to the internal resistance of the battery. The total energy consumed by the battery over time t is

$$E_{tot,sink} = \Delta f_c + Q_h \tag{7.30}$$

where Δf_c is the change in energy level of the battery's power reservoir (i.e. energy that becomes stored in the battery), and Q_h, the energy that is dissipated as heat. Following the same logic as discussed for data recorders, t is defined as the time during the timestep Δt_i during which the battery is charging. Dividing then by t, the power sinked to the battery can be similarly defined as a change in the net flow of electrical power:

$$\Delta \delta_{power} = \frac{\Delta f_c}{t} + \dot{Q}_h \tag{7.31}$$

η_c defines the ratio of $\Delta \delta_{power}$ that actually makes it into the battery. Since, by definition,

$$\frac{\Delta f_c}{t} = \Delta \delta_{power} \eta_c, \tag{7.32}$$

it follows that

$$\Delta \delta_{power} = \frac{\Delta f_c}{t \eta_c} \tag{7.33}$$

The maximum charge of the battery is $f_{max} = Q_{max}$, defined as a parameter of each battery. The maximum amount by which the battery can then be charged is then

$$\Delta f_{max} = f_{max} - f_c \tag{7.34}$$

For $\delta_{power}\eta_c\Delta t_i < \Delta f_{max}$, the battery consumes the entire net flow, returning a remainder of $r = 0$. The actual change in the charge in the reservoir is

$$\Delta f = \delta_{power}\eta_c\Delta t_i \tag{7.35}$$

For $\delta_{power}\eta_c\Delta t_i > \Delta f_{max}$, the battery becomes fully charged during this timestep without consuming the full power surplus. In this case, from Eq. 7.33, the decrease portion of the power surplus consumed is

$$\Delta\delta_{power} = \frac{\Delta f_{max}}{\Delta t_i\eta_c} \tag{7.36}$$

The remainder of the power surplus, available to charge other power stores, is then

$$r = \delta_{power} - \Delta\delta_{power} \tag{7.37}$$

When $\delta_{power} < 0$, there is a power deficit within the system. The battery will supplement power generation in the system by sourcing power from its reservoir. Like charging the battery, some power drawn from the battery will be lost for $\eta_{dc} < 1$. Over Δt_i, the energy that must be drained from the battery to compensate a power
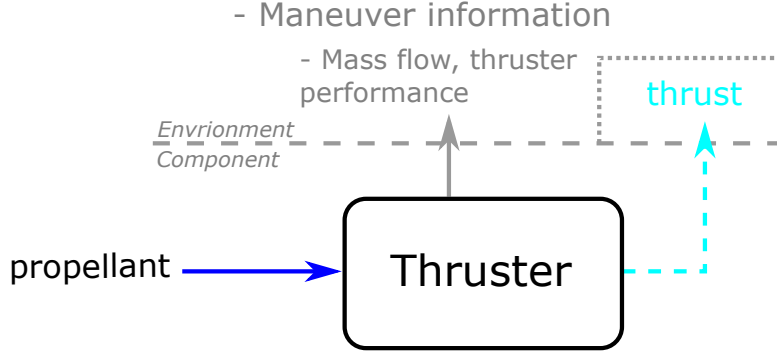
Figure 7.12: Thruster resource flow diagram.

deficit δ_{power} is

$$\Delta f_c = \frac{\delta_{power}}{\eta_{dc}} \Delta t_i \tag{7.38}$$

assuming $\Delta f_c \leq f_c - f_{min}$ for the battery, δ_{power} power will be sourced to the system by the battery, bringing the net power flow to 0, and reducing the charge of the battery by Δf_c. If $\Delta f_c > f_c - f_{min}$, the battery will supply a power of

$$\Delta \delta_{power} = \frac{\Delta f_c}{\Delta t_i} \eta_{dc}, \tag{7.39}$$

depleting the battery, and reducing the power deficit to $\delta_{power} - \Delta \delta_{power}$.

7.4.6 Thrusters

All thrusters are considered to be of the same class in the current implementation of GESDA. The thruster resource flow is given in Fig. 7.12, and the thruster input parameters are given in Table 7.14.

Table 7.14: Thruster input parameters.

property	description	units
I_{sp}	specific impulse	s
F_t	thrust	n
P_{on}	operating power	W
P_{off}	standby power	W
prop$_1$	propellant #1 type	-
prop$_2$	propellant #2 type	-
f_1	mass fraction of propellant 1	-
f_2	mass fraction of propellant 2	-

Each thruster has an associated specific impulse and thrust, supplied as input parameters. From these, the mass flowrate is defined as

$$\dot{m} = \frac{F_t}{I_{sp}g} \tag{7.40}$$

where g is the gravitational acceleration at the surface of the Earth, assumed to be 9.81 m/s^2. For any bipropellant thrusters, (those for which prop$_2$ is defined), this mass flowrate is divided into a mass flowrate for each propellant by the ratio of the propellant mass fractions:

$$\dot{m}_1 = \dot{m}\frac{f_1}{f_1 + f_2} \tag{7.41}$$

$$\dot{m}_2 = \dot{m}\frac{f_2}{f_1 + f_2} \tag{7.42}$$

Thrusters are perhaps the most complex component class included. In simulation, at any given timestep, there is a desired ΔV to perform. ΔV will be some portion of the current maneuver set in the environment. Specifically, it will be the portion of the current maneuver that is still to be completed at the beginning of the

current timestep Δt_i. To determine how many thrusters are firing simultaneously, the simulation turns on thrusters in succession, until either all operational thrusters are on, or those that are on so far are able to complete the maneuver in the current timestep. The ΔV values for each thruster thrusting individually cannot simply be summed, since each additional thruster firing will change the spacecraft mass during the maneuver, affecting the performance of all thrusters firing.

In keeping with the rules of the dynamic CR problem, a thruster cannot know anything explicitly about other thrusters in the system. Only the state of the environment. The solution taken is to track the mass flowrate $\dot{m}_j$ and thrust F_{tj} of each thruster j as they are turned on. $\dot{m}_j$ and F_{tj} can be summed across thrusters, producing

$$\dot{m}_{tot} = \sum_{j=1}^{N} \dot{m}_j \tag{7.43}$$

and

$$F_{tot} = \sum_{j=1}^{N} F_{tj} \tag{7.44}$$

which are tracked in the environment. Each successive thruster that turns on adds its own thrust and mass flowrate to the totals stored in the environment. The effective exit velocity is then

$$u_e = \frac{F_{tot}}{\dot{m}_{tot}} \tag{7.45}$$

For any set of thrusters firing, u_e can thus be determined. Given Δt_i, the total change in spacecraft mass during the maneuver is

$$\Delta m = \dot{m}_{tot}\Delta t_i \tag{7.46}$$

With this information, the rocket equation can be applied, referencing only values stored in the environment, to find the total ΔV performed by this set of thrusters over the timestep:

$$\Delta V = u_e \ln\left(\frac{m_0}{m_0 - \Delta m}\right) \tag{7.47}$$

where m_0 is the total mass of the spacecraft at the beginning of the timestep. If ΔV is smaller than the required velocity change remaining in the current maneuver, additional thrusters will be turned on to increase ΔV. If all operational thrusters are already active, the maneuver is only partially completed during this timestep, with all thrusters firing for the duration of the timestep. The sinks for each active thruster j are set as follows:

$$P_{in,j} = P_{on,j} \tag{7.48}$$

$$\dot{m}_{in_i,j} = \dot{m}_{i,j} \tag{7.49}$$

where $\dot{m}_{in,i,j}$ is the mass flowrate of the ith propellant for thruster j, and $\dot{m}_{i,j}$ is the mass flow rate for propellant i as specified by Eq. 7.41 or Eq. 7.42. The source for each active thruster j is set as:

$$T_{out,j} = F_{t,j} \tag{7.50}$$

If ΔV exceeds the required velocity change remaining for the current maneuver, the required change in mass to complete the maneuver is calculated:

$$\Delta m_{req} = m_0 \left(e^{-\Delta V/u_e} - 1\right) \tag{7.51}$$

The portion of Δt_i required to complete the maneuver is then calculated as

$$t = \frac{\Delta m_{req}}{\dot{m}_{tot}} \tag{7.52}$$

and the above sources and sinks for each thruster are scaled by the portion of Δt_i required:

$$P_{in,j} = P_{on,j} \frac{t}{\Delta t_i} \tag{7.53}$$

$$\dot{m}_{in_i,j} = \dot{m}_{i,j} \frac{t}{\Delta t_i} \tag{7.54}$$

$$T_{out,j} = F_{t,j} \frac{t}{\Delta t_i} \tag{7.55}$$

The logic stated above is for nonimpulsive maneuvers, where it is expected that the entire duration of each orbit may be used for maneuvering. For impulsive maneuvers, it is assumed that only 10% of each orbit may be used for maneuvering. As a result, the same ΔV will take longer to perform, but for any given timestep, the above equations hold by replacing Δt_i with $0.1\Delta t_i$. Note that no explicit check is performed to determine if impulsive or low thrust maneuvers are more appropriate for a given thruster. That selection is made for the entire spacecraft by the L1 genome, and thus is part of the global optimization. There is therefore an implicit

relationship between the types of thrusters used by the spacecraft and the maneuver regime. Impulsive maneuvers are preferable, but the time required to complete them will become prohibitively long for low thrust systems.

Fig. 7.13 details the update process for thrusters, as currently implemented. It is hoped that this illustration of the logic described above may make the textual description itself be more clear. There are some algebraic differences between the above explanation and the figure. These are simplifications in the text for clarity, and the end results are the same. Where there is a discrepancy, the figure describes the process as implemented in GESDA.

Within Fig. 7.13, ΔV represents the ΔV remaining in the environment's ΔV store at the beginning of the timestep. ΔV_p represents the ΔV performed over Δt_i by the currently active thrusters. Assuming the maneuver has not already been completed with earlier thrusters, and that some amount of all propellant types required for this thruster is present on the spacecraft, the thruster is activated. Its mass flowrate and thrust are added to the totals, stored in the environment. u_e and t are calculated based on Eq. 7.45 and Eq. 7.52, respectively. If the maneuver is impulsive, Δt is set 10% of Δt_i, the timestep duration. If it is not impulsive, $\Delta t = \Delta t_i$. The thruster is then activated, and a check is performed to determine if the maneuver can now be completed on this timestep. If so, ΔV_p is set to ΔV, and the resource flows are set for each active thruster following Eqs. 7.53, 7.54, and 7.55.

If the maneuver cannot be completed on this timestep, the resource flows are set following Eqs. 7.48, 7.49, and 7.50. If the maneuvers are impulsive, each of

196
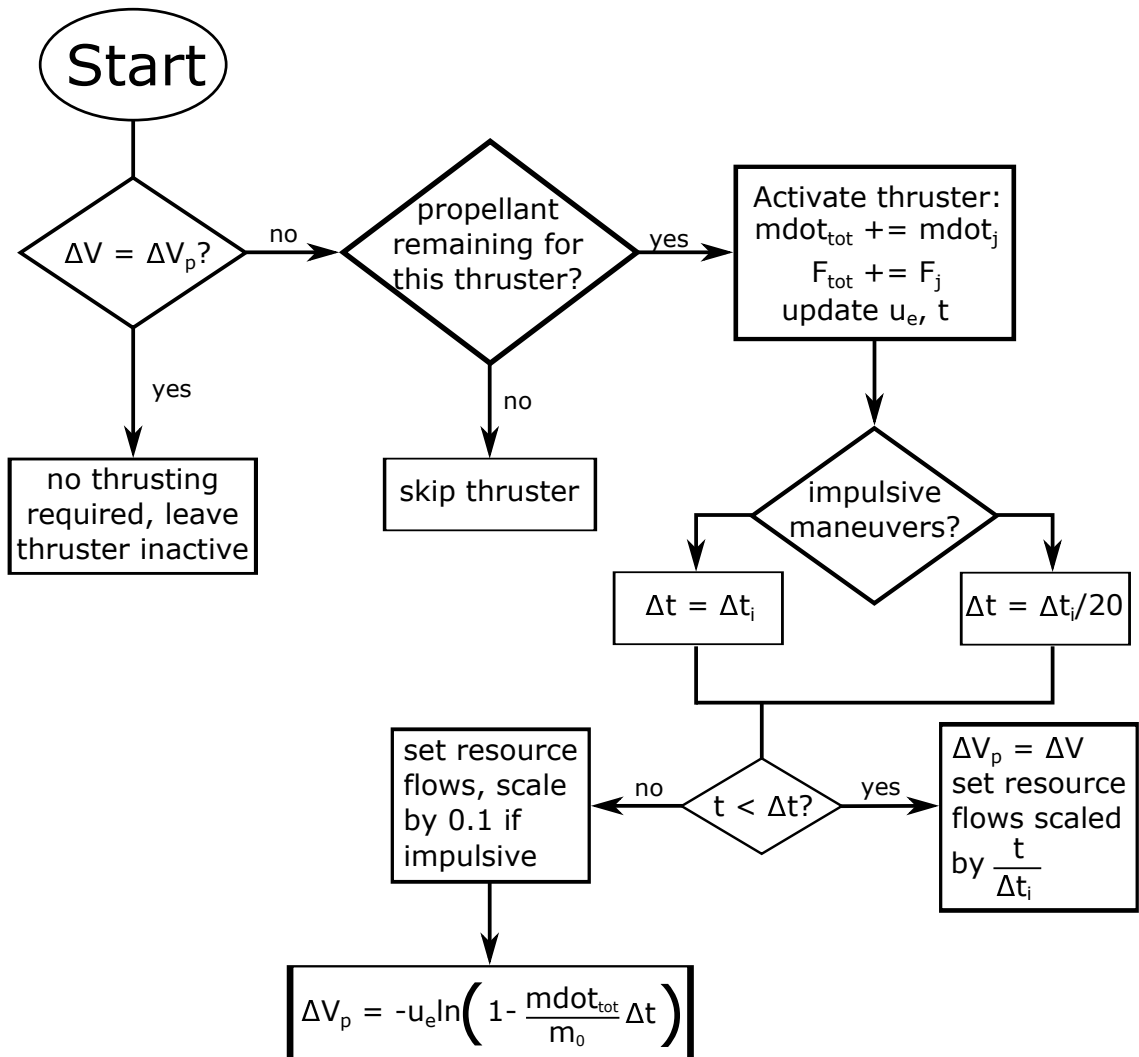
Figure 7.13: Thruster update process.
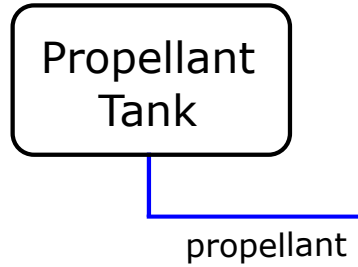
Figure 7.14: Propellant tank resource flow diagram.

these flow rates are divided by 10, since the thruster is only operating for 10% of the orbit. Finally, ΔV_p is set to

$$\Delta V_p = -u_e \ln \left(1 - \frac{\dot{m}_{tot}}{m_0} \Delta t \right) \qquad (7.56)$$

7.4.7   Propellant Tanks

Propellant tanks are fairly simple components, in the context of GESDA. They are a propellant store, providing propellant when required by thrusters as shown in Fig. 7.14 A separate subclass is defined for each type of propellant tank, as each different type of propellant is treated as a separate resource. The logic for all liquid propellant tanks is the same, the only difference being the propellant density ρ. Table 7.1 gives the relevant physical properties of all propellants considered. Table 7.15 gives the input parameters specified for each propellant tank. V_{fill} is not necessarily the full tank volume, but is the maximum volume of propellant that may be stored in the tank. p_{max}, specified only for gaseous tanks, is the maximum

Table 7.15: Propellant tank input parameters.

property	description	units
V_{fill}	fill volume	m^3
p_{max}	maximum pressure (gaseous tanks only)	Pa

pressure of propellant in the tank. All tanks are initialized at their maximum fill level. Propellant fill level is measured in propellant mass in the tank. For liquid tanks,

$$f_{max} = \rho V_{fill} \tag{7.57}$$

where ρ is the density of the propellant. For gaseous tanks, the density is defined from the ideal gas law [62]:

$$\rho = \frac{M p_{max}}{RT} \times 10^{-3} \tag{7.58}$$

where M is the molar mass of the propellant, R is the universal gas constant, assumed to be $8.314 \frac{J}{molK}$, and T is the tank temperature, assumed to be 300 K. The factor of 10^{-3} is a conversion from kg/m^3 to kg/L. With ρ in kg/L, we can calculate the mass of gaseous propellant by Eq. 7.57.

Unlike other component classes, the mass of propellant tanks can change as they are depleted. At any given time, the mass of a propellant tank is

$$m = m_{dry} + f_c \tag{7.59}$$

where m_{dry} is the dry mass of the tank, specified as a component parameter as for all other components, and f_c is the current fill level of the tank. Propellant tanks

have no behavior during the regular component update. During the store update step, they source propellant as required for thrusters of their propellant type.

7.5   Summary

In this chapter we have set up the general satellite design problem. The dynamic CR has been extended with a specific eye on spacecraft design, defining a general spacecraft topology, as well as an environment for modeling spacecraft on closed orbits. Additionally, this chapter has defined a set of general component classes whose applicability spans a wide range of missions. One particular exception is the design of payloads, which, while spoken about generally here, are by necessity mission specific. In practice, a tool like GESDA does not design a payload, but takes one produced by an external design campaign and trades spacecraft designs around it. The remaining chapters will apply the framework developed thus far to two actual spacecraft design problems, comparing the results with existing data from other studies or final flight vehicles, followed by conclusions of this work and general avenues for future follow-on work.

Chapter 8: A Passive Spacecraft Case Study: Earth Observing Cubesat

8.1 Overview

In previous chapters, a dynamic CR model and associated multiobjective optimization framework have been developed. These have then been applied to develop GESDA, a framework for facilitating spacecraft-level trade space analysis. In this chapter, an example and validation of GESDA is provided for a passive spacecraft design.

This chapter investigates the design of a spacecraft to perform the Earth observing mission currently carried out by the Dove spacecraft produced by Planet Labs [58]. A payload is developed based on what is publicly known about Planet's Dove spacecraft. A trade study is then performed using GESDA to maximize the data returned by a single spacecraft supporting the Dove payload while minimizing the spacecraft mass. Finally, the results are compared with the details known of actual flown Dove cubesats.

8.2 The Dove Spacecraft and Payload

The Dove is a class of Earth imaging 3U cubesats under development by and flown by Planet, Inc [63]. Planet has been a strong proponent of "agile aerospace," applying the principles of agile software development [64] to spacecraft design. In this context agile aerospace stresses a focus on rapid turnaround and incremental improvement through continuous tweaking of a design, and getting by with "minimal documentation." The use of agile development by Planet has been facilitated by the advent of capable, inexpensive cubesats, and a dramatic reduction in the cost to launch them [65, 66]. Unfortunately, the lack of focus on documentation associated with agile aerospace, combined with the proprietary and incrementally changing nature of the Dove payload, makes it hard to fully pin down payload specifications. The payload design used for this case study, as detailed below, is an attempt to reverse engineer PlanetScope 2 (PS2), the Dove 3 payload, from what data is available, based primarily on the Planet Labs Specifications document [63].

The payload resource flow is the same as specified by Fig. 7.3, with the exception that this is a passive spacecraft. As a result, no mass is exchanged with the environment. The payload is assumed to continuously operate, so the active state information from the orbit is not used. Therefore, the payload simply sources data and sinks electrical power, both at a constant rate.

Each Dove spacecraft is assumed to be in a 475 km circular sun-synchronous orbit, as specified for future Dove launches [63]. The orbit crosses the equator at 10:30 am local time, defining the right ascension Ω of the orbit to be 250.6°. At this

altitude, the spacecraft is assumed to have a ground sampling distance (resolution) of 3.7 m, and the imager has a field of view of 24.6 × 16.4 km. Combining these leads to an image size of approximately 6650 × 4440 pixels, or 30 megapixels (MP) per image. Images are captured in 12 bits per pixel onboard the spacecraft. According to [63], they are compressed for transmission, but for the purposes of payload development, 12 bits per pixel was assumed since this is the relevant number for the data flow **from the payload**. This leads to an image size of 360 Mb per image.

Planet downlinks 1.3 million images per day from 160 satellites [67]. This leads to a downlink of 8125 images per day per satellite. Assuming continuous imaging, this corresponds to one image every ten seconds. Taking this imaging rate, and the 360 Mb image size, the payload considered here is assumed to produce data at a rate of 36 Mbps.

No power consumption or strict mass data for the imager itself was found in existing literature. It is known that all non-in-house components that Planet uses are commercial off-the-shelf (COTS) components [68]. Specifically, the detector is an industrial, 29 MP COTS CCD detector. This matches the description of the Imperx B6640 [69], which also has approximately the same frame image dimensions (6600 x 4400 pixels). The detector has a power draw of 7.5 W, so P_{in} for the payload was assumed to be 7.5 W. Its mass of 0.37 kg is also very close to the mass of the PS2 camera as stated in the Dove 3 Orbital Debris Assessment Report (ODAR) [70]. The B6640 also features an internal 2 Gb of data storage, so a data store was added to the payload.
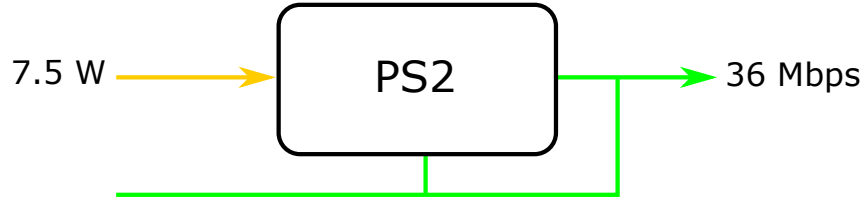
Figure 8.1: PS2 resource flow diagram.

While it was assumed that the B6640 detector and other electronics were used, it is known that the optics were different. The PS2 uses a five element optical system, which consumes most of the internal volume of the 3U x 1U Dove cubesat. Previous Dove payloads used a Maksutov Cassegrain optical system. From [70], it is known that the optical tube, assumed to approximate the mass of the optical system, was 2.08 kg. Therefore, the total payload mass is assumed to be 2.45 kg. To summarize, the payload for this design problem is as shown in Fig. 8.1, and has the parameters given in Table 8.1. Note that the payload is both a data source and a data store. As indicated, it *produces* data at a rate of 36 Mbps, but also has an internal data reservoir, which is empty at the beginning of the simulation.

Table 8.1: PS2 component parameters.

property	description	value	units
P_{in}	input power	7.5	W
m	mass	2.45	kg
r_b	data rate	36×10^6	bps
f_{max}	data capacity	2×10^9	bps
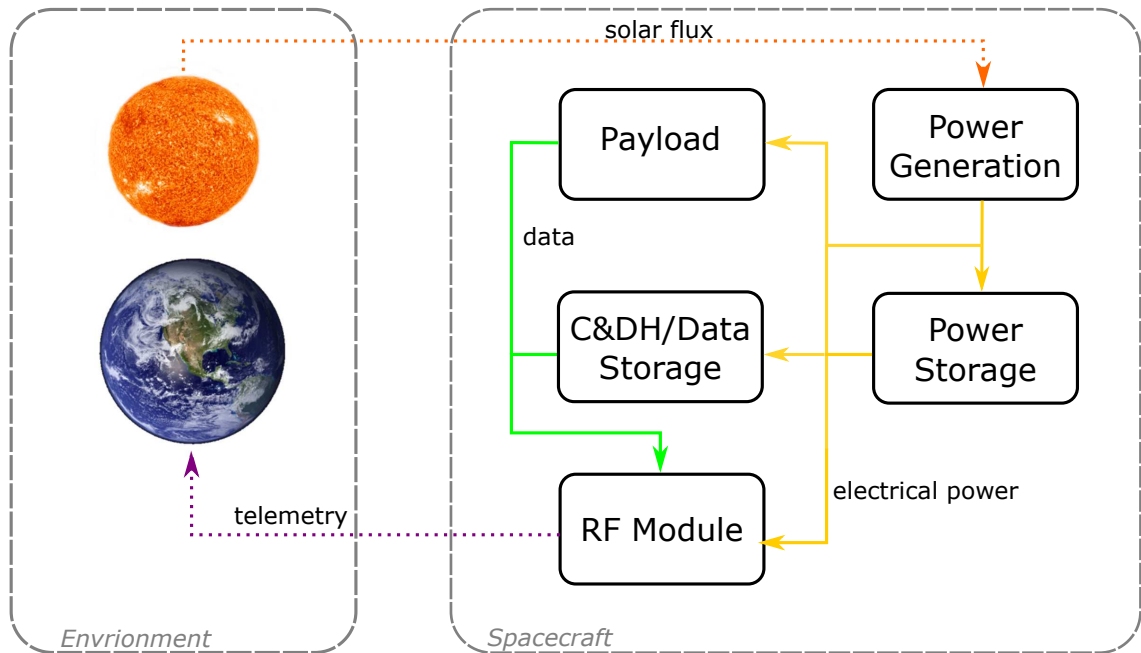
Figure 8.2: CR flow diagram for the Earth observing cubesat.

8.3 GESDA Setup

This section details the remaining problem-specific setup required to perform the desired optimization with GESDA. The CR flow diagram, given in Fig. 8.2, is somewhat simplified from the generalized spacecraft topology. Since this is a passive spacecraft problem, no thrusters or propellant tanks were included, and thrust and propellant were not included as resources.

8.3.1 L1 Genome

For this design problem, the only L1 gene is the trajectory selector. In the event that multiple orbits were under consideration, this gene would select which

orbit the environment should use. In future work, the trajectory selector may be broken into, for example, Keplerian elements. Doing so would allow the orbit design to be included as part of the global optimization. However, in the current implementation, individual orbit simulation for each design in a population of hundreds of individuals is computationally prohibitive, so this problem, as well as the LEO ADR problem discussed in the next chapter, used the same trajectory scheme across the entire population.

8.3.2 Environment

Based on the planned Dove 3 sun-synchronous orbit discussed in section 8.2, a two-orbit simulation was performed. The orbital elements are as given in Table 8.2, where a is the semimajor axis, e is the eccentricity, i is the inclination, Ω is the right ascension of the ascending node, ω is the argument of periapsis, and ν is the true anomaly at the start of the simulation. A two-orbit (actually 12140s) simulation

Table 8.2: Dove 3 simulated orbital parameters.

a (km)	e	i (deg)	Ω (deg)	ω (deg)	ν (deg)
6853.0000	3.6648×10^{-16}	98	250.6148	0	0

was performed in GMAT to find the solar flux over the simulation period. Under nominal operations, Planet points the imager on each Dove to nadir, while keeping the plane of the solar arrays parallel to the orbital plane to minimize aerodynamic drag on the spacecraft [71]. This places the solar arrays at an angle of incidence of 65.8°, reducing the solar flux on the solar arrays. To account for this, the solar flux

206

in the simulation was multiplied by a cosine loss factor of 0.41. In other words, in direct sunlight in Earth orbit, where the incident solar flux would otherwise be 1367 W/m², the solar flux would instead be 560.5 W/m².

The same orbit was simulated in STK for communications access calculations, from 12:00 UTC to 15:00 UTC on January 1, 2000. Planet uses 22 private X-band ground stations located at eight sites around the world, all providing at least 29 dB/K G/T [67]. Like the case with the payload, many of the details of these ground stations were unknown, so an attempt was made to develop a comparable setup in simulation. Additionally, the goal of the simulation and optimization is not to necessarily provide an identical simulation to the setup that Planet arrived at. It was to provide a notional simulation of the spacecraft environment for design purposes. Then, given the PS2 payload a Dove-like design could arise, but the scenario was not set up to favor it outright.

In the simulation for this design problem, two Near Earth Network ground stations were available, Troll Satellite Station in Antarctica, and Svalbard Satellite Station in Svalbard, Norway [59]. By observation of the ground site map in [67], both appear to actually host Planet ground stations as well. These ground stations, along with one in northern North America, appear to be strategically placed close enough to the poles as to have a line of sight to sun synchronous spacecraft on most orbits, ensuring an abundance of downlink opportunities.

In addition to Troll and Svalbard, one TDRSS satellite, TDRS-3 was included as a space station (i.e., a "ground station" in space). For TDRS-3, it was assumed for the scenario that coverage was only available from the start of the simulation, when

the spacecraft is already in TDRS-3's line of sight, until the spacecraft passes beyond TDRS-3's line of sight for the first time. This mimics the limited availability of TDRSS's S-Band Multiple Access (SMA) service, which is shared among numerous customers [72]. Table 8.3 gives the available bands and assumed G/T for each station. For a complete list of access data during the simulation, see Appendix D.

Table 8.3: Downlink station parameters.

station name	band	G/T (dB/K)
TDRS-3	S	4.5
Svalbard	S X	20.5 35.4
Troll	S X	19.4 32

8.3.3 Components Used

For this design problem, the payload detailed in section 8.2 was used. Other component classes used were data recorders, PVAs, batteries, and RF modules, comprising TWTAs, solid state amplifiers, LGAs, and HGAs. The internal models for each of these are as described in section 7.4. Since this is a passive satellite design problem, thrusters and propellant tanks were not included.

For optimization, a constraint of one payload per spacecraft was added as a component quantity constraint. All other component quantities were unconstrained, but seed ranges were specified for each class. These are used when initializing the first generation of designs, but do not constrain the number of components in each

class in any later generations. The seed ranges for each unconstrained class are given in Table 8.4.

Table 8.4: Seed ranges for unconstrained component classes.

class name	minimum quantity	maximum quantity
PVAs	0	10
batteries	0	10
RF modules	1	6
data recorders	0	10

8.3.4   Objective Functions

The objectives for this design problem were to minimize the spacecraft mass, and to maximize the quantity of data returned. Based on analysis of the Dove 3 ODAR [70], structural mass was found to account for 1.68 kg, out of a total spacecraft mass of 5.2 kg, leading to a structural mass fraction $\epsilon = 0.32$. For this design problem, this was assumed to account for all mass not originating from modeled components. Therefore, the total spacecraft mass, the minimization of which serves as the first objective function, is given by

$$m_{tot} = \frac{\sum_{i=1}^{N} m_i}{1 - \epsilon} \tag{8.1}$$

where m_i is the mass of the ith component of the spacecraft, out of a total of N components.

For the second objective of maximizing the data returned from the spacecraft, the net data returned was defined as

$$D_{net} = D_{collected} - \sum_{i=1}^{N} f_{c,data,i} \tag{8.2}$$

where $D_{collected}$ is the total amount of data sourced to the spacecraft by the environment, a quantity which is tracked by the environment, and $f_{c,data,i}$ is the data stored in the ith component onboard the spacecraft. That is, the total data downlinked is the data collected less the data onboard the spacecraft that has yet to be transmitted.

8.4   Results and Comparison to Dove 3

The scenario as defined was run with a population size of 100, for a maximum of 100 generations. Ten runs were performed, with the compound Pareto front of those ten runs presented in Fig. 8.3.   With increasing spacecraft mass, the Pareto front resembles a step increase between 6.25 kg and 6.5 kg. Below this region, data returned does not exceed 1.3 GB, and above it, the system achieves a data returned of 46.83 GB, which is essentially the theoretical maximum given the total simulation time and the data rate of the payload. Under the assumptions of this design problem, the actual Dove 3 spacecraft would return this theoretical maximum of data. Based on the ODAR, the Dove 3 total spacecraft mass is 5.2 kg. This places it closest to the second highest data returned design obtained with GESDA.
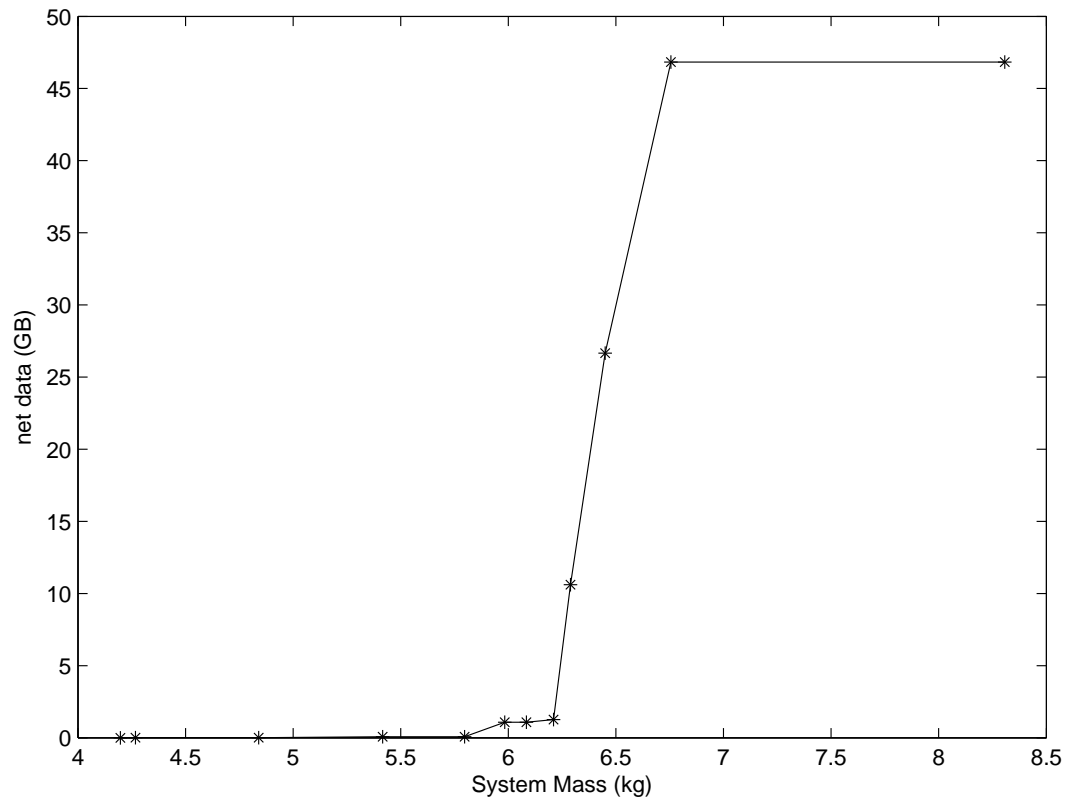
Figure 8.3: Compound Pareto front for Earth observing cubesats.

Table 8.5 compares the mass of the actual Dove 3 spacecraft to that of this most similar GESDA-determined design on the Pareto front, organized by major subsystem. Avionics includes those components that handled data, with the exception of the payload itself (i.e. RF modules and data recorders). The payload,

Table 8.5: Comparison of Dove 3 to Pareto-Optimal design.

Spacecraft	Dove 3	GESDA designed Earth Observing Cubesat
Payload mass	2.45 kg	2.45 kg
Electrical power system mass	0.61 kg	1.69 kg
Avionics mass	0.20 kg	0.46 kg
Structural subsystem mass	1.68 kg	2.16 kg
Total spacecraft mass	5.2 kg	6.76 kg

being the primary design point taken from Dove 3 and used to develop the GESDA designs, is identical in both spacecraft. All masses for Dove are taken from the Dove 3 ODAR [70]. All subsystem masses for the GESDA designs are based on the components comprising the design, with the exception of structural mass. From Eq. 8.1, this can be found to be

$$m_{struct} = \frac{\sum_{i=1}^{N} m_i \epsilon}{1 - \epsilon} \tag{8.3}$$

All of the GESDA masses are somewhat greater than the actual equivalents on Dove. The details of the electrical power systems for both spacecraft are given in Table 8.6. As can be seen, the battery masses (and presumably capacities) are essentially the same. The difference is in the solar arrays. The GESDA-derived

Table 8.6: Electrical power system comparison.

Spacecraft	Dove 3	GESDA designed Earth Observing Cubesat
PVA mass (kg)	0.40	1.09
PVA area (cm^2)	210	230
Battery mass	0.61	0.60

design has roughly the same solar array area but three times the solar array mass. A further investigation into the solar arrays used for Dove reveals the likely cause for the discrepancy. In GESDA's component library for this design problem, only space-rated cubesat solar panels were considered. However, Planet uses Triangular Advanced Solar Cells (TASC) [73, 74]. TASC are intended as terrestrial solar cells, and, at least in Planet's implementation, do not have coverglass to protect from the radiation environment. Studies into the performance of TASCs in the space radiation environment suggest a degradation to 66% of beginning of life power output after two years [75]. However, it does mean that they achieve a greater efficiency at the beginning of their life.

According to [74], a typical TASC cell produces 0.027 W/cm^2 in the Dove 3 orbital environment (i.e. 1 Sun). Typically, two TASC cells are arranged into a rectangle, with each rectangle measuring 4.93 cm^2. By observation of pre-launch imagery, Dove 3 does indeed use TASC, arranged in 3U arrays, with each array measuring 5 x 8 rectangles. This equates to 40 rectangles per array, which equates to 197 cm^2 per array. Given the rated power per unit area for TASC, this gives a power of 5.32 W per Dove array at beginning of life. Given that each Dove 3 has 7

arrays, this equates to 37.3 W at beginning of life. However, given the nonzero beta angle discussed above for Dove, and associated cosine loss factor of 0.41, each Dove 3 actually only produces 15.3 W at beginning of life. This aligns very closely with the beginning of life power of 15.0 W produced by the GESDA-based design.

In addition to the components discussed above, the RF module features two vestigial transmitters; one a 0.03 kg L-band transmitter, and the other a 0.085 kg VHF transmitter. Together, these account for around half of the mass discrepancy between the avionics subsystems. The onboard data recorders alone are 0.19 kg. Analysis of the data stored by the recorders reveals that only the first one is used, and so the others are vestigial, accounting for a mass of 0.17 kg. The total avoinics mass for the Dove 3 is 0.20 kg [70]. There are no other masses in the ODAR that could be considered to contain the mass of the transmitters. so they are assumed to be avionics mass. The combined vestigial avionics mass is then 0.28 kg. Combining the non-vestigial antenna, transmitter, and data recorder produces a "trimmed" avionics mass of 0.19 kg, very close (potentially within ODAR rounding error) to the Dove avionics mass.

Trimming the vestigial components from the GESDA design, the mass breakdown given in Table 8.7 is produced. This mass is still approximately 20% higher than the actual Dove 3. Given the known discrepancies discussed in the electrical power system, this is considered a reasonable validation of GESDA.

Table 8.7: Comparison of Dove 3 to Pareto-Optimal design.

Spacecraft	Dove 3	GESDA designed Earth Observing Cubesat
Payload mass	2.45 kg	2.45 kg
Electrical power system mass	0.61 kg	1.69 kg
Avionics mass	0.20 kg	0.17 kg
Structural subsystem mass	1.68 kg	2.03 kg
Total spacecraft mass	5.2 kg	6.3 kg

8.5   Summary

In this chapter we have demonstrated the use of GESDA for passive spacecraft trade space exploration. In comparing the results obtained to an actual flown mission carrying the same payload, this chapter serves as a validation of the CR model and GESDA. It is likely that further analysis and refinement of the simulation could produce closer results to the actual Dove 3 spacecraft. However, the results obtained do validate the framework, and further refinement would come with an increase in complexity, and likely computational requirements. It is therefore left for future work in some later revision of GESDA.

Chapter 9:   Revisiting LEO ADR: An Active Spacecraft Case Study

9.1   Overview

Ultimately, we have arrived back at the original LEO active debris removal
(ADR) design problem which was originally considered in Chap. 2, and which largely
motivated the development of GESDA, detailed throughout this dissertation up to
this point. As a final validation, GESDA is now used to repeat the design study
of Chap. 2. As such, many of the implementation decisions for this design case
were made to match the assumptions of Chap. 2, even in situations where a more
accurate treatment is facilitated by GESDA, or by enhanced knowledge since the
original publication of [76]. LEO ADR spacecraft are an active spacecraft in the
context of GESDA. The same trade study as in Chap. 2 is performed, minimizing
the cost per debris object (DO) removed, and minimizing the overall risk factor of
the debris removal program. Finally, the results are compared and contrasted with
the results from Chap. 2.

9.2 LEO ADR Payloads Considered

All seven ADR systems considered in Chap. 2 were considered here as payloads. Unlike in Chap. 2 where the ADR system and grapple arm were considered separate payloads, they are combined here where both are present. For reference, the mass and power requirements for each ADR system, taken from Tables 2.2 and 2.1 is repeated here in Table 9.1, and the mass and power requirements for the OEDMS-based grapple arm is given in 9.2. As was the case in the original LEO ADR study,

Table 9.1: ADR System Mass and Power.

ADR system	Mass (kg)	Power (W)
Conventional Tug	0	0
EDDE	80	0
LAT	42	250
KSII	74	10
TRIS	106	1
GOLD	70	0
Terminator Tether	28	0

Table 9.2: Grapple arm Mass and Power.

Manipulator	Mass (kg)	Power (W)
OEDMS-based arm	80	131

the payload is assumed to sink power at a constant rate P_{in}, the maximum of the power requirement for the manipulator and ADR system. As a result, the payload active state from the environment is again unused. Since this case study sought to replicate the design problem of Chap. 2, no data sourced from the payload was
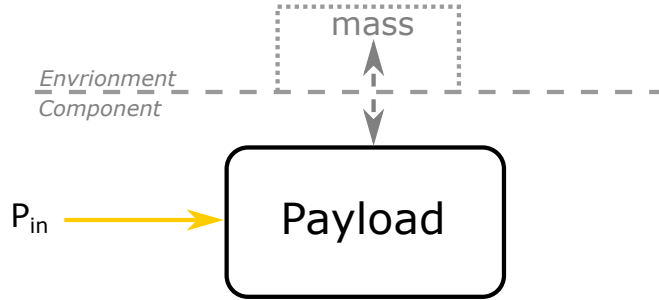
Figure 9.1: ADR payload flow diagram.

considered. As a result, no data recorder components or RF module components or subcomponents were included in this design problem. Mass increments were included. For any orbital tug ADR systems considered, the mass increment was set to $m_{deb} = 1400kg$, the mass of the model DOs. For any deorbit package (DP) ADR systems considered, the mass increment was set to m_{dp}, the mass of the ADR system, as specified in Table 2.1. The general resource flow of the payload for this design problem is as specified in Fig. 9.1.

Table 9.3 gives the relevant component input parameters for each ADR system. In the current implementation, the mass and power of any manipulator present is already included in these input values. Note that m_{dp} is only nonzero for DP ADR systems. R_{base} indicated the trajectory risk of the ADR system. Each integer value for R_{base} is a code for a corresponding ADR specific risk, as indicated in Table 9.4. For a full discussion of the last four properties in the table, see Chap. 2. If an ADR system is self-propelling, additional thrust parameters, as given in Table 2.3, are also specified.

Table 9.3: LEO ADR payload input parameters.

property	description	units
m_{dp}	DP mass	kg
P_{in}	operating power	W
R_{base}	ADR specific risk	int
A_{ADR}	Destructive collision cross section	m^2
self-propelling	self-propelling?	T/F
self-grappling	self-grappling?	T/F
self-contained	self-contained?	T/F

Table 9.4: ADR specific risk key.

R_{base}	risk level
1	low
2	medium
3	high

The payload mass was set to the sum of the manipulator mass m_{grap} and the ADR system mass m_{ADRS}.

$$m_{pld} = m_{grap} + m_{ADRS} \tag{9.1}$$

For tug ADR systems, m_{ADRS} is simply the mass listed for the appropriate system in Table 9.1. For DP ADR systems, it depends on the number of DPs onboard the spacecraft, equal to n_{targs}, the total number of DOs to be removed by a single spacecraft:

$$m_{ADRS} = n_{targs} m_{dp} \tag{9.2}$$

For this design problem, the mass increment is managed by the payload. That is, it is the payload that exchanges mass with the environment. For tug ADR systems, the mass increment is set to 1400 kg, the mass of a DO. For DPs, it is set to the mass of a single DP. This is because those are the increments by which the spacecraft mass changes for the respective mission types. A tug grapples a DO, increasing its mass by that of the DO. It then performs a series of maneuvers to place the DO on a disposal orbit, subsequently releasing it, decreasing the spacecraft mass by the mass of the DO. Conversely, an orbital tender vehicle performs plane change between each DO, attaching an onboard DP to it. In doing so, it decreases the spacecraft mass by the mass of a DP with each DO it visits.

9.3   GESDA Setup

As with the previous satellite design case, the CR flow diagram, given in Fig. 9.2, is somewhat simplified from the generalized spacecraft topology. In this case, thrusters and propellant tanks are present, as this is an active spacecraft problem. However, RF modules, their subcomponents, and data recorders (those component classes that deal only with data) are not. Data and telemetry from the generalized spacecraft topology are omitted as resources.

9.3.1   L1 Genome

The L1 genome for this design problem contains six genes, which will be designated here $L1_i$ for the ith L1 gene. They are all drawn from the genome from Chap. 2,
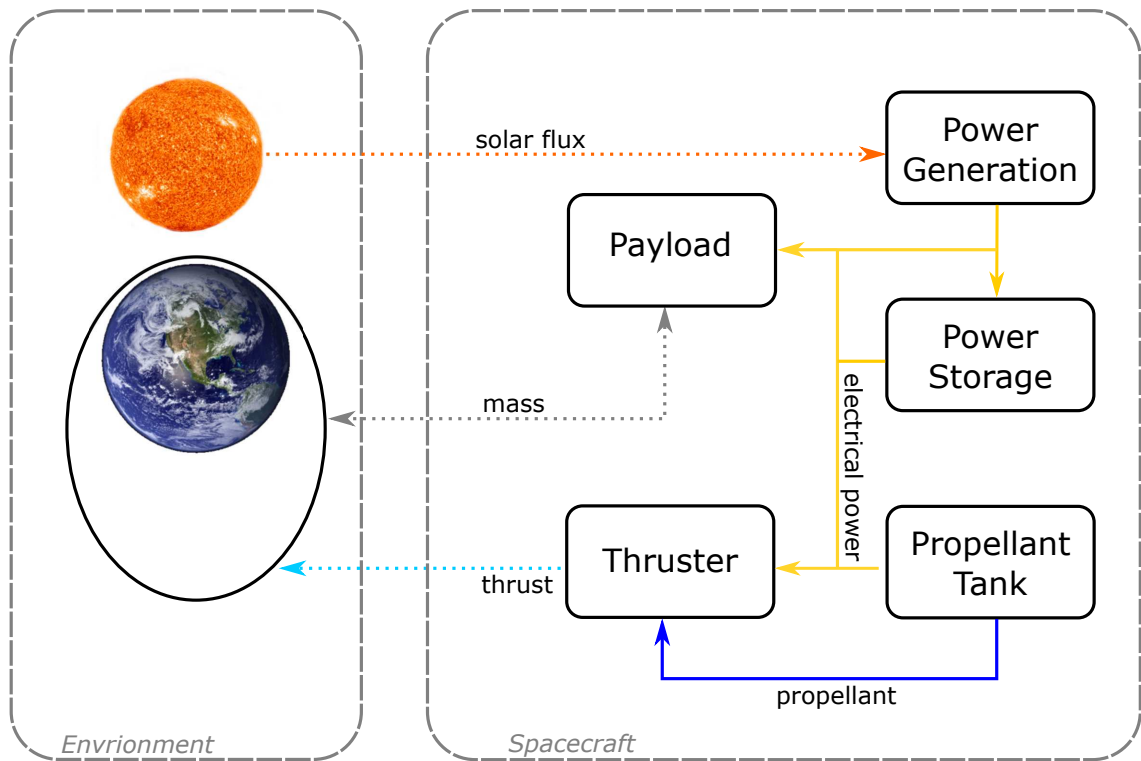
Figure 9.2: CR flow diagram for the ADR vehicle.

capturing aspects of the design that are not accounted for in other portions of the genome. $L1_1$ is n_{targs}, the number of DOs removed by each ADR vehicle. Accordingly, it can have any integer value between 1 and 55, matching the conditions from Chap. 2. $L1_2$ is a binary parameter, designating whether the spacecraft performs impulsive maneuvers, or if maneuvers are considered low thrust. This is required for any active spacecraft design problem, particularly those where the spacecraft maneuvers in the simulation, as discussed in section 7.3.2. $L1_3$, $L1_4$, and $L1_5$ are binary genes, indicating whether thrusters or payloads perform each maneuver type (orbit raising, plane change, and orbit lowering, respectively). If the ADR system cannot maneuver, these genes are ignored, and all maneuvers are performed by thrusters. Finally, $L1_6$ is a binary gene that designates whether or not an ADR vehicle holds short of high priority orbits, as discussed in Chap. 2.

9.3.2 Environment

The same model debris orbit outlined in Chap. 2 was used for this design problem. As this is a dynamic satellite design problem, with a maneuvering spacecraft, the orbit simulation was procedurally generated. The orbital elements used are given in Table 9.5. For this design problem, a heavily simplified orbital simulation

Table 9.5: LEO ADR orbital parameters, based on in Chap. 2.

a (km)	e	i (deg)
7128	0	74

was performed. The elements ω, ν, and Ω were not explicitly tracked, although $\Delta\Omega$,

222

the change in Ω between each DO orbit, as defined in Chap. 2, was. No simulation was performed in GMAT or STK. Instead, a low fidelity simulation, with only two timesteps per orbit, was performed. Matching the conditions of the original LEO ADR work, direct sunlight was assumed for half of each orbit, constituting one timestep, and complete darkness was assumed for the other half of each orbit, constituting another timestep. Given the semimajor axis of the orbit, the orbital period is 5989 seconds, or 1.66 hours. The duration Δt of each timestep was therefore set to 2995 seconds. These two-timestep orbits were procedurally added to the simulation, as dictated by section 7.3.2.

This decrease in fidelity was necessary to achieve reasonable runtimes. There was never a plan to consider data downlink from the spacecraft for this design problem. However, doing so would not even be possible with the current level of reduced fidelity. See the final chapter of this dissertation for thoughts on addressing this, should this work be extended in the future.

9.3.2.1 LEO ADR Maneuvers

This section details the logic behind the maneuver tables used for this design problem. The formulation of each ΔV given here was taken directly from the original LEO ADR work of Chap. 2. It is acknowledged that more accurate and efficient formulations exist, especially for nonimpulsive maneuvers. However, effort was made to accurately replicate the maneuver assumptions of the original LEO ADR work to allow for a fair comparison of the results. Therefore, the work presented here is

really a more in-depth derivation of the maneuvers used for the original LEO ADR work, which were preserved for the work of this chapter.

The ΔV tables for this mission take different forms depending on whether the payload is a tug or orbital tender vehicle. For an orbital tender vehicle, the spacecraft is assumed to be launched directly into the orbit of its first DO. The ΔV, therefore, only contains plane change maneuvers between each DO. As in the original LEO ADR study, nodal regression is not considered, so it is assumed that all plane change between DOs must be accomplished propulsively. As a result, each line of the ΔV table is identical, taking the form given in Table 9.6. where ΔV_Ω is

Table 9.6: ΔV table format for orbital tender vehicles.

ΔV (m/s)	t_{wait} (orbits)	mass increment	thruster class	maneuver type
ΔV_Ω	48	-1	$L1_4$	plane change

the plane change ΔV, the form of which depends on multiple L1 genes, as discussed below. A 48 orbit (3 day) wait after the completion of each maneuver is included, as was the case in the original LEO ADR study, to account for phasing and rendezvous with the next DO. The mass increment of -1 accounts for the loss of mass as each DP is removed from the spacecraft and attached to the DO. As discussed above, $L1_4$ indicates whether the ADR system or thrusters perform plane change maneuvers (the only maneuver type conducted for orbital tender vehicles). Note, however, that no DPs considered are self-propelling, so in this design study, all maneuvers for tender vehicles, including plane change maneuvers, were performed by thrusters.

The form of ΔV_Ω depends on n_{targs}, the number of DOs removed per ADR vehicle, and on whether or not the ADR vehicle performs impulsive maneuvers. Both are specified by L1 genes. n_{targs} determines $\Delta\Omega$. Taking the distribution in Ω of the model DO population, the total plane change $\Omega_{tot,min}$ of the most tightly bound group of n_{targs} DOs in the population is found. $\Delta\Omega$ is then

$$\Delta\Omega = \frac{\Omega_{tot,min}}{n_{targs}}, \tag{9.3}$$

the average plane change between successive DOs. ΔV_Ω is then a function of $\Delta\Omega$, with its form depending on whether or not maneuvers are impulsive. For impulsive maneuvers,

$$\Delta V_\Omega = 2\sqrt{\frac{\mu}{a}}\sin\left(\frac{\Delta\Omega}{2}\right) \tag{9.4}$$

Nonimpulsive maneuvers were adapted from the work of Stansbury [77], which was in turn adapted from [78]. The initial yaw angle β_0 is first found from Eq. 14.38 in [78]:

$$\beta_0 = \tan^{-1}\left(\frac{\sin\left(\frac{\pi}{2}\Delta\Omega\right)}{\frac{V0}{V_f} - \cos\left(\frac{\pi}{2}\Delta\Omega\right)}\right) \tag{9.5}$$

Where V_0 is the spacecraft velocity on the initial circular orbit, and V_f the velocity on the final circular orbit. For orbital tender vehicles, the orbital altitude does not change, so $V_0 = V_f$. With β_0, the total ΔV for the plane change maneuver is, as given in Eq. 14.73 in [78]:

$$\Delta V_\Omega = V_0\left(\cos\beta_0 - \frac{\sin\beta_0}{\tan\left(\frac{\pi}{2}\Delta\Omega + \beta_0\right)}\right) \tag{9.6}$$

Due to nodal regression, this is considered a worst case ΔV. Finally, then, the ΔV table for orbital tender vehicles is n_{targs} repetitions of Table 9.6.

For orbital tugs, the form of the maneuver table depends on whether or not maneuvers are impulsive, as well as whether or not the same thruster class is used for each maneuver type. If maneuvers are not impulsive, and the thruster class is the same for orbit raising and plane change maneuvers, these two maneuvers can be combined. Eqs. 9.5 and 9.6 can be used to calculate ΔV_c, the combined ΔV to raise the orbit and perform the necessary plane change. In this case, V_0 is the velocity of a 200 km circular orbit (the debris disposal orbit, which is also the orbit into which nonimpulsive orbital tugs are initially launched), and V_1 is the velocity in the debris orbit. If maneuvers are not impulsive and orbit raising and plane change cannot be combined, then the ΔV_Ω is computed with Eq. 9.6, and ΔV_{up}, the ΔV required for plane change, is assumed to be the difference of the velocities of the two circular orbits:

$$\Delta V_{up} = V_0 - V_1 \tag{9.7}$$

Since the nonimpulsive tug is always maneuvering between two set orbital altitudes, the debris altitude of 750 km, and the disposal altitude of 200 km, orbit raising and lowering maneuvers are of the same magnitude (though the total impulse is not, given the additional DO mass on the way down). Therefore,

$$\Delta V_{down} = \Delta V_{up} \tag{9.8}$$

226

For impulsive maneuvers, orbit raising and plane change are not combined. The ADR vehicle is assumed to start in a 750 km × 200 km orbit. For orbit raising, the vehicle circularizes itself at apogee into the debris orbit. It then performs any necessary plane change, rendezvouses with and captures the DO. For lowering the DO, a Hohmann transfer is performed, lowering the debris perigee to 200 km as specified in Chap. 2. Again, due to the symmetry of orbit raising and orbit lowering, both require the same ΔV:

$$\Delta V_{up} = \Delta V_{down} = 175 \text{ m/s} \tag{9.9}$$

Impulsive plane change is performed in the same manner as for tender vehicles, and is therefore given by Eq. 9.4, with a being the semimajor axis of the debris orbit.

For impulsive maneuvers, and nonimpulsive maneuvers where plane change and orbit raising are not combined, the ΔV table starts with the initial orbit raising after launch, and the subsequent orbit lowering after capturing the first DO, as shown in Table 9.7 For all remaining maneuvers a block of the form given in Table 9.8

Table 9.7: Initial ΔV table for orbital tugs.

ΔV (m/s)	t_{wait} (orbits)	mass increment	thruster class	maneuver type
ΔV_{up}	1	1	$L1_3$	orbit raising
ΔV_{down}	1	-1	$L1_5$	orbit lowering

is appended to the ΔV table $n_{targs} - 1$ times, to account for all DOs removed after the first.

Table 9.8: ΔV table increment for DOs past the first.

ΔV (m/s)	t_{wait} (orbits)	mass increment	thruster class	maneuver type
ΔV_{up}	1	0	$L1_3$	orbit raising
ΔV_{Ω}	48	1	$L1_4$	plane change
ΔV_{down}	1	-1	$L1_5$	orbit lowering

For nonimpulsive maneuvers where orbit raising and plane change are combined, the ΔV table is initialized similarly to impulsive maneuvers, as shown in Table 9.9: For all remaining maneuvers a block of the form given in Table 9.10 is

Table 9.9: Initial ΔV table for orbital tugs with orbit raising and plane change combined.

ΔV (m/s)	t_{wait} (orbits)	mass increment	thruster class	maneuver type
ΔV_c	1	1	$L1_3/L1_4$	orbit raising and plane change
ΔV_{down}	1	-1	$L1_5$	orbit lowering

appended to the ΔV table $n_{targs} - 1$ times, to account for all DOs removed after the first:

Table 9.10: ΔV table increment for DOs past the first (nonimpulsive combined maneuvers).

ΔV (m/s)	t_{wait} (orbits)	mass increment	thruster class	maneuver type
ΔV_c	48	1	$L1_3/L1_4$	orbit raising and plane change
ΔV_{down}	1	-1	$L1_5$	orbit lowering

In either the final impulsive or nonimpulsive case, if $L1_6$ is true, indicating a desire for the ADR vehicle to hold short for ideal phasing when crossing high priority

orbits, a pause duration of one orbit was added to each orbit lowering maneuver in the ΔV table.

9.3.2.2 Propulsive Multistep

Based on the procedural nature of the simulation, low thrust maneuvers that take many orbits to perform necessitate very large simulation files, with $2N_o$ timesteps, where N_o is the number of orbits in the simulation. For low thrust propulsion systems, which including all electric propulsion thrusters considered, as well as the LAT and EDDE payloads, N_o can be on the order of $100n_{targs}$ or greater. As a result, for practical computational reasons, it was necessary to reduce the number of timesteps actually simulated. This was accomplished with a special propulsive multistep. The propulsive multistep is, in most ways, identical to the regular multistep, discussed in section 7.3.2. While the regular multistep is only performed once a maneuver has been completed, a propulsive multistep is performed if more than ten timesteps are required to complete the current maneuver. The propulsive multistep, operates under the implicit assumption that any low thrust propulsion systems do not significantly change the mass of the spacecraft over a single maneuver. This proved to provide comparable results for this design problem, but may not be applicable in general.

If used, the propulsive multistep simulates a single orbit and performs a regular multistep internally with a number of repetitions

$$r = \text{floor}(\Delta V_i / \Delta V_p), \tag{9.10}$$

where ΔV_i is the ΔV remaining in the current maneuver, and ΔV_p is the ΔV performed over a single orbit. It then additionally calculates the total ΔV performed over the multistep

$$\Delta V_{tot} = r\Delta V_p \tag{9.11}$$

and subtracts this from the ΔV remaining in the current maneuver.

9.3.3   Components Used

The components used in this design problem correspond to the original modeled subsystems from Chap. 2. This comprises PVAs, batteries, thrusters, and propellant tanks from the general CR model for spacecraft design, as shown in Fig. 7.1, as well as payloads, as detailed in this chapter. For propellant tanks, a separate class was specified for each type of propellant included, as discussed in Chap. 7. A single list of tanks was used to populate the component library for all liquid propellant tank classes. A separate list was used to populate the component library for gaseous tank classes, of which Xenon was the only one in this design problem. Additionally, collision avoidance motors were included as a component class. They are not included in Fig. 9.2, as they do not feature any resource flow. For the purposes of the simulation, they are an additional inert mass, which influences the overall risk factor, modifying the objective functions as discussed in Chap. 2. For a complete list of components used for this design problem, see Appendix C.

For optimization, a constraint of one payload per spacecraft was added as a component quantity constraint. All other component quantities were unconstrained,

but seed ranges were specified for each class. These are used when initializing the first generation of designs, but do not constrain the number of components in each class in any later generations. The seed ranges for each unconstrained class are given in Table 9.11.

Table 9.11: Seed ranges for unconstrained component classes.

class name	minimum quantity	maximum quantity
PVAs	0	10
batteries	0	10
thrusters	1	10
collision avoidance motors	0	55
MMH tanks	1	10
NTO tanks	1	10
Aerozine 50 tanks	1	10
N_2H_4 tanks	1	10
Xenon tank	1	10

9.3.4   Objective Functions

The objectives for this design problem were to minimize c_{DO}, the cost per DO removed, and to minimize the overall risk factor ORF. The total spacecraft mass m_{tot}, and, subsequently, c_{DO}, which is a function of m_{tot} were defined as discussed in section 2.2.3.1. ORF was defined by Eq. 2.5.

9.4   Results and Comparison to Original LEO ADR Study

The baseline scenario from the original LEO ADR study was replicated with GESDA, as outlined in this chapter. Separate runs of GESDA were performed for
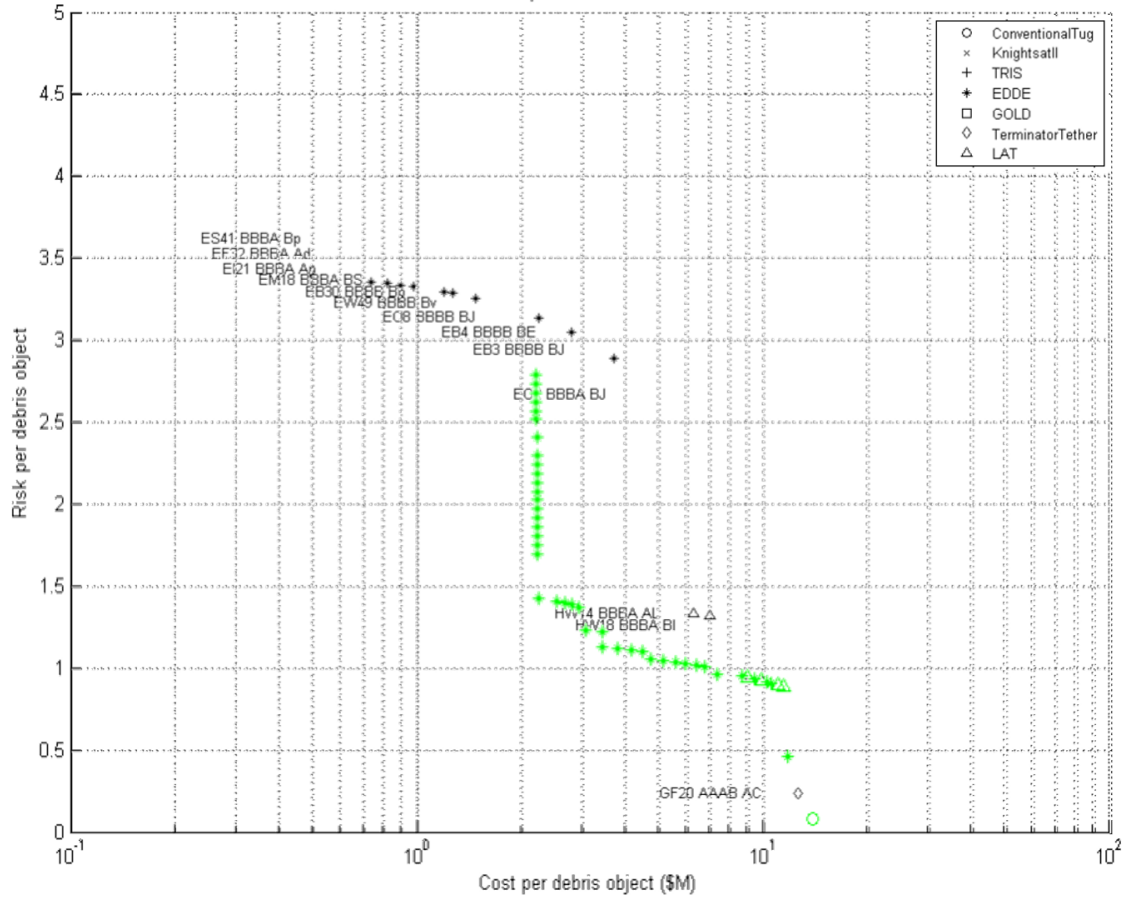
Figure 9.3: Compound Pareto front of original LEO ADR results from
Chap. 2, in black, and new, GESDA-based results in green.

each payload (each based on one of the seven ADR systems considered). Ten runs

of GESDA were performed for each payload, with a population of 200 running for a

maximum of 100 generations. Each payload was run in parallel, with the ten runs of

each given payload being run in serial, over the course of approximately 100 hours.

The compound Pareto fronts for each payload were combined into a single

compound Pareto front, given in Fig. 9.3. For clarity, a zoomed in view consisting

solely of the GESDA-based results is presented in Fig. 9.4. The ordering of the
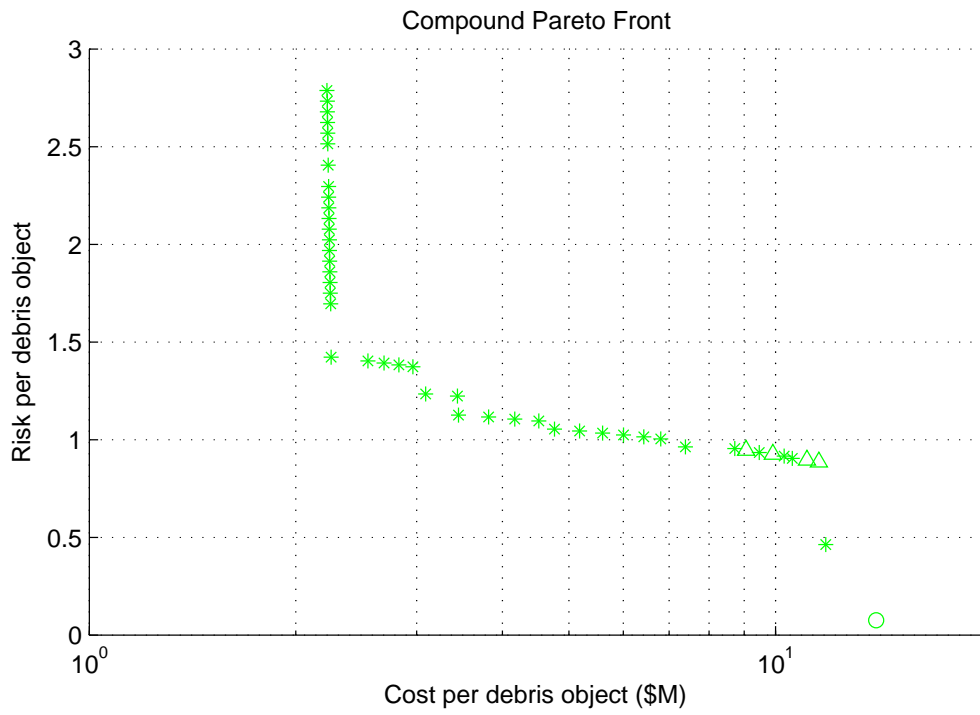
Figure 9.4: GESDA-based compound Pareto front of LEO ADR vehicles.

designs, and their share of the Pareto front, is relatively unchanged from the original LEO ADR work. The majority of the front is EDDE-based designs, which represent the highest risk/lowest cost. In the middle of the front are a relatively small number of LAT-based designs, followed by a single other design, either a conventional tug in the new results or Terminator Tether in the original results.

At first glance, the results appear complementary - filling in different portions of the same Pareto front. This is more or less true for three points on the lower right edge of the Pareto front. However, the middle "flat" portion of the new Pareto front, from a cost per DO of $2M to $11M, consists of similar designs to the remainder of the original Pareto front. Comparable designs on the new front are somewhat more expensive, while at the same time substantially lower risk than their original counterparts.

This is, regrettably, due to a bug found in the original risk calculation code, which inaccurately modified the weighted technology readiness level (WTRL) all orbital tug designs. Specifically, the error forces all orbital tug payloads to TRL 2. In the original LEO ADR work, all EDDE designs were self-contained. These designs contained no components other than the EDDE payload itself, and possibly collision avoidance motors, whose mass was insignificant to EDDE. As a result the WTRL of those spacecraft was 2 or very close to 2, compared to the WTRL of 5 it should have been. Given Eq. 2.3, this produces an RSS of 2.7 for WTRL 2 compared to 0.5 for TRL 5. Given [42], a WTRL of 5 produces a value of 1.3 for f_C, as opposed to 3 for a WTRL of 2. Since EDDE was the only self-contained ADR system, it was dramatically impacted by this error, while the Pareto-optimal
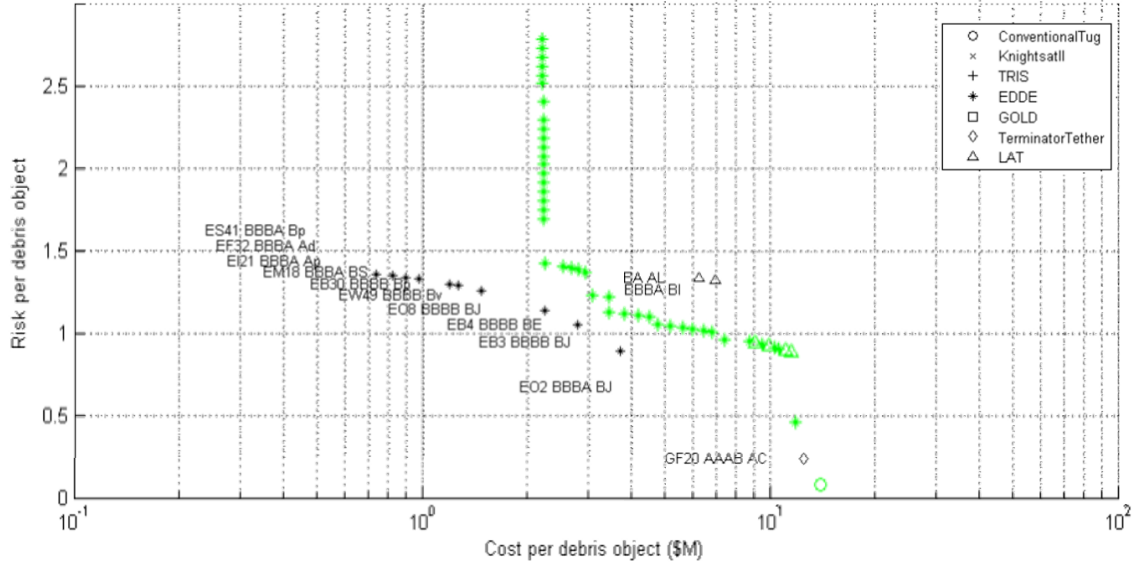
Figure 9.5: Corrected compound Pareto front.

designs utilizing other payloads were not. Fig. 9.5 presents the same data as Fig. 9.3, shifting the self-contained EDDE designs to correct for this error. As can be seen, this brings ORF values for EDDE into line with the corresponding portions of the new Pareto front.

Investigating the lowest risk LAT from both the original and new study, the risk is approximately 1.0 in the GESDA-based results, whereas it was originally 1.3. The number of DOs removed per spacecraft, as well as the respective components of ORF for these two designs is given in Table 9.12. where T_{PO} is the time per object per ADR vehicle. Note this does not necessarily directly result from n_{targs} and the requisite 100 total DOs removed. T_{PO} also takes into account the requirement that 10 DOs be removed per year, and given the average time per DO removed per ADR vehicle, increases the fleet size as necessary.

Table 9.12: Parameter comparison for old and new LEO ADR LAT results.

parameter	original value	GESDA value
m_{tot} (kg)	487	475
T_{PO} (days)	357	662
n_{targs}	14	6
N_F	10	19
$WTRL$	5.0	7.99
R_T	0.90	0.83
R_{TRL}	0.44	0.14

At a glance, the two spacecraft are physically fairly similar. Both have the same payload and very similar m_{tot}. The difference in n_{targs} directly leads to the difference in fleet size N_F required to remove the 100 objects specified for the program. This difference in N_F entirely accounts for the difference in R_T. The difference in R_{TRL} results from a difference in how WTRL is calculated between the old design optimizer and GESDA. Originally, due to the limited knowledge of individual spacecraft components, WTRL was calculated as discussed in section 2.2.3.2. In GESDA, where the individual TRL of each component is tracked, it is possible to calculate WTRL on a component-by-component basis:

$$WTRL = \sum_{spacecraft} \frac{m_{dry,i}}{m_{dry}} TRL_i \qquad (9.12)$$

where $m_{dry,i}$ is the dry mass of component i, TRL_i is the TRL of component i, and m_{dry} is the dry mass of the entire spacecraft. As opposed to in [43] where WTRL was weighted by the cost of each component, it is instead weighted here by component mass, which is used as a rough stand in for cost, since component costs

were not available. As was the case for EDDE, this difference in WTRL entirely accounts for the change in R_{TRL}.

Perhaps the two most striking differences in the Pareto front are the presence of an EDDE-based design in the lower right portion of the front, and the nearly vertical column of low cost EDDE-based designs comprising the leftmost portion of the front. The single "low risk EDDE" design is a self contained EDDE spacecraft that only removes a single debris object. In doing so, it completely eliminates its trajectory risk, but substantially increases program cost, with a separate vehicle now required for each DO. It is likely that a similar design could have been present in the original results, but due to the TRL error for EDDE, would have been dominated by other designs, and therefore not appear on the Pareto front.

All designs in the near vertical column on the far left are EDDE-based, and have $27 \leq n_{targs} \leq 29$. The difference between the designs in this "tail" is the number of collision avoidance motors attached. Based on Eq. 2.1, holding all other variables constant, each addition or removal of a collision avoidance motor causes a constant change in R_T. The addition of the mass of each motor slightly increases the spacecraft mass. As one travels up the tail, removing motors, the mass of the spacecraft decreases accordingly. If the spacecraft is otherwise identical, this will lead to a slight decrease in the cost per DO removed. An exhaustive exploration of the design space would produce similar tails, rising vertically from each Pareto-optimal design for which $R_M > 0$. However, all other tails will be dominated by the tail of lower cost designs, except for the lowest cost design, so they do not appear on the Pareto front.

It is suspected that no such tails appeared in the original LEO ADR design study due to use of single fitness function given by Eq. 2.6. This did produce a single fitness value for the multiple objectives, but likely introduced a bias towards lower risk, producing a more even spread across cost, but not fully capturing the Pareto front. Conversely, a form of NSGA-II [23], which by design favors even spread across the Pareto front, was used for GESDA.

An additional notable change is that the conventional tug is on the Pareto front, taking the approximate place of Terminator Tether from the original study. Though the conventional tug was not on the Pareto front in the original study, it was observed to be close to it. It is likely that the correction of the TRL bug for orbital tugs, discussed above, lowered the risk of the conventional tug, improving its performance. The performance of Terminator Tether is comparable to the conventional tug throughout, with both achieving an ORF of 0.0755, and with Terminator Tether achieving a cost of \$19.7M per DO. It is possible, though considered unlikely with ten trials of each payload, that random chance associated with use of a GA determines which of these two systems dominates the other.

One observation that is clear from Fig. 9.5 is a substantial increase in cost per DO across the Pareto front. Consider again the LATs investigated in Table 9.12. Their cost breakdown is given in Table 9.13. The majority of these costs are fairly comparable, with the exception of the bus development and first unit production costs, and in particular the total production cost. The bus-related costs were approximately 50% higher cost than in the original study. The differences in the bus of the two designs, leading to this discrepancy, will be discussed below. The total

Table 9.13: Cost comparison for old and new LEO ADR LAT results, with all costs in $M.

cost category	original value	GESDA value
ADR system development cost	34.1	38.9
Bus development cost	86.8	128
ADR system first unit cost	10.7	12.6
Bus first unit cost	17.8	28.5
Total production cost	191	451
Launch cost	22.6	22.5
Cost per DO removed	6.2	11.6

production cost is 2.4 times as great than in the original study. Due to the substantial difference in n_{targs} (the difference in T_{PO} also plays a role, but n_{targs} is the dominant factor), nearly double the fleet size is required to remove the requisite 100 DOs.

The difference in cost per DO between the old and new results is even more pronounced for EDDE. Compare the GESDA-based EDDE design in the lower left corner of the Pareto front (the one at the "head" of the vertical tail on the left), and the second EDDE design from the left in the original ADR study. These two are chosen for comparison as they have similar values for n_{targs}. A comparison of their parameters is given in Table 9.14. As can be seen, the risk factors are essentially identical. All parameters in the table are essentially the same, with the exception of T_{PO}. Upon further investigation of the original LEO ADR work, the original value used for the maneuvering performance of EDDE conflicts with the source used for the GESDA-based design study, both from the same author, who is the PI for EDDE. However, the time per DO removed was not an active constraint, as

Table 9.14: Parameter comparison for old and new LEO ADR EDDE results.

parameter	original value	GESDA value
m_{tot} (kg)	85	80
T_{PO} (days)	32	116
n_{targs}	32	29
N_F	4	4
$WTRL$	5	5
R_T	0.96	0.96
R_{TRL}	0.45	0.46

noted by the fact that N_F is the same for both, and therefore this discrepancy is not considered to have a substantial effect on the design space.

Table 9.15 gives the cost breakdown for the same two designs. Note that, unlike for the LAT example above, both EDDE vehicles were assumed totally self-contained in the original study. Therefore, development and production costs were not separated by bus and payload. In the work of this chapter, a lump mass 7/3 of

Table 9.15: Cost comparison for old and new LEO ADR EDDE results, with all costs in \$M.

cost category	original value	GESDA value
ADR system development cost	22.5	22.5
Bus development cost	-	62.8
ADR system first unit cost	7.68	7.68
Bus first unit cost	-	12.1
Total production cost	25	64.1
Launch cost	3	3
Cost per DO removed	0.815	2.25

the mass of the ADR system is added for EDDE (as it is for all non-self spacecraft) to account for unmodeled masses, such as structural mass, communications subsystems,

and attitude control. As a result, there are nonzero bus development and production costs, resulting in the threefold increase in EDDE production costs seen in the new results compared to the original ones. Since, even with this threefold increase, EDDE still comprises the upper left portion of the Pareto front, this discrepancy does not change the relative ordering of results on the Pareto front. Nonetheless, more thought may be warranted on what the proper treatment of EDDE compared to the other designs on the Pareto front. It is in many ways an unconventional spacecraft, and special considerations in the objective functions may be warranted to handle this. However, these considerations must be weighed against the loss of generality, and unintended consequences for introducing a different treatment of ADR systems under consideration.

This concludes the comparison of the LEO ADR vehicles designed here to those from Chap. 2. The remainder of this section provides a comparison of designs from the different "families" on the Pareto front. This is done in the same spirit as, for example, Table 2.8, though the differentiation between families of designs is far less pronounced than in the original study. This is suspected to be due to the use of an NSGA-II derived sorting algorithm, which performs more complete, continuous exploration along the Pareto front than the original fitness function used in Chap. 2. Even so, the designs can still be grouped by payload, with each payload occupying a particular portion of the Pareto front. Table 9.16 provides high-level details on the lowest cost per DO design of each family on the Pareto front. An exception is made for EDDE, where the lowest cost per DO design would be the end of the tail, which has nearly the same cost per DO as the "head" of the tail,

so that design is examined. Specifically, the table provides the objective values for each presented design, along with the mass breakdown of the different subsystems. Masses are given in kg.

Table 9.16: Summary of Pareto-optimal design families.

ADR system	EDDE	LAT	Conventional Tug
Cost per DO removed (\$2014M)	2.25	9.06	14.0
ORF	1.42	0.946	0.0755
Propulsion system mass	4.21	129	143
Propellant mass	-	-	647
Electrical power system mass	-	36	110
Payload mass	80	122	80
Unmodeled subsystems mass	110	163	110
Total spacecraft mass	194	450	1090

The EDDE vehicle considered in Table 9.16 is essentially self-contained, consisting only of itself and 25 collision avoidance motors (and the associated unmodeled subsystems). As such, all maneuvers are conducted by the EDDE payload. The spacecraft is tasked with the removal of 29 DOs, taking place over 9.2 years (a rate of approximately three DOs per year per ADR vehicle). As may be expected, this vehicle uses nonimpulsive maneuvers. As the spacecraft is essentially self-contained, no additional insight specific to this vehicle or about GESDA itself (or any of the EDDE vehicles on the Pareto front) is obtained through GESDA.

The LAT vehicle considered in Table 9.16 is more interesting. This LAT removes a total of eight DOs over the course of the program, at a rate of one DO every 270 days. As with EDDE, the LAT payload performs all maneuvers. The LAT features 20 PVA components. Combining these PVAs, the vehicle has a total

solar array area of 145 m^2, producing a total of 5.8 kW of power. This is far more than the 250 W required to power the spacecraft at any given time. Understanding the nature of this discrepancy requires a brief discussion of the state of the GESDA component libraries.

The PVA component library for this design problem included a number of simulated components. Data was only available for individual solar cells and small arrays, with component suppliers indicating that panels are built to order depending on the requirements at hand. Since GESDA relies on fixed components to operate, a workaround was implemented to add "macrocomponents" that were the equivalent of 3, 10, 30, 100, 300, and 1000 copies of the XTJ 5965 solar panel by Spectrolab, combined into a single panel. The goal of adding these components of varying sizes is to allow GESDA to build up large enough components to achieve feasibility in a small number of generations.

Of the 58.4 kW of power produced by the spacecraft while in sunlight, 48 kW resulted from two of the largest of these macrocomponents, the "1000x XTJ 5965," and an additional 9.6 kW resulted from four of the "100x XTJ 5965" macrocomponents. Each of the 1000x XTJ 5965 panels had a mass of approximately 5 kg, and each 100x XTJ 5965 panel had a mass of approximately 0.5 kg. This leaves 800 W of electrical power coming from the remaining solar arrays. Assuming perfectly efficient batteries, 500 W is required from the PVAs when in sunlight to power the spacecraft. Therefore, all of these panels are unnecessary for feasibility. However, their combined mass is only 12 kg, comprising less than 3% of the total spacecraft mass. Removing these components from the design and re-running the objective

functions, one finds that their removal has only reduced the cost per DO removed from \$9.06M to \$8.96M, a change of approximately 1.1%. This is definitely a real effect, but the change in objective performance of the overall design is not significant. Additionally, it does not affect the relative performance of the different designs present on the Pareto front.

Throughout analysis of the GESDA results, multiple cases of such "vestigial components" (to borrow a term from biological evolution) were present. That is, additional components that may have been required for feasibility or had a significant effect on performance of some ancestor of the final design. Through the GA, these components were inherited, but are not required for the feasibility of performance of final design itself. They do not adversely affect the overall performance of the final design, so they persist. Additional generations of the GA may eventually lead to their removal. However, if the design space has converged, this is not necessarily computationally efficient. If the design space has been sufficiently explored, such "trimming" may not be necessary. Perhaps a better option is, at this point, to transfer some set of Pareto-optimal designs to a human designer or concurrent design team, who would perform any final trimming before or as part of their concurrent design campaign.

A single battery is present in this LAT design, drawn from the Soil Moisture Active Passive (SMAP) spacecraft. Four thrusters are present, all assumed vestigial, since no propellant tanks are present, and all maneuvers, based on the L1 genome, are performed by the LAT payload. Thirteen collision avoidance motors are present. Removing the vestigial thrusters and PVAs lowers the mass of the spacecraft to 311

kg and lowers the cost per DO removed to \$7.9M. Interestingly, it does slightly increase the ORF to 1.01. This is a result of removing components whose TRL was actually above the WTRL of the spacecraft. Since, by Eq. 9.12, WTRL is weighted by mass, their removal lowers the WTRL of the spacecraft from 8 to 7, leading to this slight increase in risk. Interestingly, this slight increase in risk means that the design is now dominated by an EDDE-based design on the Pareto front, though the objective performance of this design is still extremely close to the Pareto front.

Finally, we arrive at the conventional tug on the Pareto front. It only removes four DOs per vehicle, limited by the propellant it must carry to reach each DO. Each ADR vehicle performs impulsive maneuvers, and as a result removes a DO approximately once every three days, deorbiting itself with the last DO at the end of a two week mission. As was the case in the original work of Chap. 2, the impulsive conventional tug minimized R_T, maneuvering each DO directly from their original orbit onto a targeted reentry trajectory. Due to the large amount of propellant required for impulsive thrusters, the spacecraft mass is large compared to the other designs on the Pareto front.

Investigating the electrical power subsystem for the conventional tug, a similar situation appears to that of the LAT, with PVAs producing a total of 29.0 kW of power. Indeed, investigation of the component structure reveals that the majority of the electrical power (23.9 kW) comes from a single vestigial 1000x XTJ 5965. The design also contains a number of vestigial thrusters. An investigation of the fill levels of onboard propellant tanks reveals that only a single R-4D thruster is used to perform all maneuvers. The design features two batteries, with a total capacity

of 756 W-h (one a 504 W-h battery, and one a 252 W-h battery). With an orbital night duration of approximately 50 minutes, and a power draw of 131 W during orbit night, this leads to a 14% depth of discharge. Therefore, both batteries are required to meet spacecraft requirements.

Removing the vestigial thrusters, propellant tanks, and PVAs, a slightly lighter spacecraft at 1015 kg is achieved. The cost per DO has decreased accordingly, to $13.8M, an approximately 1.5% decrease. The ORF of the spacecraft is unchanged. Again we see that the removal of vestigial components causes a marginal improvement, but does not significantly affect the objective performance of the design.

9.5 Summary

In this chapter we have demonstrated the use of GESDA for active spacecraft trade space exploration. The chapter has readdressed the design problem originally addressed in Chap. 2, active debris removal in Low Earth Orbit. In doing so, it provides an additional level of detail over the original study, simulating the ADR vehicle designs to a component level. The results of this chapter, while producing different numerical results, have essentially confirmed the conclusions of the primary trade study performed in Chap. 2, for the nominal scenario of that chapter. While the overall conclusions are the same, there are some notable differences. The highest cost per DO removed, lowest risk designs on the Pareto front have changed, with the single orbital tender vehicle being traded for a impulsive conventional tug.

The overall conclusions are very similar to those of Chap. 2. This agreement acts to verify the performance of GESDA for trade space exploration with active spacecraft missions. One can see that propellantless tugs dominate the Pareto front, and orbital tender vehicles are not present. The performance of propellantless tugs is, as before, due to the decoupling of their mass from the number of DOs they remove (though, to maintain the requisite removal *rate*, there is still an implicit relation between the two). Their resulting ability to deorbit a relatively large number of DOs with a single vehicle drives down the cost per DO. As before, this does carry the drawback of higher risk. The propellantless tugs considered have relatively limited maneuvering ability, so they must spiral down to a disposal orbit, detach the DO, and then spiral back up to the next DO. The disposal orbit altitude is limited to one where their limited maneuvering ability is still able to overcome atmospheric drag. As a result, the reentry of the DOs from this disposal orbit is guaranteed in a relatively short timeframe, but still long enough that the impact location is unknown.

As was originally the case, no electric propulsion systems are present in any of the designs on the Pareto front (not counting the payloads of the LAT and EDDE, which could be construed as electric propulsion systems). Investigation of dominated designs in the original study which did use electric propulsion suggests that the time per DO removed using these systems is too great to be feasible with a reasonable fleet size.

The key difference from the results of Chap. 2 is that conventional tugs have replaced Terminator Tether on the Pareto front. During the original LEO ADR

study, Terminator Tether-based designs and impulsive conventional tugs continually traded places on the Pareto front, each dominating the other in some cases. Their performance was so similar that, as indicated in Chap. 2, both were considered worthy of further study. The impulsive conventional tugs in particular are the minimum risk system on the Pareto front, but are only able to deorbit a small number of DOs per vehicle before required propellant makes their mass prohibitive. The one considered here, for example, deorbits after only removing 4 DOs. This small n_{targs} for conventional tugs makes one consider if they may be able to perform at a much reduced cost per DO removed if they were somehow reusable, able to conduct multiple 4 DO missions. Potential options include reusable spacecraft somehow capable of controlled reentry and landing, or the use of orbital fuel depots to allow the conventional tug to refuel between DOs.

Chapter 10:   Conclusions and Final Thoughts for Derived Works

At this point, this work, at least in the context of a PhD study, is considered complete. The orbital debris problem has been addressed with two different methods, producing similar results for the lowest risk and lowest cost per DO removed options. The CR model, applicable to a wide class of complex systems, has been developed. An architecture has been constructed around it, allowing automated optimization routines to understand the general spacecraft design problem from a high-level systems aspect. The framework has been applied to two spacecraft design problems, and has produced results within the range of flown vehicles and other studies. The remainder of this chapter summarizes the conclusions of the entire work, and provides some insight from the work performed to guide anyone interested in conducting follow-on work.

10.1   Summary and Conclusions

This work initially started as an attempt to provide an objective comparison of proposed systems for removing large, intact debris objects from low Earth orbit (LEO). Several payloads have been proposed, and the goal was to develop a simulated scenario that evaluates the performance of each. A framework was developed

that could take the mass, power, and maneuvering requirements properties of any such active debris removal (ADR) payloads, design spacecraft around them, and determine the risk and cost per object removed of each. The final results, which would later be largely confirmed by the final form of this work, were fairly clear. There is a clear financial advantage to the use of "propellantless" tugs, which need not carry a set mass onboard for each debris object (DO) removed. However, doing so, at least with currently available technology, does carry a substantially increased risk. As a result of this risk, a low risk, more conventional spacecraft design always accompanies these designs in the trade space.

Two propellantless systems were evaluated. The first was an electrodynamic tether propelled orbital tug (EDDE), which captures DOs in a net and maneuvers through interactions with Earth's magnetic field. The second was a laser ablation tug (LAT), which captures DOs with a robotic arm, and ablates material from the DO to provide thrust, using the DO itself as propellant. In doing so, the LAT is not propellantless in the truest sense of the word. In fact, in the case of EDDE, the Earth itself could be considered the propellant, making neither system propellantless. The key aspect is that these designs need not carry all propellant mass for their mission from one DO to the next. Investigations into other concepts which follow this same principle with more conventional spacecraft are suggested in the recommended future work below.

The elevated risk of the propellantless systems stems from two sources. One is their low technological maturity, calling into question when and if they would be ready to enter service as the debris environment continues to worsen. The other risk

is associated with the fact that both propellantless systems considered are of such low thrust that they cannot place DOs tugged onto a targeted reentry trajectory. They must, with DO in tow, spiral down to a disposal orbit low enough that the DOs will reenter in a relatively short timeframe, but high enough that, after releasing the DO, the vehicle itself is capable of escaping the thin atmosphere to capture the next DO.

The lower risk system appearing on the Pareto front was always a conventional orbital tug, or a low risk orbital tender vehicle. The conventional orbital tug consists of a robotic arm and conventional impulsive propulsion system for moving the DO in orbit. It can be assembled entirely out of currently flight proven components, with the exception of hardware for grappling an uncooperative DO, and associated sensor systems. Both of these technologies are on track for flight validation in the immediate future [79–81]. The other low risk system appearing on the Pareto front is an orbital tender vehicle delivering Terminator Tether [31] to a number of DOs. Terminator Tether was a package that could be attached to a DO, and could extend or retract a drag tether to lower the DO's orbit. Due to its ability to retract, it was capable of targeted reentry, eliminating the biggest source of risk of the propellantless tugs.

The key takeaway is that, from an engineering standpoint, active debris removal in LEO is viable with current technologies. Depending on the level of risk that society deems acceptable, this debris removal can be accomplished with current technologies for approximately $10M, and with technologies under active development for single millions of dollars. The work detailed in this section was originally

251

conducted from 2013 to 2016. Trends in the space industry since that time have intensified the need for this sort of debris removal program. At the same time, many of these same trends (the move towards smallsats and large constellations of cubesats) will likely help facilitate such a program.

The work of Chapter 2, as well as associated small bodies mission and robotic satellite servicing work being conducted simultaneously by the author, led to the idea of creating a generalized framework that, with little to no modification, could perform systems-level analysis of a wide range of space missions. This concept motivated the remainder of the dissertation. Chapters 3 through 6 presented the Component-Resource (CR) model and associated Vehicle Encoding Genetic Algorithm (VEGA). The CR model presents a uniform method of analyzing any complex system that comprises discrete components and resources flowing among them. It facilitates feasibility analysis of such a system in a uniform way, based on the resource flows. VEGA then performs optimization of such systems, using the CR model to evaluate constraints in a uniform way, facilitating optimization of a wide range of complex systems.

Chapter 7 presented a VEGA-based Generalized Evolutionary Spacecraft Design Architecture (GESDA) to perform spacecraft design optimization. GESDA maintains the driving philosophy of generality, while acknowledging that certain design problem-specific considerations are unavoidable. It attempts to present a general framework that is at least capable of addressing a wide range of *spacecraft* design problems. In doing so it separated spacecraft into two general categories; passive and active spacecraft.

Passive spacecraft are assumed to be on a fixed orbit trajectory, and as such are evaluated in a fixed simulation. They do not manipulate or physically interact with their environment (that is, the environment is unaffected by what the spacecraft is doing). This covers any mission types that could be analyzed with the GINA model [22]. Active spacecraft can maneuver and manipulate portions of their environment. As a result, they introduce additional complexity into the simulation, requiring a lower fidelity simulation to maintain computational feasibility.

Finally, Chapters 8 and 9 presented active and passive use cases of GESDA, respectively. Chapter 8 sought to evaluate designs for an Earth observing cubesat. It did so by developing spacecraft to support the PlanetScope 2 (PS2) payload carried by the Dove spacecraft produced by Planet Labs. In doing so it explored a relevant trade space to the Dove spacecraft; the trade between spacecraft mass, assumed to correlate with program cost, and imaging data returned. The results were a Pareto front containing designs which came relatively close to the performance of the Dove spacecraft (around 120% of the mass for the same data returned). Given the step function-like nature of the Pareto front, it is likely that there are other trade spaces of interest to this mission.

Some difference is acknowledged between the simulated mission profile implemented in Chapter 8 and the actual Dove 3 mission profile. This is partially due to simplifying assumptions made to streamline the simulation, and partially due to the limited data available on the Dove mission design. Nonetheless, the results of Chapter 8, which did come reasonably close to the actual Dove spacecraft design, are considered informative in selecting a spacecraft design for further evaluation.

Interestingly, the "agile aerospace" design philosophy behind the Dove spacecraft is simultaneously very similar to and at odds with the design philosophy assumed by this work. It rejects the aerospace industry convention of detailed concurrent design of monolithic, high reliability, risk averse spacecraft comprising all or nearly all flight proven, space grade hardware. Instead, Planet operates with a large quantity of small, expendable spacecraft with terrestrial commercial off-the-shelf (COTS) components. This facilitates design iteration, incremental improvement, and experimentation in flight. They launch tens of Dove spacecraft at a time, with a total on-orbit constellation of hundreds at any given time. This paradigm may seem at odds with the structured concurrent design that the work of this dissertation is intended to supplement.

At the same time, Planet's philosophy can be viewed as something resembling a population-based metaheuristic (which is at the heart of GESDA's optimization) with a high level of elitism, manifested in reality. Planet launches an entire "population" of Dove spacecraft at a time. Most are proven designs from the previous generations. However, a small subset of the population contains perturbations in their design. All are evaluated in the same objective space, with their relative performance informing the design of the next generation.

Finally, Chapter 9 provided a validation of the active satellite design capabilities of GESDA, revisiting the active debris removal design problem of Chapter 2. The trends found strongly resembled those of Chapter 2, with the few discrepancies discussed in the chapter. In most cases, these discrepancies resulted from the greater level of detail included in the GESDA-based designs, and general simulation

improvements resulting from the structure of GESDA's general simulation environment. An effort was made to replicate the assumptions of the original study over increased fidelity and accuracy, in order to facilitate as accurate of a validation as possible. This was balanced against a desire to not modify the generalized aspects of GESDA.

In general, the results obtained with GESDA were similar to the designs obtained from the points of comparison (i.e., the actual Dove 3 design details, and the work of Chapter 2). Chapters 8 and 9 are therefore considered to validate GESDA as a method of performing the spacecraft design for which it is intended. One interesting note is that nearly all designs obtained by GESDA did contain "vestigial" components. That is, components which do not contribute to the overall performance of the design, but do not significantly diminish it. As a result, they are inherited from previous generations where they may have served an important purpose. Performance of the spacecraft will likely be improved by "trimming" and further optimization of designs provided by GESDA.

This illustrates an important point. GESDA should not be used alone for conducting concurrent spacecraft design. It is is a powerful tool for identifying trends and gaining insight in a trade space of interest, and suggesting point designs that may serve as the starting point for a concurrent design campaign. However, the results of a GESDA run must undergo verification, which would be accomplished by existing concurrent design teams. Additionally, there is likely the potential for further optimization through application of human intuition and prior experience,

as well as general tweaking to address certain behaviors of the framework, such as the presence of vestigial components.

The work conducted up to this point is considered a validation of the general architecture of the CR model and GESDA. However, practical improvements are required for GESDA to be a useful tool to concurrent design groups. Runtime of the implemented framework is on the order of days, comparable to a concurrent design campaign. With performance improvements outlined in the next section, the same analysis should be possible on the order of hours. Access to proprietary cost models and other objective functions, as well as component libraries, would allow more accurate results from GESDA.

As may be evident, these performance improvements are important to make the framework useful, but are not fundamentally novel or practical in the context of a PhD study. Therefore, it seems logical to conclude the present work here, with an outline of further development needed to bring GESDA's use to fruition. Once the outlined improvements are realized, GESDA has the potential to become a vital tool for groups conducting concurrent spacecraft design.

10.2   Recommended Future Work

While the work of this dissertation is considered complete, there are clearly several new topics stemming from it that warrant further study. They have not been pursued as part of this work either because they are beyond the scope of the work, or

because practical considerations and the availability of information has made their pursuit infeasible in the current context.

10.2.1   Future Investigations Regarding Active Debris Removal

As stated, it is the opinion of the author that this work has confirmed the feasibility of active debris removal in LEO with technologies currently existing or well into development. In fact, one could consider the deorbit of the space station Mir in 2001 to be the first active debris removal operation, with a targeted reentry conducted by a "conventional" tug [82]. What task remains, from an engineering standpoint, is to confirm the economic viability of a debris removal program. With some level of technological investment, propellantless tugs may lead to costs per DO removed in the single digits millions of dollars.

With conventional tugs using the concept of operations proposed in Chapter 2, a cost per DO removed of ∼$14M could be achieved. As was mentioned briefly in Chapter 9, a conventional tug could in principle make use of on-orbit refueling to gain the primary advantage of propellantless tugs - removal of the need to carry mass for the removal of any but the current target DO. This concept would use an orbital fuel depot, which the ADR vehicle would visit between removal of each DO. Doing so would free the tug to only carry the propellant required to reach a single DO, place it on a disposal trajectory, and then transit back to the fuel depot. Such a mission carries its own complications, with many technologies for orbital fuel depots yet to be proven.

Additional attention should be paid to improvements to the concept of operations for orbital tender vehicles as well. Specifically, investigation into use of nodal regression for plane change, and the introduction of "propellantless" maneuvering technologies used by the orbital tugs evaluated. Finally, it may be worth repeating the study described in chapters 2 and 9 with additional candidate populations of DOs to determine if there is any sensitivity in the trends found connected to the difference in the orbits of the debris clusters identified by Liou [9].

10.2.2 Improvements to Component Libraries

One of the larger (and certainly more time consuming) challenges of this work was obtaining spacecraft component data to populate component libraries. Much of this data is proprietary or export controlled, making organizations hesitant to provide it at all, and especially for research intended to be published. Therefore, all components considered in the design problems addressed here are those obtainable from public supplier websites, as well as NASA databases and publications. For GESDA to be useful to existing concurrent design teams, its component libraries must contain at least the same breadth of components as those teams' libraries.

Conversely, it became evident towards the end of this work - particularly with the introduction of macrocomponents and inspection of resulting design - that an exhaustive listing of real components is not necessary. What is important is that the libraries are representative of available components. Therefore, a future iteration of the GESDA component libraries need not necessarily contain a full list of existing

components. An item of future work is to identify a minimum subset of components of each class that constitute a fully representative sample of available components.

10.2.3   Enhanced Component-Level Models

The present work has been conducted with fairly simplistic component-level models. The goal of this work is not to develop a high-fidelity component simulation. It is to validate the system-level model and spacecraft design framework. It is considered to have done so, even with the simplistic component-level models, given the results of Chapters 8 and 9. However, it is acknowledged that actual concurrent design teams will likely desire some higher fidelity component-level models and simulation. Many such models already exist, used by the discipline engineers on concurrent design teams. Therefore, an item of future work by any concurrent design team implementing a framework based on GESDA is to integrate component and subsystem level simulations as they find necessary to provide the desired level of fidelity.

10.2.4   Extended Simulation for Different Mission Types

The passive and active spacecraft schemes, as presented in the present work, are capable of addressing a wide range of space missions in Earth orbit. However, work remains to truly address any space mission, with varying levels of work required for varying mission types. Robotic satellite servicing is, in principal, fairly close to active debris removal, and so the work needed to address it should be minimal.

Different operating modes would likely be required to address the differing payload requirements over the many mission phases. This functionality could be captured in the framework as defined by simply modifying the payload active state, from a binary to integer value that can specify different modes for each payload.

The framework as written should be able to handle interplanetary missions with little to no change. If an interplanetary mission under consideration is an active mission, consideration would have to be given to how to procedurally generate the trajectory. In all other aspects, no changes to the framework are anticipated to handle interplanetary missions. In principle, the framework could be extended to handle crewed space missions as well. Presumably, any habitat could be considered a very specialized payload, and the same sort of analysis could be performed.

10.2.5 Additional Capabilities and Performance Improvements for GESDA

Several performance improvements and additional capabilities to the GESDA core are desirable, but are beyond the scope of validation of this work. First and foremost is the inclusion of robustness in the environment simulation. This was not included in the present work partially due to the nontrivial task of defining reasonable probability distributions for any varied parameters, and partially due to concerns over increased computational time. To implement robustness, environmental parameters could be varied based on some probability distribution for each. Additionally, the potential for failure of individual components at each timestep

could be considered, as a function of mean time between failures defined for each component. Unfortunately, these data were not available from the repositories used. If this sort of robustness is implemented, those components currently viewed as vestigial may actually prove advantageous, incorporating redundancy into a design, making it more robust.

A major limiting factor to the current implementation of the framework is the simulation runtime required. That runtime is currently on the order of days. Focus throughout this work was given to prototyping a proof of concept version of GESDA for validation purposes. Computational improvements are therefore necessary to make use of GESDA practical. The entire framework has been written in MATLAB due to the author's familiarity with the MATLAB environment, and due to MATLAB's wealth of built in functionality and handling of overhead, allowing a more complete focus on prototyping the novel aspects of the framework. The component level simulations, which take the vast majority of runtime, should be re-coded in a faster language, such as C. Additionally, the population-based nature of VEGA lends itself naturally to parallelization, which has not been utilized to date. Parallelizing, even on a standard desktop, would likely lead to an order of magnitude decrease in runtime. Far greater gains are possible if executed on a larger cluster.

In addition to enhancing the viability of the current framework, these performance improvements can extend the quality of the results found by GESDA. Greatly reduced computation time allow GESDA to determine the robustness of designs obtained. This could be accomplished through multiple simulations for each individual in the population. For example, for any feasible designs in the baseline

scenario in a given generation, a Monte Carlo analysis could be performed, varying the environment properties within each individual simulation based on some probability distribution function of potential values. The robustness of a design could then be quantified by the portion of these runs for which it remains feasible.

Appendix A: Original LEO ADR Genome

This appendix details the genome encoding for the original LEO ADR vehicle optimization performed in Chap. 2. It provides an in-depth description of the potential values for each input parameter. IP_1 designates the ADR system used as the payload for the ADR vehicle. The ADR system provides the mass, power, and trajectory requirements that the spacecraft must support to complete its mission. All options for IP_1 are provided in Table A.1. Options C, E, and H designate orbital tugs, where the mass and power requirement on the spacecraft is based on a single ADR system. Options B, D, F, and G designate DPs, where the total mass of the ADR system is assumed to be the specified mass multiplied by the number of DOs being removed by a single ADR vehicle. The total ADR mass then decreases every time a DP is attached to a DO.

Table A.1: Main thrusters considered.

IP_1 Value	ADR system	Mass (kg)	Power (W)	Tug or DP?
B	KSII	74	10	DP
C	Conventional Tug	0	0	Tug
D	TRIS	106	1	DP
E	EDDE	80	0	Tug
F	GOLD	70	0	DP
G	Terminator Tether	28	0	DP
H	LAT	42	250	Tug

IP_2 specifies the thruster used as the main propulsion system by the ADR vehicle. A listing of all thrusters considered is provided below in Table A.2. Bipropellant thrusters are assumed to consume N_2H_4 and N_2O_4 as fuel. Monopropellant thrusters, the resistojet, and arcjets considered use N_2H_4 as fuel. The resistojet considered has an I_{sp} of 300s, consumes 900 W of electrical power while running, produces 0.8145 N of thrust, uses N_2H_4 as propellant, and has a mass of 0.9 kg. The PPT considered uses Teflon as propellant, and all Ion engines and Hall thrusters considered use Xenon.

IP_3 designates the number of DOs to be removed by a single ADR vehicle. This can range anywhere from 1, designating removal of a single DO, to 55, designating removal of all DOs in the simulated debris belt considered. Some of the ADR systems considered are capable of propelling the spacecraft independent of the main thruster.

IP_4, IP_5, and IP_6 designate whether a given maneuver type is performed by the spacecraft's ADR system, or by the main thruster. IP_4 selects which system performs maneuvers to raise the ADR vehicles orbit. IP_5 selects which system performs plane change maneuvers. IP_6 selects which system performs orbit lowering maneuvers, performed by tugs with a DO attached. IP_4 is only used once by tender vehicles, and IP_6 is unused, since these vehicles do not normally perform these maneuver types. For each of these input parameters, a value of A indicates the maneuver is performed by the ADR system, and B indicates the maneuver is performed by the dedicated propulsion system.

IP_7 indicates whether a maneuver is considered impulsive or low thrust. Impulsive maneuvers are restricted to 10% of the spacecraft's orbital period, but require less ΔV than low thrust maneuvers. For most chemical thrusters, maneuvers are naturally less than 10% of the spacecraft's orbital period, so impulsive maneuvers are naturally superior. For most electrical thrusters, maneuver times are usually substantially longer than 10% or the spacecraft's orbital period. As a result, the necessary ΔV must be broken up into multiple maneuvers, increasing the total maneuver time by a factor of ten.

IP_8 determines whether or not the ADR vehicle takes actions to hold short of active spacecraft. Much like performing non-impulsive maneuvers, this option comes with the tradeoff of time spent removing each DO. For orbital tugs, this action involves holding position above a high priority orbit for some number of days before crossing it. This allows for safe separation between the ADR spacecraft and other active spacecraft by waiting for favorable phasing.

IP_9 specifies some number of collision avoidance motors to be added to the ADR vehicle, with the letter value specifying the number of motors. For example, A designates 0 motors, B designates 1 motor, and so on. The motors are sized so that they each provide sufficient ΔV to lower the ADR vehicles periapsis by 1 km, while attached to a DO. These motors allow the ADR vehicle to avoid a short-notice collision with an active spacecraft.

Table A.2: IP_1 Value Key.

IP2 Value	Thruster Name	Thruster Type
B	AJ10	Bipropellant
C	R-6D	Bipropellant
D	R-1E	Bipropellant
E	R-4D	Bipropellant
F	HiPAT	Bipropellant
G	R-42	Bipropellant
H	R-40B	Bipropellant
I	MR103D	Monopropellant
J	MR103G	Monopropellant
K	MR103M	Monopropellant
L	MR104	Monopropellant
M	MR111C	Monopropellant
N	MR-106E	Monopropellant
O	MR-80B	Monopropellant
P	Resistojet	Resistojet
Q	MR-510	Arcjet
R	MR-509	Arcjet
S	PRS-101	PPT
T	BPT-4000-1	Hall Effect Thruster
U	BPT-4000-2	Hall Effect Thruster
V	BPT-4000-3	Hall Effect Thruster
W	BPT-4000-4	Hall Effect Thruster
X	BPT-4000-5	Hall Effect Thruster
Y	BPT-4000-6	Hall Effect Thruster
Z	HET	Hall Effect Thruster
a	NEXT	Ion Engine
b	NSTAR	Ion Engine
c	Dawn Thruster	Ion Engine
d	XIPS-25	Ion Engine
e	T5	Ion Engine
f-i	-	No DPS

Appendix B: Table Design Example Component Libraries

This appendix lists all components, by class, that comprised the component libraries for the worked example presented in Chap. 5.

B.1   Payload

Only a single payload component was included in this design problem. Its only property was its mass, which was 100 kg.

B.2   Surfaces

The component properties for all surfaces considered in Chap. 5 are listed in Table B.1. Surface properties were drawn from the Ikea Table Top Catalog [83].

Table B.1: Real surface properties.

ID	model number	l (m)	w (m)	t (m)	m (kg)	L_{max} (N)
1	002.511.35	1	0.6	0.034	5.92	500
2	002.513.43	1.2	0.6	0.034	6.4	500
3	102.513.52	1.5	0.75	0.034	9.6	500
4	501.067.73	1.55	0.75	0.03	26.4	500
5	202.406.26	1.2	0.6	0.05	11	500

B.3 Real Supports

The component properties for all real supports considered in Chap. 5 are listed in Table B.2. Properties were drawn from the McMaster-Carr catalog of 80/20 beams and solid 6060 Aluminum rods.

Table B.2: Real support properties.

ID	name	I (m^4)	E (Pa)	λ (kg/m)
1	8020-30-6060	3.66E-07	7.03E+10	2.57
2	8020-30-3060	5.55E-08	7.03E+10	1.64
3	8020-40-4040	1.38E-07	7.03E+10	2.36
4	8020-25-2525	1.77E-08	7.03E+10	0.74
5	8020-20-4040	7.84E-08	7.03E+10	1.67
6	6060 Rod-15mm	7.95E-08	7.00E+10	0.47
7	6060 Rod-30mm	1.27E-06	7.00E+10	1.91

B.4 Real Supports

The full set of properties for notional support are computed as a function of material parameters, specified in Table B.3, and level 3 genes, as specified in section 5.4.3.2.

Table B.3: Notional support material properties.

material	E (Pa)	ρ (kg/m^3)
2024 Aluminum	7.30E+10	2780
4130 Steel	2.05E+11	7850
6061 Aluminum	6.90E+10	2700
Cast Iron – Ductile	1.65E+11	7300
Cast Iron – Gray	1.00E+08	7200
Stainless Steel	2.00E+11	7950
Wood	1.10E+10	750

Appendix C: GESDA Component Libraries

This appendix lists all components, by class, that comprised the component libraries for the implementation of GESDA presented in this dissertation, and used to produce the results of Chap. 8 and Chap. 9. Payloads are specific to each design problem, and are fully detailed in their respective chapters, so they are omitted here. For components with a known flight heritage, a current or previous mission on which the component was used is prepended to the component name for reference. Unless otherwise noted, all components are drawn from the NASA SPOON database.

C.1 Data Recorders

The component properties for all data recorders considered in GESDA are listed in Table C.1. Where no read or write rate is specified, the rate in question is assumed infinite. That is, it is never limited by the component, only by the net data flows of the system. In some cases, for the current GESDA implementation, some complete onboard computers in SPOON whose capabilities include storing science data were listed here as data recorders.

Table C.1: Data Recorder Properties.

name	mass (kg)	operating power (W)	data capacity (bits)	read rate (bps)	write rate (bps)	TRL
TacSat3 AiTech S990	3.00E-01	4	8.00E+09	2.00E+08	2.00E+08	9
LADEE Moog BRE CASI	0.28	4.5	5.12E+08			9
TESS FMC Gen3	0.68	5	1.54E+12	5.80E+08	6.15E+08	9
ISIS iOBC	0.076	0.4	2.56E+11	2.40E+12	2.40E+12	9
SpaceMicro FlashSSB	0.15	3.5	1.02E+12			9
Xiphos Q6	0.017	1	32000000000	2.40E+12	2.40E+12	7
Xiphos Q7	0.024	1	2.56E+11	2.40E+12	2.40E+12	9
CASSIOPE Honeywell DataStorageUnit	12	56	1.00E+12	3.50E+08	4.00E+08	6
SwRI Nextgen Maxwell750	7.5	39	7.68E+11	2.00E+08	8.00E+07	6
LADEE MOOG BRE MOAB	0.35	6	6.14E+09	5.00E+07	5.00E+07	9
MDA CDH	11	38	1.60E+10	2.00E+08	2.00E+08	9
NigeriaSat2 SSTL HSDR	1	15	1.28E+11	5.00E+09	5.00E+09	9
SpaceDynamics PEARL	0.35	2	9.60E+10			7
SWRI PPC Integrated Avionics	0.5	9	1.60E+10			8
AITech S950	0.45	1.5	5.12E+11	1.04E+09	1.04E+09	8
Genesat Atmel AT45DB161D	0.0002275	0.0252	1.60E+07			9
SDL MODAS	3	20	8.00E+09	2.00E+08	2.00E+08	7
SwRI SC9 VME11	10	36	1.60E+10	3.00E+08	3.00E+08	8
WISE FMC Gen2	0.77	6		5.80E+08	6.15E+08	9

C.2   RF Modules

For RF modules, there is a separate component library for each subcomponent class. Each are listed here in their respective subsections.

C.2.1   Traveling Wave Tube Amplifiers (TWTAs)

All TWTAs used in this work are listed in Table C.2. Properties listed in include both the TWTA itself and the associated electrical power conditioner. As modeled, TWTAs do not consider warmup. They are either fully off or fully on in RF transmit mode. For TWTAs with a range of operating powers, separate versions of the component operating at maximum and minimum output power were defined.

Table C.2: TWTA Properties.

name	mass (kg)	output power (W)	band	minimum frequency (Hz)	maximum frequency (Hz)	input power (W)	efficiency	TRL
L3 83200H Lband Max	4.15	250	L	1.00E+09	2.00E+09	3.63E+02	6.89E-01	5
L3 83200H Lband Min	4.15	150	L	1.00E+09	2.00E+09	2.27E+02	6.89E-01	5
L3 83200H Lband Max Dual	7.65	500	L	1.00E+09	2.00E+09	7.26E+02	6.89E-01	5
L3 83200H Lband Min Dual	7.65	300	L	1.00E+09	2.00E+09	4.54E+02	6.89E-01	5
L3 8412HR Sband Max	2.45	140	S	2.30E+09	2.80E+09	2.17E+02	6.45E-01	9
L3 8412HR Sband Min	2.45	90	S	2.30E+09	2.80E+09	1.40E+02	6.45E-01	9
L3 8412HR Sband Max Dual	4.25	280	S	2.30E+09	2.80E+09	4.34E+02	6.45E-01	9
L3 8412HR Sband Min Dual	4.25	180	S	2.30E+09	2.80E+09	2.79E+02	6.45E-01	9
L3 84250HR Sband Max	3.45	300	S	2.30E+09	2.80E+09	4.05E+02	7.40E-01	9
L3 84250HR Sband Min	3.45	200	S	2.30E+09	2.80E+09	2.70E+02	7.40E-01	9
L3 84250HR Sband Max Dual	6.25	600	S	2.30E+09	2.80E+09	8.11E+02	7.40E-01	9
L3 84250HR Sband Min Dual	6.25	400	S	2.30E+09	2.80E+09	5.41E+02	7.40E-01	9
L3 8555HR Cband Max	2.27	120	C	3.40E+09	4.20E+09	1.76E+02	6.80E-01	9
L3 8555HR Cband Min	2.27	20	C	3.40E+09	4.20E+09	2.94E+01	6.80E-01	9
L3 8555HR Cband Max Dual	3.89	240	C	3.40E+09	4.20E+09	3.53E+02	6.80E-01	9
L3 8555HR Cband Min Dual	3.89	40	C	3.40E+09	4.20E+09	5.88E+01	6.80E-01	9
L3 86160HR Xband Max	2.55	165	X	7.00E+09	9.00E+09	2.70E+02	6.10E-01	9
L3 86160HR Xband Min	2.55	25	X	7.00E+09	9.00E+09	4.10E+01	6.10E-01	9
L3 86160HR Xband Max Dual	4.45	330	X	7.00E+09	9.00E+09	5.41E+02	6.10E-01	9
L3 86160HR Xband Min Dual	4.45	50	X	7.00E+09	9.00E+09	8.20E+01	6.10E-01	9
L3 9100HR Kband Max	2.195	130	K	1.70E+10	2.20E+10	1.97E+02	6.60E-01	9
L3 9100HR Kband Min	2.195	30	K	1.70E+10	2.20E+10	4.55E+01	6.60E-01	9

name	mass (kg)	output power (W)	band	minimum frequency (Hz)	maximum frequency (Hz)	input power (W)	efficiency	TRL
L3 9100HR Kband Max Dual	3.74	260	K	1.70E+10	2.20E+10	3.94E+02	6.60E-01	9
L3 9100HR Kband Min Dual	3.74	60	K	1.70E+10	2.20E+10	9.09E+01	6.60E-01	9
L3 999H Kband Max	2.695	200	Ka	2.20E+10	4.00E+10	3.64E+02	5.50E-01	9
L3 999H Kaband Min	2.695	20	Ka	2.20E+10	4.00E+10	3.64E+01	5.50E-01	9
L3 999H Kaband Max Dual	4.74	400	Ka	2.20E+10	4.00E+10	7.27E+02	5.50E-01	9
L3 999H Kaband Min Dual	4.74	40	Ka	2.20E+10	4.00E+10	7.27E+01	5.50E-01	9

C.2.2 Solid State Amplifiers

All TWTAs used in this work are listed in Table C.3. For any amplifiers for which no frequency range was specified, it is assumed that their frequency range is the entire range of their operational bands. For any components without a maximum data rate specified, their data rate was assumed unlimited (by the component itself).

Table C.3: Solid State Amplifier Properties.

name	mass (kg)	output power (W)	band	minimum frequency (Hz)	maximum frequency (Hz)	input power (W)	maximum bitrate (bps)	TRL
ST5 AeroAstro Sband Tx	0.2	0.50	S			8.00	1.00E+07	9
ST5 AeroAstro Sband Tx WithHPA	0.4	5.00	S			34.00	1.00E+07	9
Emheiser ETT 01EBA102	0.0567	1.00	S	2.20E+09	2.40E+09	7.80		4
MER SSPA Xband	1.37	17.00	X	7.80E+09	8.80E+09	60.00		9
L3 CTK830	2.834	0.00	Ka	1.90E+10	2.80E+10	30.00	1.20E+09	9
Ikonos L3 CTX886	3.9	6.00	X	8.00E+09	8.40E+09	75.00	3.20E+11	9
L3 T715 TDRSS Sband	2.17	6.30	S			37.00	6.00E+04	8
L3 T719 TDRSS Sband	2.27	7.08	S			37.00		8
L3 PA805S	0.1106	5.00	S	2.20E+09	2.40E+09	24.00		9
Mitsubishi TD-SS-001 44W	0.56	4.40	S	2.17E+09	2.20E+09	16.30		8
Mitsubishi TD-SS-001 88W	0.56	8.80	S	2.17E+09	2.20E+09	32.60		8
AAC Clyde STX	0.1	1.00	S	2.40E+09	2.45E+09	5.00	2.00E+06	9
Deimos1 SSTL Sband Tx	2	4.00	S	2.20E+09	2.30E+09	38.00	8.00E+06	8
SpaceQuest TX2400 Sband	0.07	10.00	S	2.20E+09	2.29E+09	20.00		7
ISIS TXS	0.3	2.00	S	2.20E+09	2.29E+09	9.20	3.40E+06	8
ISIS TXUHF	0.075	0.50	UHF	4.35E+08	4.38E+08	4.00	9.60E+03	8
ISIS TXVHF	0.085	0.20	VHF	1.46E+08	1.46E+08	1.70	9.60E+03	8
Deimos1 SSTL Xband	3.25	6.00	X	8.00E+09	8.50E+09	55.00	300000000	8
SpaceMicro KaBand	2.3	0.00	Ka	2.00E+10	3.20E+10	50.00	3200000000	7
Alcatel Sband Transponder	4	5.00	S	2.20E+09	2.30E+09	32.00	2.56E+05	9
Astrodev HE100 UHF	0.078	3.00	UHF	4.00E+08	4.50E+08	6.00	3.64E+04	8
Innoflight SCR100	0.29	1.00	S	2.20E+09	2.30E+09	10.00	100000	9
L3 CTT505 UHF	2.07	13.80	UHF	4.00E+08	5.00E+08	60.00	2.56E+05	8
L3 CXS 610	2.49	5.00	S	2.20E+09	2.30E+09	40.50	4.00E+06	8

name	mass (kg)	output power (W)	band	minimum frequency (Hz)	maximum frequency (Hz)	input power (W)	maximum bitrate (bps)	TRL
L3 Cadet Radio	0.08	2.00	UHF, L, S, C, X, Ku			12.00	1.00E+05	8
L3 MSX765	1.9	5.00	S	2.20E+09	2.30E+09	43.50	5.00E+06	9
Genesat MicroHard MHX2420	0.055	1.00	S	2.40E+09	2.48E+09	8.00	2.30E+05	7
Genesat MicroHard MHX2400	0.075	1.00	S	2.40E+09	2.48E+09	3.00	1.15E+05	7
LADEE SpaceMicro STDN Sband	4.7	5.00	S	2.20E+09	2.30E+09	35.00	524288	9
EOS SpaceMicro uSTDN	1.1	10.00	S	2.20E+09	2.30E+09	35.00	1500000	7
TES Sband Transciever	1.1	2.00	S	2.20E+09	2.29E+09	9.20	400000	9
ISIS TRXUV VHFUHF	0.17	0.16	UHF, VHF	4.00E+08	4.50E+08	1.55	9600	9
ClydeSpace VUTRX 2W	0.09	10.00	UHF, VHF	4.20E+08	4.50E+08	2.00	9600	9
ClydeSpace VUTRX halfW	0.09	4.00	UHF, VHF	4.20E+08	4.50E+08	0.50	9600	9
Sunjammer Vulcan CSR SDR SS	0.37	4.00	S	2.29E+09	2.30E+09	18.00	3000000	6
AeroCube3 Transceiver	0.2	0.01	ISM	9.00E+08	9.28E+08	0.15	500000	6
Canopus Ka NanaSat Tx	0.7	0.50	Ka	2.55E+10	2.70E+10	10.00		8
GD Multimode Sband Tx	2.27	5.00	S	2.20E+09	2.30E+09	36.00	6000000	9
GD SDST	3.2	0.00	X, Ka	8.40E+09	3.23E+10	19.50	30000000	9
TechEdSat Globalstar GSP1720	0.06	0.80	L	1.61E+09	1.63E+09	5.00	38000	8
TechEdSat Iridium 9602	0.03	1.60				7.50		7
IRIS JPL Xband Transponder	0.4	2.00	X	8.40E+09	8.45E+09	15.00	256000	4
L3 CTT510 Electra Lite	3	10.70	UHF	3.90E+08	4.05E+08	80.00	12000000	8
L3 CXS2000	3.94	5.00	S	2.20E+09	2.30E+09	56.00	8000000	8
SpaceQuest TR150	0.21	6.00	VHF	1.30E+08	1.60E+08	32.00	10000	9
Astrodev Lithium1	0.052	4.00	UHF, VHF	1.30E+08	4.50E+08	10.00	9600	9
GOMSpace NanoCom AX100	0.0245	1.00	UHF, VHF			4.08	115200	9

C.2.3 Low Gain Antennas (LGAs)

Approximately half of the LGA data was drawn from SPOON. Of the other half, much was drawn from JPL's Deep Space Communications and Navigation Systems Center, DESCANSO, with some components drawn from a number of other technical sources. Components drawn from SPOON are listed in Table C.4. Those from other sources are listed in Table C.5, along with the source documents for each. No TRL was assigned for non-SPOON LGAs. For these, a default TRL of 6 was assumed. Additionally, bands were not specified for these components. As a result, compatible bands were determined based on the frequency ranges for each component.

Table C.4: LGAs from SPOON.

name	mass (kg)	downlink gain (dB)	uplink gain (dB)	band	beam width (deg)	maximum input power (dB)	TRL
ADC Microstrip STDN sband singlef	0.16	11.8	11.8	S	40		8
MOST ADC Xband QuadHelix LEO	0.22	2	2	X	160	12	8
Stardust ADC xband horn	0.8	21	21	X	14	10	9
ADC MGA Patch linear	0.155	10.5	10.5	L, S, C, X	45	14	7
ADC MGA Patch circular	0.155	10.5	10.5	L, S, C, X	45	14	7
Genesis ADC Microstrip Patch xband linear	0.08	6	6	X	70	10	8
Genesis ADC Microstrip Patch xband circular	0.08	6	6	X	70	10	8
Genesis ADC Microstrip Patch sband linear	0.08	6	6	S	80	10	8
Genesis ADC Microstrip Patch sband circular	0.08	6	6	S	80	10	8
AstroDev Sband Patch	0.004	3	2	S	120	4.77	8
ISIS Deployable UHF	0.01	0	0	UHF, VHF	45	3	8
RUAG Ka Pipe	0.019	8	8	Ka	80	10	
Maruwa SL3101	0.029	2	2	L	120	3	7
PhoneSat Monopole UHF	0.015	0	0	UHF	90	3	7
RUAG Sband Helix	0.28	4		S	55	10	
RUAG Sband TTC Helix	0.25	3	3	S	40		
RUAG Sband Omni	0.75	3	3	S	180		
Surrey Xband Horn	2.7	15	15	X	20	20	9
ST5 EA Antenna	0.165	3		X			7
Taoglas WLP.2450.25.4.A	0.05	5	5	S	60	9	6
RUAG Xband pec	0.016	7	7	X	90	10	
ST5 ADC Quad Helix Xband	0.22	2	2	X		10	7

Table C.5: LGAs from other sources.

name	mass	gain (dB)	minimum frequency (Hz)	maximum frequency (Hz)	beam width (deg)	maximum input power (W)	source
Cassini LGA1	0.5	8.94	8.43E+09	8.43E+09	24		[84]
Cassini LGA2	0.5	9	8.43E+09	8.43E+09	40		[84]
DAWN LGA	0.5	6	7.17E+09	8.45E+09	90		[85]
DeepImpact LGA1	0.06	3	8.44E+09	8.44E+09	90		[86]
ISEE-C	0.95	7	2.22E+09	2.27E+09	12	13	[87]
Omni AS-48915	0.312	4	1.75E+09	2.30E+09	45	10	[88]
ISEE-A	0.95	3	2.22E+09	2.26E+09	60	13	[87]
ISEE-C	0.95	7	2.22E+09	2.27E+09	12	13	[87]
Juno MGA	0.5	18.8	7.15E+09	8.40E+09	18.6		[86]
Juno TLGA	1.9	6.5	7.15E+09	8.40E+09	20		[86]
MarsOdyssey LGA	0.04	7	7.16E+09	7.16E+09	82		[86]
MRO Electra Antenna	1.4	5	4.37E+08	4.37E+08	70		[86]
MRO LGA	0.8	8.8	7.15E+09	8.44E+09	80		[86]
Shaped Omni (NASA–TR-100680)	2.27	0	2.09E+09	2.31E+09	170	10	[87]
SAAB LCROSS PEC	0.325	12.5	1.98E+09	2.20E+09	50		[89]
SAAB X Helix 60EOC	0.4	2	7.25E+09	8.40E+09	160		[89]
SMAP SLGA	0.25	0	2.00E+09	2.30E+09	190	10	[86]
SMAP XLGA	0.4	1.5	8.03E+09	8.33E+09	160	10	[86]

C.2.4 High Gain Antennas (HGAs)

HGAs were drawn primarily from DESCANSO. Their properties are listed in Table C.6. All are assumed to be parabolic reflectors. Like with the LGAs drawn from non-SPOON sources, no TRL was assigned for non-SPOON LGAs. TRL and communications bands were assigned as specified for LGAs.

Table C.6: HGAs considered.

name	mass (kg)	nominal gain (dB)	nominal wavelength (m)	diameter (m)	source
Cassini HGAS	100.6	46.6	0.035583675	4	[90]
Dawn HGA	7	39.6	0.035539928	1.524	[85]
Deep Impact HGA	2.8	35.6	0.035541489	1	[91]
Juno HGA	21.3	44.5	0.035672015	2.5	[92]
LRO HGAS	50.1	44	0.011687815	0.75	[93]
Mars Odyssey HGAS	3.15	38.3	0.03566049	1.3	[84]
MRO HGAS	65.7	56.4	0.009368514	3	[94]
Voyager HGAS	53	48	0.035602978	3.66	[95]

C.3 Solar Panels (PVAs)

A subset of PVAs, given in Table C.7, was used in Chap. 8. In Chap. 9, the additional PVAs in Table C.8 were considered as well. The final six components in Table C.8 are artificially created macrocomponents.

C.4 Batteries

All batteries considered are listed in Table C.9. Data is drawn primarily from SPOON. For EnerSys batteries, additional data was drawn from [96].

Table C.7: PVAs considered in Chap. 8.

name	mass (kg)	efficiency	area (m^2)	TRL
DHV CS 10	0.05	2.19E-01	8.09E-03	7
EXA DSA 1A 1panel NEMEA highpower	0.067	6.48E-01	8.13E-03	9
EXA DSA 1A 1panel NEMEA lowcost	0.067	2.47E-01	8.13E-03	9
EXA DSA 1A 1panel noNEMEA highpower	0.057	6.48E-01	8.13E-03	9
EXA DSA 1A 1panel noNEMEA lowcost	0.057	2.47E-01	8.13E-03	9
EXA DSA 1A 2panels NEMEA highpower	0.115	5.93E-01	1.48E-02	9
EXA DSA 1A 2panels NEMEA lowcost	0.115	2.12E-01	1.48E-02	9
EXA DSA 1A 2panels noNEMEA highpower	0.087	5.93E-01	1.48E-02	9
EXA DSA 1A 2panels noNEMEA lowcost	0.087	2.12E-01	1.48E-02	9
EXA DSA 1A 3panels NEMEA highpower	0.135	5.72E-01	2.15E-02	9
EXA DSA 1A 3panels NEMEA lowcost	0.135	2.13E-01	2.15E-02	9
EXA DSA 1A 3panels noNEMEA highpower	0.107	5.72E-01	2.15E-02	9
EXA DSA 1A 3panels noNEMEA lowcost	0.107	2.13E-01	2.15E-02	9
ISIS 1U PVA	0.05	0.208	0.00809	9
ISIS 2U PVA	0.1	0.208	0.0162	9
ISIS 3U PVA	0.15	0.208	0.0243	9
ISIS 6U PVA	0.3	0.256	0.0485	9

C.5 Thrusters

All thrusters used were drawn from the original component library from the work of [76]. Where available, this data was supplemented with data from SPOON.

C.6 Propellant Tanks

All liquid propellant types had component libraries based on the same set of tank components, given in Table C.11. Xenon tanks were based on a separate list of gaseous tank components, given in Table C.12. All tanks were drawn from SPOON.

Table C.8: Additional PVAs considered for LEO ADR.

name	mass (kg)	efficiency	area (m^2)	TRL
AzurSpace 3G30A GaAs Assy	0.003797267	0.28	0.003218023	9
AzurSpace 3G30A 8x8 GaAs Assy	7.20E-03	0.28	6.04E-03	9
Emcore ATJ	2.23E-03	0.275	2.66E-03	9
SpectroLab Space SolarPanel ITJ 2662	2.24E-03	0.268	2.66E-03	9
SpectroLab Space SolarPanel ITJ 5965	5.01E-03	0.268	5.97E-03	9
SpectroLab Space SolarPanel UTJ 2662	2.24E-03	0.283	2.66E-03	9
SpectroLab Space SolarPanel UTJ 5965	5.01E-03	0.283	5.97E-03	9
SpectroLab Space SolarPanel XTJ 2662	2.24E-03	0.293	2.66E-03	9
SpectroLab Space SolarPanel XTJ 5965	5.01E-03	0.293	5.97E-03	9
SpectroLab TASC	5.12E-04	0.27	0.00049764	9
DHV eHAWK	3.50E-01	0.283	0.108566126	9
MMA eHaWK SolarArray 6U	0.6	0.28	0.18810743	9
GOMSpace Nanopower MSP A 1 1	0.032	0.298	3.02E-03	9
GOMSpace Nanopower MSP A 2 1	0.06	0.298	6.04E-03	9
GOMSpace Nanopower MSP A 3 1	0.086	0.298	9.05E-03	9
GOMSpace Nanopower MSP A 4 1	0.109	0.298	1.21E-02	9
GOMSpace Nanopower MSP A 5 1	0.135	0.298	1.51E-02	9
GOMSpace Nanopower MSP A 6 1	0.162	0.298	1.81E-02	9
GOMSpace Nanopower MSP A 7 1	0.19	0.298	2.11E-02	9
GOMSpace Nanopower MSP B 4 4	0.438	0.298	4.83E-02	9
GOMSpace Nanopower MSP B 8 2	0.438	0.298	4.83E-02	9
GOMSpace Nanopower MSP C 4 1	0.132	0.298	1.21E-02	9
GOMSpace Nanopower MSP C 5 1	0.132	0.298	1.51E-02	9
GOMSpace Nanopower MSP C 4 1	0.112	0.298	1.81E-02	9
DAWN SolarArray Wing	63	0.191600025	19.09	9
3xXTJ 5965	6.71E-03	0.293	7.99E-03	9
10xXTJ 5965	5.01E-02	0.293	5.97E-02	9
30xXTJ 5965	1.50E-01	0.293	1.79E-01	9
100xXTJ 5965	5.01E-01	0.293	5.97E+00	9
300xXTJ 5965	1.50E+00	0.293	1.79E+00	9
1000xXTJ 5965	5.01E+00	0.293	5.97E+01	9

Table C.9: Batteries considered.

name	cell chemistry	capacity (Wh)	mass (kg)	self-discharge rate (%/day)	TRL
TechEdSat Cannon BP930	Li-Ion	22.2	0.225		7
Kepler Enersys ABSL 8s16p	Li-Ion	691	6.8		9
Enersys ABSL 2s4p	Li-Ion	42	0.6		7
Enersys ABSL 2s7p	Li-Ion	73.5	0.73		7
Enersys ABSL 4s6p	Li-Ion	126	1.2		7
Enersys ABSL 6s2p	Li-Ion	63	0.6		7
Enersys ABSL 6s6p	Li-Ion	189	1.9		7
Enersys ABSL 6s9p	Li-Ion	283.5	2.8		7
Enersys ABSL 6s11p	Li-Ion	346.5	3.4		7
Enersys ABSL 6s16p	Li-Ion	504	4.9		7
Enersys ABSL 6s24p	Li-Ion	756	7		7
Enersys ABSL 6s64p	Li-Ion	2016	18.6		7
Enersys ABSL 7s2p	Li-Ion	73.5	0.73		7
Enersys ABSL 7s3p	Li-Ion	110.25	1.1		7
Enersys ABSL 8s1p	Li-Ion	42	0.625		7
KSLV Enersys ABSL 8s1p	Li-Ion	43.2	1.07		9
KSLV Enersys ABSL 8s3p	Li-Ion	129.6	1.6		9
Enersys ABSL 8s8p	Li-Ion	336	3.3		7
SMAP Enersys ABSL 8s10p	Li-Ion	432	4.4		9
SAC D Enersys ABSL 8s20p	Li-Ion	863	9.3		9
Enersys ABSL 8s32p	Li-Ion	1344	12.8		7
Enersys ABSL 8s44p	Li-Ion	1848	20.98		7
Enersys ABSL 8s50p	Li-Ion	2100	20.2		7
SMAP Enersys ABSL 8s52p	Li-Ion	2246	20.7		9
Enersys ABSL 8s60p	Li-Ion	2520	28.37		7
Enersys ABSL 8s72p	Li-Ion	3024	28		7
LRO Enersys ABSL 8s84p	Li-Ion	3628.8	40		9
Enersys ABSL 8s96p	Li-Ion	4032	41		7
SDO Enersys ABSL 8s104p	Li-Ion	4492.8	49.9		9
Enersys ABSL 9s10p	Li-Ion	472.5	4.7		7
Enersys ABSL 9s56p	Li-Ion	2646	25.5		7
Enersys ABSL 10s24p	Li-Ion	1260	12.5		7
Enersys ABSL 10s30p	Li-Ion	1575	16.4		7
Enersys ABSL 10s32p	Li-Ion	1680	16.8		7
Enersys ABSL 10s72p	Li-Ion	3780	38.3		7

name	cell chemistry	capacity (Wh)	mass (kg)	self-discharge rate (%/day)	TRL
Enersys ABSL 12s24p	Li-Ion	518.4	14.4		7
Enersys ABSL 12s28p	Li-Ion	697.2	16.6		7
Enersys ABSL 16s16p	Li-Ion	1344	14.5		7
Enersys ABSL 84s2p	Li-Ion	882	11.5		7
Enersys ABSL 3s4p	Li-Ion	125	0.98		7
CS 1U	LiPo	10	0.062		
GomSpace 1800mAh battery	Li-Ion	13.32	0.095	0.00001	9
GomSpace BP4 2p2s	Li-Ion	38.5	0.258		8
GomSpace BP4 1p4s	Li-Ion	38.5	0.258		8
Mitsubishi 5kW LI battery	Li-Ion	8620	81	0.001	8
Genesat Rose LiIon 2200mAh	Li-Ion	16.2	0.098		9
Saft 60145B 8s LD25P	Li-Ion	162	2.2	0.0024161	
GIOVEB Saft VES 100	Li-Ion	95.6	0.81		9
Saft VL48E	Li-Ion	172.5	1.15		
Sony 18650	Li-Ion	5.4	0.042		9
SpaceQuest BAT 4	Li-Ion	4.9	0.16		7
X37B Yardney Lithion 9553HV	Li-Ion	1814	26.3		6
MarsLander Yardney Lithion LP3028	Li-Ion	950.4	17.8		7
X37 Yardney LP30950	Li-Ion	1238.4	13.5		
MER Yardney LP30990	Li-Ion	604.8	7.9		9
Yardney LP31685	Li-Ion	1238.4	12.62		
Yardney NCP05	Li-Ion	0.24	0.004		
Yardney NCP25 1	Li-Ion	129	0.89		
Yardney NCP25 2	Li-Ion	95	0.908		
Yardney NCP3501	Li-Ion	1414	6.67	0.0001	
Yardney NCP431	Li-Ion	180	1.27	0.0001	
Yardney NCP552	Li-Ion	198	1.582	0.0001	
NASA CBSF B79010 10	Li-S	900	3.8555	5.50E-05	5
CS Standalone 30Whr	LiPo	30	0.26	0.005	8
GOMSpace Nanopower P31u s2p	Li-Ion	20	0.2		9
LG ICR18650	Li-Ion	10.5	0.047	0.003	7
CS LiPo 6 25 Ah	LiPo	150	1		8
Mitsubishi 4.4kw LIB0003a	Li-Ion	7560	67.2	0.001	8
Orbtronic 18650	Li-Ion	12.2	0.046		

name	cell chemistry	capacity (Wh)	mass (kg)	self-discharge rate (%/day)	TRL
Genesat Rose LiIon 4400mAh	Li-Ion	32.4	0.19		9
Saft 15s3p MPS176065	Li-Ion	1125	9.9		7
Saft VES140	Li-Ion	142.38	1.13		9
Saft VES180	Li-Ion	194.25	1.11		9
Samsung 18650	Li-Ion	9.33	0.048		9
XSS11 Yardney Lithion LP31105	Li-Ion	864	9.18		9
SpectrumAstro Yardney Lithion LP31280	Li-Ion	1728	20.32		
NextSat Yardney Lithion LP31500	Li-Ion	864	11.35		
Yardney LP30588	Li-Ion	43	0.422	0.0001	
Yardney NCP7	Li-Ion	27	0.245	0.0001	

Table C.10: Thrusters considered.

name	mass	I_{sp}	F_t	P_{on} (W)	prop$_1$	f_1	prop$_2$	f_2	TRL
R-4D	4.31	316	489	46	MMH	1	NTO	1.73	9
AJ10	100	320	44000	0	Aerozine50	1	NTO	1.9	9
R-6D	0.454	294	22	5	MMH	1	NTO	1.65	9
R-1E	2	280	111	36	MMH	1	NTO	0.85	9
HiPAT	5.44	323	445	46	MMH	1	NTO	0.85	9
R-42	4.53	303	890	46	MMH	1	NTO	1.73	9
R-40B	6.8	293	4000	70	MMH	0.52	NTO	0.838	9
MR103D	0.33	217	1.02	8.25	N2H4	1			9
MR103G	0.33	213	1.13	8.25	N2H4	1			9
MR103M	0.16	213	0.99	7.1	N2H4	1			9
MR104	1.86	240	440	30	N2H4	1			9
MR111C	0.33	222	4	8.25	N2H4	1			9
MR-106E	0.635	232	22	25.3	N2H4	1			9
MR-80B	8.51	200	3100	168	N2H4	1			9
MR-502	0.9	300	0.8145	900	N2H4	1			9
MR-510	5.5	585	0.23	2200	N2H4	1			9
MR-509	5.5	502	0.23	1800	N2H4	1			8
PRS-101	4.75	1350	0.0125	1350	Teflon	1			9
BPT-4000-1	25	1676	1.32E-01	2000	Xenon	1			9
BPT-4000-2	25	1700	0.195	3000	Xenon	1			9
BPT-4000-3	25	1790	0.29	4500	Xenon	1			9
BPT-4000-4	25	1858	0.117	2000	Xenon	1			9
BPT-4000-5	25	1920	0.17	3000	Xenon	1			9
BPT-4000-6	25	2020	0.254	4500	Xenon	1			9
NEXT	47.2	4190	0.236	7200	Xenon	1			6
NSTAR	25.5	3200	0.08	1950	Xenon	1			9
DawnThruster	23.34	3100	0.092	2500	Xenon	1			9
XIPS-25	37	3400	0.165	4500	Xenon	1			9
T5	20	3200	0.018	476	Xenon	1			9

Table C.11: Liquid propellant tanks considered.

name	mass (kg)	fill volume (L)	TRL
ATK PSI 80225-1	3.701	22.532	9
ATK PSI 80228-1	19.958	132.079	9
ATK PSI 80276-1	4.309	30.152	9
ATK PSI 80285-1	6.985	33.577	9
ATK PSI 80290-1	2.54	12.454	9
ATK PSI 80315-1	44.452	458.837	9
ATK PSI 80323-1	14.288	113.398	9
ATK PSI 80348-1	19.504	167.393	9
ATK PSI 80362-1	7.348	72.574	9
ATK PSI 80373-1	13.834	337.229	9
ATK PSI 80388-1	7.03	72.574	9
ATK PSI 80389-1	3.719	22.532	9
ATK PSI 80453-1	7.03	72.27	9
ATK PSI 80512-1	6.01	45.03	9
ATK PSI 80156-1	1.319	4.752	9
ATK PSI 80222-1	1.292	4.752	9
ATK PSI 80275-1	5.76	32.036	9
ATK PSI 80339-1	13.653	249.022	9
ATK PSI 80356-1	27.215	438.353	9
ATK PSI 80364-1	5.669	68.038	9
ATK PSI 80376-1	34.473	345.898	9
Ariane5 BT01 0	8.5	39	9
Globalstar OST31 1	6.4	78	9
MicroAerospaceSolutions Tank	0.11	0.03	6
ATK PSI 80216-1	2.721	12.454	9
ATK PSI 80263-201	34.473	345.898	9
ATK PSI 80266-1	2.222	12.454	9
ATK PSI 80287-1	19.05	157.512	9
ATK PSI 80303-1	5.896	32.167	9
Skynet ATK PSI 80308-101	5.624	37.648	9
ATK PSI 80319-101	5.987	28.267	9
ATK PSI 80342-1	2.721	14.453	9
ATK PSI 80358-1	5.896	32.2	9
ATK PSI 80360-1	5.669	65.77	9
ATK PSI 80370-1	34.473	345.898	9
ATK PSI 80375-1	8.618	114.758	9
ATK PSI 80392-1	5.624	37.648	9
ATK PSI 81214-1	3.583	24.826	9
ATK PSI 80271-3	5.17	24.908	9
ATK PSI 80273-3	12.246	55.224	9

name	mass (kg)	fill volume (L)	TRL
ATK PSI 80274-1	6.01	45.031	9
ATK PSI 80281-3	9.071	101.567	9
ATK PSI 80297-1	19.504	141.715	9
ATK PSI 80304-1	3.515	38.493	9
ATK PSI 80325-1	19.958	132.079	9
ATK PSI 80337-1	6.35	28.267	9
ATK PSI 80359-1	6.985	25.973	9
ATK PSI 80359-1	34.518	345.898	9
ATK PSI 80359-1	7.03	72.574	9
ATK PSI 80263-101	34.473	345.898	9
ATK PSI 80280-103	10.659	73.886	9
ATK PSI 80298-1	9.525	8.178	9
ATK PSI 80309-1	8.073	149.415	9
ATK PSI 80353-1	3.855	58.583	9
ATK PSI 80384-1	5.896	32.2	9

Table C.12: Gaseous tanks considered.

name	mass (kg)	fill volume (L)	max pressure (Pa)	TRL
ATK PSI 80186-1	10.569	28.86	2.50E+07	9
ATK PSI 80198-1	7.666	18.8	2.50E+07	9
ATK PSI 80374-1	9.979	67.27	3.10E+07	9
Aerojet Plenum	0.072	0.033	8.96E+06	9
Shuttle Arde C4284-2	0.517	0.983	2.07E+07	9
X33 C4683	4.309	13.32	2.21E+07	6
Shuttle Arde D4051	0.916	2.933	7.24E+06	9
Shuttle Arde D4554	30.391	132.08	3.10E+07	9
Arde D4607	24.948	85.29	2.76E+07	6
Arde D4619	18.28	96.96	3.10E+07	9
ATK PSI 80119-105	0.839	7.489	4.14E+06	9
ATK PSI 80194-1	5.375	15.65	2.48E+07	9
ATK PSI 80314-201	16.012	36.05	2.48E+07	9
Cassini Arde D4575	3.357	6.55	2.48E+07	9
ISS Arde D4636	7.711	27.53	2.07E+07	9
SAFER Arde D4639	1.769	2.79	6.89E+07	9
Olympus Arde E4070	10.206	30.81	2.76E+07	9
GOES Arde E4256	19.731	75.34	2.76E+07	9
Eurostar EADS LV 35 5L	7.8	35.5	2.76E+07	9
ATK PSI 80221-1	24.857	87.31	2.07E+06	9
ATK PSI 80295-1	1.451	1.639	5.52E+07	9
ATK PSI 80326-1	1.533	3.851	2.48E+07	9
ATK PSI 80383-1	16.012	36.05	2.48E+07	9
Arde D3961	0.807	0.9	4.14E+07	9
UoSat Arde D4598	4.899	9.996	2.07E+07	9
UoSat Arde D4600-1	0.916	1.311	4.14E+06	9
ISS Arde D4708	1.5	2.868	2.07E+07	9
EADS LV110L	23	110	3.10E+07	8
ATK PSI 80202-1	7.167	14.519	3.10E+07	9
ATK PSI 80333-1	36.242	105.7	2.80E+07	9
ATK PSI 80458-101	19.05	119.63	1.86E+07	9

name	mass (kg)	fill volume (L)	max pressure (Pa)	TRL
Shuttle Arde C4285-1	0.517	1.311	2.07E+07	9
IABS Arde D4307	10.659	51.73	3.10E+07	9
Arde D4678	2.268	1.88	2.21E+07	9
Shuttle Arde D4097	2.903	14.257	4.24E+06	9
ISS Arde D4406	3.538	13.88	8.27E+06	9
Dawn Carleton 7169	22.2	268	8.62E+06	9
EADS LV18 3L	4.3	18.3	2.65E+07	9
EADS LV300L	81	300	4.00E+07	9
EADS LV51L	11.5	51	2.95E+07	9
EADS LV80L	17.7	80	3.10E+07	9
ATK PSI 80195-1	5.443	9.373	1.84E+07	9
ATK PSI 80345-1	3.357	6.555	3.10E+07	9
Arde D4600-3	0.816	0.869	4.14E+06	9
Rosetta EADS LV68L	15.6	68	3.10E+07	9

Appendix D: DOVE Simulation Data

This appendix lists all access data used during the simulation described in Chap. 8. Each section below contains data from a given station. Each table within a section gives data on a given pass for that station. In each table, time is measured in elapsed seconds since the beginning of the simulation. Properties at a given simulation timestep during an access window are linearly interpolated between the nearest points given in the appropriate table. Elevation angles are measured from the spacecraft to the station. As a result, all elevation angles are negative for ground stations.

D.1   SG1 (Svalbard)

elapsed time (s)	range (km)	elevation (degrees)
897.855	2548.775	-21.746
957	2154.629	-22.095
1017	1769.159	-23.36
1077	1412.368	-26.035
1137	1114.423	-30.526
1197	935.210	-35.271
1257	945.684	-34.966
1317	1140.528	-30.089
1377	1446.412	-25.793
1437	1806.806	-23.29
1497	2193.793	-22.132
1552.685	2565.077	-21.843

elapsed time (s)	range (km)	elevation (degrees)
6580.262	2551.140	-21.758
6640	2206.744	-22.023
6700	1894.455	-22.839
6760	1636.911	-24.164
6820	1464.616	-25.562
6880	1409.965	-26.137
6940	1486.160	-25.402
7000	1675.095	-23.991
7060	1943.442	-22.75
7120	2262.136	-22.034
7172.303	2565.562	-21.847

D.2 TrollSat (Troll)

elapsed time (s)	range (km)	elevation (degrees)
4208.496	2563.836	-21.833
4268	2189.875	-22.12
4328	1835.280	-23.129
4388	1521.281	-25.05
4448	1280.093	-27.679
4508	1159.550	-29.594
4568	1197.342	-28.882
4628	1380.477	-26.304
4688	1661.020	-23.893
4748	1997.471	-22.402
4808	2364.993	-21.762
4835.613	2540.540	-21.693

elapsed time (s)	range (km)	elevation (degrees)
9808.641	2563.535	-21.831
9868	2142.903	-22.205
9928	1721.310	-23.692
9988	1309.647	-27.315
10048	924.450	-35.601
10108	620.663	-54.226
10168	556.123	-63.421
10228	791.975	-41.002
10288	1156.617	-29.542
10348	1561.344	-24.57
10408	1980.520	-22.444
10468	2405.233	-21.733
10486.994	2540.134	-21.691

D.3 TDRS-3

elapsed time (s)	range (km)	elevation (degrees)
0	35282.231	-86.9
60	35279.220	-86.915
120	35303.669	-86.798
180	35355.433	-86.566
240	35434.217	-86.244
300	35539.576	-85.859
360	35670.924	-85.434
420	35827.536	-84.987
480	36008.566	-84.532
540	36213.046	-84.079
600	36439.908	-83.635
660	36687.990	-83.207
720	36956.047	-82.799
780	37242.768	-82.414
840	37546.784	-82.056
900	37866.682	-81.726
960	38201.016	-81.426
1020	38548.316	-81.158
1080	38907.098	-80.922
1140	39275.875	-80.718
1200	39653.164	-80.547
1260	40037.493	-80.41
1320	40427.404	-80.304
1380	40821.466	-80.231
1440	41218.274	-80.19
1500	41616.454	-80.18
1560	42014.669	-80.2
1620	42411.618	-80.25
1680	42806.040	-80.328
1740	43196.719	-80.434
1800	43582.479	-80.565
1860	43962.190	-80.723
1920	44334.770	-80.904
1980	44699.178	-81.108
2031.39	45004.045	-81.3

Bibliography

[1] B. Randolph, W. Hreha, and A. Q. Rogers, "Key technology, programmatic drivers, and lessons learned for production of proliferated small satellite constellations,"

[2] B. Doncaster, J. Shulman, J. Bradford, and J. Olds, "Spaceworks' 2016 nano/microsatellite market forcast," in *Proceedings of the 30th annual AIAA/USU Conference on Small Satellites*, vol. 30, 2016.

[3] V. L. Foreman, A. Siddiqi, and O. De Weck, "Large satellite constellation orbital debris impacts: Case studies of oneweb and spacex proposals," in *AIAA SPACE and Astronautics Forum and Exposition*, p. 5200, 2017.

[4] J. Radtke, E. Stoll, H. Lewis, and B. B. Virgili, "The impact of the increase in small satellite launch traffic on the long-term evolution of the space debris environment," in *Proc. 7th European Conference on Space Debris*, 2017.

[5] Space Exploration Holdings, LLC, "Spacex non-geostationary satellite system - technical attachment," November 2016.

[6] Space Exploration Holdings, LLC, "Request for modification of the authorization for the spacex ngso satellite system," April 2019.

[7] H. Jones, "The recent large reduction in space launch cost," 48th International Conference on Environmental Systems, 2018.

[8] H. Crisp, "Incose systems engineering vision 2020," tech. rep., INCOSE-TP-2004-004-02, September, 2007.

[9] J.-C. Liou, "An active debris removal parametric study for leo environment remediation," *Advances in Space Research*, vol. 47, no. 11, pp. 1865–1876, 2011.

[10] P. D. Anz-Meador, J. N. Opiela, D. Shoots, and J.-C. Liou, "History of on-orbit satellite fragmentations,"

[11] D. J. Kessler and B. G. Cour-Palais, "Collision frequency of artificial satellites: The creation of a debris belt," *Journal of Geophysical Research: Space Physics*, vol. 83, no. A6, pp. 2637–2646, 1978.

[12] B. Wielinga and G. Schreiber, "Configuration-design problem solving," *IEEE Expert*, vol. 12, no. 2, pp. 49–56, 1997.

[13] N. Nassar and M. Austin, "Model-based systems engineering design and trade-off analysis with rdf graphs," *Procedia Computer Science*, vol. 16, pp. 216–225, 2013.

[14] J. Knizhnik, M. Austin, and C. Carignan, "Robotic satellite servicing trade space down-selection," in *INCOSE International Symposium*, vol. 27, pp. 1491–1505, Wiley Online Library, 2017.

[15] M. Ryerkerk, R. Averill, K. Deb, and E. Goodman, "Optimization for variable-size problems using genetic algorithms," in *12th AIAA Aviation Technology, Integration, and Operations (ATIO) Conference and 14th AIAA/ISSMO Multidisciplinary Analysis and Optimization Conference*, p. 5569, 2012.

[16] L. Bianchi, M. Dorigo, L. M. Gambardella, and W. J. Gutjahr, "A survey on metaheuristics for stochastic combinatorial optimization," *Natural Computing*, vol. 8, no. 2, pp. 239–287, 2009.

[17] J. Wertz and W. J. Larson, *Space Mission Analysis and Design, Third Edition*. Microcosm Press and Kluwer Academic Publishers, El Segundo, CA, USA,, 1999.

[18] C. D. Jilla and D. W. Miller, "Multi-Objective, Multidisciplinary Design Optimization Methodology for Distributed Satellite Systems," *Journal of Spacecraft and Rockets*, vol. 41, pp. 39–50, Jan. 2004.

[19] T. Mosher, "Conceptual Spacecraft Design Using a Genetic Algorithm Trade Selection Process," *Journal of Aircraft*, vol. 36, Jan. 1999.

[20] L. J. Paxton, "faster, better, and cheaper at nasa: Lessons learned in managing and accepting risk," *Acta Astronautica*, vol. 61, no. 10, pp. 954–963, 2007.

[21] M. Sorgenfrei and E. Chester, "Exploration of the Mars entry, descent, and landing design space by means of a genetic algorithm," in *AIAA Infotech@Aerospace Conference* (A. I. of Aeronautics and Astronautics, eds.), no. 2013-4569, 2013.

[22] G. B. Shaw, *The Generalized Information Network Analaysis Methodology for Distributed Satellite Systems*. PhD thesis, Massachusetts Institute of Technology, Oct. 1998.

[23] K. Deb, A. Pratap, S. Agarwal, and T. Meyarivan, "A fast and elitist multiobjective genetic algorithm: NSGA-II," *IEEE Transactions on Evolutionary Computation*, vol. 6, pp. 182–197, Apr 2002.

[24] C. Lee and E. Antonsson, "Variable length genomes for evolutionary algorithms.," in *GECCO*, vol. 2000, p. 806, 2000.

[25] C.-K. Ting, C.-N. Lee, H.-C. Chang, and J.-S. Wu, "Wireless heterogeneous transmitter placement using multiobjective variable-length genetic algorithm," *IEEE Transactions on Systems, Man, and Cybernetics, Part B (Cybernetics)*, vol. 39, no. 4, pp. 945–958, 2009.

[26] B. D. Yost, D. J. Mayer, C. D. Burkhard, S. V. Weston, and J. L. Fishman, "Small spacecraft systems virtual institute's federated databases and state of the art of small spacecraft technology report," 2018.

[27] T. M. Espero, "Orbital express: A new chapter in space."

[28] M. Pfisterer, K. Schillo, C. Valle, K.-C. Lin, and C. Ham, "The development of a propellantless space debris mitigation drag sail for leo satellites," in *Proceedings of the 15th World Multi-Conference on Systemics, Cybernetics and Informatics, WMSCI*, pp. 19–22, 2011.

[29] D. Beckett, B. Carpenter, and C. Cassapakis, "Rapid de-orbit of leo space vehicles using towed rigidizable inflatable structure (tris) technology: concept and feasibility assessment," 2004.

[30] K. Nock, K. Gates, K. Aaron, and A. McRonald, "Gossamer orbit lowering device (gold) for safe and efficient de-orbit," in *AIAA/AAS Astrodynamics specialist conference*, p. 7824, 2010.

[31] R. L. Forward, R. P. Hoyt, and C. W. Uphoff, "Terminator tether: a spacecraft deorbit device," *Journal of spacecraft and rockets*, vol. 37, no. 2, pp. 187–196, 2000.

[32] J. Pearson, J. Carroll, E. Levin, and J. Oldson, "Edde: Electrodynamic debris eliminator for active debris removal," in *NASA-DARPA International Conference on Orbital Debris Removal, Chantilly, VA*, vol. 8, 2009.

[33] E. S. Smith, R. J. Sedwick, J. F. Merk, and J. McClellan, "Assessing the potential of a laser-ablation-propelled tug to remove large space debris," *Journal of Spacecraft and Rockets*, vol. 50, no. 6, pp. 1268–1276, 2013.

[34] W. J. Larson, ed., *Smace Misison Analysis and Design*, 2nd *ed.* Microcosm.

[35] "Space launch system (sls) program misison planner's guide (mpg) executive overview."

[36] D. Akin, "Cost estimation and engineering economics.".

[37] J. Goodwin and P. Wegner, "Evolved expendable launch vehicle secondary pay-load adapter-helping technology get to space," in *AIAA Space 2001 Conference and Exposition*, p. 4701, 2001.

[38] S. Dodge, "Orbital debris management & risk mitigation," _, *Sept*, 2015.

[39] "U.s. government orbital debris mitigation standard practices."

[40] M. Sampson and V. Derevenko, "Interface definition document (idd) for inter-national space station (iss) visiting vehicles (vvs)," *NASA Technical Report*, 2000.

[41] J. C. Mankins, "Technology readiness levels: A white paper," *http://www. hq. nasa. gov/office/codeq/trl/trl. pdf*, 1995.

[42] P. Malone, R. Smoker, H. Apgar, and L. Wolfarth, "The application of trl met-rics to existing cost prediction models," in *2011 Aerospace Conference*, pp. 1–12, IEEE, 2011.

[43] G. F. Dubos, J. H. Saleh, and R. Braun, "Technology readiness level, schedule risk, and slippage in spacecraft design," *Journal of Spacecraft and Rockets*, vol. 45, no. 4, pp. 836–842, 2008.

[44] J.-C. Liou, "Active debris removal-a grand engineering challenge for the twenty-first century," 2011.

[45] I. S. J., H. J. P., and H. J., *International Reference Guide to Space Launch Vehicles. 3rd Ed.*

[46] J. J. Young, *A value proposition for lunar architectures utilizing on-orbit pro-pellant refueling*. PhD thesis, Georgia Institute of Technology, 2009.

[47] N. Armaroli and V. Balzani, "Towards an electricity-powered world," *Energy Environ. Sci.*, vol. 4, pp. 3193–3222, 2011.

[48] D. J. Bayley, R. J. Hartfield, J. E. Burkhalter, and R. M. Jenkins, "Design optimization of a space launch vehicle using a genetic algorithm," *Journal of Spacecraft and Rockets*, vol. 45, no. 4, pp. 733–740, 2008.

[49] D. B. Riddle, R. J. Hartfield, J. E. Burkhalter, and R. M. Jenkins, "Genetic-algorithm optimization of liquid-propellant missile systems," *Journal of Space-craft and Rockets*, vol. 46, no. 1, pp. 151–159, 2009.

[50] L. Dudzinski, "Rps mission planning considering the us pu-238 supply."

[51] "Announcement of opportunity - discovery 2019."

[52] "Announcement of opportunity - new frontiers 4."

[53] D. E. Goldberg and K. Deb, "A comparative analysis of selection schemes used in genetic algorithms," in *Foundations of genetic algorithms*, vol. 1, pp. 69–93, Elsevier, 1991.

[54] J. Zhong, X. Hu, J. Zhang, and M. Gu, "Comparison of performance between different selection strategies on simple genetic algorithms," in *International Conference on Computational Intelligence for Modelling, Control and Automation and International Conference on Intelligent Agents, Web Technologies and Internet Commerce (CIMCA-IAWTIC'06)*, vol. 2, pp. 1115–1121, IEEE, 2005.

[55] O. Rudenko and M. Schoenauer, "A steady performance stopping criterion for pareto-based evolutionary algorithms," in *Proceedings of the 6th International Multi-Objective Programming and Goal Programming Conference*, 2004.

[56] J. W. Dally and R. J. Bonenberger, *Mechanics II: Mechanics of Materials*. College House Enterprises, LLC., 2010.

[57] I. Y. Kim and O. De Weck, "Variable chromosome length genetic algorithm for progressive refinement in topology optimization," *Structural and Multidisciplinary Optimization*, vol. 29, no. 6, pp. 445–456, 2005.

[58] D. Doan, R. Zimmerman, L. Leung, J. Mason, N. Parsons, and K. Shahid, "Commissioning the worlds largest satellite constellation," in *Proceedings of the 31st annual AIAA/USU Conference on Small Satellites*, vol. 31, 2017.

[59] National Aeronautics and Space Administration, *Near Earth Network User's Guide*, February 2016.

[60] D. Israel, "Enae 693: Spacecraft communications: Transmitter power, path loss, and receiver gain.".

[61] J. Bruder, J. Carlo, J. Gurney, and J. Gorman, "Ieee standard for letter designations for radar-frequency bands," *IEEE Aerospace & Electronic Systems Society*, pp. 1–3, 2003.

[62] L. Brown, L. S. Brown, and T. Holme, *Chemistry for engineering students*. Nelson Education, 2014.

[63] "Planet labs technical specifications: Spacecraft operations & ground systems," June 2015.

[64] K. Beck, M. Beedle, A. van Bennekum, A. Cockburn, W. Cunningham, M. Fowler, J. Grenning, J. Highsmith, A. Hunt, R. Jeffries, J. Kern, B. Marick, R. C. Martin, S. Mellor, K. Schwaber, J. Sutherland, and D. Thomas, "Manifesto for agile software development," 2001.

[65] A. Chin, R. Coelho, L. Brooks, R. Nugent, and J. Puig-Suari, "Standardization promotes flexibility: A review of cubesats success," *Aerospace Engineering*, vol. 805, pp. 756–5087, 2008.

[66] K. Woellert, P. Ehrenfreund, A. J. Ricco, and H. Hertzfeld, "Cubesats: Cost-effective science and technology platforms for emerging and developing nations," *Advances in Space Research*, vol. 47, no. 4, pp. 663–684, 2011.

[67] K. Devaraj, R. Kingsbury, M. Ligon, J. Breu, V. Vittaldev, B. Klofas, P. Yeon, and K. Colton, "Dove high speed downlink system," 2017.

[68] C. Boshuizen, J. Mason, P. Klupar, and S. Spanhake, "Results from the planet labs flock constellation," in *Proceedings of the 28th annual AIAA/USU Conference on Small Satellites*, vol. 28, 2014.

[69] IMPERX, "Bobcat b6640 specifications." `https://www.imperx.com/wp-content/uploads/2017/11/bobcat_B6640.pdf`, 2014. (Accessed on 09/17/2019).

[70] Cosmologia (now Planet), "Dove 3 orbital debris assessment report (ODAR)," October 2012.

[71] C. Foster, J. Mason, V. Vittaldev, L. Leung, V. Beukelaers, L. Stepan, and R. Zimmerman, "Constellation phasing with differential drag on planet labs satellites," *Journal of Spacecraft and Rockets*, vol. 55, no. 2, pp. 473–483, 2018.

[72] National Aeronautics and Space Administration, *Space Network User's Guide*, August 2012.

[73] Cosmologia (now Planet), "Dove 1 technical description."

[74] Spectrolab, *Triangular Advanced Solar Cells*, April 2002.

[75] C. Schaffer, "A study on the usage of tasc and utj solar cells in the design of a magnetically clean cubesat," in *Proceedings of the 27th annual AIAA/USU Conference on Small Satellites*, vol. 27, 2013.

[76] M. L. Marcus and R. J. Sedwick, "Low earth orbit debris removal technology assessment using genetic algorithms," *Journal of Spacecraft and Rockets*, vol. 54, no. 5, pp. 1110–1126, 2017.

[77] S. Stansbury, "Low thrust transfer to geo: Comparison of electric and chemical propulsion."

[78] V. A. Chobotov, *Orbital mechanics*. American Institute of Aeronautics and Astronautics, 2002.

[79] W. J. Gallagher, K. Solberg, G. G. Gefke, and B. Roberts, "A survey of enabling technologies for in-space assembly and servicing," in *2018 AIAA SPACE and Astronautics Forum and Exposition*, p. 5116, 2018.

[80] B. R. Sullivan, J. Parrish, and G. Roesler, "Upgrading in-service spacecraft with on-orbit attachable capabilities," in *2018 AIAA SPACE and Astronautics Forum and Exposition*, p. 5223, 2018.

[81] W.-J. Li, D.-Y. Cheng, X.-G. Liu, Y.-B. Wang, W.-H. Shi, Z.-X. Tang, F. Gao, F.-M. Zeng, H.-Y. Chai, W.-B. Luo, *et al.*, "On-orbit service (oos) of spacecraft: A review of engineering developments," *Progress in Aerospace Sciences*, 2019.

[82] V. Luchinski, R. Murtazin, O. Sytin, and Y. Ulybyshev, "Mission profile of targeted splashdown for space station mir," *Journal of spacecraft and rockets*, vol. 40, no. 5, pp. 665–671, 2003.

[83] "Ikea table tops."

[84] J. Taylor, K.-M. Cheung, and C.-J. Wong, "Mars global surveyor telecommunications," *NASA DESCANSO Design and Performance Summary Series*, 2001.

[85] J. Taylor, "Dawn telecommunications," *NASA DESCANSO Design and Performance Summary Series*, vol. 13, 2009.

[86] A. Makovsky, A. Barbieri, and R. Tung, "Odyssey telecommunications," *JPL, Descanso Series on Design & Performance Summary*, 2002.

[87] L. M. Hilliard, "Performance characteristics of omnidirectional antennas for spacecraft using nasa networks," no. NASA-TR-100680, 1987.

[88] Harris Corporation, *AS-48915 Series Omnidirectional Conical Spiral Antenna*, October 2010.

[89] J. Zackrisson, "Wide coverage antennas," in *Proceedings of the 21st annual AIAA/USU Conference on Small Satellites*, vol. 21, 2007.

[90] J. Taylor, L. Sakamoto, and C.-J. Wong, "Cassini orbiter/huygens probe telecommunications," *JPL, Descanso Series on Design & Performance Summary*, 2002.

[91] J. Taylor and D. Hansen, "Deep impact flyby and impactor telecommunications," *NASA DESCANSO Design and Performance Summary Series*, 2005.

[92] R. Mukai, D. Hansen, A. Mittskus, J. Taylor, and M. Danos, "Juno telecommunications," *NASA DESCANSO Design and Performance Summary Series*, 2012.

[93] "Lunar reconnaissance orbiter project technical resource allocations specification," no. NASA 431-SPEC-000112, 2007.

[94] J. Taylor, D. K. Lee, and S. Shambayati, "Mars reconnaissance orbiter telecommunications," *DESCANSO Design and Performance Summary Series*, vol. 12, 2006.

[95] R. Ludwig and J. Taylor, "Descanso design and performance summary series article 4: Voyager telecommunications," *Washington: NASA*, pp. 1–6, 2002.

[96] EnerSys, "Enersys absl longmont brochure."